



universität  
wien

# DISSERTATION

Titel der Dissertation

Nanoscale Thermoelectric Materials

Verfasser

Fainan Failamani

angestrebter akademischer Grad

Doktor der Naturwissenschaften (Dr.rer.nat.)

Wien, 2015

Studienkennzahl lt. Studienblatt:

A 796 605 419

Dissertationsgebiet lt. Studienblatt:

Chemie

Betreuer:

Univ.-Prof. Dr. Wolfgang Kautek

*To my beloved mother, the most amazing person I have ever known ....*

## Abstract

Thermoelectric (TE) materials directly convert thermal energy to electrical energy when subjected to a temperature gradient, whereas if electricity is applied to thermoelectric materials, a temperature gradient is formed. The performance of thermoelectric materials is characterized by a dimensionless figure of merit ( $ZT = S^2T/\rho\lambda$ ), which consists of three parameters, Seebeck coefficient ( $S$ ), electrical resistivity ( $\rho$ ) and thermal conductivity ( $\lambda$ ). To achieve good performance of thermoelectric power generation and cooling,  $ZT$ 's of thermoelectric materials must be as high as possible, preferably above unity.

This thesis comprises three main parts, which are distributed into six chapters: (i) nanostructuring to improve TE performance of trivalent rare earth-filled skutterudites (chapter 1 and 2), (ii) interactions of skutterudite thermoelectrics with group V metals as potential electrode or diffusion barrier for TE devices (chapter 3 and 4), and (iii) search for new materials for TE application (chapter 5 and 6).

Addition of secondary phases, especially nano sized phases can cause additional reduction of the thermal conductivity of a filled skutterudite which improves the figure of merit ( $ZT$ ) of thermoelectric materials. In chapter 1 we investigated the effect of various types of secondary phases (silicides, borides, etc.) on the TE properties of trivalent rare earth filled Sb-based skutterudites as commercially potential TE materials.

In this context the possibility to introduce borides as nano-particles (via ball-milling in terms of a skutterudite/boride composite) is also elucidated in chapter 2. As a preliminary study, crystal structure of novel high temperature FeB-type phases found in the ternary Ta-{Ti,Zr,Hf}-B systems were investigated. In case of Ti and Hf this phase is the high temperature stabilization of binary group IV metal monoborides, whereas single crystal study of (Ta,Zr)B proves that it is a true ternary phase as no stable monoboride exist in the binary Zr-B system. Interestingly, the FeB phases are formed only by addition of small amounts of group IV metals to TaB. These high temperature phases may serve as nano particles to decrease the thermal conductivity of the composite by reducing the phonon mean free path on the grain boundaries, thus improving  $ZT$ .

In order to define an electrode material suitable for long-term operation in contact with Sb-based skutterudite thermoelectrics at the hot end of the TE-device, the detailed knowledge of the binary metal - antimony phase diagrams and properties of phases formed in the diffusion zone are required. Hitherto, only the Nb-Sb phase diagram has been reported with some controversial results, whilst the {V,Ta}-Sb phase diagrams have not been constructed yet. Chapter 3 summarizes the investigation on the {V,Nb,Ta}-Sb systems to close this gap and to remove ambiguities from the Nb-Sb diagram. Moreover physical properties of {V,Nb,Ta}Sb<sub>2</sub> that are formed in the diffusion zones have been studied in the temperature region relevant for automotive application of skutterudite thermoelectrics (up to 600°C).

A novel ternary compound with composition close to "Ba<sub>2</sub>V<sub>5</sub>Sb<sub>9</sub>" was observed in the diffusion zones between V and n-type Ba<sub>0.3</sub>Co<sub>4</sub>Sb<sub>12</sub> at 600°C. Structural investigation revealed the correct formula as Ba<sub>5</sub>V<sub>12</sub>Sb<sub>19+x</sub>, isotypic with Ba<sub>5</sub>Ti<sub>12</sub>Sb<sub>19+x</sub>, however, with some additional site occupation and disorder. Search for isotypic compounds among the rest of early transition metals revealed that Nb and Ta form the corresponding phases at 700°C. However, only the formation of Ba<sub>5</sub>Nb<sub>12</sub>Sb<sub>19+x</sub> was confirmed by both XRPD and XRSC data, while neither the bulk nor the single crystal of Ba<sub>5</sub>Ta<sub>12</sub>Sb<sub>19+x</sub> could be

obtained to confirm its formation. A detailed study on the crystal structure and its impact on the physical (transport and thermal) properties of these compounds are presented in chapter 4.

In our search for new TE materials we studied the {La,Ce}-(Ni,Zn)-Si systems. The investigation of the Ce-Zn-Si system at 800°C by Malik et al. gave hints on the formation of two new compounds (labelled as  $\tau_5$  and  $\tau_6$ , structures unknown), which could be useful for TE application. The content of chapter 5 focuses on the investigation of the crystal structures, phase relations, mechanism of formations and stabilities, as well as the physical properties of the novel compounds. An interesting stabilization of hypothetical binary " $\text{Ce}_7\text{Zn}_{23}$ " by Ge has been elucidated from density functional theory (DFT) calculations discussing the electronic structure in terms of the density of states (DOS) and defining enthalpies of formation for  $\text{Ce}_7\text{Zn}_{23-x}\text{Ge}_x$  ( $x = 0, 0.5, 2$ ) as well as for several neighbouring binary Ce–Zn phases. Chapter 6 deals with the quaternary solid solution of  $\text{Ce}(\text{Ni}_{1-x}\text{Zn}_x)_2\text{Si}_2$ , which extends at 800°C from  $\text{CeNi}_2\text{Si}_2$  to  $\text{CeNiZnSi}_2$ , but on further Ni/Zn substitution changes (a) the stoichiometry towards  $\tau_6$  ( $\sim\text{CeZn}_{2.5}\text{Si}_{1.5}$ ) and (b) thermal stability below 700°C. The concomitant change of the ground state of the Ce-atom as a function of Ni/Zn exchange has been monitored by physical property measurements.



## Kurzfassung

Thermoelektrische (TE) Materialien sind einerseits in der Lage thermische Energie direkt in elektrische Energie umzuwandeln, wenn sie sich in einem Temperaturgradienten befinden (thermoelektrischer Generator), andererseits wird ein Temperaturgradient entstehen wenn sie von elektrischem Strom durchflossen werden (Peltier Kühlung). Das thermoelektrische Potenzial eines Materials wird durch die dimensionslose thermoelektrische Gütekennzahl  $ZT$  ausgewiesen ( $ZT = S^2T/\rho\lambda$ ), die sich aus drei Parametern zusammensetzt, den Seebeck Koeffizienten ( $S$ ), den elektrischen Widerstand ( $\rho$ ) und die thermische Leitfähigkeit ( $\lambda$ ). Um einen guten thermoelektrischen Wirkungsgrad in der Erzeugung elektrischer Energie bzw. in der thermoelektrischen Kühlung zu erzielen, sollen  $ZT$  Werte so hoch wie möglich sein, jedenfalls aber höher als 1.

Die vorliegende Dissertation umfasst drei wesentliche Teile die in 6 Kapiteln gegliedert sind: (i) Nanostrukturierung von Skutteruditen, die mit dreiwertigen Seltenerdmetallen gefüllt sind, um das TE-Verhalten zu verbessern (Kapitel 1 und 2), (ii) Untersuchung der Wechselwirkung zwischen Skutterudit-basierenden Thermoelektrika mit Metallen der Gruppe V, die als Elektrodenmaterial oder als Diffusionsbarrieren in TE-Modulen eingesetzt werden (Kapitel 3 und 4), und (iii) Suche nach neuen Materialien für thermoelektrische Anwendungen (Kapitel 5 und 6).

Zusätze von Sekundärphasen zu den thermoelektrischen Skutteruditen, insbesondere im Nanobereich können eine zusätzliche Herabsetzung der thermischen Leitfähigkeit bewirken, die die thermoelektrische Gütekennzahl  $ZT$  erhöht. Im Kapitel 1 wird der Einfluss verschiedener Sekundärphasen (Silizide, Boride, etc.) auf die TE Eigenschaften von Sb-Skutteruditen untersucht, die mit dreiwertigen Seltenerdmetallen gefüllt sind, und die Potenzial in kommerzieller Verwendung besitzen.

In diesem Zusammenhang wird im Kapitel 2 auch die Möglichkeit Boride als Sekundärphasen (in Form eines Komposites Skutterudit/Borid) einzubringen studiert. Dazu werden im Vorfeld die Kristallstrukturen (FeB-Typ) neuer Boride untersucht, die bei hohen Temperaturen in den ternären Systemen Ta- $\{Ti, Zr, Hf\}$ -B aufgefunden wurden. Im Falle von Ti und Hf können diese Phasen als Stabilisierung der binären Metall-Monoboride der Gruppe IV Metalle zu hohen Temperaturen aufgefasst werden, während die Einkristallstudie von (Ta,Zr)B zeigt dass in diesem Fall eine rein ternäre Verbindung vorliegt, da im System Zr-B kein stabiles Monoborid gebildet wird. Interessanter Weise bilden sich die ternären Phasen vom FeB-Typ nur bei kleinen Mengen der Gruppe IV Metalle in der Nähe des TaB. Diese Hochtemperaturphasen können auf Grund ihrer hohen Stabilität (Inertheit gegenüber dem Skutterudit) als Nanopartikel dienen, die in feiner Verteilung die thermische Leitfähigkeit im Nanokomposite durch Reduktion der mittleren freien Weglänge der Phononen im Gitter herabsetzen und damit  $ZT$  erhöhen.

Um ein passendes Elektrodenmaterial auszuwählen bzw. definieren zu können, das Langzeitstabilität im Kontakt mit auf Sb basierenden Skutterudit-Thermoelektrika am heissen Ende eines TE-Moduls garantiert, ist eine detaillierte Kenntnis der binären Phasendiagramme Elektrodenmetall - Antimon nötig sowie auch der Eigenschaften der in der Diffusionszone gebildeten Phasen. Bislang wurde nur über das Phasendiagramm Nb-Sb mit einigen kontroversiellen Informationen berichtet, während die  $\{V, Ta\}$ -Sb Phasendiagramme noch nicht erstellt wurden. Um diese Wissenslücke zu schliessen fasst das Kapitel 3 die Untersuchungen in den Systemen  $\{V, Nb, Ta\}$ -Sb zusammen und räumt die bisherigen Unsicherheiten im Diagramm Nb-Sb aus. Darüber hinaus werden auch die

physikalischen Eigenschaften der Verbindungen  $\{V, Nb, Ta\}Sb_2$  untersucht, die in den Diffusionszonen aufgefunden wurden und zwar in einem Temperaturbereich, relevant für die Verwendung von Skutterudit Thermoelektika in Fahrzeugen ( $< 600^\circ C$ ).

Eine neue ternäre Verbindung mit der ungefähren Zusammensetzung “ $Ba_2V_5Sb_9$ ” wurde in der Diffusionszone zwischen dem Vanadiummetall und dem n-type  $Ba_{0.3}Co_4Sb_{12}$  bei  $600^\circ C$  gebildet. Die Untersuchung der Kristallstruktur mittels Einkristallen ergab die Formel  $Ba_5V_{12}Sb_{19+x}$ , isotyp mit der Struktur von  $Ba_5Ti_{12}Sb_{19+x}$ , allerdings mit zusätzlicher atomarer Besetzung und atomarer Ungeordnetheit. Die Suche nach isotypen Vertretern dieses Strukturtyps unter den d-elektronenarmen Übergangsmetallen zeigte dass auch Nb und Ta bei  $700^\circ C$  entsprechende Phasen bilden können. Es konnte jedoch nur  $Ba_5Nb_{12}Sb_{19+x}$  mit XRPD und XRSC Analysen bestimmt werden, da im Falle von  $Ba_5Ta_{12}Sb_{19+x}$  weder die Phase selbst in ausreichender Menge noch ein Einkristall erhalten werden konnten. Das Kapitel 4 liefert detaillierte Resultate zur Untersuchung der Kristallstruktur sowie zum Einfluss der atomaren Unordnung auf die physikalischen Eigenschaften (Transporteigenschaften) der Verbindungen.

Auf der Suche nach neuen TE Materialien wurden die  $\{La, Ce\}$ -(Ni,Zn)-Si näher betrachtet. Schon die Untersuchungen des Systems Ce-Zn-Si bei  $800^\circ C$  durch Malik et al. lieferten Hinweise auf die Bildung von zwei neuen Verbindungen, die eventuell für thermoelektrische Anwendungen nützlich sein könnten (diese Verbindungen, deren Struktur bislang unbekannt war, werden mit  $\tau_5$  und  $\tau_6$  bezeichnet). Der Inhalt des Kapitels 5 befasst sich mit der Untersuchung der Kristallstrukturen, der thermodynamischen Phasenbeziehungen, mit der Bildung und den thermodynamischen Stabilitäten, sowie mit den physikalischen Eigenschaften dieser neuen Verbindungen. Dichtefunktionaltheorie Rechnungen beschäftigen sich (a) mit der Stabilisierung hypothetischer binärer Verbindungen “ $Ce_7Zn_{23}$ ” durch kleinste Mengen Si/Ge (Berechnung der Bildungsenthalpien für  $Ce_7Zn_{23-x}Ge_x$  ( $x = 0, 0.5, 2$ ) in Relation zu den benachbarten Phasen), sowie (b) mit der elektronischen Struktur (DOS). Das Kapitel 6 betrifft die quaternäre feste Lösung  $Ce(Ni_{1-x}Zn_x)_2Si_2$ , die sich bei  $800^\circ C$  von  $CeNi_2Si_2$  bis zu  $CeNiZnSi_2$  erstreckt, die sich aber bei weiterem Ni/Zn Ersatz verändert: (a) die Stöchiometrie tendiert zu  $\tau_6$  ( $\sim CeZn_{2.5}Si_{1.5}$ ) und (b) die thermische Stabilität sinkt unter  $700^\circ C$ . Der durch Ni/Zn Ersatz veränderte Grundzustand des Ce-atoms wird durch physikalische Messungen begleitet.

## Table of Content

Abstract.....	i
Kurzfassung.....	iii
Introduction .....	1
1.    Motivations.....	1
1.1.    Thermoelectric materials .....	1
1.2.    Electrode material development.....	3
1.3.    Search for new TE materials .....	4
2.    Tasks of the present work.....	4
3.    References .....	5
Chapter 1 Nanostructuring of CoSb <sub>3</sub> -based Skutterudites via Chemical Disproportionation	8
Abstract.....	9
1.    Introduction .....	9
2.    Experimental Methods.....	10
3.    Results and Discussion.....	11
3.1.    Unfilled CoSb <sub>3</sub> /(W,TaSb <sub>2</sub> ) .....	11
3.2.    Single-filled Ce <sub>y</sub> Co <sub>4</sub> Sb <sub>12</sub> /CoSi .....	12
3.3.    Multifilled RE <sub>y</sub> Co <sub>4</sub> Sb <sub>12</sub> /CoSi .....	13
3.4.    Multifilled RE <sub>y</sub> Co <sub>4</sub> Sb <sub>12</sub> /RESb <sub>2</sub> .....	14
4.    Conclusion.....	14
5.    Acknowledgement.....	14
6.    References .....	15
Chapter 2 High Temperature FeB-type Phases in the Systems Ta-{Ti,Zr,Hf}-B.....	22
Abstract.....	23
1.    Introduction .....	23
2.    Experimental Details .....	24
3.    Results and Discussion.....	25
3.1.    Formation of FeB-type Compounds in the Systems Ta-{Ti,Zr,Hf}-B.....	25
3.2.    The Crystal Structure of Ta <sub>0.78</sub> Zr <sub>0.22</sub> B with FeB-type .....	28
4.    Conclusions .....	29
5.    Acknowledgements .....	30
6.    References .....	30
Chapter 3 Constitution of the Systems {V,Nb,Ta}-Sb and Physical Properties of di- antimonides {V,Nb,Ta}Sb <sub>2</sub> .....	42
Abstract.....	43
1.    Introduction .....	44
2.    Experimental Methods.....	44
3.    Results and Discussions .....	47
3.1.    The V-Sb system .....	47
3.2.    The Nb-Sb system .....	54
3.3.    The Ta-Sb system.....	55
3.4.    Physical Properties of Binary Antimonides {V,Nb,Ta}Sb <sub>2</sub> .....	56
4.    Conclusions .....	61
5.    Acknowledgements .....	62
6.    References .....	62
Chapter 4 Ba <sub>5</sub> {V,Nb} <sub>12</sub> Sb <sub>19+x</sub> , Novel Variants of the Ba <sub>5</sub> Ti <sub>12</sub> Sb <sub>19+x</sub> -type: Crystal Structure and Physical Properties.....	78
Abstract.....	79

1. Introduction .....	79
2. Experimental Methods.....	80
3. Results and Discussion .....	83
3.1. Structure solution and refinement.....	83
3.2. Structural chemistry of the phases $Ba_5\{V,Nb\}_{12}Sb_{19+x}$ .....	86
3.3. Physical properties.....	87
4. Conclusions .....	94
5. Acknowledgement .....	95
6. References .....	95
Supplementary .....	107
Chapter 5 The System Ce-Zn-Si for <33.3 at.% Ce: Phase Relations, Crystal Structures and Physical Properties .....	109
Abstract.....	110
1. Introduction .....	110
2. Experimental Methods and Density Functional Theory Calculation .....	112
3. Results and Discussions .....	115
3.1. Binary boundary systems .....	115
3.2. Crystal structure of ternary compounds in the Ce-Zn-Si system.....	115
3.3. Phase stability of $Ce_7Zn_{23-x}Ge_x$ .....	118
3.4. Partial isothermal section at 600°C for less than 33.3 at% Ce .....	120
3.5. Formation of $\tau_5$ and $\tau_6$ and partial Schulz-Scheil diagram .....	122
3.6. Physical Properties of $\tau_5$ -CeZn( $Zn_{1-x}Si_x$ ) <sub>2</sub> and $\tau_6$ -CeZn <sub>2</sub> ( $Zn_{0.28}Si_{0.72}$ ) <sub>2</sub> .....	125
4. Conclusions .....	127
5. Acknowledgements .....	128
6. References .....	128
Supplementary .....	145
Chapter 6 BaAl <sub>4</sub> Derivative Phases in the Sections {La,Ce}Ni <sub>2</sub> Si <sub>2</sub> -{La,Ce}Zn <sub>2</sub> Si <sub>2</sub> : Phase Relations, Crystal Structures and Physical Properties .....	147
Abstract.....	148
1. Introduction .....	148
2. Experimental Methods.....	150
3. Results and Discussion .....	151
3.1. The BaAl <sub>4</sub> -type derivative phases in the systems La-Ni-Si and Ce-Ni-Si .....	151
3.2. The quaternary solution phases La(Ni <sub>1-x</sub> Zn <sub>x</sub> ) <sub>2</sub> Si <sub>2</sub> and Ce(Ni <sub>1-x</sub> Zn <sub>x</sub> ) <sub>2</sub> Si <sub>2</sub> .....	154
3.3. Physical properties of La(Ni <sub>1-x</sub> Zn <sub>x</sub> ) <sub>2</sub> Si <sub>2</sub> and Ce(Ni <sub>1-x</sub> Zn <sub>x</sub> ) <sub>2</sub> Si <sub>2</sub> .....	156
4. Conclusions .....	159
5. Acknowledgements .....	160
6. References .....	160
Summary.....	174
Acknowledgements .....	178
Curriculum Vitae .....	179
List of Publications.....	180
List of Conference Contributions .....	181

# Introduction

## 1. Motivations

### 1.1. Thermoelectric materials

Global energy consumption has always been a major problem to overcome, especially due to its increase over the years, together with the diminishing source of fossil fuels as the main energy source. Other alternative energy sources, e.g. nuclear, geothermal etc provide solutions to the fossil fuel problem. However, in most cases the majority of the produced energy is lost in form of waste heat (up to 70%) [1].

Thermoelectric (TE) devices offer a possibility to directly convert waste heat into electricity (thermoelectric generator), thus providing a promising solution to increase the efficiency of the energy usage in the future. The performance of a thermoelectric device is represented by the dimensionless figure of merit ( $ZT$ ), which depends on the electrical resistivity ( $\rho$ ), Seebeck coefficient ( $S$ ), and the thermal conductivity<sup>1</sup> ( $\lambda$ ):

$$ZT = \frac{S^2 T}{\rho \lambda} \quad (1).$$

The combination of terms in equation (1) already defines the optimization routes to obtain high  $ZT$  materials: unfortunately all three main parameters are interdependent, therefore any optimization has to find the best compromise.

$S$  and  $\rho$  ( $= 1/\sigma$ )<sup>2</sup> are interlinked via the charge carrier density ( $n$ ) by Mott's formula [2]

$$S = \frac{2\pi^2 k_B^2 m_e}{|e| \hbar^2 (3n\pi^2)^{2/3}} T \quad (2),$$

where  $m_e$  is the electron mass ( $9.11 \times 10^{-31}$  kg),  $\hbar$  is the reduced Planck's constant ( $1.055 \times 10^{-34}$  Js), and  $k_B$  is the Boltzmann constant ( $1.38 \times 10^{-23}$  J/K).  $\rho$  and  $\lambda$  are partially connected via the Wiedemann Franz law [3]

$$\lambda_e = \frac{LT}{\rho} \quad (3),$$

where  $L$  is the Lorenz number ( $L_0 = 2.45 \times 10^{-8}$  W $\Omega$ K<sup>-2</sup> for metals and degenerate semiconductors).

---

<sup>1</sup> ( $\lambda = \lambda_{ch} + \lambda_{ph}$ , where  $\lambda_{ch}$  is the thermal conductivity of the charge carriers and  $\lambda_{ph}$  is the thermal conductivity of the lattice phonons)

<sup>2</sup>  $\sigma = n\mu|e|$ , where  $n$  is the charge carrier concentration,  $\mu$  is the charge carrier mobility and  $e$  is the elementary charge ( $1.602 \times 10^{-19}$  C)

The overall efficiency ( $\eta$ ) of a TE generator device depends also on the temperature gradient between the hot ( $T_H$ ) and the cold side ( $T_C$ ) as proposed by Ioffe [4]:

$$\eta = \frac{T_H - T_C}{T_H} \frac{\sqrt{ZT_{av} + 1}}{\sqrt{ZT_{av} + 1} + \frac{T_C}{T_H}} \quad (2)$$

involving  $ZT_{av}$ , which is the average  $ZT$  in the temperature interval of the T-gradient supplied. The use of TE power generators has been demonstrated since years, particularly for the deep space exploration where solar energy is inaccessible. In this case the large temperature gradient between the heat produced by the radioisotope decay and the temperature of the outer space provide enough conversion efficiency to power the space station.

The automotive application of a TE generator, however, is limited by its smaller temperature gradient. Moreover the best known TE material,  $\text{Bi}_2\text{Te}_3$  is known to have low thermal stability ( $T_{\text{melt}} = 586^\circ\text{C}$ ) [5], and maximum TE performance at  $\sim 150^\circ\text{C}$  [3]. The small abundance of Te in the earth's crust and its toxicity become a problem for future large scale productions. Therefore high performance TE materials with high thermal stability ( $T_{\text{melt}} > 650^\circ\text{C}$ ) are preferable for such an application. Several materials have been known to fulfil such requirements, such as lead telluride based materials, skutterudites, half Heusler alloys, intermetallic clathrates, and some Zintl compounds [6].

Among those classes of materials, skutterudites<sup>3</sup> are one of the most promising TE materials, not only due to their excellent TE properties but also due to the relatively high abundance of the constituents [1]. Via optimization of (i) the semiconducting band edge (by introducing various amounts and kinds of filler atoms) as well as by (ii) chemical substitution on Co and Sb sites, maximum  $ZT$ 's of 1.8 [9] and 1.4 [10] have been achieved for bulk n- and p-type skutterudites, respectively. Nanostructuring of these skutterudites

---

<sup>3</sup> Skutterudites derive from parent  $\text{CoAs}_3$ , a body centered cubic crystal structure of low Laue symmetry  $Im\bar{3}$ , with a 3-dimensional As-metal framework (As in sites 24g), which encloses Co-atoms at the centers of tilted As-octahedra (sites 8c) and provides ample icosahedral space (in sites 2a) for the incorporation of "filler" atoms [7]. Thermoelectric skutterudites are mainly based on  $\text{CoSb}_3$ . Correspondingly, filled skutterudites have a structural-chemical formula  $\text{EP}_y(\text{Co}_{1-x}\text{T}_x)_4(\text{Sb}_{1-z}\text{X}_z)_1$ , where EP is usually an electropositive element species (alkaline, alkaline earth, rare earth metals, Ga, In, Tl), T is one of the iron group metals (Fe, Ni etc.) and X stands for Sn, Ga, In etc [7].

Thermoelectric skutterudites are viewed as examples of the so called PGEC concept (Phonon Glass and Electron Crystal) proposed by Slack [8]: an open crystallographic structure, where framework atoms provide excellent electronic properties, whilst filling the voids with "rattling" fillers (= weakly bound atoms in the oversized icosahedral cage) reduces the lattice thermal conductivity to values characteristic for amorphous structures via enhanced scattering of the heat carrying phonons.

particularly via high pressure torsion<sup>4</sup> (HPT) have increased the ZT value even up to ~2.0 [12]. However, the nanostructuring effect was found to be partially cancelled out during a short heat treatment, even during the measurement at high temperature. Moreover the mechanical stability of HPT treated alloys is in general lower than that of untreated alloys as shown by formation of microcracks and pores after HPT [13].

Another approach to introduce nanostructuring in skutterudite can be performed via nano inclusion/precipitation of secondary phases. In uniform distribution these nano-precipitates enhance phonon-scattering and thereby lower the phonon thermal conductivity. These methods have been proven to be effective to produce thermally stable bulk nanostructured skutterudites [12,14–16]. The most prominent effect of this kind of nanostructuring can be seen in the reduction of lattice thermal conductivity, which leads to an increase of the ZT value.

It is worth mentioning that most of the best n-type skutterudites require divalent fillers such as Yb, Ba, Sr, etc [9,17,18]. The alkaline earth elements are known for their high reactivity; therefore it is inconvenient to use such elements in a large scale production. Ytterbium on the other hand is easier to handle, however, its relatively low abundance in the earth's crust compared to the other rare earth (RE) metals such as cerium, lanthanum, and yttrium would also pose a problem in future productions. Therefore it would be preferable to have high TE performance skutterudites with abundant RE as the main fillers for the commercial purpose.

## **1.2. Electrode material development**

Beside the good performance of the p- and n-type TE materials, a suitable contact material is also an important factor defining the overall performance of the TE devices. For high temperature application this has become a more important issue since at high temperature interaction between electrode and the TE materials is unavoidable. Thus it is important that the interaction between the electrode and the TE materials is minimized. Moreover the mechanical compatibility, e.g. the thermal expansion coefficient, good thermal and electrical transport between the electrode and the TE materials have to be maintained. For Sb-based skutterudites, several metals have been studied as the potential electrode materials. In general electrode based on 3d metals exhibit severe interactions, i.e. formation of intermetallic compound(s) with the skutterudite after long term thermal aging

---

<sup>4</sup> HPT is a process of severe plastic deformation for grain refining (into the nanosize regime) introducing new grain boundaries, dislocations, defects, cracks and pores, all serving as centers for phonon scattering [11].

[19–22], therefore in some cases a diffusion layer based on early transition metals such as Mo and Ti was used [23]. For such purposes knowledge of binary phase diagrams electrodemetal-antimony as well the transport and mechanical properties of the phases formed in diffusion zones are required.

### 1.3. Search for new TE materials

Despite the excellent TE properties of skutterudites, the improvement of the ZT values seems to reach a saturation value of  $\sim 2.0$ . Therefore it is deemed necessary to explore new systems to find new materials with promising TE performance. As mentioned above La and Ce are among the most abundant rare earth metals. A few La and Ce compounds have been found to exhibit promising TE properties such as  $\text{CePd}_3$  [24] and  $\text{La}_3\text{Te}_4$  [25].

## 2. Tasks of the present work

Based on the motivations mentioned above the present work is divided into five parts, which are distributed into six chapters:

1. Investigation of n-type skutterudites with trivalent rare earth fillers and of the effect of nano precipitates/composites of various kinds: metals, antimonides, and silicides.
2. Furthermore, the possibility of using high temperature borides as composites is envisaged. In this context a study of the formation and the crystal structure of novel high temperature FeB type phases  $\text{Ta}\{\text{Ti}, \text{Zr}, \text{Hf}\}\text{B}$  was performed.
3. In order to define a suitable electrode/diffusion barrier for skutterudites TE, interaction between various metals, particularly group V metals with p- and n-type skutterudite were studied. Here the binary phase diagrams of group V metals and antimony, as well as the physical properties of the binary compounds  $\{\text{V}, \text{Nb}, \text{Ta}\}\text{Sb}_2$  formed in the diffusion zones were investigated.
4. Interaction between vanadium and n-type  $\text{Ba}_{0.3}\text{Co}_4\text{Sb}_{12}$  revealed the formation of a new compound with chemical formula of  $\text{Ba}_5\text{V}_{12}\text{Sb}_{19+x}$ . It was further discovered that Nb forms an isotypic compound. In order to get information on the suitability of V, Nb, Ta metals as a diffusion barrier for the hot electrode in a TE-generator the crystal structures and physical properties of the novel compounds formed were investigated.
5. A previous study by Zahida Malik [26] on the phase equilibria in the  $\{\text{La}, \text{Ce}\}-\{\text{Ni}, \text{Zn}\}-\text{Si}$  systems gave hints to the formation of several new ternary and quaternary phases. Preliminary formulae were derived for novel Ce-Zn-Si compounds, for which electron counts in some cases suggested a Zintl behaviour interesting for thermoelectric



behaviour. Therefore a detailed and systematic investigation of the phase relations, crystal structures and physical properties deemed necessary to characterize the compounds in the Zn-rich part of the Ce-Zn-Si system at 600°C as well as for the isopleths  $\{La,Ce\}\{Ni,Zn\}_2Si_2$ . Among these studies an interesting case was observed (and investigated) in the stabilisation of ternary compounds  $\{La,Ce\}_7Zn_{21}[Zn_{1-x}Si(Ge)_x]_2$  by extremely small amounts of tetrel elements (as low as 1 at.% Ge) suggesting hypothetical binary phases “ $\{La,Ce\}_7Zn_{23}$ ”.

For all these investigations standard sample preparation methods were used such as arc melting, powder metallurgy, and flux growth (for single crystals). X-ray (powder and single crystal) diffraction served as the main structural elucidation method, while the compositions were defined from electron probe microanalysis (EPMA). Various physical properties, e.g. electrical resistivity, specific heat, magnetic susceptibility, etc were measured on commercial and home made equipments as described in ref. [27] and in the individual chapters.

### 3. References

- [1] M. Rull-Bravo, A. Moure, J.F. Fernández, M. Martín-González, Skutterudites as thermoelectric materials: revisited, *RSC Adv.* 5 (2015) 41653–41667.
- [2] G.J. Snyder, E.S. Toberer, Complex thermoelectric materials, *Nat. Mater.* 7 (2008) 105–114.
- [3] H.J. Goldsmid, *Introduction to Thermoelectricity*, Springer Berlin Heidelberg, Berlin, Heidelberg, 2010.
- [4] A.F. Ioffe, *Semiconductor thermoelements, and Thermoelectric cooling*, Infosearch, London, 1957.
- [5] *Pauling File Binary Edition*, Version 1.0, Release 2002/1, ASM international, Materials Park, OH, USA, 2002.
- [6] P. Sundarraj, D. Maity, S.S. Roy, R.A. Taylor, Recent advances in thermoelectric materials and solar thermoelectric generators – a critical review, *RSC Adv.* 4 (2014) 46860–46874.
- [7] P. Villars, K. Cenzual, *Pearson’s Crystal Data—Crystal Structure Database for Inorganic Compounds*, release 2014/15, ASM International, Materials Park, OH, USA, 2014.
- [8] G. A. Slack, New Materials and Performance Limits for Thermoelectric Cooling, in: D. Rowe (Ed.), *CRC Handbook of Thermoelectrics*, CRC Press, 1995.

- [9] G. Rogl, A. Grytsiv, K. Yubuta, S. Puchegger, E. Bauer, C. Raju, et al., In-doped multifilled n-type skutterudites with  $ZT = 1.8$ , *Acta Mater.* 95 (2015) 201–211.
- [10] G. Rogl, A. Grytsiv, P. Heinrich, E. Bauer, P. Kumar, N. Peranio, et al., New bulk p-type skutterudites  $DD_{0.7}Fe_{2.7}Co_{1.3}Sb_{12-x}X_x$  ( $X = Ge, Sn$ ) reaching  $ZT > 1.3$ , *Acta Mater.* 91 (2015) 227–238.
- [11] E. Schafler, K. Simon, S. Bernstorff, P. Hanák, G. Tichy, T. Ungár, et al., A second-order phase-transformation of the dislocation structure during plastic deformation determined by in situ synchrotron X-ray diffraction, *Acta Mater.* 53 (2005) 315–322.
- [12] G. Rogl, A. Grytsiv, P. Rogl, N. Peranio, E. Bauer, M. Zehetbauer, et al., n-Type skutterudites  $(R,Ba,Yb)_yCo_4Sb_{12}$  ( $R = Sr, La, Mm, DD, SrMm, SrDD$ ) approaching  $ZT \approx 2.0$ , *Acta Mater.* 63 (2014) 30–43.
- [13] G. Rogl, A. Grytsiv, J. Bursik, J. Horky, R. Anbalagan, E. Bauer, et al., Changes in microstructure and physical properties of skutterudites after severe plastic deformation, *Phys. Chem. Chem. Phys.* 17 (2015) 3715–3722.
- [14] J. Eilertsen, Y. Surace, S. Balog, L. Sagarna, G. Rogl, J. Horky, et al., From Occupied Voids to Nanoprecipitates: Synthesis of Skutterudite Nanocomposites in situ, *Z. Anorg. Allg. Chem.* 641 (2015) 1495–1502.
- [15] J. Eilertsen, S. Rouvimov, M.A. Subramanian, Rattler-seeded InSb nanoinclusions from metastable indium-filled  $In_{0.1}Co_4Sb_{12}$  skutterudites for high-performance thermoelectrics, *Acta Mater.* 60 (2012) 2178–2185.
- [16] Z. Xiong, X. Chen, X. Huang, S. Bai, L. Chen, High thermoelectric performance of  $Yb_{0.26}Co_4Sb_{12}/yGaSb$  nanocomposites originating from scattering electrons of low energy, *Acta Mater.* 58 (2010) 3995–4002.
- [17] G. Rogl, A. Grytsiv, N. Melnychenko-Koblyuk, E. Bauer, S. Laumann, P. Rogl, Compositional dependence of the thermoelectric properties of  $(Sr_xBa_xYb_{1-2x})_yCo_4Sb_{12}$  skutterudites, *J. Phys.: Condens. Matter.* 23 (2011) 275601.
- [18] X. Shi, J. Yang, J.R. Salvador, M. Chi, J.Y. Cho, H. Wang, et al., Multiple-Filled Skutterudites: High Thermoelectric Figure of Merit through Separately Optimizing Electrical and Thermal Transports, *J. Am. Chem. Soc.* 133 (2011) 7837–7846.
- [19] M. Gu, X. Xia, X. Li, X. Huang, L. Chen, Microstructural evolution of the interfacial layer in the  $Ti-Al/Yb_{0.6}Co_4Sb_{12}$  thermoelectric joints at high temperature, *J. Alloy Compd.* 610 (2014) 665–670.
- [20] D. Zhao, H. Geng, L. Chen, Microstructure Contact Studies for Skutterudite Thermoelectric Devices, *Int. J. Appl. Ceram. Tech.* 9 (2012) 733–741.

- [21] D. Zhao, C. Tian, S. Tang, Y. Liu, L. Jiang, L. Chen, Fabrication of a CoSb<sub>3</sub>-based thermoelectric module, *Mat. Sci. Semicon. Proc.* 13 (2010) 221–224.
- [22] D. Zhao, H. Geng, X. Teng, Fabrication and reliability evaluation of CoSb<sub>3</sub>/W–Cu thermoelectric element, *J. Alloy Compd.* 517 (2012) 198–203.
- [23] X.C. Fan, M. Gu, X. Shi, L.D. Chen, S.Q. Bai, R. Nunna, Fabrication and reliability evaluation of Yb<sub>0.3</sub>Co<sub>4</sub>Sb<sub>12</sub>/Mo–Ti/Mo–Cu/Ni thermoelectric joints, *Ceram. Int.* 41 (2015) 7590–7595.
- [24] S.R. Boona, D.T. Morelli, Relationship between structure, magnetism, and thermoelectricity in CePd<sub>3</sub>M<sub>x</sub> alloys, *J. Appl. Phys.* 112 (2012) 063709.
- [25] A.F. May, J.-P. Fleurial, G.J. Snyder, Optimizing Thermoelectric Efficiency in La<sub>3-x</sub>Te<sub>4</sub> via Yb Substitution, *Chem. Mater.* 22 (2010) 2995–2999.
- [26] Z.P. Malik, On the quaternary systems Ce-Ni-Zn {B, Si}, Ph.D. Thesis, University of Vienna, 2012.
- [27] I. Zeiringer, Non-centrosymmetric superconducting compounds, Ph.D. Thesis, University of Vienna, 2015.

# Chapter 1 Nanostructuring of CoSb<sub>3</sub>-based Skutterudites via Chemical Disproportionation

F. Failamani<sup>a,b</sup>, A. Grytsiv<sup>a,d</sup>, P. Rogl<sup>a,d</sup>, E. Bauer<sup>c,d</sup>

<sup>a</sup> *Institute of Material Chemistry and Research, University of Vienna, Währingerstraße 42 A-1090 Vienna, Austria*

<sup>b</sup> *Institute of Physical Chemistry, University of Vienna, Währingerstraße 42 A-1090 Vienna, Austria*

<sup>c</sup> *Institute of Solid State Physics, Vienna University of Technology, Wiedner Hauptstraße 8-10, A-1040 Vienna, Austria*

<sup>d</sup> *Christian Doppler Laboratory for Thermoelectricity, Vienna, Austria*

(to be submitted)

Contributions to this paper:

- F. Failamani : samples preparation, analysis, TE properties measurements and evaluation, writing the paper
- A. Grytsiv : diffusion couple experiments, discussions and advice, TE properties measurements, proofreading
- P. Rogl : discussions and advice, proofreading
- E. Bauer : discussions and advice, proofreading

## Abstract

Nano-structuring is known as an efficient way to improve thermoelectric (TE) properties. Here we propose a novel method for the formation of in-situ nano-precipitates of secondary phases in a skutterudite matrix via a chemical disproportionation reaction. Preparation methods were developed in order to induce nano precipitation of metals, silicides, and antimonides in n-type  $\text{Ep}_y\text{Co}_4\text{Sb}_{12}$  ( $\text{Ep} = \text{La, Ce, Pr, Sm}$ ) skutterudites. The influence of different types of precipitates, their size and distribution on TE properties was investigated. Furthermore, combinations of various trivalent rare earth fillers were studied. The optimisation of composition and preparation techniques performed during the current investigation resulted in a maximum  $ZT_{700\text{K}}=1.3(1)$  for  $(\text{Ce,Sm,Pr})_{0.13}\text{Co}_4\text{Sb}_{12}$ , being among the highest values for n-type skutterudites filled with trivalent rare-earths.

*Keywords: skutterudites, nano precipitates, thermoelectric, disproportionation*

## 1. Introduction

Not long after its structural characterization in 1954 by Rosenqvist [1],  $\text{CoSb}_3$  attracted attention due to its excellent thermoelectric potential [2]. The only problem is that  $\text{CoSb}_3$  possesses a rather high thermal conductivity, which is unfavourable to achieve a high ZT. In the 1970's Jeitschko and Braun [3] discovered that electropositive elements could be incorporated in the icosahedral void in the skutterudite structure (at site  $2a$ ). This discovery then led to the synthesis of various compounds belonging to a new class of materials called filled skutterudites. Few years later, some of the filled skutterudite compounds were found to exhibit superconductivity at low temperature [4].

In 1994 Slack proposed the so called phonon glass-electron crystal (PGEC) concept, which is essentially separating the phonon transport from electron transport. Therefore it is possible to achieve low thermal conductivity while keeping good electrical properties. This concept was demonstrated for the filled skutterudite  $\text{CeFe}_4\text{Sb}_{12}$  [5], and some other skutterudites by the same group of authors [6–8,8–10], with ZT values exceeding unity at  $600^\circ\text{C}$  for p-type  $\text{CeFe}_{3.5}\text{Co}_{0.5}\text{Sb}_{12}$  [6].

Further development of skutterudite TEs by filling and doping resulted in ZT above unity for both p- and n-type materials [11–15]. Moreover, nanostructuring was found to provide effective ways to further reduce the lattice thermal conductivity of skutterudites. There are several ways to introduce bulk-nanostructuring in skutterudite: (i) reduction of crystallite size either via ball-milling or severe plastic deformation, e.g. high pressure torsion [13,16–20], (ii) introducing a nano-sized secondary phase [16,20–22]. In both cases,

nanostructuring serves to create additional phonon scattering on nano-particles within grains or at grain boundaries besides scattering on defects, dislocations, pores/micro-cracks.

Diffusion couple experiments between various skutterudites and metals, particularly tungsten at a first glance revealed in micrographs several “new compounds” in the W-Co-Sb system with composition close to  $\sim W_xCoSb$  and  $\sim W_xCo_4Sb_{12}$  (see left panel in Figure 1). Careful investigation of these “new compounds” revealed that it was actually a very fine precipitate of tungsten on binary  $CoSb_x$ , as the X-ray powder diffraction spectra from various samples were completely indexed on the basis of binary and unary constituents (see right panel in Figure 1). In this case the initially dissolved W in Co matrix (or in form of intermetallic compound(s)) was released as an equilibrium phase forming a fine precipitate on binary  $CoSb_x$ . The reaction can be generally written as:  $Ep_xA_yCo_4 + 12Sb \rightarrow Ep_xCo_4Sb_{12} + y(A)$ ; where (A) could be a single element or an intermetallic compound, depending on the equilibrium conditions.

Based on this observation we tried to implement this method to introduce various nano precipitates in the skutterudite matrix in order to reduce the lattice thermal conductivity via grain boundary phonon scattering. Preparation methods were developed in order to induce nano precipitation of various type of materials: metals, silicides, antimonides, and borides in n-type skutterudites  $Ep_yCo_4Sb_{12}$  ( $Ep = La, Ce, Pr, Sm$ ). The influence of different types of precipitates, their size and distribution on TE properties was investigated. Furthermore, thermoelectric properties of the nano-structured materials were compared with reference skutterudites of same composition without nano precipitates.

## 2. Experimental Methods

Samples were prepared by powder metallurgical techniques from rare earth pieces, freshly prepared cobalt pieces and powder, silicon pieces (all of minimum purity of 99.9 mass%), antimony powder, and tungsten powder. Tungsten powder and antimony ingots prior to use were purified by remelting them in a Ti-gettered Argon arc furnace. Antimony powders were prepared by crushing the remelted ingots inside an Ar-filled glove box and sieving below 300  $\mu m$ . Master alloys  $RE_xCo_4(prec)_y$  (prec stands for precipitating element) were prepared by arc melting proper ratios of pieces of rare earth, cobalt and precipitating elements. Master alloys were remelted twice to ensure homogeneity and then were crushed below 150  $\mu m$  inside an oxygen and water monitored glove box and mixed with antimony powder. An extra 3 weight percent of antimony was added to compensate the losses during

reaction. Samples were sealed under vacuum and reacted at various temperatures for two to four days. In case of reference samples, master alloys were prepared without precipitating element and were prepared at a RE-rich composition. Master alloys then were powderized and mixed with proper amounts of cobalt and antimony powders and then were processed in the same way as the samples with precipitation. After reaction, samples were quenched in cold water and powderized and/or ball milled to homogenize them. Densification was performed by hot pressing in a 1 cm diameter graphite die at 700°C for 1 hour under Ar at a pressure of 56 MPa. Relative densities of hot pressed samples were measured by Archimedes' method and were found to be at least 98%.

X-ray powder diffraction patterns were collected with Cu-K $\alpha_1$  employing a Guinier-Huber image plate recording system. Initial sample purity was confirmed from Rietveld refinement using the program FullProf [23]. Precise lattice parameters were calculated by least squares methods with program STRUKTUR [24] employing Si/Ge as internal standards. Sample homogeneity and quantitative elemental analysis were performed by SEM on a Zeiss Supra 55 VP equipped with an energy dispersive X-ray (EDX) detector operated at 20 kV. For this purpose, samples were mounted in a conductive phenolyc resin and polished with standard metallographic procedures. Prior to SEM-EDX analysis, polished samples were examined with light optical microscope (LOM).

Seebeck coefficient and electrical resistivity were measured in a ZEM3 (ULVAC-RIKO Japan) on a bar-shaped sample, while the thermal conductivity was measured with a laser flash method in a Flashline 3000 (ANTER-USA). Details on the sample preparation and measurement methods can be found in ref. [15].

### **3. Results and Discussion**

#### **3.1. Unfilled CoSb<sub>3</sub>/(W,TaSb<sub>2</sub>)**

In order to demonstrate the effect of the nano precipitates on the TE properties of skutterudite, we performed a preliminary study of W and TaSb<sub>2</sub> precipitates on unfilled CoSb<sub>3</sub> in order to check whether it is possible to reduce its lattice thermal conductivity. Microstructural analysis revealed the formation of nano-sized precipitates on skutterudite (see Figure 2).

Indeed thermal conductivity measurements revealed reduced lattice thermal conductivities in all samples compared to pristine CoSb<sub>3</sub>, where the lowest value is found for the TaSb<sub>2</sub>/CoSb<sub>3</sub> alloy. Addition of W and TaSb<sub>2</sub> seems to affect the transport properties as indicated by the different behaviour of each sample (see Figure 3). EPM analysis, however,

did not reveal any sign of incorporation of the precipitating elements inside the skutterudite lattice. Since the unfilled  $\text{CoSb}_3$  does not possess a high power factor, and the addition of precipitating elements in some cases reduced the power factor, additions of W and  $\text{TaSb}_2$  do not improve the overall TE performance of  $\text{CoSb}_3$ . Nevertheless the idea to reduce the lattice thermal conductivity of  $\text{CoSb}_3$  by introducing in-situ nano precipitates proved to be successful.

### 3.2. Single-filled $\text{Ce}_y\text{Co}_4\text{Sb}_{12}/\text{CoSi}$

From the preliminary study on unfilled  $\text{CoSb}_3$  it is obvious that the filling level in filled skutterudite compounds is one of the key factors that determine its thermoelectric properties [25]. Based on the Zintl count,  $\text{CoSb}_3$  is a charge balanced compound, thus introducing a filler atom in the 2a site will increase the number of free electrons and as a consequence filled  $\text{RE}_y\text{Co}_4\text{Sb}_{12}$  are expected to be n-type semiconductors. A small degree of filling of Ce in the icosahedral void was found to increase the TE properties of skutterudite significantly, as the electrical resistivity and the thermal conductivity are significantly reduced while the Seebeck coefficient remains at a reasonable value [9].

From an early study of Ce-filled skutterudite  $\text{Ce}_y\text{Co}_4\text{Sb}_{12}$  [9], the maximum filling level (y) was then believed to be  $y=0.1$ . However, during the investigation of the isothermal section of the Ce-Co-Sb system at  $400^\circ\text{C}$ , Luo et al. [26] reported nearly a zero filling level of Ce in  $\text{CoSb}_3$ . In our investigation, we hardly saw signs of Ce-filling in  $\text{CoSb}_3$  at  $600^\circ\text{C}$ . Our measured lattice parameters from samples prepared by isothermal reaction at  $600^\circ\text{C}$  showed only slightly higher values than for unfilled  $\text{CoSb}_3$ , indicating a small filling level at this temperature. This result seems to suggest a strong temperature dependence of the Ce filling level in  $\text{CoSb}_3$ . Samples prepared at  $700^\circ\text{C}$  gave significantly higher lattice parameters, which are comparable with  $y=0.1$  from the result of Uher et al. [9]. Recently, an unexpectedly high filling level ( $y\sim 0.2$  at 1123 K) and consequently a  $ZT\sim 1.3$  were reported for single filled  $\text{Ce}_y\text{Co}_4\text{Sb}_{12}$  [27].

Our first attempt was initially designed to introduce  $\text{CeSi}_2$  as the precipitating phase in skutterudite.  $\text{CeSi}_2$  was chosen due to its moderate thermoelectric properties (Seebeck coeff.  $\sim -50 \mu\text{V/K}$ ) [28]. However, the equilibrium condition does not allow skutterudite to be compatible with  $\text{CeSi}_2$ . Instead binary  $\text{CoSi}$  was found to form in equilibrium with skutterudite.

Microstructures of  $\text{Ce}_y\text{Co}_4\text{Sb}_{12}/\text{CoSi}$  samples are shown in Figure 4. One can see that at  $600^\circ\text{C}$  the  $\text{CoSi}$  precipitates are well distributed with smaller size compared to those in



samples prepared at 700°C. Interestingly, the filling level of the  $\text{Ce}_y\text{Co}_4\text{Sb}_{12}/\text{CoSi}$  sample prepared at 600°C showed a significant increase of lattice parameter, which corresponds to  $y = 0.09$ . The filling level of samples prepared at 700°C, as mentioned above, is slightly higher ( $y = 0.12$ ). This finding seems to confirm the previous results that the maximum filling level in skutterudites strongly depends on the neighbouring equilibrium phases, particularly equilibrium with liquid Sb favours the lower filling level [27,29].

Despite the smaller size and fine distribution of the precipitates in the sample prepared at 600°C, the filling level seems to exert a stronger effect on the overall ZT. As shown in Figure 5 the electrical resistivity is slightly reduced by addition of CoSi, whereas the Seebeck coefficient is practically unaffected by this addition. The lattice thermal conductivity, however, is strongly reduced by addition of 5% CoSi at 700°C. This results in a slight increase of ZT (~10 %) as compared to the sample without addition of CoSi. A maximum ZT value of 1.2(1) was obtained in this series for the sample with 5% CoSi prepared at 700°C.

### 3.3. Multifilled $\text{RE}_y\text{Co}_4\text{Sb}_{12}/\text{CoSi}$

As the filling level in single-filled skutterudite  $\text{Ce}_y\text{Co}_4\text{Sb}_{12}$  is limited to  $y \approx 0.1$  at 700°C, it was difficult to achieve a high ZT value in single-filled  $\text{Ce}_y\text{Co}_4\text{Sb}_{12}$ . Attempts to investigate combinations of various trivalent fillers revealed that multiple filling with La, Ce, Pr, and Sm significantly increased lattice parameters of the skutterudite phases at 600°C, which is in line with an increase of their filling level. Similar to the single filled skutterudite, at 700°C the filling level increased as indicated by the increase in lattice parameter. Therefore in our preparation method 700°C was chosen as reaction temperature. Moreover, 700°C is also an ideal temperature to reach high sample density.

In this attempt we used combinations of La, Ce, and Sm as filler atoms, together with CoSi as the precipitating phase. The maximum filling level, however, is still relatively low ( $y = 0.09$ ) even at 700°C. Most of the TE quantities: Seebeck coefficient, electrical resistivity and thermal conductivity are not significantly affected, likely due to the small amount of the precipitating phase. Nevertheless, a maximum ZT of 1.2(1) was found in pristine  $(\text{La,Ce,Sm})_y\text{Co}_4\text{Sb}_{12}$  and in the alloy with 0.7 wt.% CoSi, and in general all alloys in this series reach a ZT close to unity i.e.  $1.0 \pm 0.1$ .

### 3.4. Multifilled $\text{RE}_y\text{Co}_4\text{Sb}_{12}/\text{RESb}_2$

Another attempt to introduce nano precipitates was performed on multifilled  $(\text{Ce,Pr,Sm})_y\text{Co}_4\text{Sb}_{12}$  with addition of Y as the precipitating element. Yttrium itself was reported to be an inefficient filler, however, the segregated YSb phase formed was found to be an effective phonon scatterer [30]. Despite yttrium alone has no ability to fill the icosahedral void in the skutterudite structure, EPM analysis of Y-added  $(\text{Ce,Pr,Sm})_y\text{Co}_4\text{Sb}_{12}$  revealed incorporation of a small amount of Y inside the skutterudite phase. In both cases (with or without Y) the filling level remains about the same at 600°C ( $\sim 0.08$ ) and at 700°C ( $\sim 0.13$ ). In this case fine precipitation of YSb was not observed, instead the remaining yttrium together with the rest of the rare earth fillers segregated into the  $\text{RESb}_2$  phase (see Figure 8).

Due to their lower filling level, the samples prepared at 600°C show higher electrical resistivity. The Seebeck coefficient and thermal conductivity are not significantly affected by this different heat treatment. The lattice thermal conductivities, however, are close to the minimum value of  $\sim 6 \text{ mW/cmK}$ , calculated using the equation proposed by Cahill and Pohl [31] assuming a Debye temperature of 325 K [32]. The maximum ZT of 1.3 was found in the sample without Y-addition prepared at 700°C.

## 4. Conclusion

Formation of in-situ nano precipitates via a disproportionation reaction was investigated on various systems with various types of precipitates: metals, silicides, and antimonides. Significant reduction of lattice thermal conductivity was found in case of unfilled  $\text{CoSb}_3$  with addition of W or  $\text{TaSb}_2$ . For filled skutterudites, silicides ( $\text{CoSi}$ ) form fine precipitates and increased the filling level of single filled  $\text{Ce}_y\text{Co}_4\text{Sb}_{12}$  at 600°C. Rare earth di-antimonides generally are not a good choice for precipitation since they tend to coagulate upon their formation, thus reducing their ability to scatter phonons via grain boundary scattering. In the current investigation a maximum ZT of 1.3(1) was obtained for multifilled  $(\text{Ce,Sm,Pr})_{0.13}\text{Co}_4\text{Sb}_{12}$  at 700 K.

## 5. Acknowledgement

The research reported herein was supported by the Austrian Federal Ministry of Science and Research (BMWF) under the scholarship scheme: Technology Grant Southeast Asia (Ph.D.) in the frame of the ASEA UNINET. The work was supported in part by the Christian Doppler Laboratory for Thermoelectricity.

## 6. References

- [1] T. Rosenqvist, Magnetic and crystallographic studies on the higher antimonides of iron, cobalt, and nickel., *Acta Crystallogr.* 7 (1954) 636.
- [2] L.D. Dudkin, N.K. Abrikosov, Thermoelectric properties of cobalt antimonides., *Vop.. Met. I Fiz. Poluprovodnikov* (Moscow: Akad Nauk S.S.S.R.) Sbornik. (1957) 97–109.
- [3] W. Jeitschko, D. Braun,  $\text{LaFe}_4\text{P}_{12}$  with filled  $\text{CoAs}_3$ -type structure and isotypic lanthanoid–transition metal polyphosphides, *Acta Crystall. B Stru.* 33 (1977) 3401–3406.
- [4] G.P. Meisner, Superconductivity and magnetic order in ternary rare earth transition metal phosphides, *Physica B&C.* 108 (1981) 763–764.
- [5] D.T. Morelli, G.P. Meisner, Low temperature properties of the filled skutterudite  $\text{CeFe}_4\text{Sb}_{12}$ , *J. Appl. Phys.* 77 (1995) 3777–3781.
- [6] J.-P. Fleurial, A. Borshchevsky, T. Caillat, D.T. Morelli, G.P. Meisner, High figure of merit in Ce-filled skutterudites, in: *Int. Conf. Thermoelect. Proc.*, 1996: pp. 91–95.
- [7] J.-P. Fleurial, T. Caillat, A. Borshchevsky, Low thermal conductivity skutterudite materials for high performance thermoelectric power generation., *Proc. Intersoc. Energy Convers. Eng. Conf.* 31st (1996) 914–919.
- [8] B. Chen, J.-H. Xu, C. Uher, D.T. Morelli, G.P. Meisner, J.-P. Fleurial, et al., Low-temperature transport properties of the filled skutterudites  $\text{CeFe}_{4-x}\text{Co}_x\text{Sb}_{12}$ , *Phys. Rev. B.* 55 (1997) 1476–1480.
- [9] C. Uher, B. Chen, S. Hu, D.T. Morelli, G.P. Meisner, Transport properties of partially-filled  $\text{Ce}_y\text{Co}_4\text{Sb}_{12}$ , in: *Mater. Res. Soc. Symp. P.*, 1997: pp. 315–320.
- [10] C. Uher, S. Hu, J. Yang, Cerium filling and lattice thermal conductivity of skutterudites, in: *Int. Conf. Thermoelect. Proc.*, 1998: pp. 306–309.
- [11] X. Shi, S. Bai, L. Xi, J. Yang, W. Zhang, L. Chen, et al., Realization of high thermoelectric performance in n-type partially filled skutterudites, *J. Mater. Res.* 26 (2011) 1745–1754.
- [12] G. Rogl, A. Grytsiv, K. Yubuta, S. Puchegger, E. Bauer, C. Raju, et al., In-doped multifilled n-type skutterudites with  $\text{ZT} = 1.8$ , *Acta Mater.* 95 (2015) 201–211.
- [13] G. Rogl, A. Grytsiv, P. Rogl, E. Bauer, M. Zehetbauer, A new generation of p-type didymium skutterudites with high ZT, *Intermetallics.* 19 (2011) 546–555.

- [14] G. Rogl, A. Grytsiv, N. Melnychenko-Koblyuk, E. Bauer, S. Laumann, P. Rogl, Compositional dependence of the thermoelectric properties of  $(\text{Sr}_x\text{Ba}_x\text{Yb}_{1-2x})_y\text{Co}_4\text{Sb}_{12}$  skutterudites, *J. Phys. Condens. Matter.* 23 (2011) 275601.
- [15] G. Rogl, A. Grytsiv, E. Bauer, P. Rogl, M. Zehetbauer, Thermoelectric properties of novel skutterudites with didymium:  $\text{DD}_y(\text{Fe}_{1-x}\text{Co}_x)_4\text{Sb}_{12}$  and  $\text{DD}_y(\text{Fe}_{1-x}\text{Ni}_x)_4\text{Sb}_{12}$ , *Intermetallics.* 18 (2010) 57–64.
- [16] L. Zhang, A. Grytsiv, M. Kerber, P. Rogl, E. Bauer, M.J. Zehetbauer, et al., MmFe<sub>4</sub>Sb<sub>12</sub>- and CoSb<sub>3</sub>-based nano-skutterudites prepared by ball milling: Kinetics of formation and transport properties, *J. Alloy Compd.* 481 (2009) 106–115.
- [17] G. Rogl, A. Grytsiv, P. Rogl, E. Bauer, M.B. Kerber, M. Zehetbauer, et al., Multifilled nanocrystalline p-type didymium - Skutterudites with  $\text{ZT} > 1.2$ , *Intermetallics.* 18 (2010) 2435–2444.
- [18] Rogl, G., Zehetbauer, M., Kerber, M., Rogl, P., Bauer, Impact of ball milling and high-pressure torsion on the microstructure and thermoelectric properties of p- and n-type Sb-based skutterudites, *Mater. Sci. Forum.* 667-669 (2011) 1089–1094.
- [19] G. Rogl, A. Grytsiv, P. Rogl, E. Bauer, M. Hohenhofer, R. Anbalagan, et al., Nanostructuring of p- and n-type skutterudites reaching figures of merit of approximately 1.3 and 1.6, respectively, *Acta Mater.* 76 (2014) 434–448.
- [20] G. Rogl, A. Grytsiv, P. Rogl, N. Peranio, E. Bauer, M. Zehetbauer, et al., n-Type skutterudites  $(\text{R},\text{Ba},\text{Yb})_y\text{Co}_4\text{Sb}_{12}$  ( $\text{R} = \text{Sr}, \text{La}, \text{Mm}, \text{DD}, \text{SrMm}, \text{SrDD}$ ) approaching  $\text{ZT} \approx 2.0$ , *Acta Mater.* 63 (2014) 30–43.
- [21] J. Eilertsen, S. Rouvimov, M.A. Subramanian, Rattler-seeded InSb nanoinclusions from metastable indium-filled  $\text{In}_{0.1}\text{Co}_4\text{Sb}_{12}$  skutterudites for high-performance thermoelectrics, *Acta Mater.* 60 (2012) 2178–2185.
- [22] Z. Xiong, X. Chen, X. Huang, S. Bai, L. Chen, High thermoelectric performance of  $\text{Yb}_{0.26}\text{Co}_4\text{Sb}_{12}/\text{yGaSb}$  nanocomposites originating from scattering electrons of low energy, *Acta Mater.* 58 (2010) 3995–4002.
- [23] J. Rodriguez-Carvajal, FULLPROF: a program for Rietveld refinement and pattern matching analysis, in: *Satellite Meeting on Powder Diffraction of the XV Congress of the IUCr*, 1990.
- [24] W. Wacha, Program STRUKTUR, Diploma thesis, Technische Universität Wien, 1989.

- [25] C. Uher, Chapter 5 Skutterudites: Prospective novel thermoelectrics, in: T.M. Tritt (Ed.), Recent Trends in Thermoelectric Materials Research I, Elsevier, 2001: pp. 139 – 253.
- [26] R.M. Luo, F.S. Liu, J.Q. Li, X.W. Feng, The isothermal section of the Ce–Co–Sb ternary system at 400 °C, J. Alloy Compd. 471 (2009) 60–63..
- [27] Y. Tang, R. Hanus, S. Chen, G.J. Snyder, Solubility design leading to high figure of merit in low-cost Ce-CoSb<sub>3</sub> skutterudites, Nat. Commun. 6 (2015).
- [28] A.V. Morozkin, V.A. Stupnikov, V.N. Nikiforov, N. Imaoka, I. Morimoto, Thermoelectric properties of the solid solutions based on ThSi<sub>2</sub>-type CeSi<sub>2</sub> compound, J. Alloy Compd. 415 (2006) 12–15.
- [29] A. Grytsiv, P. Rogl, H. Michor, E. Bauer, G. Giester, In<sub>7</sub>Co<sub>4</sub>Sb<sub>12</sub> Skutterudite: Phase Equilibria and Crystal Structure, J. Electron. Mater. 42 (2013) 2940–2952.
- [30] G. Nakamoto, Y. Yoshida, L. Van Vu, N.T. Huong, D.T.K. Anh, M. Kurisu, Effect of segregated impurity phases on lattice thermal conductivity in Y-added CoSb<sub>3</sub>, Scripta Mater. 56 (2007) 269–272.
- [31] D.G. Cahill, S.K. Watson, R.O. Pohl, Lower limit to the thermal conductivity of disordered crystals, Phys. Rev. B. 46 (1992) 6131–6140.
- [32] G. Rogl, P. Rogl, Mechanical properties of skutterudites, Sci. Adv. Mater. 3 (2011) 517–538.

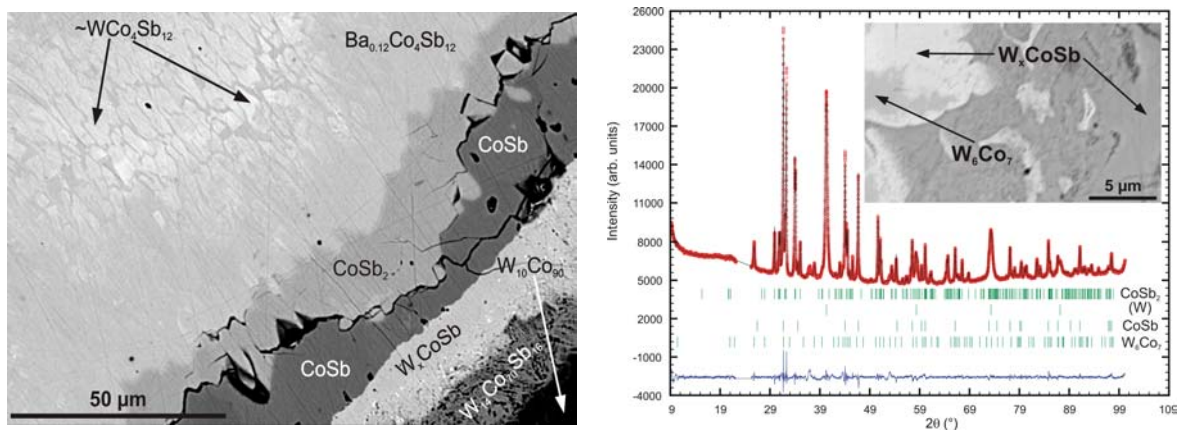


**Figure 1.** Left panel: Diffusion couple between Ba<sub>0.3</sub>Co<sub>4</sub>Sb<sub>12</sub> and Co<sub>90</sub>W<sub>10</sub> annealed at 600°C for 40 days; right panel: X-ray diffraction pattern and micrograph of sample with nominal composition of WCoSb, annealed and hot pressed at 600°C (right).

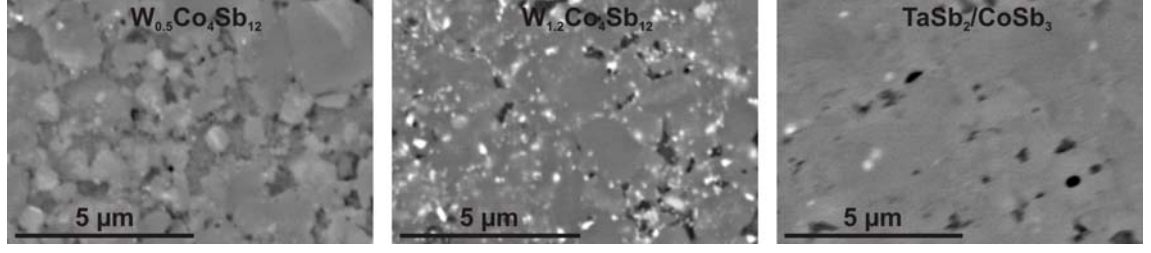


**Figure 2.** Micrograph of W and TaSb<sub>2</sub> precipitates on CoSb<sub>3</sub>. The bright spots are the precipitating phase (W or TaSb<sub>2</sub>), the black spots are residual holes from polishing.

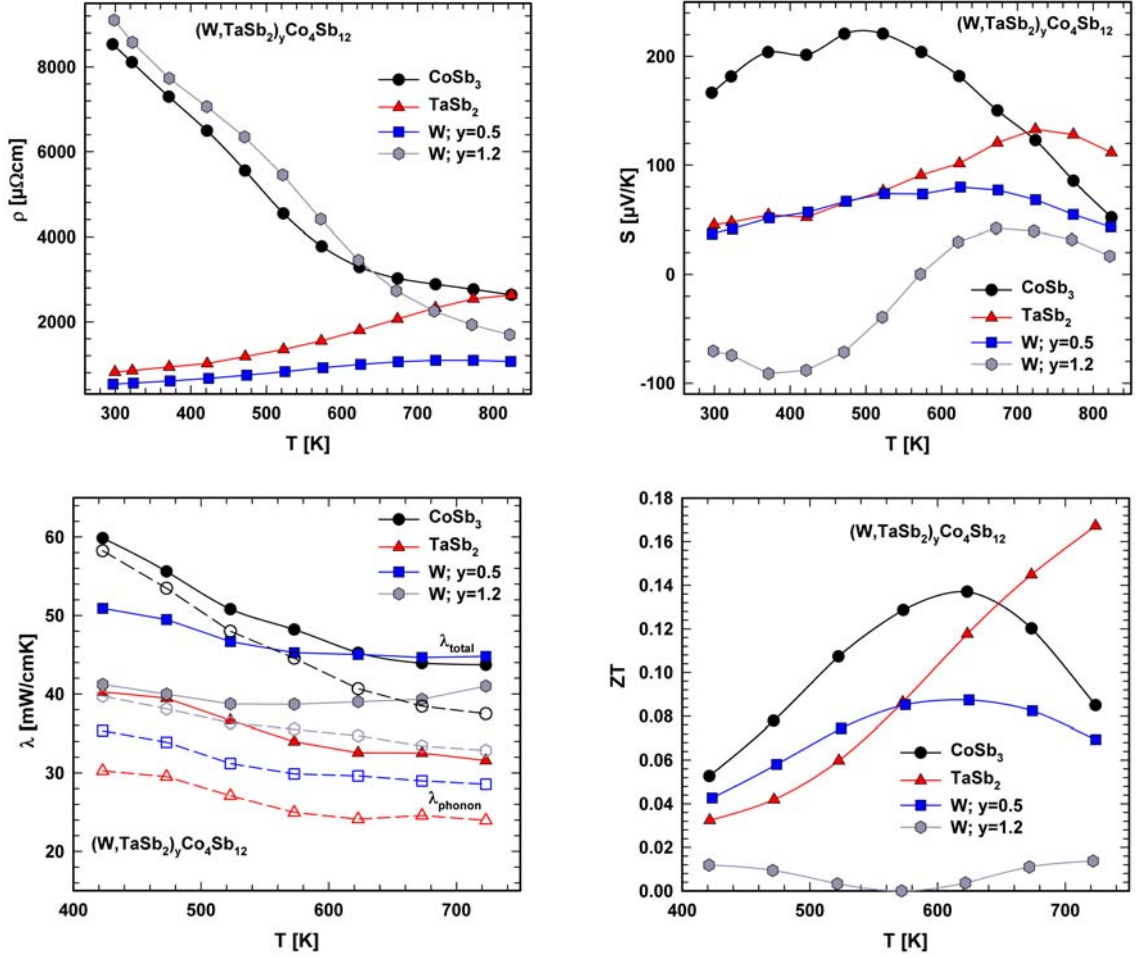


**Figure 3.** Thermoelectric properties of CoSb<sub>3</sub>/(W,Ta)Sb<sub>2</sub> alloys. The open symbols denote the lattice contribution to the thermal conductivity. The solid and dashed lines are guides to the eyes.

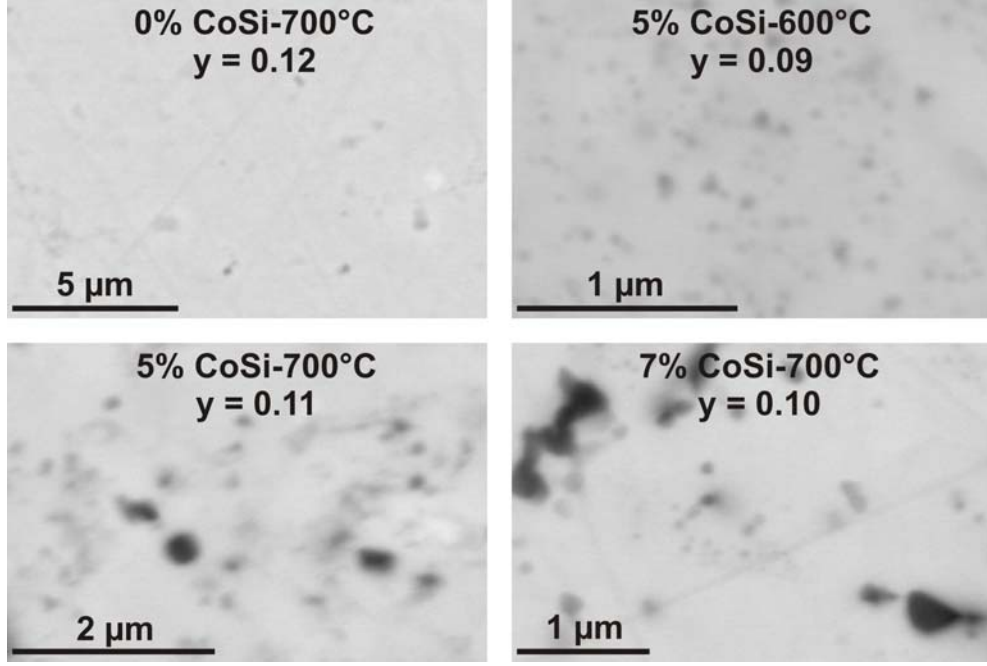


**Figure 4.** Microstructure of  $\text{Ce}_y\text{Co}_4\text{Sb}_{12}/\text{CoSi}$  samples. The black spots are CoSi precipitates.

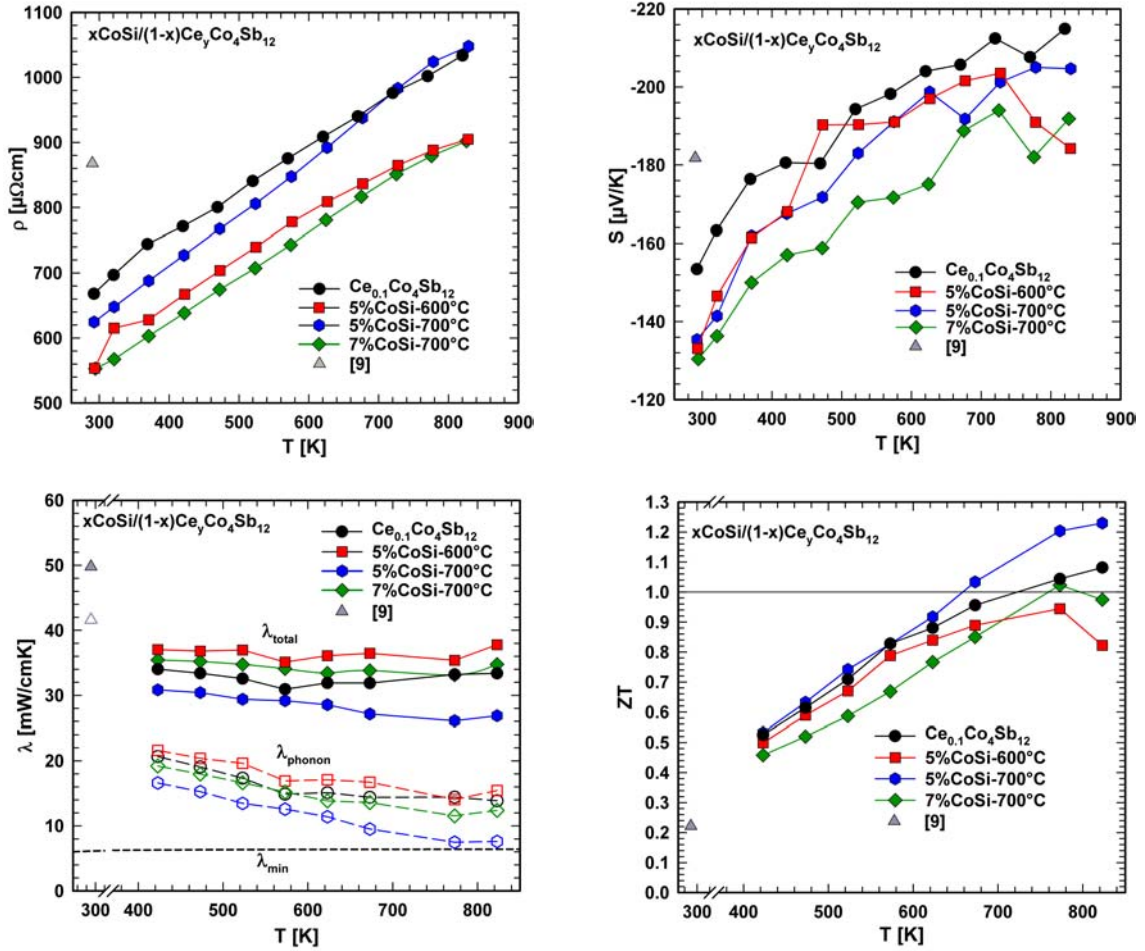


**Figure 5.** Thermoelectric properties of  $\text{Ce}_y\text{Co}_4\text{Sb}_{12}/\text{CoSi}$  alloys. The open symbols denote the lattice contribution to the thermal conductivity. The solid and dashed lines are guides to the eyes.



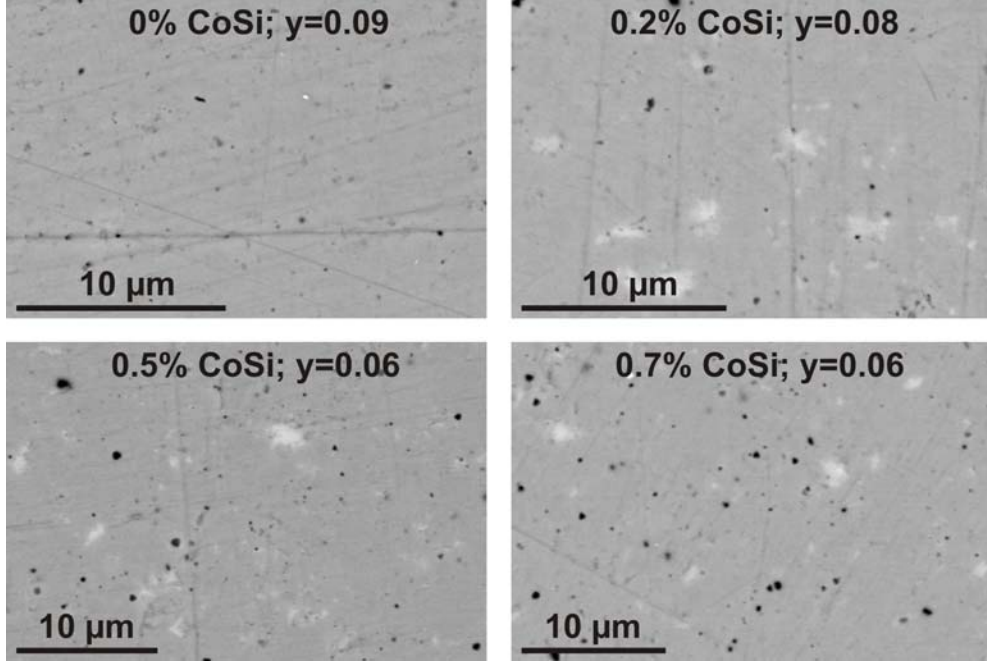


**Figure 6.** Microstructure of  $\text{RE}_y\text{Co}_4\text{Sb}_{12}/\text{CoSi}$  samples. The white spots are from secondary phases ( $\text{RESb}_2$ ).

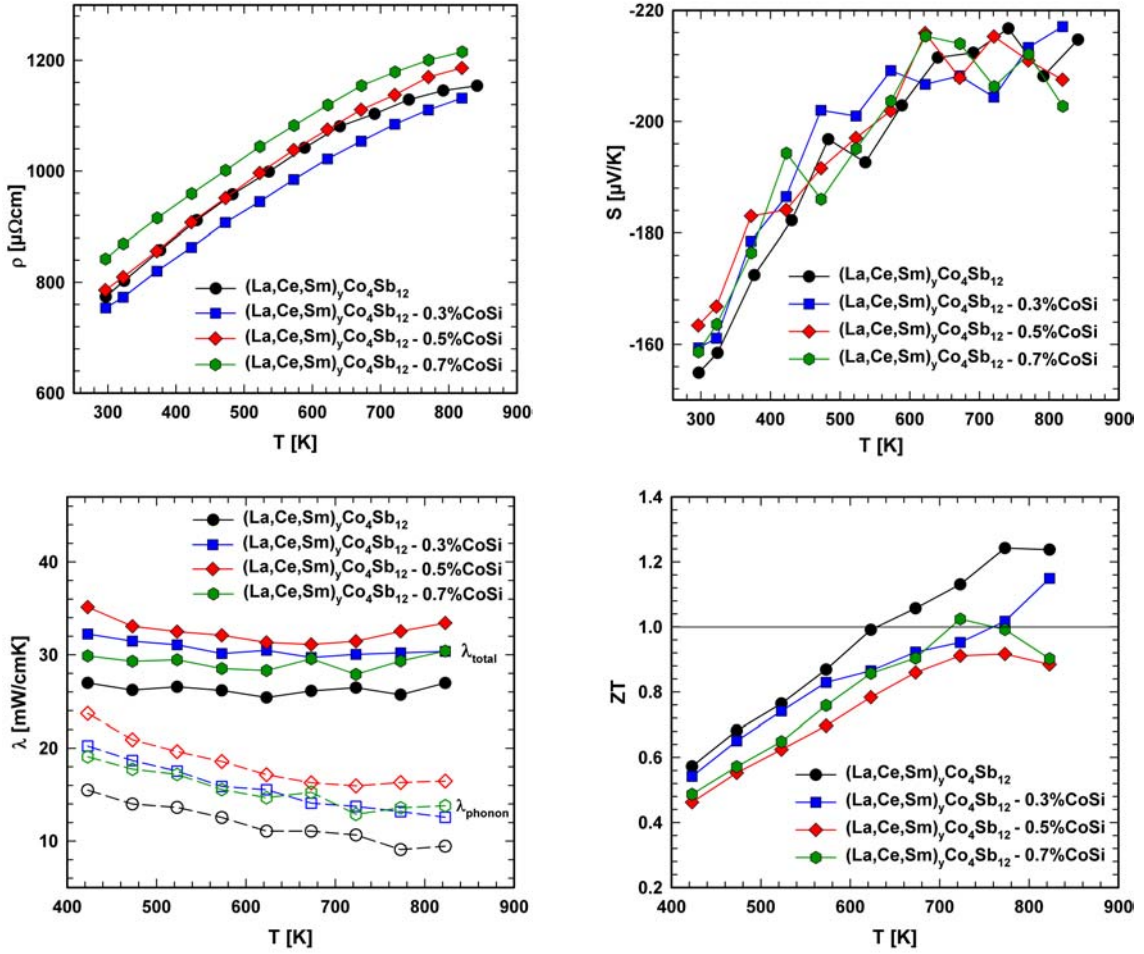


**Figure 7.** Thermoelectric properties of  $\text{RE}_y\text{Co}_4\text{Sb}_{12}/\text{CoSi}$  alloys. The open symbols denote the lattice contribution to the thermal conductivity. The solid and dashed lines are guides to the eyes.



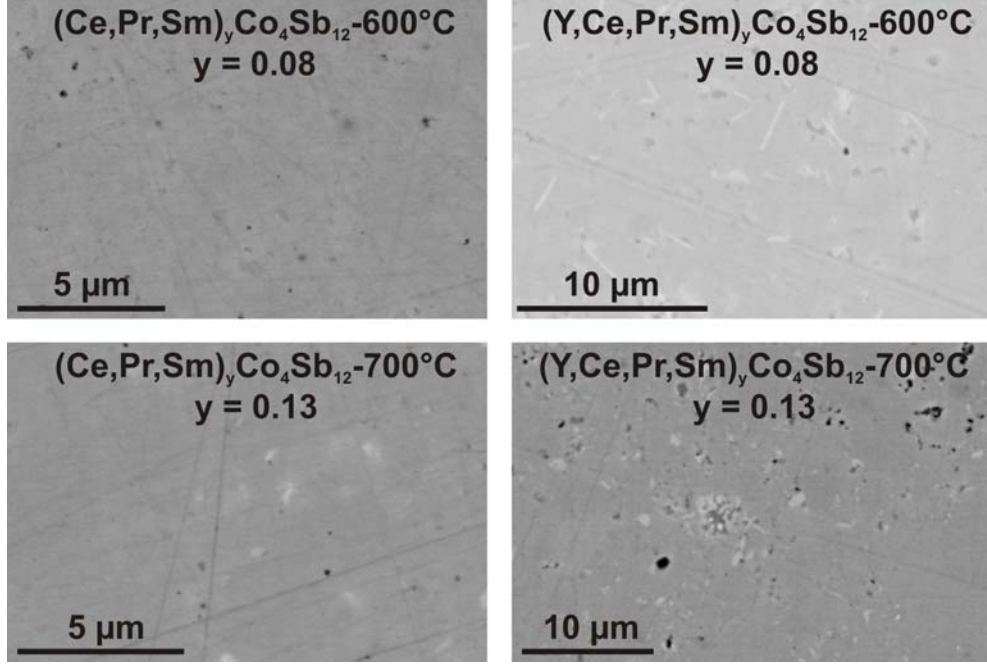


**Figure 8.** Microstructure of  $\text{RE}_y\text{Co}_4\text{Sb}_{12}/\text{RESb}_2$  samples. The white phases are secondary  $\text{RESb}_2$ .

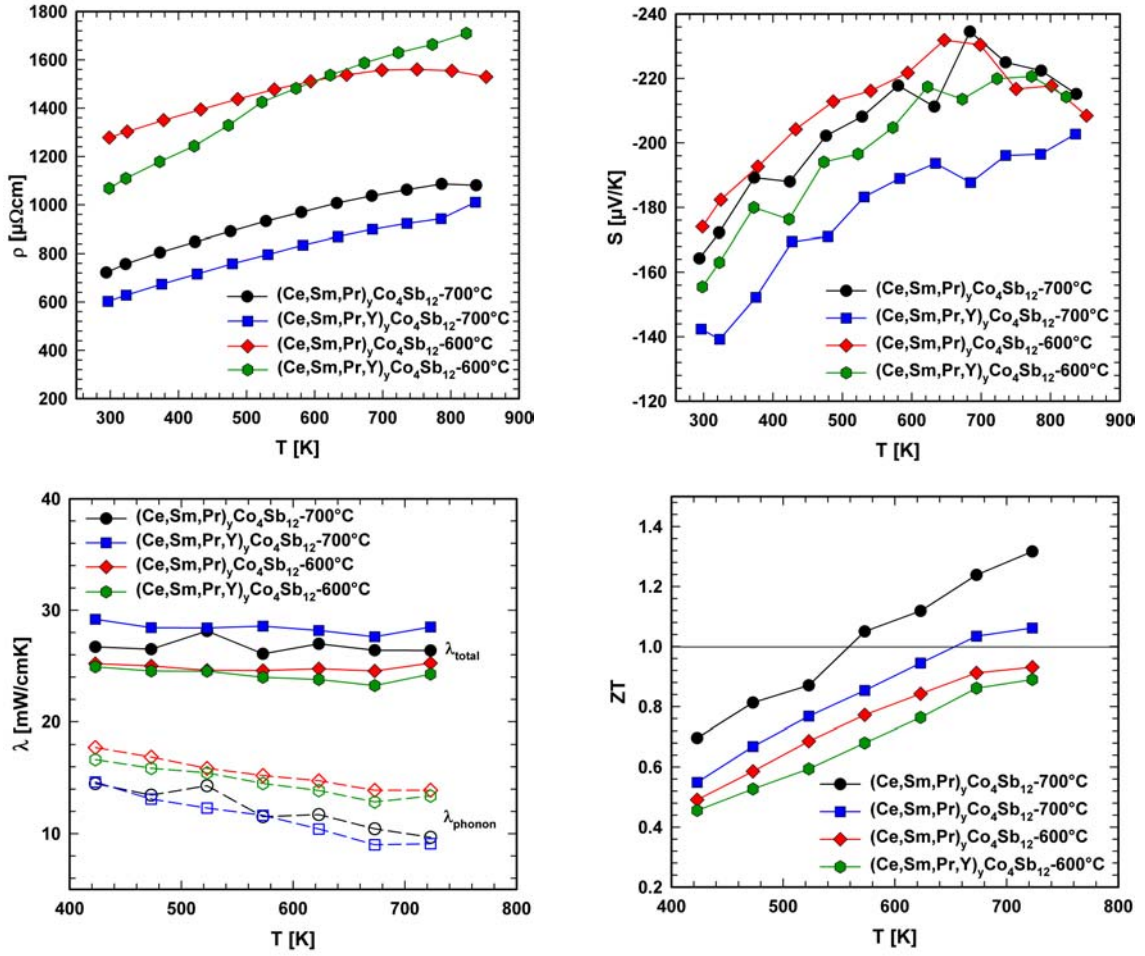


**Figure 9.** Thermoelectric properties of  $\text{RE}_y\text{Co}_4\text{Sb}_{12}/\text{RESb}_2$  alloys. The open symbols denote the lattice contribution to the thermal conductivity. The solid and dashed lines are guides to the eyes.

## Chapter 2 High Temperature FeB-type Phases in the Systems Ta- {Ti,Zr,Hf}-B

F. Failamani<sup>1</sup>, K. Göschl<sup>2</sup>, G. Reisinger<sup>2</sup>, C.A. Nunes<sup>3</sup>, G.C. Coelho<sup>3,4</sup>, A. J. da Silva Machado<sup>3</sup>, L. E. Correa<sup>3</sup>, J. C. P. dos Santos<sup>3</sup>, G. Giester<sup>5</sup>, P. Rogl<sup>2</sup>

<sup>1</sup>*Institute of Physical Chemistry, University of Vienna, Währingerstrasse 42, A-1090 Wien, Austria*

<sup>2</sup>*Institute of Materials Chemistry and Research, University of Vienna, Währingerstrasse 42, A-1090 Wien, Austria*

<sup>3</sup>*Universidade de São Paulo (USP), Escola de Engenharia de Lorena (EEL), Polo Urbano Industrial Gleba AI-6, Caixa Postal 116, 12602-810 Lorena, SP, Brazil*

<sup>4</sup>*Mestrado Profissional em Materiais, Centro Universitário de Volta Redonda, Av. Paulo Erlei Alves Abrantes 1325, 27240-560 Volta Redonda-RJ, Brazil*

<sup>5</sup>*Institute of Mineralogy and Crystallography, University of Vienna, Althanstrasse 14, A-1090 Wien, Austria*

(submitted to Journal of Phase Equilibria and Diffusion)

Contributions to this paper:

F. Failamani : sample characterization, analysis and evaluation, writing the paper

K. Göschl and G. Reisinger: sample characterization, analysis and evaluation, proofreading

C.A. Nunes, G.C. Coelho, A. J. da Silva Machado, L. E. Correa, J. C. P. dos Santos: supply of the samples, comments and proofreading

G. Giester : single crystal data collection

P. Rogl : preliminary single crystal test, discussions, comments, and proofreading

## Abstract

Novel FeB -type phases have been evaluated in the systems Ta-{Ti,Zr,Hf}-B either from as cast or arc treated samples by X-ray powder and single crystal diffraction as well as electron probe microanalysis. In each of the three systems the formation of the FeB-type phase suggests a high temperature stabilization of a binary group IV metal monoboride with FeB-type. This holds true for Ti and Hf, while for Zr the single crystal study of (Ta,Zr)B proves that it is a true ternary phase, as no stable monoboride exists in the binary Zr-B system. EPMA analyses reveal that the FeB-type phases Ta{Ti,Zr,Hf}B are formed by substitution of Ta in TaB by rather small amounts of group IV elements (~3 at. % of Zr, ~7 at. % Hf, and ~10 at.% Ti).

*Keywords: A. refractory materials; B. Crystal structure; C. Microstructure; D. X-ray analysis.*

## 1. Introduction

Monoborides of transition metals (T) constitute a unique group of crystal structures with characteristic infinite boron zig-zag chains compatible with covalent single bonds at a distance of  $0.165\text{nm} < d_{\text{B-B}} < 0.190\text{ nm}$  and a bond angle of  $\sim 115^\circ$ .<sup>[1]</sup> As the boron atoms are coordinated by trigonal metal prisms, which share two of their rectangular faces, the crystal structures consist of infinite rows of metal prisms. The structure types of FeB, CrB (also described as T $\ell$ I-type) and  $\alpha$ MoB are the most widely found binary monoborides.<sup>[1,2]</sup> As shown in Figure 1, simple geometrical relationships exist, which shift blocks of FeB- into CrB-type<sup>[3]</sup> or blocks of CrB-type into  $\alpha$ MoB-type.<sup>[4]</sup> Due to these geometrically defined shift operations, randomly appearing shifts reduce the intensities of certain X-ray powder reflections in for instance a powder spectrum recorded on fine FeB powders synthesized at 650°C (for details see ref. <sup>[5]</sup>). A random stacking of CrB- and FeB-type units may freeze as an orthorhombic low temperature modification of FeB ( $< 650^\circ\text{C}$ ).<sup>[6]</sup> From near-neighbor diagrams it became obvious that the monoborides follow strong metal-boron interactions.<sup>[7]</sup> Simple shifts of structure slabs usually do not involve large transformation energies - thus most binary metal monoborides exhibit low and high temperature modifications for which a graphical distribution is shown in Figure 2. Whereas the FeB-type involves the electropositive metals Ti, Hf as well as the 3d-metals Mn, Fe, Co, we see a gradual decrease in stability towards CrB and MoB variants moving towards the more electronegative metals. It is interesting to note that the monoborides of the Cr, Mo, W group exhibit a CrB-type high

temperature modification and a low-temperature  $\alpha$ MoB-type, but we so far only know the CrB-type for the neighbouring V,Nb,Ta group. The group of platinum metals sees a set of structures which are prone to defect sublattices such as  $\{\text{Ru,Os}\}\text{B}$  (WC-type =  $\text{AlB}_2$ -type with ordered B-defect), RhB and  $\text{PtB}_{1-x}$  (NiAs-type) etc. (for details see refs. [1,2] and refs. therein).

Adding to binary transition metal borides a second transition metal component to form a ternary mono-boride  $\text{TI}_{1-x}\text{TII}_x\text{B}$  (TI and TII are transition metals) usually leads to extended solid solutions eventually stabilizing one of the other monoboride structures or a novel arrangement such as the  $\text{NbCoB}_2$ -type, which is an ordered combination of FeB- and CrB-type units.<sup>[1]</sup> From the unsymmetrical distribution of the binary monoboride structure types among the transition metals, it appeared of interest to investigate the most refractory metal-boron combinations such as  $\{\text{Ti,Zr,Hf}\}\text{-Ta-B}$ . The corresponding phase equilibria have hitherto been determined at moderate temperatures (see Figure 3) and, for the sections  $\text{TaB-}\{\text{Ti,Zr,Hf}\}\text{B}$ , have revealed extended solution phases of Ti,Zr,Hf in TaB and Ta in TiB.<sup>[8-10]</sup> It should be noted here that HfB (FeB-type) was not considered for the equilibria at 1400°C,<sup>[10]</sup> although earlier studies have documented its existence and peritectic decomposition at 2218°C.<sup>[11-13]</sup> ZrB with NaCl-type is impurity (C,N,O) stabilized, but the degree of thermodynamic stability of the ZrB-phase with FeB-type has been evaluated.<sup>[14]</sup> With an estimated heat of formation of  $\Delta H_f^0 \sim -84 \text{ kJ}/(\text{mol.ZrB})$  it was shown that ZrB with FeB-type can only be stable below 590°C with respect to  $\alpha\text{Zr}$  and  $\text{ZrB}_2$ .<sup>[14]</sup>

A preliminary check of arc melted monoboride alloys  $\text{Ta}_{1-x}\{\text{Ti,Zr,Hf}\}_x\text{B}$  ( $x \sim 0.2$ ) interestingly revealed in all three cases a major phase fraction of an FeB-type compound (i) either supporting a stabilization of the group-IV FeB-type phase, or (ii) a novel ternary phase separated from both metal binaries. In any case the extended CrB-type phase solutions  $\text{Ta}_{1-x}\{\text{Zr,Hf}\}_x\text{B}$  (up to  $x \sim 0.6$ ) claimed in the literature<sup>[9,10]</sup> (for details see Fig. 3) are not seen at subsolidus temperatures. Therefore this paper will address the formation of ternary FeB-type monoborides in the afore mentioned combinations at elevated temperatures.

## 2. Experimental Details

Alloys  $\text{Ta}_{1-x}\text{T}_x\text{B}$  ( $x=0.32$  for  $\text{T=Ti}$ ;  $x=0.2, 0.22$  for Hf and  $x=0.2, 0.3$  for Zr) were prepared from metal ingots of Ti,Zr,Hf (purity 99.9 mass %), Ta-foil (99.9%) and pieces of crystallized B (purity 99.5 mass %), all from Alfa Johnson Matthey GmbH, Germany, by repeated arc melting under argon. B-pieces - although wrapped in the corresponding mass of Ta-foil - tend to shatter under the arc and were replenished in several meltings so that

overall weight losses were kept below 1 %, however, the Ta:T ratio after synthesis was always within 0.1 % of the nominal values (as monitored by EPMA-see below). With a melting temperature of TaB at  $3090 \pm 15^\circ\text{C}$ ,<sup>[13,15]</sup> subsolidus temperatures of the alloys near TaB are significantly higher than temperatures available for annealing in W-mesh furnaces. Therefore some reguli have been "heat-treated" directly after arc melting at subsolidus temperatures for 5 min running the arc at slightly lower energy than needed for melting. In the following, these alloys are labeled as "low-arc" samples.

Lattice parameters and standard deviations were determined by least squares refinements of room temperature X-ray powder diffraction (XRD) data obtained from a Guinier-Huber image plate employing monochromatic Cu  $K\alpha_1$  radiation and Ge as internal standard ( $a_{\text{Ge}} = 0.565791$  nm). XRD-Rietveld refinements were performed with the FULLPROF program<sup>[16]</sup> with the use of its internal tables for atom scattering factors.

All samples were polished using standard procedures. Microstructures/phase distributions were examined by scanning electron microscopy. For composition analyses, electron probe microanalysis (EPMA) measurements (point measurements and scans) were performed on a Zeiss Supra 55 VP scanning electron microscope, operated at 20 kV and  $\sim 60$   $\mu\text{A}$  employing energy dispersive X-ray (EDX) analysis for determining the metal ratios Ta:{Ti,Zr,Hf}. Pure elements served as standards.

Single crystals of  $\text{Ta}_{1-x}\text{Zr}_x\text{B}$  were isolated via mechanical fragmentation of an arc melted specimen with nominal composition  $\text{Ta}_{0.80}\text{Zr}_{0.20}\text{B}$ . X-ray single crystal diffraction (XSCD) data were collected at room temperature on a Bruker APEXII diffractometer equipped with a CCD area detector and an Incoatec Microfocus Source I $\mu$ S (30 W, multilayer mirror, Mo  $K_\alpha$ ). Several sets of phi- and omega-scans with  $2.0^\circ$  scan width were measured at a crystal-detector distance of 3 cm (full sphere;  $2^\circ < 2\theta < 70^\circ$ ). The crystal structures were solved applying direct methods (program SHELXS-97) and refined against  $F^2$  (SHELXL-97-2)<sup>[17]</sup> within the program WinGX.<sup>[18]</sup> The crystal structures were all standardized with the program Structure Tidy.<sup>[19]</sup> Further details concerning the experiments are given in Table 1.

### 3. Results and Discussion

#### 3.1. Formation of FeB-type Compounds in the Systems Ta-{Ti,Zr,Hf}-B

Table 1 summarizes the results of the combined evaluation of X-ray lattice parameters and EPMA-compositions of the phases in the ternary alloys investigated. X-ray powder patterns in most cases document the existence of three-phases: (i) a CrB-type phase (presumably linking to a solid solution extending from binary TaB, (ii) an FeB-type phase (which defines

the ternary T-substituted phase) and (iii) in smaller amounts a softer matrix phase with W-type structure (consistent with the binary Ta-T solid solutions). EPMA line-scans over the large monoboride dendrites in the microstructures revealed significant coring effects in the solidification process, which is also obvious from the corresponding X-ray powder patterns: central and peripheral areas of the dendrites (or small dendrites) give rise to broadened X-ray intensity peaks. Furthermore primary dendrites and secondary precipitates in solidification produce identical X-ray intensity patterns (FeB-type) but with slightly different lattice parameters (doubling of peaks). Although derived from non-equilibrium alloys - some slowly cooled in the arc, some "quenched" (equivalent to cooling in the argon filled arc melter by removing the arc) from high temperature, the spread of lattice parameters and corresponding compositions of the FeB-type phase in each alloy can be taken as a sign for the extent of a phase region in the phase diagram.

For the binary Ta-B system, EPMA data as well as Rietveld refinement of an as cast alloy with composition of Ta<sub>50</sub>B<sub>50</sub> (in at.%) clearly document CrB-type as the only phase constituent. Whereas FeB-type solid solutions for T = Ti, Zr, Hf comprise the compositions Ta<sub>1-x</sub>Ti<sub>x</sub>B for 0.22 < x < 0.26 and Ta<sub>1-x</sub>Zr<sub>x</sub>B for 0.06 < x < 0.24; the dendrites of Ta<sub>1-x</sub>Hf<sub>x</sub>B indicate a composition range for 0.12 < x < 0.20 (see Figure 4). From the three transition elements zirconium is unique, as hitherto there has been no binary FeB-type compound ZrB experimentally observed.<sup>[13,20]</sup> Therefore FeB-type Ta<sub>1-x</sub>Zr<sub>x</sub>B is a truly ternary phase, whilst the solutions Ta<sub>1-x</sub>Ti<sub>x</sub>B for T = Ti, Hf may be considered as a simple stabilization of binary FeB-type phases TiB (T<sub>m</sub>=2190±25°C),<sup>[12,13]</sup> and HfB (T<sub>m</sub>=2100±20°C)<sup>[12,13]</sup> to higher temperatures via Ta/T-substitution. A similar situation is met for the homologous section Nb<sub>1-x</sub>Ti<sub>x</sub>B for which large ternary mutual solid solubilities in the corresponding CrB- and FeB-type phases extend far into the ternary and which at 2650±15°C are separated by a small two-phase region of about 5 at.% metal.<sup>[21]</sup>

### 3.1.1. The Ta-Ti-B System

Two samples in the Ta-Ti-B system with nominal composition Ta<sub>0.68</sub>Ti<sub>0.32</sub>B were subjected to two different processing conditions: slow cooling by gradually reducing the power of the arc (#1) and arc treatment at low power (#2). Microstructure analyses of both samples (see Figure 5a,b) show a significant segregation, where in one side the overall composition shifts towards the B-rich side, thus contains B-rich binary (Ta,Ti)-B phases such as (Ta,Ti)<sub>3</sub>B<sub>4</sub> and (Ta,Ti)B<sub>2</sub>. The other part of the samples shows only monoboride phase(s). This observation

was also confirmed by analysis of XRPD patterns via Rietveld refinements, which document B-rich binary (Ta,Ti)-B phases and monoborides with FeB/CrB-type.

Sample #1 (see Fig. 5a) shows significant coring effects in the B-poor side, which is not visible in sample #2 (Fig. 5b). Note that the different contrast in sample #2 is due to grain orientation effects. The slowly cooled sample shows two FeB-type phases, (Ta,Ti)B, with very close Bragg positions. On the other hand the XRPD pattern of sample #2 does not reveal any doubling of FeB-type peaks, and the pattern could be satisfactorily refined with only one FeB-type phase. Despite XRPD shows a small quantity of (Ta,Ti)B with CrB-type (~8 wt.%), it was not possible to distinguish the CrB-type from the FeB-type by phase composition, i.e. from the Ta:Ti ratio as EDX measurement showed rather similar values. Nevertheless, we can differentiate three groups of data (only two in sample #2), one with a highest Ta/Ti ratio (4.4), and two sets with a lower Ta/Ti ratio (3.5 and 2.9) (see Table 1 for details). In such a case, however, we can assume that the monoboride with the highest Ta:Ti ratio belongs to the CrB-type, i.e. the maximum amount of Ti solved in the ternary solid solution (Ta,Ti)B with CrB-type, whereas the higher Ti content represents the end of the (Ta,Ti)B solid solution with FeB-type.

### **3.1.2. The Ta-Zr-B System**

Formation of the FeB-type phase (Ta,Zr)B in the Ta-Zr-B system has been investigated with four samples: three with nominal composition  $Ta_{0.80}Zr_{0.20}B$  and one with  $Ta_{0.70}Zr_{0.30}B$ . In most cases samples look homogeneous except for  $Ta_{0.70}Zr_{0.30}B$  where some parts contain a larger amount of (Ta,Zr) phase with W-type. In all cases (Ta,Zr)B with FeB-type is the major constituent.

Figure 6a,b shows the XRPD patterns and micrographs of two  $Ta_{0.80}Zr_{0.20}B$  samples with different phase constituents. Sample #1 (Fig. 6a) shows only two FeB-type phases (Ta,Zr)B in combination with smaller amounts of (Ta,Zr) matrix (W-type), with a high amount of Zr solved in the (Ta,Zr) matrix (>70 at.%). This situation is also observed in the sample with higher amount of Zr ( $Ta_{0.7}Zr_{0.3}B$ ). On the other hand sample #2 (Fig. 6b) shows almost equal amounts of FeB- and CrB-type phases (Ta,Zr)B. In this sample the (Ta,Zr) matrix shows more Ta (~80 at.%) than Zr. The difference in the phase constitutions may arise from a somewhat lower B content in sample #2. Note that in both samples the difference in the Ta:Zr ratio for the monoborides between different grains is not greater than 5 at.%. Similar to the Ta-Ti-B system, one can assume that the monoboride with the higher Ta:Zr ratio corresponds to the CrB-type.

### 3.1.3. The Ta-Hf-B System

Two samples with nominal composition  $\text{Ta}_{0.80}\text{Hf}_{0.20}\text{B}$  and  $\text{Ta}_{0.78}\text{Hf}_{0.22}\text{B}$  reveal only (Ta,Hf)B monoborides with FeB-type. Both samples exhibit coring and secondary precipitation, which results in broadening and doubling of XRPD reflections. The doubling can be identified easily in the  $\text{Ta}_{0.80}\text{Hf}_{0.20}\text{B}$  sample (Fig 7a), whilst for  $\text{Ta}_{0.78}\text{Hf}_{0.22}\text{B}$  the reflections between the two FeB-type phases (Ta,Hf)B closely overlap (see Figure 7b). This phenomenon is also confirmed by EPMA measurements, which show significant differences in the Ta:Hf ratio measured throughout the sample  $\text{Ta}_{0.80}\text{Hf}_{0.20}\text{B}$  (~5 at. %) whilst the difference for alloy  $\text{Ta}_{0.78}\text{Hf}_{0.22}\text{B}$  is less than 2 at. %. These differences are seen in EPMA line scans across large grains with coring effect, whereas small grains reveal compositions corresponding to the outer rims of the cored large grains.

### 3.2. The Crystal Structure of $\text{Ta}_{0.78}\text{Zr}_{0.22}\text{B}$ with FeB-type

In order to prove the FeB-type structure, a single crystal (SC) was chosen from the system Ta-Zr-B. The crystal was broken from an arc melted specimen with nominal composition  $\text{Ta}_{0.8}\text{Zr}_{0.2}\text{B}$ , for which EPMA revealed a composition  $\text{Ta}_{38}\text{Zr}_{12}\text{B}_{50}$  (in at.%  $\equiv \text{Ta}_{0.76}\text{Zr}_{0.24}\text{B}$ ) for rather homogeneous crystallites of ~25  $\mu\text{m}$  diameter, suitable for X-ray structure analysis. An FeB-type compound in this system will thus constitute a truly ternary phase, as a stable monoboride phase was hitherto experimentally not recorded in the high purity binary Zr-B phase diagram. The "ZrB"-phase with NaCl-type, which is occasionally listed in structure and phase diagram compilations, was shown to be a (C,N,O)-stabilized phase (for a detailed discussion see ref.<sup>[14]</sup>).

Analyses of the X-ray single crystal intensity data, particularly of the systematic extinctions (observed for  $0kl$ ,  $k = 2n+1$  and  $hk0$  for  $h = 2n+1$ ), prompted an orthorhombic unit cell ( $a = 0.617526(11)$  nm,  $b = 0.31626(5)$ ,  $c = 0.47009(9)$  nm) consistent with space group symmetry *Pnma* (No. 62), which, as the highest symmetric one, was chosen for further structure analysis. Direct methods delivered a structure solution with metal atoms in site 4c. The boron atoms were unambiguously located via a difference Fourier synthesis in a further 4c-site. A free variable on the Ta/Zr ratio yields only a slightly higher Zr content than that determined by EPMA. With only one 4c-site for the metal atoms, no ordering among Ta/Zr atoms is possible and no evidence exists from the X-ray diffraction spectra for supercell reflections. A final refinement (with Ta/Zr ratio inserted from EPMA) inferring anisotropic atom displacement parameters (ADP's) in general but isotropic ADP's for the boron site converged to an R-value  $R_{F2} = 0.0165$  with Fourier ripples in the electron density of less than



3.2 e<sup>-</sup>/Å<sup>3</sup> at 0.09 nm from B. The value of the isotropic ADP of boron atoms confirms full occupancy of the B-site corresponding to a B-defect free monoboride. The parameters derived from refinement for Ta<sub>0.78</sub>Zr<sub>0.22</sub>B are listed in Table 3 including interatomic distances. A search for the structure type in Pearson's Crystal Data <sup>[1]</sup> and in ICSD (Fachinformationszentrum Karlsruhe)<sup>[22]</sup>, involving also the Wyckoff sequence  $c^2$ , prompted isotypism with the (undisturbed) structure of FeB in its high temperature form.

Interatomic distances in Table 3 show that boron-boron distances,  $d_{B-B} = 0.188$  nm, in for Ta<sub>0.78</sub>Zr<sub>0.22</sub>B appear somewhat increased with respect to the boron chain in binary FeB with significantly smaller metal (Fe) atoms:  $d_{B-B} = 0.1785$  nm (from X-ray SC data,<sup>[23]</sup> or  $d_{B-B} = 0.1783$  nm, from unpolarized neutron diffraction SC data <sup>[24]</sup>). Bonds from B to the six Ta/Zr atoms within the trigonal prisms are rather homogeneous,  $0.240 \text{ nm} < d_{B-Ta/Zr} < 0.243$  nm, and are close to the sum of radii ( $R_{Ta} = 0.1467$  nm,  $R_{Zr} = 0.1602$ ,  $R_B = 0.088$  nm <sup>[25]</sup>) documenting a strong metal-boron interaction. The characteristic feature of compounds with the FeB-type structure (see Figures 1,8) is the infinite boron zig-zag chain (along the *b*-axis) with a bond distance range of  $0.165 \text{ nm} < d_{B-B} < 0.190$  nm, and with bond angles of  $\phi_{B-B-B} \sim 115^\circ$ .<sup>[2]</sup> As each boron atom is close to the centre of a triangular metal prism, infinite columns of those prisms connected along their rectangular faces follow the direction of the boron chains. One of the rectangular faces of the triangular metal prism is capped by a metal atom linking adjacent columns of prisms. With  $d_{B-Ta/Zr} = 0.2614$  nm the distance to the capping metal atom is only slightly longer than those to the prism forming Ta/Zr atoms. Due to strong covalent boron-boron bonds, boron defects in the metal borides with CrB-type, MoB-type and FeB-type are rare (see ref. 2).

#### 4. Conclusions

The existence of novel high temperature FeB-type phases Ta{Ti,Zr,Hf}B have been confirmed either from as cast or arc treated samples by X-ray powder and single crystal diffraction and electron probe microanalysis. In most cases the FeB-type monoboride is the major constituent, which suggests that this phase is the high temperature stabilization of a binary group IV metal monoboride. This holds true for Ti and Hf, while for Zr the evaluation proves that (Ta,Zr)B with FeB-type is a true ternary phase, as no stable FeB-type monoboride has been documented in the binary Zr-B system. An X-ray single crystal study of Ta<sub>0.78</sub>Zr<sub>0.22</sub>B unambiguously proved isotypism of the crystal structure with the FeB-type. EPMA evaluations show that the novel FeB-type phases Ta<sub>1-x</sub>{Ti,Zr,Hf}<sub>x</sub>B form via

substitution of Ta in TaB by small amounts of group IV elements ( $\sim 3$  at. % of Zr,  $\sim 7$  at. % Hf, and  $\sim 10$  at.% Ti).

## 5. Acknowledgements

The research reported herein was supported by the Austrian Federal Ministry of Science and Research (BMWF) under the scholarship scheme: Technology Grant Southeast Asia (Ph.D) in the frame of the ASEA UNINET. The authors furthermore acknowledge FAPESP (São Paulo, Brazil), grant 97/06348-4, for financial support. Part of this research was supported by the European Commission under the 6<sup>th</sup> Framework program through the Key Action: Strengthening the European Research Area, Research Infrastructures; Contract n.: RII3-CT-2003-505925.

## 6. References

1. Villars, P.; Cenzual, K. *Pearson's Crystal Data—Crystal Structure Database for Inorganic Compounds, Release 2014/15*; ASM International: Materials Park, OH, USA, 2014.
2. Rogl, P. Formation of Borides. In *Inorganic Reactions and Methods: Formation of Bonds to Group-I, -II, and -IIIB Elements*; Zuckerman, J. J., Hagen, A. P., Eds.; John Wiley & Sons, Inc., 1991; Vol. 13, p 84–85.
3. Hohnke, D.; Parthé, E. AB Compounds with ScY and Rare Earth Metals. II. FeB and CrB Structures of Monosilicides and Germanides. *Acta Crystallogr.* **1966**, *20* (4), p 572–582.
4. Boller, H.; Rieger, W.; Nowotny, H. Systematische Stapelfehler in der  $\delta$ -WB-Phase bei Bor-Unterschuß. *Monatshefte Für Chem. Verwandte Teile Anderer Wiss.* **1964**, *95* (6), p 1497–1501, in German.
5. Smid, I.; Rogl, P. Phase Equilibria and Structural Chemistry in Ternary Systems: Transition Metal-Boron-Nitrogen. In *Science of Hard Materials, Inst. Phys. Conf.Ser.75*; Almond, E. A., Brookes, C. A., Warren, R., Eds.; Adam Hilger Ltd. Bristol: Boston, 1986; p 249–257.
6. Kanaizuka, T. Invar like Properties of Transition Metal Monoborides  $Mn_{1-x}Cr_xB$  and  $Mn_{1-x}Fe_xB$ . *Mater. Res. Bull.* **1981**, *16* (12), p 1601–1608.
7. Pearson, W. B. *The Crystal Chemistry and Physics of Metals and Alloys*; Wiley-Interscience, 1972, p 520-523

8. Sobolev, A. S.; Kuz'ma, Y. B.; Soboleva, T. E.; Fedorov, T. F. Phase Equilibria in Tantalum-Titanium-Boron and Tantalum-Molybdenum-Boron Systems. *Sov. Powder Metall. Met. Ceram.* **1968**, 7 (1), p 48–51.
9. Voroshilov, Y. V.; Kuz'ma, Y. B. Reaction of Zirconium with the Transition Metals and Boron. *Sov. Powder Metall. Met. Ceram.* **1969**, 8 (11), p 941–944.
10. Kuz'ma, Y. B.; Svarichevskaya, S. I.; Telegus, V. S. Systems Titanium-Tungsten-Boron, Hafnium-Tantalum-Boron, and Tantalum-Tungsten-Boron. *Sov. Powder Metall. Met. Ceram.* **1971**, 10 (6), p 478–481.
11. Rogl, P.; Potter, P. E. A Critical Review and Thermodynamic Calculation of the Binary System: Hafnium-Boron. *Calphad* **1988**, 12 (3), p 207–218.
12. Bittermann, H.; Rogl, P. Critical Assessment and Thermodynamic Calculation of the Ternary System Boron-Hafnium-Titanium (B-Hf-Ti). *J. Phase Equilibria* **1997**, 18 (1), p 24–47.
13. E. Rudy. *Ternary Phase Equilibria in Transition Metal-Boron-Carbon-Silicon Systems, Part V*; Compendium of Phase Diagram Data, Technical Report AFML-TR-65-2, Part V; Air Force Materials Laboratory Wright Patterson Air Force Base: Ohio, USA, 1969; p 1–698.
14. Rogl, P.; Potter, P. E. A Critical Review and Thermodynamic Calculation of the Binary System: Zirconium-Boron. *Calphad* **1988**, 12 (2), p 191–204.
15. V.M. Chad; F.F. Ferreira; B. Paulino; C.G. Coelho; C.A. Nunes. Thermodynamic Modelling of the Ta-B System. In *Congresso Anual da ABM 63rd*; 2008; p 1412–1423, in Portuguese.
16. Rodríguez-Carvajal, J. Recent Developments of the Program FULLPROF. *Comm. Powder Diffraction. IUCr Newsl.* **2001**, 26, p 12–19.
17. Sheldrick, G. M. A Short History of SHELX. *Acta Crystallogr. A* **2007**, 64 (1), 112–122.
18. Farrugia, L. J. WinGX Suite for Small-Molecule Single-Crystal Crystallography. *J. Appl. Crystallogr.* **1999**, 32 (4), p 837–838.
19. Gelato, L. M.; Parthé, E. STRUCTURE TIDY – a Computer Program to Standardize Crystal Structure Data. *J. Appl. Crystallogr.* **1987**, 20 (2), p 139–143.
20. Bittermann, H.; Rogl, P. In *Phase Diagrams of Ternary Metal-Boron-Carbon Systems*; Effenberg, G., Ed.; ASM Intl.: Ohio, USA, 1998; p 1–525.
21. Borisov, D. B.; Artyukh, L. V.; Bondar, A. A.; Martsenyuk, P. S.; Samelyuk, A. V.; Tsiganenko, N. I.; Fomichov, O. S.; Velikanova, T. Y. Titanium-Boride Eutectic

- Materials. Structure of the Ti-Nb-B Alloys and Phase Equilibria. *Powder Metall. Met. Ceram.* **2007**, 46 (1-2), p 58–71.
22. *Inorganic Crystal Structure Database 2014/1*; Fachinformationszentrum: Karlsruhe, Germany, 2014.
23. Kapfenberger, C.; Albert, B.; Pöttgen, R.; Huppertz, H. Structure Refinements of Iron Borides Fe<sub>2</sub>B and FeB. *Z. für Krist.* **2006**, 221 (5-7/2006), p 477–481.
24. Perkins, R. S.; Brown, P. J. Charge and Spin Density in the Iron Borides. *J. Phys. F Met. Phys.* **1974**, 4 (6), p 906–920.
25. Teatum, E.; Gschneidner, K.; Waber, J. *LA-2345*; US Department of Commerce: Washington, DC, 1960; reproduced in W.B. Pearson, *The Crystal Chemistry and Physics of Metals and Alloys*, Wiley, New York, 1972, p. 151.

**Table 1.** Lattice parameters (from XPD) and corresponding EPMA data for the phases in  $Ta_{1-x}T_xB$  alloys, T=Ti,Zr,Hf.

Composition/ code	PC <sup>#</sup>	Phase (structure type)	Lattice parameters (nm)			EPMA (at. %) ( $\pm 0.5$ )			Mass %
			a	b	c	T	Ta	B <sup>§</sup>	
TaB	arc	TaB (CrB)	0.32795(2)	0.8671(2)	0.31552(1)	-	49.0	51.0	100
$Ta_{0.8}Zr_{0.2}B$	arc*	TaB (FeB)	0.6207(10)	0.3174(2)	0.4749(8)	3.8	46.2	50	73
		TaB (FeB)	0.6153(11)	0.31648(5)	0.4674(7)	12.0	38.0	50	26
		Ta(Zr) (W)	-	-	-	92.5	7.5	-	1
$Ta_{0.8}Zr_{0.2}B$ #1	arc (1)*	TaB (FeB)	0.6134(25)	0.31689(9)	0.4839(73)	3.2	46.8	50	35
		TaB (FeB)	0.6162(3)	0.31627(5)	0.4704(1)	7.1	42.9	50	63
		Ta(Zr) (W)				73.5	26.5		2
$Ta_{0.8}Zr_{0.2}B$ #2	arc (2)*	TaB (FeB)	0.6147(1)	0.31638(5)	0.46754(3)	3.4	46.6	50	43
		TaB (CrB)	0.32865(7)	0.8687(11)	0.31659(3)	4.5	45.5	50	42
		Ta(Zr) (W)				18.7	81.3	-	15
$Ta_{0.7}Zr_{0.3}B$	arc	TaB (FeB)	0.6162 (2)	0.31616(1)	0.4717(2)	8.5	41.5	50	38
		TaB (FeB)	0.6258 (1)	0.31647(1)	0.46861(3)	6.1	43.9	50	58
		Ta(Zr) (W)				89.9	10.1	-	4
$Ta_{0.8}Hf_{0.2}B$	arc	TaB (FeB)	0.6188 (4)	0.31576(1)	0.4711(3)	9.6	40.4	50	74
		TaB (FeB)	0.6148(17)	0.3170 (1)	0.4646(45)	5.8	44.2	50	26
$Ta_{0.78}Hf_{0.22}B$	arc	TaB (FeB)	0.61800(7)	0.31577(2)	0.47025(4)	8.6	41.4	50	58
		TaB (FeB)	0.6168(2)	0.31593(3)	0.4693(2)	7.2	42.8	50	23
		Ta(Hf) (W)	0.3376(1)	-	-	41.3	58.7	-	19
$Ta_{0.68}Ti_{0.32}B$ #1	slow cooled	Ta <sub>3</sub> B <sub>4</sub> (own)	0.30961(3)	0.32768(3)	1.3921(5)	11.4	28.8	59.9	23
		TaB (CrB)	0.32645(1)	0.86517(1)	0.31387(1)	9.3	40.7	50	4
		TaB (FeB)	0.6121(4)	0.31166(4)	0.4646(1)	12.8	37.2	50	46
		TaB (FeB)	0.6158(2)	0.31163(3)	0.4685(1)	11.0	39.0	50	13
		TaB <sub>2</sub> (AlB <sub>2</sub> )	0.30509(3)	-	0.32412(5)	13.4	19.7	66.9	13
		Ta(Ti) (W)	-	-	-	-	-	-	<1
$Ta_{0.68}Ti_{0.32}B$ #2	low arc	Ta <sub>3</sub> B <sub>4</sub> (own)	0.3099(2)	0.3277(2)	1.396(5)	10.3	34.6	55.1	9
		TaB (CrB)	0.32761(3)	0.8729(5)	0.31253(2)	9.3	40.7	50	7
		TaB (FeB)	0.61222(8)	0.31216(1)	0.46469(4)	12.8	37.2	50	72
		TaB <sub>2</sub> (AlB <sub>2</sub> )	-	-	-	15.4	17.0	67.7	5
		Ta(Ti) (W)	0.3288(8)	-	-	-	-	-	7

<sup>#</sup> PC stands for processing conditions

<sup>§</sup> For all transition metal monoborides, the B content is assumed to be 50 at. %

\* Same nominal composition prepared in different batches

**Table 2.** Structural data for (Ta,Ti)B from Rietveld refinement (Guinier-Huber Image Plate, Cu K $\alpha$  8 $\leq 2\Theta \leq 100^\circ$ ); standardized with program *Structure Tidy*.<sup>[19]</sup>

Parameter/compound	Ta <sub>1-x</sub> Ti <sub>x</sub> B, x= 0.25
Structure type	FeB
Space group type (No.)	<i>Pnma</i> (62)
<i>a</i> [nm]	0.61222(8)
<i>b</i> [nm]	0.31216(1)
<i>c</i> [nm]	0.46469(4)
Reflections in refinement	61
Number of variables	16
$R_F = \Sigma  F_o - F_c  / \Sigma F_o$	0.0217
$R_I = \Sigma  I_o - I_c  / \Sigma I_o$	0.0314
$R_{wp} = [\Sigma w_i  y_{oi} - y_{ci} ^2 / \Sigma w_i  y_{oi} ^2]^{1/2}$	0.113
$R_p = \Sigma  y_{oi} - y_{ci}  / \Sigma  y_{oi} $	0.10
$R_e = [(N - P + C) / \Sigma w_i y_{oi}^2]^{1/2}$	0.0272
$\chi^2 = (R_{wp} / R_e)^2$	17.25
<b>M</b> in 4c (x, 1/4, z); occ.	x= 0.1758(1); z= 0.6239(1); 0.75(1) Ta+0.25(1) Ti;
B <sub>iso</sub> (10 <sup>2</sup> nm <sup>2</sup> )	0.56
<b>B</b> in 4c (x, 1/4, z); occ.	x= 0.037(1); z= 0.111(2); 1.00(-);
B <sub>iso</sub> (10 <sup>2</sup> nm <sup>2</sup> )	0.54

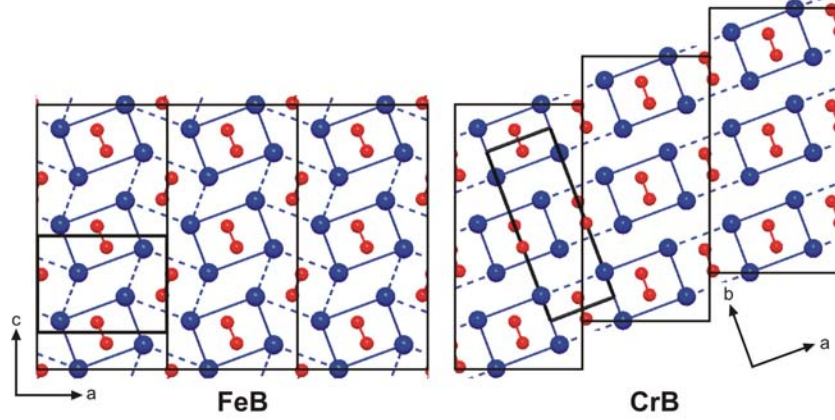
**Table 3.** X-Ray single crystal data for Ta<sub>0.78</sub>Zr<sub>0.22</sub>B (FeB-type; space group *Pnma*) at RT (anisotropic displacement parameters U<sub>ij</sub> in [10<sup>-2</sup>nm<sup>2</sup>]). Data standardized with program *Structure Tidy*.<sup>[19]</sup>

Parameter/compound	Ta <sub>0.78</sub> Zr <sub>0.22</sub> B
Phase composition (EPMA, at.%)*	Ta <sub>38</sub> Zr <sub>12</sub> B <sub>50</sub>
Composition from refinement (at.%)	Ta <sub>37</sub> Zr <sub>13</sub> B <sub>50</sub>
<i>a</i> [nm]	0.617256(11)
<i>b</i> [nm]	0.316427(5)
<i>c</i> [nm]	0.469934(9)
θ range (deg)	2.7 < θ < 80.74
Mosaicity	0.54
Number of variables	10
Reflections in refinement	282 ≥ 4σ(F <sub>o</sub> ) of 319
R <sub>F2</sub> = Σ F <sub>o</sub> <sup>2</sup> - F <sub>c</sub> <sup>2</sup>  /ΣF <sub>o</sub> <sup>2</sup>	0.0165
wR2	0.0451
R <sub>Int</sub>	0.053
GOF	1.203
Extinction (Zachariasen)	0.007(1)
Residual density e <sup>-</sup> /Å <sup>3</sup> ; max; min	3.21; -3.14
<b>Atom Positions</b>	
<b>0.78(1) Ta+ 0.22 Zr</b> in 4c (x, ¼, z)	x=0.17579(3); z=0.62342(5)
U <sub>11</sub> ; U <sub>22</sub> ; U <sub>33</sub> ; U <sub>23</sub> =U <sub>12</sub> =0; U <sub>13</sub>	0.00211); 0.0026(1); 0.0019(1); 0.0002(1)
<b>B</b> in 4c (x, ¼, z); occ.	x =0.0315 (9); z =0.1004(13); 1.00(1)
U <sub>iso</sub>	0.0055(9)

\*The highest Zr/Ta ratio (after EPMA) for the sample from where the single crystal was selected.

<b>Interatomic distances [nm]; Standard deviation &lt; 0.0001</b>		
Atom 1	Atom 2	Distance [nm]
B	2 B	0.1883
	2 Ta/Zr	0.2404
	2 Ta/Zr	0.2412
	Ta/Zr	0.2413
	Ta/Zr	0.2434
	Ta/Zr	0.2614
Ta/Zr	2 B	0.2404
	2 B	0.2412
	B	0.2413
	B	0.2434
	B	0.2614

	2 Ta/Zr	0.2925
	4 Ta/Zr	0.2977
	2 Ta/Zr	0.3164
	2 Ta/Zr	0.3307
<b>Bonding angle</b> in boron zig-zag chain: $\phi_{B-B-B} = 114.3^\circ$		



$$V_{FeB} = V_{CrB} \Leftrightarrow a_{FeB} \times b_{FeB} \times c_{FeB} = a_{CrB} \times b_{CrB} \times c_{CrB}$$

$$a_{FeB} = \frac{2 \times a_{CrB} \times b_{CrB}}{\sqrt{a_{CrB}^2 + b_{CrB}^2}}; \quad b_{FeB} = c_{CrB}; \quad c_{FeB} = \frac{1}{2} \sqrt{a_{CrB}^2 + b_{CrB}^2}$$

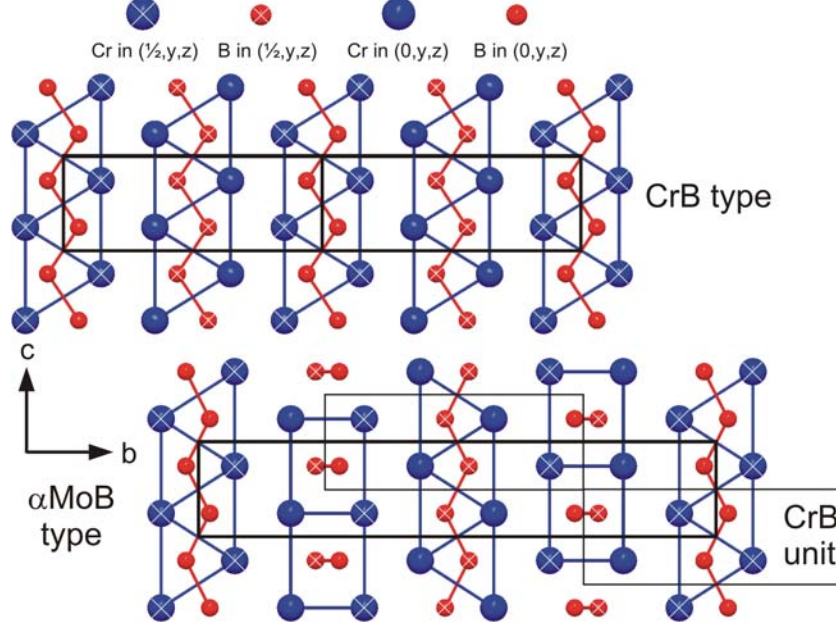


Figure 1. (a) upper panel, left: projection of the FeB structure along its b-axis; upper panel, right: shift of three slabs of the FeB-type atom arrangement along  $\frac{1}{2} c$  creating the atom arrangement of the CrB-type. Metal atoms in blue; boron atoms in red. The unit cells of FeB and CrB (both orthorhombic) are outlined with bold frames. (b) lower panel, top: the structures of CrB and of  $\alpha$ MoB, both projected along the a-axis; lower panel, bottom: schematic arrangement of CrB-type slabs; every second CrB slab is shifted by  $\frac{1}{2} a + \frac{1}{2} c$  and creates the atom arrangement of  $\alpha$ MoB. Random stacking faults may appear creating diffuse X-ray reflections.



Ti		V		Cr	hT	Mn	ℓT	Fe	ℓT	Co		Ni	
					ℓT	hT		hT					
Zr		Nb		Mo	hT								
					ℓT								
Hf		Ta		W	hT								
					ℓT								

MoB-type  
 CrB-type  
 FeB-type

**Figure 2.** Distribution of monoboride structure types among transition metals.

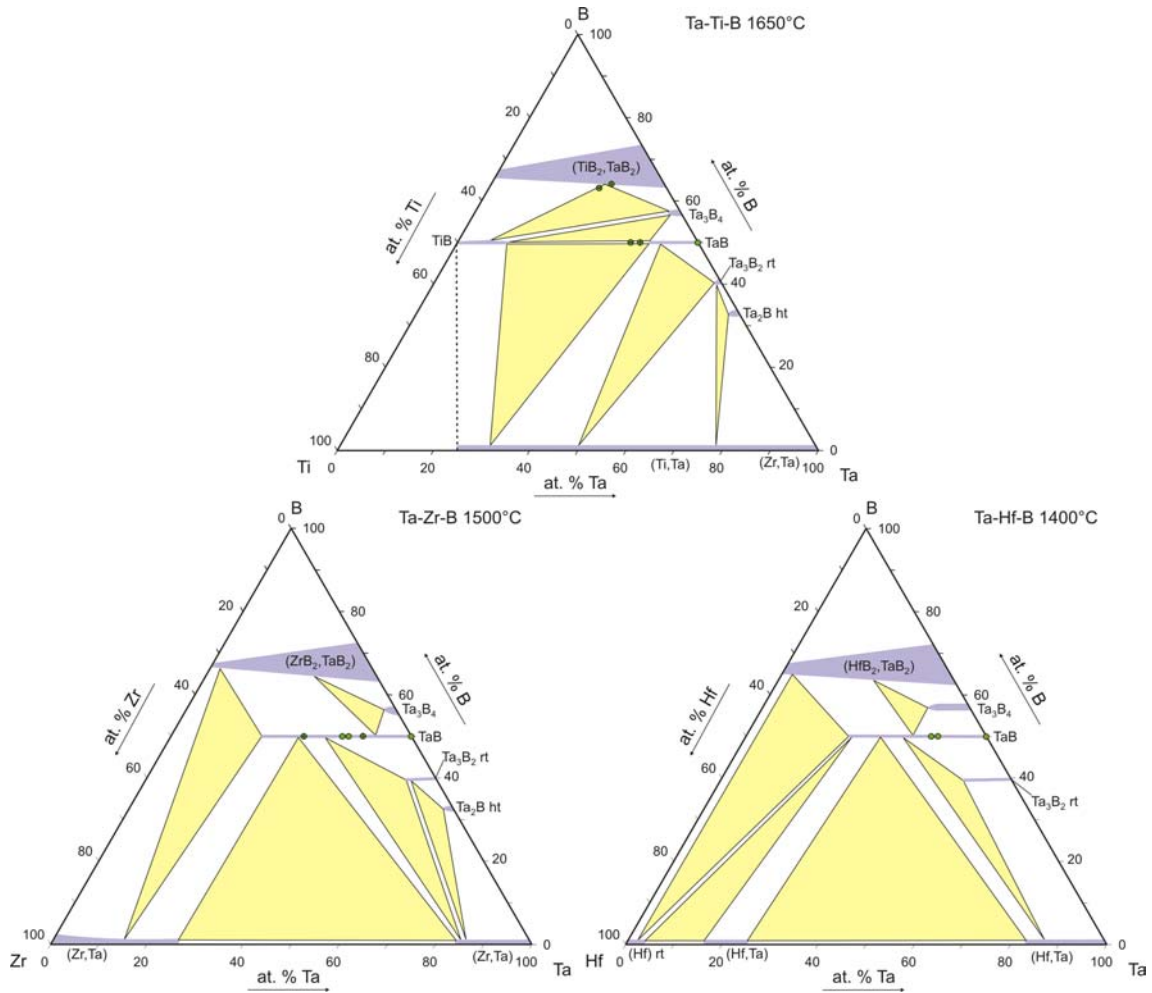


**Figure 3.** Phase relations in isothermal sections as shown in the literature for the ternary diagrams Ti-Ta-B (1650°C),<sup>[8]</sup> Zr-Ta-B (1500°C),<sup>[9]</sup> and Hf-Ta-B (1400°C).<sup>[10]</sup>

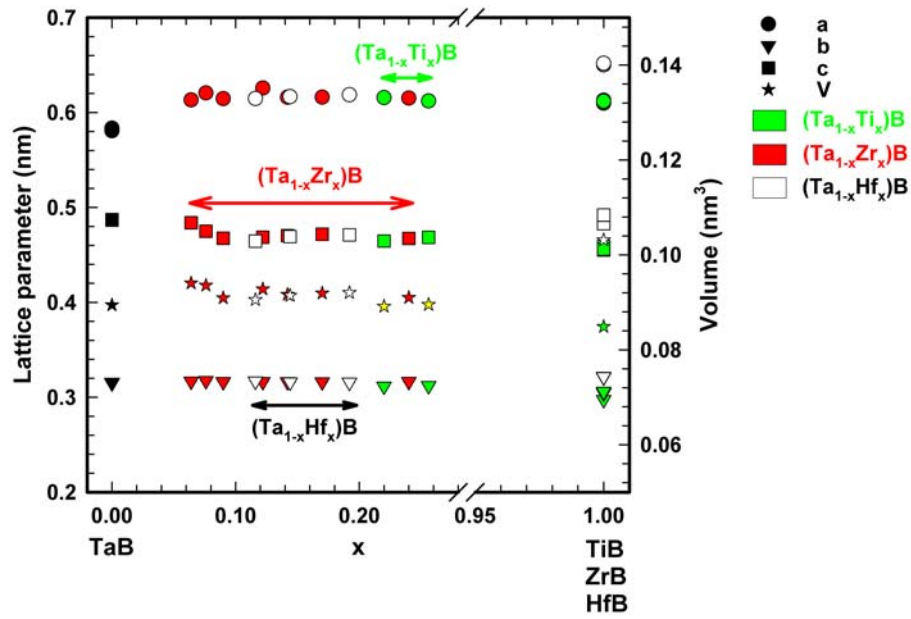


**Figure 4.** Compositional dependence of lattice parameters and ranges of existence (indicated by arrows) of the FeB-type phases  $\text{Ta}_{1-x}\{\text{Ti,Zr,Hf}\}_x\text{B}$ .

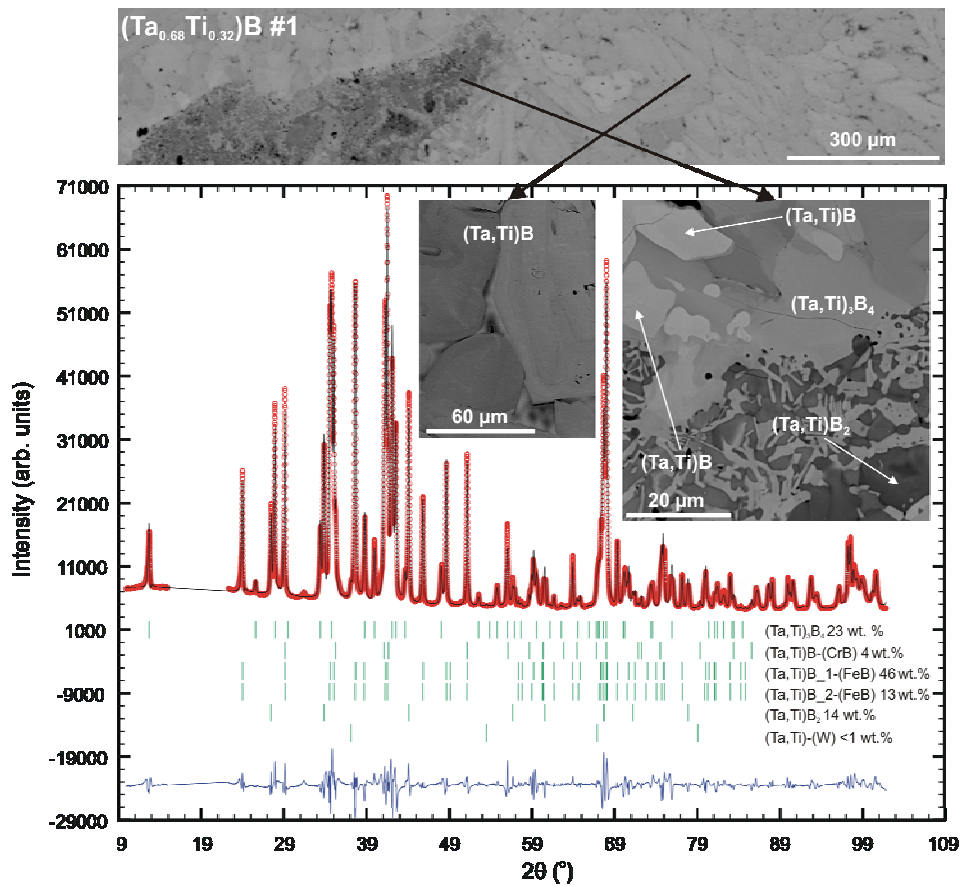


**Figure 5a.** XRPD pattern and micrographs of  $\text{Ta}_{0.68}\text{Ti}_{0.32}\text{B}$  #1 (slowly cooled) samples.

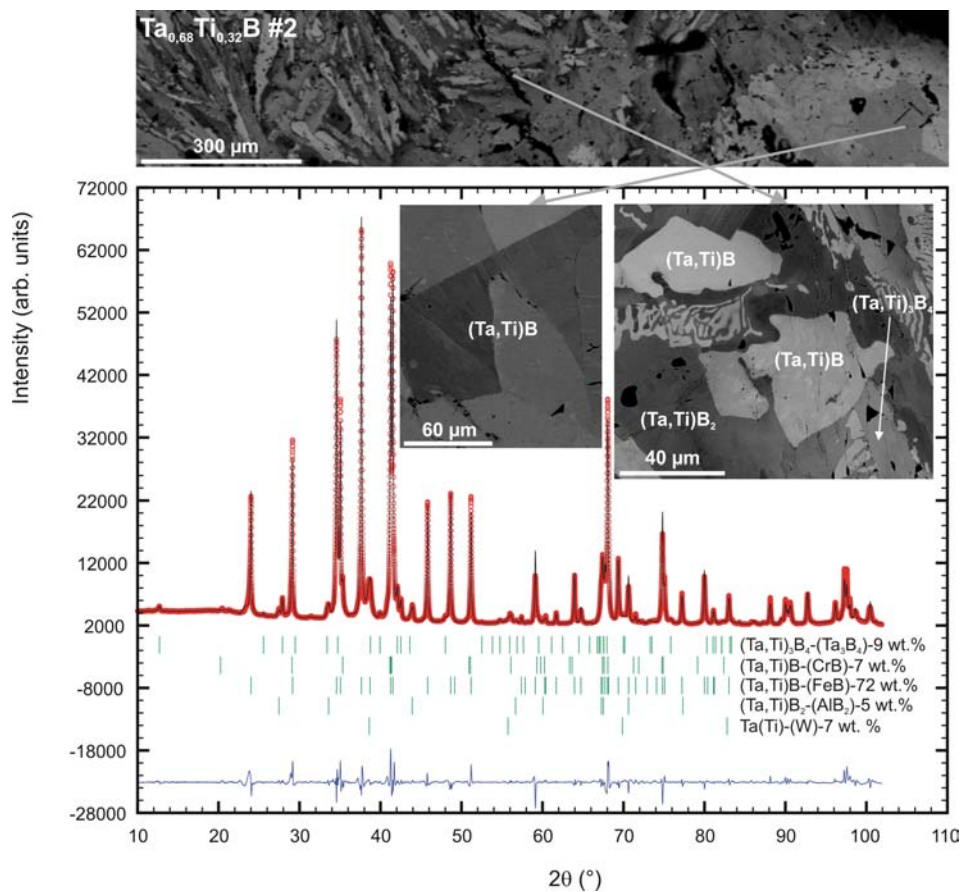


**Figure 5b.** XRPD pattern and micrographs of  $\text{Ta}_{0.68}\text{Ti}_{0.32}\text{B}$  #2 (low arc power treated) sample.

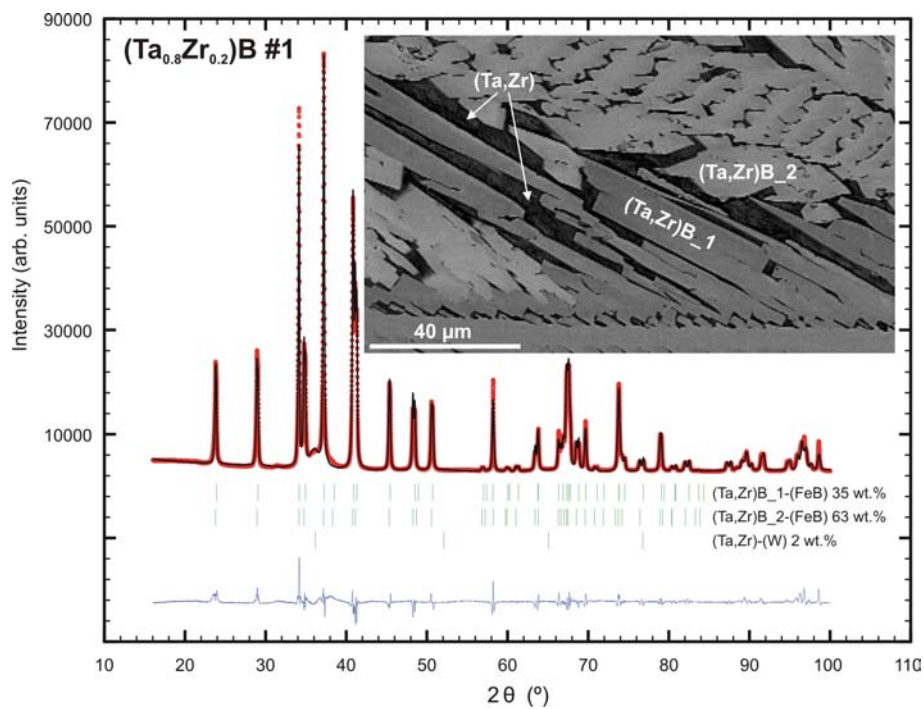


**Figure 6a.** XRPD pattern and micrographs of  $\text{Ta}_{0.80}\text{Zr}_{0.20}\text{B}$  #1 sample.

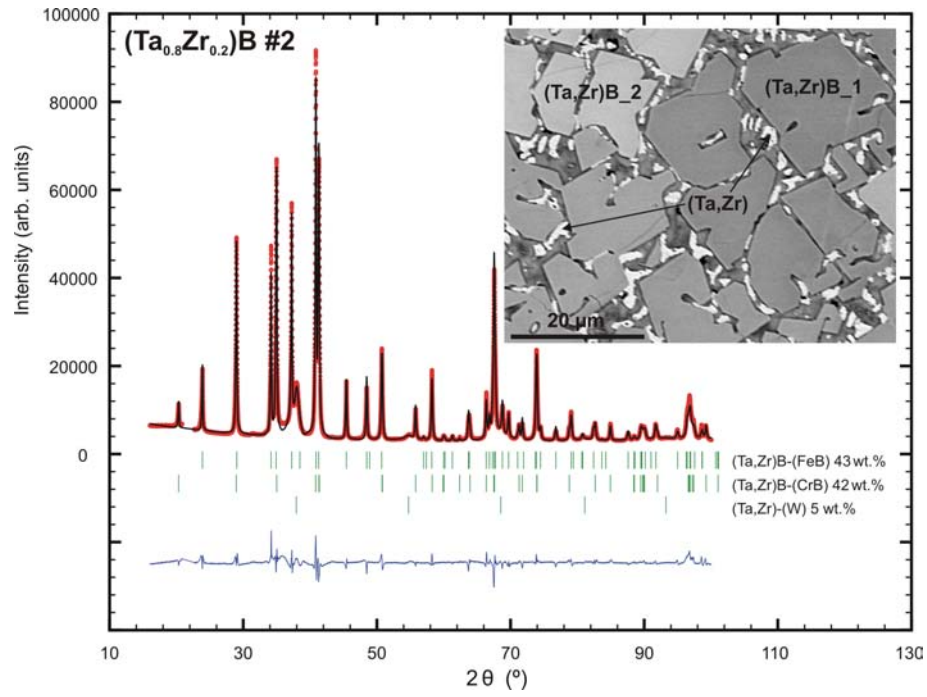


**Figure 6b.** XRPD pattern and micrographs of  $\text{Ta}_{0.80}\text{Zr}_{0.20}\text{B}$  #2 sample.

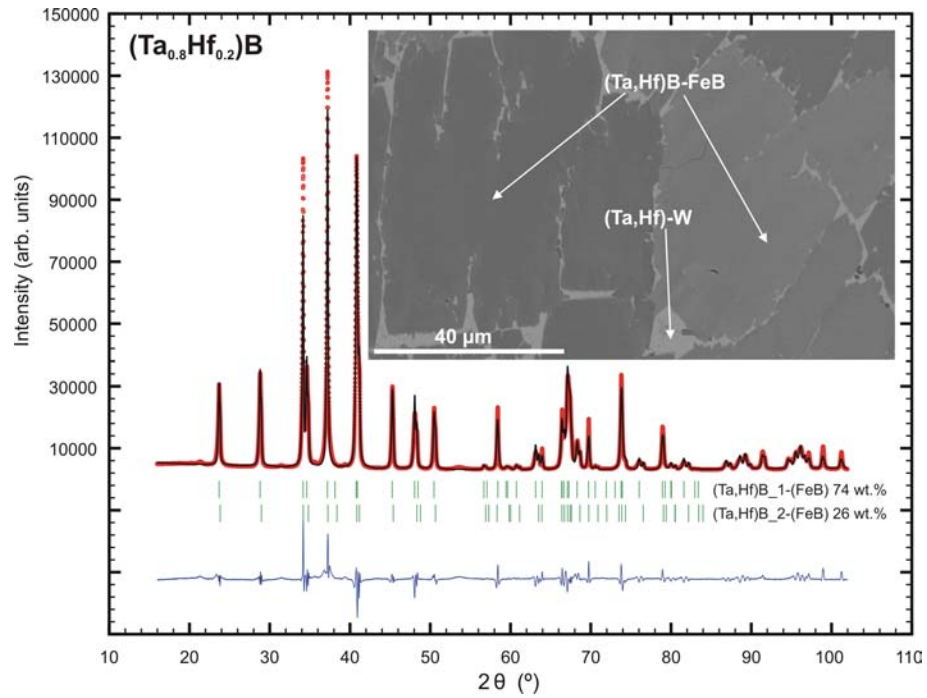


**Figure 7a.** XRPD pattern and micrographs of  $\text{Ta}_{0.80}\text{Hf}_{0.20}\text{B}$  sample.



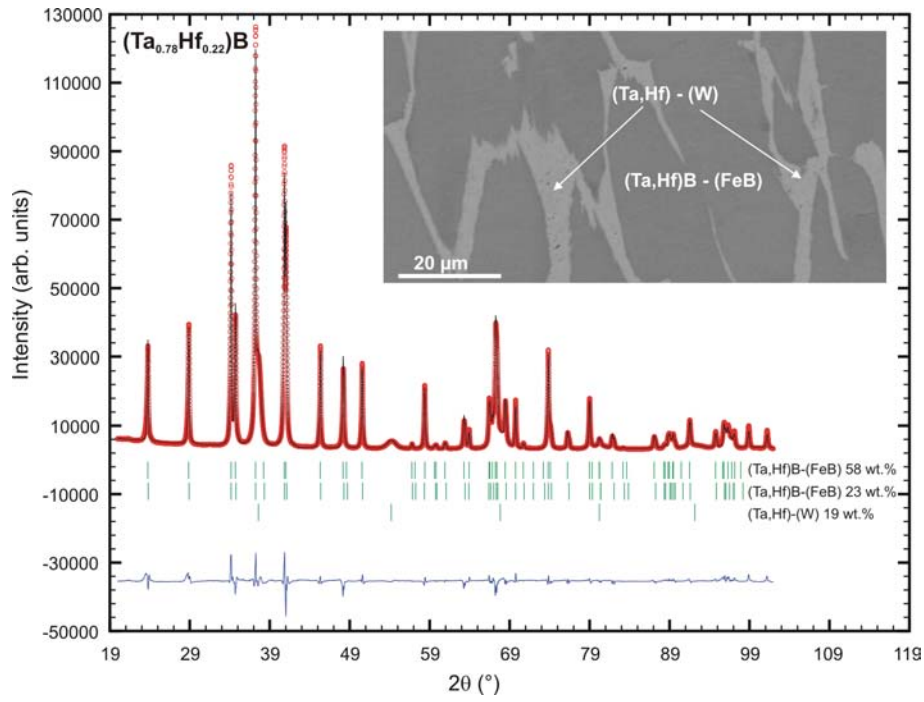


**Figure 7b.** XRPD pattern and micrographs of  $\text{Ta}_{0.78}\text{Hf}_{0.22}\text{B}$  sample.

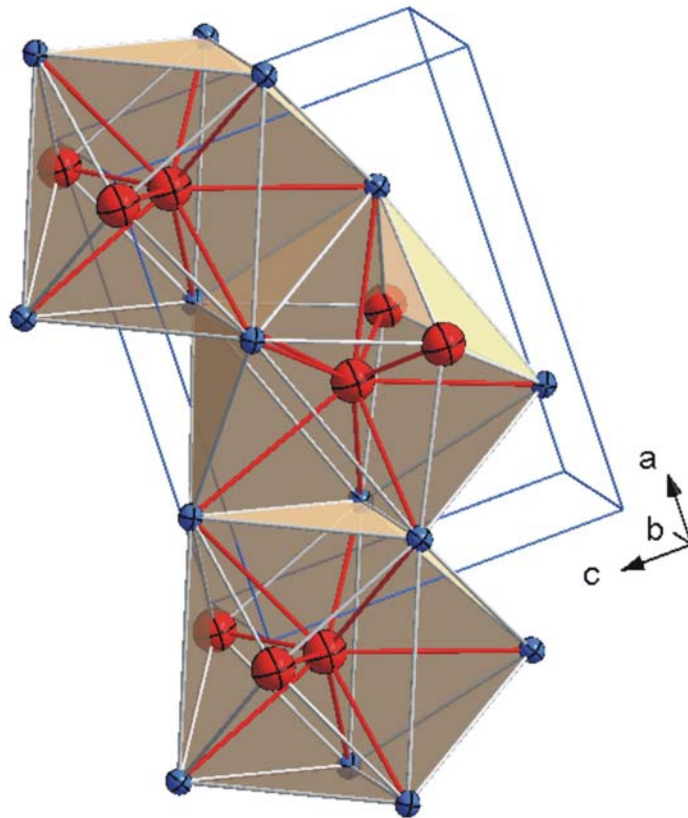


**Figure 8.** Connectivity of mono-capped triangular prisms of Ta/Zr-atoms in  $\text{Ta}_{0.8}\text{Zr}_{0.2}\text{B}$  sharing triangular faces. Each mono-capped metal prism is centered by a boron atom:  $[\text{Ta}(\text{Zr})_7]\text{B}$  forming infinite -B-B-B- chains running parallel to the b-axis inferring also infinite chains of Ta/Zr-prisms sharing their rectangular faces. Ta/Zr-atoms in blue are presented with ADPs from single crystal refinement, isotropic B-atoms (ADP from SC refinement) are red.

## Chapter 3 Constitution of the Systems {V,Nb,Ta}-Sb and Physical Properties of di-antimonides {V,Nb,Ta}Sb<sub>2</sub>

F. Failamani<sup>a</sup>, P. Broz<sup>b,c</sup>, D. Macciò<sup>d</sup>, S. Puchegger<sup>e</sup>, H. Müller<sup>f</sup>, L. Salamakha<sup>f</sup>, H. Michor<sup>f</sup>, A. Grytsiv<sup>a,g</sup>, A. Saccone<sup>d</sup>, E. Bauer<sup>f,g</sup>, G. Giester<sup>h</sup>, P. Rogl<sup>a,g</sup>.

<sup>a</sup>*Institute of Physical Chemistry, University of Vienna, Währinger Straße 42, A-1090 Vienna, Austria*

<sup>b</sup>*Masaryk University, Faculty of Science, Department of Chemistry, Kotlarska 2, 611 37, Brno, Czech Republic*

<sup>c</sup>*Masaryk University, Central European Institute of Technology, CEITEC, Kamenice 753/5, Brno 62500, Czech Republic*

<sup>d</sup>*Dipartimento di Chimica e Chimica Industriale, Università di Genova, Via Dodecaneso 31, I-16146 Genova, Italy*

<sup>e</sup>*Faculty Center for Nanostructure Research, Faculty of Physics, University of Vienna, Boltzmanngasse 5, A-1090 Wien, Austria*

<sup>f</sup>*Institute of Solid State Physics, Vienna University of Technology, Wiedner Hauptstraße 8-10, A-1040 Vienna, Austria*

<sup>g</sup>*Christian Doppler Laboratory for Thermoelectricity, Vienna, Austria*

<sup>h</sup>*Institute of Mineralogy and Crystallography, University of Vienna, Althanstraße 14, A-1090 Vienna, Austria*

(Intermetallics 65 (2015) 94-110)

Contributions to this paper:

F. Failamani : samples preparation and characterization, transport properties measurements, writing the paper

P. Broz : DTA measurements in quartz crucible, discussions, proofreading

D. Macciò and A. Saccone: DTA measurements in Ta crucible, discussions, proofreading

S. Puchegger : elastic moduli measurements, proofreading

H. Müller : thermal expansion coefficient measurements, proofreading

L. Salamakha : resistivity measurement under various magnetic fields

H. Michor : specific heat measurement, discussions, comments, proofreading

A. Grytsiv : diffusion couple experiments, preliminary single crystal test, discussions, comments, proofreading

E. Bauer and P. Rogl: discussions, comments, proofreading

G. Giester : single crystal data collection

## Abstract

The binary phase diagrams {V,Nb,Ta}-Sb below 1450°C were studied by means of XRPD, EPMA, and DTA measurements. In the V-Sb system, five stable binary phases were observed in this investigation:  $V_{3+x}Sb_{1-x}$ ,  $\ell T-V_3Sb_2$ ,  $hT-V_{2-x}Sb$ ,  $V_{7.46}Sb_9$ ,  $V_{1-x}Sb_2$ . The V-Sb phase diagram is characterized by two degenerate eutectic reactions:  $L \leftrightarrow V_{3+x}Sb_{1-x} + (V)$  ( $T > 1450^\circ C$  at 18.1 at.% Sb) and  $L \leftrightarrow V_{1-x}Sb_2 + (Sb)$  ( $T = (621 \pm 5)^\circ C$  at ~99 at.% Sb), three peritectic reactions:  $L + V_{3+x}Sb_{1-x} \leftrightarrow hT-V_{2-x}Sb$  ( $T = (1230 \pm 10)^\circ C$  at ~42 at.% Sb),  $L + hT-V_{2-x}Sb \leftrightarrow V_{7.46}Sb_9$  ( $T = (920 \pm 10)^\circ C$  at ~87 at.% Sb), and  $L + V_{7.46}Sb_9 \leftrightarrow V_{1-x}Sb_2$  ( $T = (869 \pm 5)^\circ C$  at ~88 at.% Sb), a peritectoid reaction:  $V_{3+x}Sb_{1-x} + hT-V_{2-x}Sb \leftrightarrow \ell T-V_3Sb_2$  at  $(875 \pm 25)^\circ C$ , a eutectoid reaction:  $hT-V_{2-x}Sb \leftrightarrow \ell T-V_3Sb_2 + V_{7.46}Sb_9$  at  $(815 \pm 15)^\circ C$  and congruent melting of  $V_{3+x}Sb_{1-x}$  ( $T > 1450^\circ C$ ). An X-ray single crystal study of  $V_5Sb_4C_{1-x}$  proved the existence of interstitial elements in the octahedral voids of a partially filled  $Ti_5Te_4$ -type structure ( $x \sim 0.5$ ;  $R_{F2} = 0.0101$ ), therefore this phase (earlier labeled “ $V_5Sb_4$ ”) was excluded from the binary equilibrium phase diagram.  $V_5Sb_4C_{1-x}$  is the first representative of a filled  $Ti_5Te_4$ -type structure.

A re-investigation of the Nb-Sb system removed the contradiction between the hitherto reported phase diagrams and confirmed the version derived by Melnyk et al. (see ref. [1]). Three binary phases exist in the Ta-Sb system:  $Ta_{3+x}Sb_{1-x}$ ,  $Ta_5Sb_4$ ,  $TaSb_2$ . Due to instrumental limits ( $\leq 1450^\circ C$ ), only the peritectic reaction of  $TaSb_2$ :  $L + Ta_5Sb_4 \leftrightarrow TaSb_2$  ( $(1080 \pm 10)^\circ C$  at ~92 at.% Sb) and a degenerate Sb-rich eutectic reaction ( $L \leftrightarrow TaSb_2 + (Sb)$ ;  $(622 \pm 5)^\circ C$ ; ~99 at.% Sb) have been determined.

Physical properties (mechanical and transport properties) of binary di-antimonides were investigated with respect to a potential use of these metals either as diffusion barriers or electrodes for thermoelectric devices based on skutterudites. All group-V metal di-antimonides have low metallic-type resistivity and relatively high thermal conductivity. Magnetic field has little influence on the resistivity of  $V_{1-x}Sb_2$  at low temperature, while on {Nb,Ta} $Sb_2$  it increases the resistivity, especially on Nb $Sb_2$ . The coefficient of thermal expansion (CTE) decreases from  $V_{1-x}Sb_2$  to  $TaSb_2$ , particularly the CTE value of Nb $Sb_2$  is in range of average n-type filled skutterudites. In contrast to the CTE value, elastic moduli increase from  $V_{1-x}Sb_2$  to  $TaSb_2$ . The value for  $V_{1-x}Sb_2$  is in the range of Sb-based skutterudites, whereas the values for {Nb,Ta} $Sb_2$  are significantly higher.

*Keywords:* A. intermetallics (antimonides), B. electrical properties, B. mechanical properties, F. differential thermal analysis, F. diffraction/scattering.

## 1. Introduction

Antimony (Sb) - based skutterudites are known for their high thermoelectric (TE) performance [2–4]. For device fabrication not only a high thermoelectric efficiency of the p- and n-legs is required, but also electric contact materials i.e. particularly the hot electrodes should warrant long-term operation, good transport properties, and mechanical properties compatible with p- and n- legs. Group-V metals are known to have high melting points, good mechanical strength, high electrical conductivity and good corrosion resistance and thus could function as potential hot electrode. Moreover, they should have elastic moduli and coefficients of thermal expansion close to Sb-based skutterudites [5]. In order to define an electrode material suitable for long-term operation in contact with skutterudite based thermoelectrics at the hot end of the TE-device, the detailed knowledge of the binary metal - antimony phase diagrams and properties of phases formed in the diffusion zone are required. Hitherto, only the Nb-Sb phase diagram has been reported [1,6–8] although with some controversial results, whilst the {V,Ta}-Sb phase diagrams have not been constructed yet. The present paper tries to close this gap and to remove ambiguities from the Nb-Sb diagram. Several reports on the physical properties of {V,Nb,Ta}Sb<sub>2</sub> can be found in the literature [9–17]. However, no detailed studies of thermal, transport, and mechanical properties of these compounds were performed in the temperature region relevant for automotive application of skutterudite thermoelectrics (up to 600°C). Therefore in this paper we investigate the thermal, transport, and mechanical properties of {V,Nb,Ta}Sb<sub>2</sub> in view of a potential use of these metals as electrode or diffusion barriers for Sb-based skutterudites thermoelectric devices, since these compounds form in the diffusion zones between metal and skutterudite (see Figure 1).

## 2. Experimental Methods

All binary {V,Nb,Ta}-Sb samples (about 1 gram each) were prepared from intimate blends of freshly prepared vanadium filings (filed with a diamond file from vanadium chunks, purity 99.8%), powders of vanadium rich master alloys (15-25 at.% Sb), powders of niobium (<500 ppm Ta), tantalum (<50 ppm Nb) and antimony, all of purity better than 99.9 wt.% (metal basis, excluding the afore mentioned impurities). Vanadium rich master alloys were prepared by direct arc melting of vanadium and antimony pieces with about 5 wt.% extra Sb to compensate the evaporation losses. The well-mixed powder blends were cold pressed in a steel die without lubricant, sealed in quartz ampoules under vacuum and heat treated at different temperatures for 1 week. In order to ensure complete/better



equilibration, after quenching in cold water, samples were re-powderized and sieved to a grain size below 53  $\mu\text{m}$  inside an Ar-filled glove box. Powders were then cold pressed and sintered or hot pressed to obtain dense samples. Weight losses due to Sb evaporation during this process were less than 0.1 wt.%. As cast alloys were prepared by argon arc melting of sintered samples under low current with a non-consumable tungsten electrode.

For sample characterization we used Scanning Electron Microscopy (SEM, electron probe microanalysis (EPMA)) and X-ray powder diffraction (XRPD). EPMA measurements were performed on a Zeiss Supra 55 VP scanning electron microscope, operated at 20 kV employing energy dispersive X-ray (EDX) analysis for determining the chemical composition. Prior to EPMA measurement, samples were polished with standard methods and analysed with a Light Optical Microscope (LOM). XRPD was carried out at room temperature and ambient pressure on powders dispersed on mylar foils used in transmission geometry on a Guinier-Huber image plate recording system (Ge-monochromated  $\text{Cu-K}\alpha_1$  radiation; theta range:  $8^\circ < 2\theta < 110^\circ$  in steps of  $0.005^\circ$ ). The lattice parameters were determined by least squares fits to the indexed  $2\theta$  values using germanium as internal standard. For Rietveld refinements of the X-ray powder intensity patterns we used the FULLPROF program [18].

DTA measurements were performed on annealed samples in sealed quartz ampoules up to  $1080^\circ\text{C}$  in a Netzsch 409 CD/3/403/5/G. Recordings at temperatures up to  $1450^\circ\text{C}$  were performed in a Netzsch DSC 404 C Pegasus on samples weld-sealed under 0.2 bar argon in tantalum crucibles with internal linings of tungsten. Measurements were repeated twice to ensure reproducibility. Within the various heating ramps (1K/min, 2K/min 3K/min and 5K/min) tested, within the error bars no significant trend was seen on the recorded isothermal reaction temperatures.

A single crystal of “ $\text{V}_5\text{Sb}_4$ ” ( $\text{V}_5\text{Sb}_4\text{C}_{1-x}$ ) suitable for X-ray single crystal structure analysis was isolated from a mechanically crushed V22Sb78 alloy (in at.%) annealed at  $860^\circ\text{C}$  in a long quartz tube to separate the crystal from antimony. X-ray single crystal diffraction (XSCD) data were collected at room temperature on a Bruker APEXII diffractometer equipped with a CCD area detector and an Incoatec Microfocus Source  $\text{I}\mu\text{S}$  (30 W, multilayer mirror,  $\text{Mo-K}\alpha$ ). Several sets of phi- and omega-scans with  $2.0^\circ$  scan width were measured at a crystal-detector distance of 3.5 cm (full sphere;  $5.9^\circ < 2\theta < 80.5^\circ$ ). The crystal structures were solved applying direct methods (SHELXS-97) and refined against  $F^2$  (SHELXL-97-2) [19] within the program WinGX [20].

Single-phase samples of di-antimonides  $\{V,Nb,Ta\}Sb_2$  were prepared from powders of Nb, Ta, Sb and small pieces of V mixed in stoichiometric ratio with an extra 3-5 wt.% antimony to compensate losses during heat treatment. The mixtures were treated in a similar way as the samples for the phase diagram. Heat treatments were performed at 800°C for  $VSb_2$  and 900°C for  $NbSb_2$  and  $TaSb_2$ . After the reactions were complete, samples were re-powderized in the way mentioned above, loaded inside a graphite die, and hot pressed under uniaxial pressure of 56 MPa at 800°C for 30 minutes for  $VSb_2$  and 900°C for 1 hour for  $\{Ta,Nb\}Sb_2$ , respectively. Densities of hot pressed samples, measured by the Archimedes method, were at least 97% of X-ray density. XRPD and EPMA measurements were performed to ensure single-phase condition and homogeneity of samples prior to physical properties measurements. For resistivity and low temperature thermal conductivity measurements samples were cut with a low-speed diamond saw into cuboids ( $\sim 10 \times 1.5 \times 1.5 \text{ mm}^3$ ), whilst high temperature thermal conductivity measurements were performed on ultrasonically shaped disks ( $d=6 \text{ mm}$ ,  $h=1 \text{ mm}$ ). In order to avoid heating of samples all cutting processes were performed under inert lubricant and the speed was kept below 15 rpm. A small sample piece ( $\sim 1 \times 1 \times 1 \text{ mm}^3$ ) was used for the measurement of thermal expansion coefficient, while a larger part of the hot pressed samples ( $d=10 \text{ mm}$ ,  $h=3-5 \text{ mm}$ ) served for measurements of elastic properties and low temperature specific heat.

Low temperature resistivity measurements were carried out by a standard four-probe a.c. bridge technique in a home made equipment from 4.2-300 K, whereas the high temperature part (300-823 K) together with Seebeck coefficient was measured simultaneously with an ULVAC-ZEM3 instrument. Magnetoresistance was recorded from 0.3 to 300 K in a  $^3\text{He}$  cryostat with various magnetic fields from 0-12 T.

Low temperature thermal conductivity was measured in a homemade equipment from 4.2 - 300 K, whilst high temperature thermal conductivity and corresponding specific heat data were obtained from a flash method in an Anter Flashline-3000 from 423 - 823 K, using NIST austenite steel as standard. A homemade calorimeter with an adiabatic step heating method was used to measure specific heat from 4.2 - 300 K [21–23].

A capacitance dilatometer [24] served to acquire thermal expansion coefficients in the temperature range 4.2 - 300 K. Resonant ultrasound spectroscopy (RUS) was employed to obtain room temperature elastic properties: Young's moduli (E) and Poisson's ratio ( $\nu$ ).

### 3. Results and Discussions

#### 3.1. The V-Sb system

The constitution of the binary V-Sb phase diagram has never been determined before, although thermal stability and crystal data of some binary phases in this system can be found in the literature [14,16,17,25–28]. Six binary phases have hitherto been reported in this system:  $V_3Sb$ ,  $\ell T-V_3Sb_2$  (earlier labelled as  $V_6Sb_5$  [27]),  $hT-V_{2-x}Sb$  (earlier labelled as “VSb”[27,29]),  $V_{7.46}Sb_9$  [25],  $V_5Sb_4$  [27,30,31],  $V_{1-x}Sb_2$  [14], and their crystal structures have been elucidated either from XRPD or XRSC data [7,32]. All crystallographic and stability data are summarized in Table 1. From the 6 phases mentioned above, only 5 phases could be reliably identified in this investigation:  $V_{3+x}Sb_{1-x}$ ,  $\ell T-V_3Sb_2$ ,  $hT-V_{2-x}Sb$ ,  $V_{7.46}Sb_9$  and  $V_{1-x}Sb_2$ .

XRPD, EPMA, and DTA data from as cast and annealed alloys served to construct the V-Sb phase diagram presented in Figure 2 (see also Table 2).

From all binary compounds, only  $V_{3+x}Sb_{1-x}$  exhibits a wide homogeneity range extending at 1100°C from 18.4 to 24.4 at.% Sb ( $0.02 < x < 0.26$ ). Rietveld refinements for sample V90Sb10 in as cast state revealed a mixed occupancy of V and Sb at the Sb site of  $V_{3+x}Sb_{1-x}$ , whereas the Sb-rich boundary (from EPMA) is consistent with the rather stoichiometric composition  $V_3Sb$ . It is interesting to note that arc melted samples in the composition range from 18 to 25 at.% V show almost single phase microstructures in XPRD and SEM-EPMA suggesting congruent phase formation. EPMA and XRPD of an as cast alloy with composition of V80Sb20 (in at.%) indicated crystallization of primary and secondary  $V_{3+x}Sb_{1-x}$  phases with two different compositions,  $V_{75}Sb_{24}$  and  $V_{81}Sb_{19}$ , respectively. The solidification of V80Sb20 in combination with congruent melting of  $V_{3+x}Sb_{1-x}$  suggest a eutectic reaction  $L \leftrightarrow V_{3+x}Sb_{1-x} + (V)$ . Indeed EPM analyses of as cast alloys in the two-phase region  $(V) + V_{3+x}Sb_{1-x}$  clearly defined (i) primary crystallization of vanadium that solves at least 8 at % Sb and (ii) a degenerated eutectic at 18.1 at.% Sb (Figure 3(a,b)) that is very close to the vanadium rich end of the homogeneity region of  $V_{3+x}Sb_{1-x}$  (18.4 at % Sb at 1200 °C).

Neither the eutectic point nor the congruent melting temperatures of  $V_{3+x}Sb_{1-x}$  were within the reach of our DTA instrument (temperature limit at 1450°C) situating the eutectic ( $L \leftrightarrow V_{3+x}Sb_{1-x} + (V)$ ) and melting temperature of  $V_{3+x}Sb_{1-x}$  above 1450°C.

As cast samples with more than 30 at.% Sb revealed a wide field of primary crystallization for  $V_{3+x}Sb_{1-x}$  (Figure 3c) up to 42 at.% Sb, and for  $hT-V_{2-x}Sb$  (Figure 3(d,e)) up to 87 at.%

Sb, respectively. The primary crystallization field of  $V_{1-x}Sb_2$  (Figure 3f) starts from 87 at.% Sb. In addition to the previously mentioned binary phases, a small amount of  $\ell T-V_3Sb_2$  was present in the as cast state together with  $hT-V_{2-x}Sb$ . These observations suggest a peritectic formation of  $hT-V_{2-x}Sb$  and  $V_{1-x}Sb_2$ , and a fast kinetic for the transformation from  $hT-V_{2-x}Sb$  to  $\ell T-V_3Sb_2$ .

The invariant reaction concerning the peritectic formation of  $hT-V_{2-x}Sb$  ( $L+V_{3+x}Sb_{1-x} \leftrightarrow hT-V_{2-x}Sb$ ) could be determined via DTA at  $(1230 \pm 10)^\circ C$ . The homogeneity regions of  $hT-V_{2-x}Sb$  at  $900^\circ C$  were defined by EPMA from 42.0 to 43.1 at.% Sb, and this compound decomposes eutectoidally into the low temperature modification  $\ell T-V_3Sb_2$  and  $V_{7.46}Sb_9$  (Figure 3(g,h)). Due to the generally low heat contents of transformations in the solid state, a signal for the eutectoid decomposition of  $hT-V_{2-x}Sb$  was not observed during DTA. As mentioned before, the kinetic of this transformation is quite high, indicated by the presence of  $\ell T-V_3Sb_2$  in as cast state. This may hint to a rather low heat content involved. A second order transformation is forbidden by symmetry, since there is no group-subgroup relation between  $hT-V_{2-x}Sb$  ( $P6_3/mmc$ ,  $Ni_2In$ -type) and  $\ell T-V_3Sb_2$  ( $R\bar{3}m$ ,  $Fe_3Sn_2$ -type). Isothermal annealing at 700, 750, 780, 800, 830, 850 and  $900^\circ C$  followed by rapid quenching of alloys in the composition range 44-53 at.% Sb finally yielded the eutectoid decomposition between 800 and  $830^\circ C$ , which therefore was set at  $(815 \pm 15)^\circ C$ .

DTA measurements (Ta crucible) of a sample with 38 at % Sb from the two-phase region  $V_{3+x}Sb_{1-x}+V_3Sb_2$  yielded a very weak thermal effect at  $967^\circ C$  on heating, which could correspond to the peritectoid decomposition temperature of  $\ell T-V_3Sb_2$  but with much higher temperature due to a kinetically suppressed transformation or due to interaction with the Ta crucible. For a further check the DTA for this sample was also performed in quartz ampoules, detecting a weak thermal effect in the temperature range from 955 to  $963^\circ C$  during several DTA runs on heating up to  $1050^\circ C$ . The difficulties to detect the thermal effect related to the transformation from  $hT-V_{2-x}Sb$  to  $\ell T-V_3Sb_2$  indicated that the heat content of this transformation is small. In order to determine the phase transformation, samples in the two phase regions involving  $V_{3+x}Sb_{1-x}$  were annealed at 700, 850, 900, 950, 1000 and  $1100^\circ C$ .  $\ell T-V_3Sb_2$  was found in equilibrium with  $V_{3+x}Sb_{1-x}$  at  $850^\circ C$ , while  $hT-V_{2-x}Sb$  appeared after heat treatment at  $900^\circ C$ . The samples annealed at higher temperatures consist mainly of  $V_{3+x}Sb_{1-x}$  and  $hT-V_{2-x}Sb$  with small amounts of  $\ell T-V_3Sb_2$  that form during quenching. As mentioned above,  $\ell T-V_3Sb_2$  was frequently observed also in as-cast alloys (Figure 3(c,d)), however, we never observe this phase in equilibrium with liquid in samples annealed in the temperature range from 600 to  $1100^\circ C$ . In such

contradictory situation we relied on the data on thermal stability of the phases obtained from annealing at different temperatures and therefore the peritectoid reaction of  $V_{3+x}Sb_{1-x} + hT-V_{2-x}Sb \leftrightarrow \ell T-V_3Sb_2$  is assigned at  $(875 \pm 25)^\circ C$ .

The phase transformation involving  $V_{1-x}Sb_2$  was found to be complicated: DTA runs on single-phase  $V_{1-x}Sb_2$  (hot pressed at  $800^\circ C$ ) presented two thermal effects at  $868$  and  $923^\circ C$ . Heat treatment of the same sample and a sample in the two phase field  $V_{1-x}Sb_2 + V_{7.46}Sb_9$  at  $900^\circ C$  revealed that  $V_{7.46}Sb_9$  is in equilibrium with an Sb-rich liquid, with  $V_{1-x}Sb_2$  formed around the grains of  $V_{7.46}Sb_9$  (Figure 3i). Note that due to its narrow crystallization range (Figure 2) at high temperature (i.e. reaction kinetics high enough to dissolve the grains formed during cooling), the phase  $V_{7.46}Sb_9$  is not observed in as cast state (Figure 3e). Whilst microstructures of alloys heat treated at  $850^\circ C$  clearly show that  $V_{1-x}Sb_2$  is still stable at this temperature (Figure 3j), microstructure analysis of a sample in the two-phase region  $V_{1-x}Sb_2 + V_{7.46}Sb_9$ , annealed at  $920^\circ C$ , clearly documents that  $V_{7.46}Sb_9$  is stable in equilibrium with the liquid. Further heat treatment at  $950^\circ C$  finally revealed the decomposition of  $V_{7.46}Sb_9$ . Based on these observations, we conclude for a peritectic formation of both  $V_{1-x}Sb_2$  and  $V_{7.46}Sb_9$ :  $L + V_{7.46}Sb_9 \leftrightarrow V_{1-x}Sb_2$  at  $(869 \pm 5)^\circ C$  and  $L + hT-V_{2-x}Sb \leftrightarrow V_{7.46}Sb_9$  at  $(920 \pm 10)^\circ C$ . Our decomposition temperature of  $V_{7.46}Sb_9$  agrees well with the temperature earlier reported by Furuseth et al. [25] ( $1205 \pm 10$  K or  $932^\circ C$ ). However, these authors propose that  $V_{7.46}Sb_9$  is formed via a peritectoid reaction from  $hT-V_{2-x}Sb$  and  $V_{1-x}Sb_2$ .

DTA runs of samples in the two-phase field  $V_{1-x}Sb_2 + V_{7.46}Sb_9$  also showed two thermal effects similar to those for single-phase  $V_{1-x}Sb_2$ , however, with slightly lower onset values ( $855$  and  $915^\circ C$ ). Similar thermal effects were also observed for samples in the two-phase region  $\ell T-V_3Sb_2 + V_{7.46}Sb_9$ . In this case the thermal effect at  $\sim 850^\circ C$  could be observed only after the first heating run (performed up to  $1080^\circ C$ ) due to incongruent solidification with formation of  $V_{1-x}Sb_2$ .

The peritectic formation of  $V_{1-x}Sb_2$  may explain the observation of Havinga et al. [41] on unindexed peaks for the X-ray diffraction pattern of  $VSb_2$  annealed at  $900^\circ C$  for 2 weeks. Havinga et al. [41] attributed the non-indexed peaks to the possible existence of a low temperature modification. However, in our investigation the sample annealed at  $900^\circ C$  could be fully indexed as phase mixture of  $V_{7.46}Sb_9$ ,  $V_{1-x}Sb_2$ , (Sb) and small amounts of  $V_5Sb_4$ . According to EPMA of this samples the three latter phases simply formed via non-equilibrium solidification of liquid. Furthermore, our X-ray patterns of single-phase  $V_{1-x}Sb_2$  annealed at  $600$  and  $800^\circ C$  were completely indexed as  $CuAl_2$ -type and do not

support any low temperature modification in line with earlier unsuccessful attempts to find a low temperature version after annealing at 150°C for 14 months [42]. The DSC-curve (10K/min) obtained by Armbruster [42] on single-phase  $V_{1-x}Sb_2$ , revealing two sharp peaks at 901 and 939°C (which he attributed to the peritectic decomposition of  $V_{1-x}Sb_2$  and the liquidus, respectively), does not comply with our independent observations from two calibrated but different DSC equipments (5K/min) and crucible-types. The higher heating rate (10K/min) may have shifted both effects by about 20-30°C to higher temperatures, the lower one recording the peritectic decomposition of  $V_{1-x}Sb_2$ , the second one the peritectic decomposition of  $V_{7.46}Sb_9$ , because the liquidus (at  $V_{1-x}Sb_2$ ) cannot be observed below ~1050°C (see also Figure 2).

X-ray single crystal structure analysis by Armbrüster et al. [14,28,42] unambiguously defined a small defect in the V-site corresponding to a small homogeneity range of  $V_{1-x}Sb_2$  ( $0.04 < x < 0.05$ ). In good agreement, our EDX analysis showed a hyperstoichiometric composition (67.4 at.% Sb) for the Sb-rich boundary of  $V_{1-x}Sb_2$ . A Rietveld refinement confirmed vacancies in the V-site. Despite EDX measurements (accuracy  $\pm 0.5$  wt. %) suggest full stoichiometry for the Sb-poor boundary, Rietveld refinement of a sample in the two-phase field  $V_{7.46}Sb_9 + V_{1-x}Sb_2$  clearly indicates a small defect in the V-site. Attempts to fix the full occupancy in the V-site resulted in a significant increase of its thermal displacement parameter, which was more than twice higher than that of the Sb-site. Moreover, lattice parameters on both the Sb-rich and Sb-poor boundary remain within their error bars (Table 1) confirming the result of Armbrüster et al. [14,42] on a narrow homogeneity range of  $V_{1-x}Sb_2$  excluding the stoichiometric composition at  $x=0$ .

### 3.1.1. The Phase $V_5Sb_4X_{1-x}$ (earlier " $V_5Sb_4$ ")

A long lasting point of controversy is the formation of the phase " $V_5Sb_4$ ", first reported by Meissner and Schubert [27] to adopt the tetragonal  $Ti_5Te_4$ -type (space group (SG)  $I4/m$ ), and to be stable up to 830°C. Their X-ray structure analysis on the basis of single crystal Weissenberg photographs, however, yielded poor consistency with the  $Ti_5Te_4$ -type as the R-value obtained was only  $R=0.33$  (for  $(hk0)$  intensities) [30]. Later Furuseth et al. [25] claimed from X-ray single crystal refinement data that the correct formula for this phase might be  $V_{7.46}Sb_9$  (space group  $P4/nmm$ ). Indeed the lattice parameters of these two phases formally suggest that  $V_{7.46}Sb_9$  exhibits a  $2c$  superstructure of the  $Ti_5Te_4$ -type, although crystal symmetry does not support a second order relation since SG no. 129 ( $P4/nmm$ )

cannot be related to SG no. 87 ( $I4/m$ ). Indeed, the atom arrangement in the crystal structure of  $V_{7.46}Sb_9$  has little resemblance to the structure type of  $Ti_5Te_4$  [25].

In our investigations " $V_5Sb_4$ " was never observed in major quantity even at its stoichiometric composition. Small amounts of this phase were frequently observed in samples with more than 40 at % Sb, which significantly increased after annealing in equilibrium with antimony rich liquid at temperatures above 800°C (Figure 3i). Despite of that " $V_5Sb_4$ " was never observed in as-cast state, one can see that both phases  $V_{7.46}Sb_9$  and " $V_5Sb_4$ " are in equilibrium with liquid at 900°C and one may suggest that such microstructures resemble those of a ternary system. It may thus be safe to assume that " $V_5Sb_4$ " is stabilized by a small amount of impurity elements or is a metastable phase. The amount of " $V_5Sb_4$ ", however, significantly increased when the alloy V22Sb78, which after DTA was rather porous, was cut via a diamond saw under cutting oil into a smaller piece that was cleaned and annealed at 860°C for 48 hrs. As the oil was not removed quantitatively from the deep pores it introduced enough carbon to form " $V_5Sb_4$ " as the major phase. Careful EDX analysis indeed revealed about  $2.4 \pm 0.5$  wt.% C in the grains of " $V_5Sb_4$ ", but no oxygen or nitrogen was detected. The amount of carbon is consistent with the formula  $V_5Sb_4C$ . In order to check on a possible stabilization by incorporation of interstitial elements, a single crystal of the  $V_5Sb_4C$ -phase was selected from the aforementioned alloy V22Sb78 annealed at 860°C in a long quartz tube to separate the crystal from antimony. X-ray diffraction analyses (see Table 3) confirmed unit cell and tetragonal low Laue symmetry,  $4/m$ , as earlier reported by Schubert [27]. Structure determination via direct methods proved consistency with the  $Ti_5Te_4$ -type and refinement with anisotropic atom displacement parameters (ADPs) converged to an R-value as low as ~2 %, however, prompted a large anisotropic ellipsoid in the direction of the c-axis around the V2 atom in site 2a (0,0,0). A difference Fourier analysis revealed two overlapping peaks located just slightly off the mirror plane  $4/m$  (Figure 4) suggesting a split of the 2a site. Accordingly the V2 atoms were placed on the 4e site (0,0,z;  $z \approx 0.07$ ) with fixed occupancy of 0.5 due to a full occupancy in the unsplit 2a site. Attempts to further refine the occupancy did not result in any significant deviation from half occupancy. Refinement at this stage alerted for a residual electron density of  $12 \text{ e}^-/\text{\AA}^3$  at the centre (site 2b (0,0, $\frac{1}{2}$ )) of an octahedron formed by vanadium atoms at a distance of ~0.20 nm. Assigning this residual electron density to a carbon atom resulted in an occupancy of about 56 % (see Table 3). The structure refinement with ADPs for metal atoms but isotropic temperature factors for the light atom finally converged to  $R_{F2} = 0.0101$  with a negligible residual

electron density  $<0.83 \text{ e}^-/10^{-3} \text{ nm}^3$  thereby confirming a partially filled  $\text{Ti}_5\text{Te}_4$ -type structure with split V2 position  $\text{V}_5\text{Sb}_4\text{C}_{1-x}$  ( $x \sim 0.5$ ; see also Table 3).

Please note that due to the presence of the interstitial C atom the standardized dataset derived by program Structure Tidy [44] slightly differs from the reported  $\text{Ti}_5\text{Te}_4$ -type, however, in Table 3 we present the dataset according to the parent  $\text{Ti}_5\text{Te}_4$ -type to show the relation with its parent structure (see Fig. 5). Interatomic distances are summarized in Table 4 and are consistent with the sum of the atom radii [43]. Particularly the distances from the octahedron center (C-atom) to the surrounding vanadium atoms,  $d_{\text{C-V}2} = 0.20168 \text{ nm}$ ,  $d_{\text{C-V}1} = 0.21182 \text{ nm}$ , perfectly correspond the sum of atom radii [43]:  $R_{\text{V}} + R_{\text{C}} = 0.135 + 0.077 = 0.212 \text{ nm}$ .

The initial hypothesis that " $\text{V}_5\text{Sb}_4$ " can easily be stabilized by the presence of foreign elements seems to be confirmed by our findings in Figure 1, where in the diffusion zones between V and p-type skutterudite ( $\text{MmFe}_3\text{CoSb}_{12}$ ) a rather thick layer was formed with a composition that resembles " $\text{V}_5\text{Sb}_4$ " ( $\text{V}_{40.5}\text{Fe}_{15.6}\text{Sb}_{43.9}$  or  $\text{V}_{5-x}\text{Fe}_x\text{Sb}_4$ ;  $x=1.42$ ). In this case Fe is the stabilizing element as no carbon was detected. Interestingly neither " $\text{V}_5\text{Sb}_4$ " nor  $\text{V}_{40.5}\text{Fe}_{15.6}\text{Sb}_{43.9}$  were observed during the investigation of the ternary system V-Fe-Sb, particularly at  $600^\circ\text{C}$  (870 K) [26], which might be caused by the slow diffusion in the as cast ternary alloy at  $600^\circ\text{C}$ . This could also explain their report on negligible solubility of Fe in  $\ell\text{T-V}_3\text{Sb}_2$ , whereas in our diffusion couple this phase seems to solve up to 9.2 at.% Fe at  $600^\circ\text{C}$  ( $\text{V}_{50.9}\text{Fe}_{9.2}\text{Sb}_{39.9}$  or  $\text{V}_{3-x}\text{Fe}_x\text{Sb}_2$ ;  $x=0.46$ ). A more detailed study of the multi-component system V + p-type skutterudite will be necessary in future to shed more light on these observations.

### 3.1.2. The Phase " $\text{VSb}$ "

"VSb" is another phase for which existence and phase relations are still not clear. "VSb" was first characterized by Grison and Beck [29] from XRPD photographs and estimated intensities from which a NiAs type structure was assigned. A careful XRPD study by Bouwma et al. [16] concluded that "VSb" exhibits a very small homogeneity region at  $1000^\circ\text{C}$  around  $\text{V}_{1.4}\text{Sb}$  (58.3 at.% V). An alloy  $\text{V}_{50}\text{Sb}_{50}$  annealed and quenched from  $750^\circ\text{C}$  did not show any signs of a NiAs-type phase, but was said to reveal a complicated XRPD spectrum [16]. Furuseth et al. [25] confirmed these findings as they were unable to obtain a NiAs-phase near the composition "VSb" but instead observed the phase  $\text{V}_{7.46}\text{Sb}_9$ , which was found to decompose peritectoidally on heating in  $\text{V}_{1.4}\text{Sb}$  (NiAs-type) and  $\text{VSb}_2$ .



Despite the clarifying work of Furuseth et al. [25], several research groups still adhered to a "VSb"-phase. Konyk et al. [45] claimed a NiAs-type solid solution  $V_{1-x}Cu_xSb$  at about 50 at.% Sb ( $x_{max}=0.18$ ) in the isothermal section of the V-Cu-Sb system at 500°C. EPMA data were presented for  $x_{Cu}=0.115, 0.134, 0.181$ , but data were neither given for smaller Cu-concentrations nor for the binary V-Sb phase. The most recent investigation of V-Zn-Sb isothermal section at 450°C [46] also reported the existence of VSb that solves up to 9 at.% Zn. Similar observations were reported by Lomnytska et al. in the systems V-Ni-Sb [47] and V-Sb-Si [48] at 800°C. In the V-Ni-Sb system at 800°C, the VSb phase was reported to solve up to 16 at.% Ni ( $V_{0.84}Ni_{0.32}Sb_{0.84}$ ) [47], while the solubility of Si in the same phase at the same temperature was not more than 5 at.% [48]. During the investigation of the V-Ni-Sb system, Lomnytska et al. also performed an investigation on the binary V-Sb boundary in the region between 42 and 56 at.% Sb every 2 at.% by sintering of powder compacts at 800°C, from which they derived a homogeneity range of VSb from 50 to 52 at.% Sb [47].

Another contradiction in the literature can be found in the V-Fe-Sb system where Romaka et al. [26] particularly studied the extent of a  $Ni_2In$ -type phase in the V-Fe-Sb isothermal sections at 600°C and 800°C starting at  $Fe_{2-x}Sb$ . At these two temperatures neither NiAs type nor the  $Ni_2In$  type phase were observed for V-Sb, instead the  $\ell T-V_3Sb_2$  participates in the equilibria. The result of Romaka et al. [26] is essentially in good agreement with our defined transformation temperature of  $hT-V_{2-x}Sb$  to  $\ell T-V_3Sb_2$  ( $815\pm 15^\circ C$ ). The reason why the authors mentioned above [26,45–48] did not observe the  $V_{7.46}Sb_9$  phase in their investigations may rest in a negligible solubility of the third component in this phase and/or its existence in a narrow phase field close to the binary boundary system.

In our investigation, we never observed any "VSb" phase with composition 1:1 in the temperature range 600-1100°C. Instead, the nonstoichiometric  $Ni_2In$ -type,  $hT-V_{2-x}Sb$  (42.0-43.1 at.% Sb at 900°C;  $0.62 < x < 0.68$ ), was observed as stable phase including the composition reported by Bouwma et al. [16], whereas the NiAs-type compound  $V_{\sim 1.7}Sb$  (nearly single phase alloy V63Sb37, annealed at 1250°C) reported by Meissner and Schubert [27] seems to be consistent with the vanadium rich phase boundary of  $hT-V_{2-x}Sb$ . It should be mentioned here, that the NiAs-type contains voids, which on filling continuously lead to the  $Ni_2In$  structure. Rietveld refinement of a sample with composition of V58Sb42 (see Figure 6), annealed at 950°C clearly showed  $V_{2-x}Sb$  with  $Ni_2In$  type as majority phase with a minor amount of  $\ell T-V_3Sb_2$  and  $V_{3+x}Sb_{1-x}$  as secondary phases.

Further refinement on the V2 occupancy ( $x=0.6$ ) yielded the same value of occupancy as obtained by Bouwma [16].

### 3.2. The Nb-Sb system

Figure 7 summarizes the three variants of the phase diagrams hitherto published for Nb-Sb [1,6–8]. As the most recent investigation of the binary Nb-Sb system by Lomnytska et al. [6] on the basis of LOM and XRPD contradicts earlier results obtained by Melnyk et al. [1] (XRPD and DTA) we re-investigated these points of controversy (see Figure 7). Particularly, the decomposition temperatures of  $\text{NbSb}_2$  (760°C) and  $\text{Nb}_5\text{Sb}_4$  (1020°C) reported by Lomnytska et al. [6] are rather low compared to the results of Melnyk et al. [1]. Although Lomnytska et al. [6] were not aware of the publication by Melnyk et al. [1], they independently confirmed  $\text{Nb}_3\text{Sb}$ ,  $\text{Nb}_5\text{Sb}_4$  and  $\text{NbSb}_2$  as the only binary compounds. As far as the isothermal reactions presented by Lomnytska et al. [6] are concerned, it seems that the older DTA data by Myzenkova et al. [8] have been used, which served as the basis for the diagram in Massalski [7]. Lomnytska et al. [6] removed the non verified phase “ $\text{Nb}_3\text{Sb}_2$ ” together with its original reaction isotherm at 1140°C [8], changed the phases “ $\text{NbSb}$ ” and “ $\text{Nb}_4\text{Sb}_5$ ” (both phases not verified) to  $\text{Nb}_5\text{Sb}_4$  and  $\text{NbSb}_2$ , respectively, but kept the original isothermal reactions at 1020°C and 760°C from Myzenkova et al. [8]. In order to remove the ambiguities on the reaction temperatures mentioned above, we designed and evaluated two experiments: (1) a sample in the two-phase region between  $\text{Nb}_5\text{Sb}_4$  and  $\text{NbSb}_2$  was heat treated at 800°C for 2 months, and finally showed only  $\text{Nb}_5\text{Sb}_4$  and  $\text{NbSb}_2$  as constituents (see Rietveld refinement in Figure 8); (2) powders of single-phase  $\text{NbSb}_2$  were hot pressed at 900°C for 1 hour, however, did not show any formation of liquid and were single-phase after hot processing. These two experiments are incompatible with the low temperature of 760°C reported by Lomnytska et al. [6] for the peritectic formation of  $\text{NbSb}_2$ , however, are fully consistent with the decomposition temperature of  $\text{NbSb}_2$  as given by Melnyk et al. [1] at 1080°C. Note that Lomnytska et al. [6] also performed a similar experiment as described in (1): heat treatment of the alloy with composition of Nb50Sb50 at 800°C, yielding only  $\text{NbSb}_2$  and  $\text{Nb}_5\text{Sb}_4$  as constituents: this result even contradicts their version of the Nb-Sb phase diagram. Our new experiments remove all doubts on the Nb-Sb phase diagram as determined by Melnyk et al. [1].

### 3.3. The Ta-Sb system

Similar to the V-Sb system, the Ta-Sb system has never been constructed so far, however, three binary phases are known in this system:  $\text{Ta}_{3+x}\text{Sb}_{1-x}$ ,  $\text{Ta}_5\text{Sb}_4$ , and  $\text{TaSb}_2$  [7,17,32] (see Table 1). All binary phases are isostructural with those in the Nb-Sb system, which suggests similar behaviour in their phase relations.

The phase diagram in the Sb rich region was constructed on the basis of our XRPD, EPMA and DTA of as cast and annealed alloys (see Table 5 and Figure 9). Indeed the binary phases of the Ta-Sb system show a similar chain of peritectic reactions as in the Nb-Sb system:  $\text{L}+(\text{Ta})\leftrightarrow\text{Ta}_{3+x}\text{Sb}_{1-x}$ ,  $\text{L}+\text{Ta}_{3+x}\text{Sb}_{1-x}\leftrightarrow\text{Ta}_5\text{Sb}_4$  and  $\text{L}+\text{Ta}_5\text{Sb}_4\leftrightarrow\text{TaSb}_2$  (Figure 10). Lattice parameter and EPMA data indicated that all phases except  $\text{Ta}_{3+x}\text{Sb}_{1-x}$  are practically line compounds without any significant homogeneity range. Due to the large difference in the melting points of tantalum and antimony and the high vapour pressure of antimony, homogeneous as-cast samples could only be prepared in the Sb-rich region ( $\geq 80$  at.% Sb). Attempts to prepare as-cast samples in the Ta-rich region resulted in a significant loss of antimony due to evaporation and segregation between Ta-rich and poor liquid. Nevertheless, the inhomogeneous as-cast samples in the Ta-rich side gave a clear proof of the peritectic formation of  $\text{Ta}_5\text{Sb}_4$  and  $\text{Ta}_{3+x}\text{Sb}_{1-x}$ .

In contrast to the V-Sb system,  $\text{Ta}_{3+x}\text{Sb}_{1-x}$  has a rather narrow homogeneity region from 17.9 to 18.5 at.% Sb at 1400°C. This is in line with the small change of the lattice parameter of this phase when it is compared with isostructural  $\text{V}_{3+x}\text{Sb}_{1-x}$  (Table 1). Similar to  $\text{V}_{3+x}\text{Sb}_{1-x}$ , nonstoichiometric  $\text{Ta}_{3+x}\text{Sb}_{1-x}$  ( $0.26 < x < 0.28$ ) can be explained by a random mixing of Ta and Sb in the Sb site (see Rietveld refinement in Figure 11).

DTA measurements performed up to 1100°C of annealed alloys ( $\geq 66.7$  at.% Sb) gave clear signals for the degenerate eutectic,  $\text{L}\leftrightarrow\text{TaSb}_2+(\text{Sb})$  at 621°C and 99.9 at.% Sb and for the peritectic formation of  $\text{TaSb}_2$ ,  $\text{L} + \text{Ta}_5\text{Sb}_4 \leftrightarrow \text{TaSb}_2$  at  $(1080\pm 10)^\circ\text{C}$  (Figure 9).

DTA for Ta rich samples (35 and 45 at.% Ta) were performed in Ta crucibles for temperatures up to 1450°C. DTA confirms the temperature of  $(1080\pm 10)^\circ\text{C}$  for the decomposition of  $\text{TaSb}_2$  revealing also broad thermal effects at 1204°C and 1180°C. EPMA and XRPD measurements of these samples after DTA, showed only  $\text{Ta}_5\text{Sb}_4$ ,  $\text{TaSb}_2$ , and (Sb) as constituents and microstructure shows that  $\text{Ta}_5\text{Sb}_4$  was in equilibrium with liquid, whilst  $\text{TaSb}_2$  and (Sb) were forming during cooling in DTA. From this observation we conclude that  $\text{Ta}_5\text{Sb}_4$  is stable at least up to 1450°C. Therefore the thermal effect above 1100°C cannot be attributed to either a decomposition of  $\text{Ta}_5\text{Sb}_4$  or melting of the samples,

but rather to an interaction of antimony vapor with the Ta crucible. Heat treatment of single phase TaSb<sub>2</sub> (hot pressed at 900°C) at 1000°C for one day did not reveal any changes on the microstructure, phase constituents, and overall composition while heat treatment on the same alloy at 1100°C for the same duration revealed a clear sign of peritectic decomposition of TaSb<sub>2</sub> into Ta<sub>5</sub>Sb<sub>4</sub>+L(Sb). Moreover liquid segregation and evaporation of antimony shifted the overall composition to the two-phase region Ta<sub>5</sub>Sb<sub>4</sub>+TaSb<sub>2</sub> (Ta42.2Sb57.8). These observations deny the earlier claim of thermal decomposition of TaSb<sub>2</sub> at 1000°C and Ta<sub>5</sub>Sb<sub>4</sub> at 1150°C by Furuseth et al. [10], which most likely was accompanied by evaporation of antimony due to its high vapour pressure. Details on the microstructure of selected alloys are given in Figure 10.

In addition to the afore mentioned thermal effects, a weak thermal effect at 969°C was observed in alloy Ta45Sb55 at a similar temperature as in the Nb-Sb system and hitherto cannot be attributed to any formation or decomposition of new binary phases in this system.

The peritectic decomposition temperature of Ta<sub>3+x</sub>Sb<sub>1-x</sub> and Ta<sub>5</sub>Sb<sub>4</sub> were too high to be measured in our apparatus. The large difference in the melting points of Ta and Sb results in a steep slope of the liquidus curve, which created difficulty to detect the liquidus points from DTA measurements. The difficulties in detecting the liquidus also arise from the fact that measurements in quartz ampoules are limited to ~1080°C, whereas measurements in Ta-crucible lead to interaction between Sb vapour and the crucible.

### 3.4. Physical Properties of Binary Antimonides {V,Nb,Ta}Sb<sub>2</sub>

Despite having a similar formula, the crystal structures of VSb<sub>2</sub> and {Nb,Ta}Sb<sub>2</sub> are different. VSb<sub>2</sub> crystallizes in a body centred tetragonal unit cell (SG no. 140, *I4/mcm*), whilst {Nb,Ta}Sb<sub>2</sub> crystallize in a lower symmetry C-centred monoclinic cell (SG no. 12, *C2/m*). Despite the latter can be related to *I4/mcm* by a group-subgroup relation, no structural relation could be established between these two atom arrangements.

Upon their discovery, several physical properties of {V,Nb,Ta}Sb<sub>2</sub> were investigated. Furuseth et al. reported diamagnetic susceptibilities for TaSb<sub>2</sub> [11] and NbSb<sub>2</sub> [10], whereas VSb<sub>2</sub> was said to exhibit weak paramagnetism with a slight temperature dependency [12]. <sup>121</sup>Sb Mössbauer studies on TaSb<sub>2</sub> and NbSb<sub>2</sub> at 4.2 K [9] showed only one sharp peak for Sb, which could arise from overlapping signals with similar Mössbauer parameters from two Sb sites in the crystal structure. Mössbauer studies on VSb<sub>2</sub> and several other MSb<sub>2</sub> compounds (M=Ti-Ni) with various structure types revealed similar

chemical shifts which indicate similar valence states of Sb in these compounds [12] (see also [49]). The possibility to use NbSb<sub>2</sub> as electrode for Li-ion batteries has been mentioned in several reports [50,51]. Recently, anisotropic colossal magnetoresistance was found in single crystalline NbSb<sub>2</sub> [15].

Resistivity measurements carried out for TaSb<sub>2</sub>, NbSb<sub>2</sub>, and V<sub>0.97</sub>Sb<sub>2</sub>, recorded metallic behaviour from 4.2 - 823 K (see Figure 12a). Neither a crossover from metallic to semiconducting behaviour nor superconducting transitions were detected down to 400 mK. The resistivity behaviour of V<sub>0.97</sub>Sb<sub>2</sub> obtained in our measurement agrees well with previous reports [13,14,52] (see inset Figure 12a).

The Bloch-Grüneisen model with a Mott-Jones term was used to account for the temperature dependent electrical resistivity,  $\rho$ , of the present samples, i.e.,

$$\rho(T) = \rho_0 + \Re \left( \frac{T}{\theta_D} \right)^5 \int_0^{\frac{\theta_D}{T}} \frac{z^5}{(e^z - 1)(1 - e^{-z})} dz + AT^3 \quad (1)$$

with  $\rho_0$  ... residual resistivity,  $\Re$  ... electron-phonon interaction parameter,  $\theta_D$  ... Debye temperature and  $A$  ... material dependent constant in the Mott-Jones term. For V<sub>0.97</sub>Sb<sub>2</sub>, Eqn. 1 could be applied in the entire temperature range, while this model was applicable only to the low temperature part of TaSb<sub>2</sub> and NbSb<sub>2</sub>. From least squares fits of Eqn. 1 to the experimental data, Debye temperatures of 170 K, 267 K and 225 K were obtained for V<sub>0.97</sub>Sb<sub>2</sub>, NbSb<sub>2</sub>, and TaSb<sub>2</sub>, respectively. Room temperature values of the electrical resistivity of all three compounds are in a typical range for intermetallics, from about 80 to 100  $\mu\Omega\text{cm}$ . At low temperatures, however, the vacancies in V<sub>0.97</sub>Sb<sub>2</sub> provoke a much larger residual resistivity, approximately 10 times larger than for NbSb<sub>2</sub>, and TaSb<sub>2</sub>. This is in line with the residual resistivity ratio ( $\rho_{RT}/\rho_0$ ) of 1.9, 37, and 20 for V<sub>0.97</sub>Sb<sub>2</sub>, NbSb<sub>2</sub>, and TaSb<sub>2</sub>, respectively. The existence of vacancies in V<sub>0.97</sub>Sb<sub>2</sub> is also reflected in the suppression of the maximum in the phonon part of low temperature thermal conductivity ( $\lambda_{ph}$ ) (see Figure 13), whereas this feature is present in the OsGe<sub>2</sub>-type phases {Nb,Ta}Sb<sub>2</sub>. The phonon part was calculated by subtracting the electronic part from the total thermal conductivity,  $\lambda_{tot} = \lambda_e + \lambda_{ph}$ , via the Weidemann-Franz law (Eqn. 2)

$$\lambda_e(T) = \frac{L_0 T}{\rho(T)} \quad (2)$$

where  $L_0$  is the Lorentz number ( $2.45 \times 10^{-8} \text{ W}\Omega/\text{K}^2$ ). Although at RT the total thermal conductivity of V<sub>0.97</sub>Sb<sub>2</sub> is lower than that of the OsGe<sub>2</sub>-type phases {Nb,Ta}Sb<sub>2</sub> the total

thermal conductivities of all three compounds is significantly higher than those of the skutterudite thermoelectrics.

Formally, the much steeper increase of  $\rho(T)$  of both latter compounds in comparison to  $V_{0.97}Sb_2$  indicates much stronger electron – phonon interaction constants  $\mathfrak{R}$  determining the slope of  $\rho(T)$  at higher temperatures (compare Eqn. 1). The negative Seebeck coefficient (see Figure 12b) refers to electrons as the majority charge carriers. The low temperature resistivity of polycrystalline  $V_{0.97}Sb_2$  is in good agreement with results obtained by Armbrüster et al. from an oriented single crystal sample if  $\rho_{av}$  values,  $\rho_{av} = \frac{2\rho_{11} + \rho_{13}}{3}$ , are calculated from the average of the single crystal data  $\rho_{11}$  and  $\rho_{13}$ , considering tetragonal symmetry.

While the temperature dependent Seebeck coefficient of  $V_{0.97}Sb_2$  shows an almost continuous rise of  $|S(T)|$ ,  $NbSb_2$ , and  $TaSb_2$  exhibit a temperature dependence reminiscent of heavily doped semiconductors. In fact, electronic structure calculations performed for  $VSb_2$  by Armbrüster et al. [14] revealed 7.2 states/unit at the Fermi energy,  $E_F$ , which clearly evidences a metallic state. On the other hand, DFT calculations carried out for  $TiSb_2$  demonstrated a pseudogap right at  $E_F$  [14] and thus the possibility of a semiconducting-like state in  $MSb_2$  compounds. This holds true for  $NbSb_2$  [15] and possibly  $TaSb_2$ . Assuming a similar electronic structure owing to the similar crystal structure, the minimum in  $S(T)$  can be related with the gap in the electronic density of states by Goldsmid's formula [53],

$$S_{max} = \frac{E_g}{2eT_{max}} \quad (3).$$

Here,  $S_{max}$  is the absolute value of the Seebeck coefficient at the temperature  $T_{max}$  where the Seebeck coefficient assumes an extremum;  $E_g$  is the gap width and  $e$  is the unit charge. Employing Eqn. 3 reveals band gaps ( $E_g$ ) of 19.8 and 14.7 meV for  $NbSb_2$  and  $TaSb_2$ , respectively. A poor metallic behaviour with a pseudogap in  $NbSb_2$  [15] and possibly in  $TaSb_2$  follows from specific heat data (Figure 14). The low temperature part of the specific heat reveals Sommerfeld coefficients of  $NbSb_2$  and  $TaSb_2$  (about 1 mJ/molK<sup>2</sup>) being approximately ten times smaller than that of  $V_{0.97}Sb_2$ ; the large value of the latter is a consequence of rather flat bands just at the Fermi energy [14]. The negative signature of the Seebeck coefficient would then refer to the Fermi energy being located slightly above that pseudogap, near the bottom of the conduction band.

The application of magnetic fields enhances the overall resistivity of all three compounds as a result of the classical magnetoresistance. Magnetic fields up to 12 T, however, do not seem to affect the resistivity of  $V_{0.97}Sb_2$  distinctly (Figure 15a), while a significant influence is seen on the two OsGe<sub>2</sub>-type compounds NbSb<sub>2</sub> and TaSb<sub>2</sub> (Figure 15b and Figure 15c). The colossal magnetoresistance of about 10<sup>5</sup> % in single crystalline NbSb<sub>2</sub> ( $I//b$ ,  $H//ac$ ) could not be observed in the polycrystalline bulk sample. Still the magnetoresistance of these compounds is quite high:  $MR=(\rho(H)-\rho(0))/\rho(0) \times 100\%$  of about 191% and 138% were obtained for NbSb<sub>2</sub> and TaSb<sub>2</sub> at 4.1 K and in a field of 12 T. Here,  $\rho(H)$  is the resistivity value at the magnetic field (H) and  $\rho(0)$  is the resistivity value at zero field.

The heat capacity  $C$  of simple non-magnetic materials is, in general, described in terms of an electronic  $C_{el}$  and a lattice contribution  $C_{latt}$ , i.e.,

$$C=C_{el}+C_{latt}=\gamma T+\beta T^3 \quad (4).$$

Here,  $\gamma$  is the Sommerfeld value and  $\beta$  is proportional to the Debye temperature  $\theta_D$ . The corresponding low temperature fits and the resulting values of  $\gamma$  and  $\theta_D$  are shown in Figure 14. The limitation of the applicability of Eqn. 4 to very low temperatures ( $T < 6$  K) necessitates a more sophisticated modelling of the experimental heat capacity data. Accordingly, we apply the model of Junod [54,55] to achieve a better understanding of the approximate phonon density of states (PDOS),  $F(\omega)$  of these two different structure types. It was shown that a certain functional of the lattice specific heat, particularly  $5/4R\pi^4 C_{latt} T^{-3}$  takes the form of convolutions of the phonon spectrum, in this case  $\omega^{-2}F(\omega)$  for  $\omega=4.93$  T. The phonon frequency  $\omega$  is represented in Kelvin. In this model the electronic part of specific heat was subtracted from the total specific heat and the resulting lattice heat capacity is plotted in Figure 16 on a logarithmic temperature scale. The PDOS obtained by fitting two variants of the Junod model to the experimental lattice heat capacity data is drawn as solid lines in Figure 16 in a  $\omega^{-2}F(\omega)$  versus  $(\omega/4.93)$  representation.

In addition to the Debye function with  $\theta_{D2}=269$  K, the phonon spectrum of  $V_{0.97}Sb_2$  can be fitted with two Einstein modes,  $\theta_{E1}=64.2$  K with a spectral width of 37.3 K and  $\theta_{E2}=123.4$  K with a spectral width of 41.2 K. Alternatively the spectrum can be fitted with only one Einstein mode  $\theta_E=126.2$  K with a wider width of 108.8 K. The corresponding Debye temperature for this model ( $\theta_{D1}=257$  K) is slightly lower than the previous one.

In contrast to  $V_{0.97}Sb_2$  where two Einstein modes have close widths, the phonon spectra of  $\{Nb,Ta\}Sb_2$  consist of two Einstein modes with big differences in widths. For NbSb<sub>2</sub> two

Einstein modes,  $\theta_{E1} = 61.6$  K with a width of 3.4 K and  $\theta_{E2} = 142.1$  K with a width of 90.6 K were extracted from the least squares fits, whereas for  $\text{TaSb}_2$   $\theta_{E1} = 70.0$  K with a width of 4.5 K and  $\theta_{E2} = 134.1$  K with a width of 87.6 K were obtained. The corresponding Debye temperatures ( $\theta_{D2}$ ) for this model are 314 K and 291 K for  $\text{NbSb}_2$  and  $\text{TaSb}_2$ , respectively. The spectrum for both compounds can also be fitted well with only one Einstein mode  $\theta_E = 146.3$  K with a width of 142.2 K and  $\theta_E = 132.8$  K with a width of 117.3 K for  $\text{NbSb}_2$  and  $\text{TaSb}_2$ , respectively. Similar to  $\text{V}_{0.97}\text{Sb}_2$  the corresponding Debye temperatures for one Einstein mode are slightly lower ( $\theta_{D1} = 302$  K and 287 K for  $\text{NbSb}_2$  and  $\text{TaSb}_2$ , respectively). These results suggest that the contributions of the lower energy Einstein modes in  $\{\text{Nb,Ta}\}\text{Sb}_2$  are rather small.

Temperature dependent thermal expansion data,  $\Delta l/l$ , of  $\{\text{V,Nb,Ta}\}\text{Sb}_2$  are presented in Figure 17. From a linear fit in the region 150-300 K we obtain the linear coefficient of thermal expansion  $\alpha = 14.1 \times 10^{-6} \text{ K}^{-1}$ ,  $8.4 \times 10^{-6} \text{ K}^{-1}$ ,  $7.5 \times 10^{-6} \text{ K}^{-1}$  for  $\text{V}_{0.97}\text{Sb}_2$ ,  $\text{NbSb}_2$ , and  $\text{TaSb}_2$ , respectively. The CTE value of  $\text{V}_{0.97}\text{Sb}_2$  is higher than the maximum reported value for p-type skutterudites [5], while the values of  $\{\text{Nb,Ta}\}\text{Sb}_2$  are closer to the n-type skutterudites [5].

For a further analysis of  $\Delta l/l$ , the semi-classical model of Mukherjee [56] as given in equations (5) can be considered,

$$\frac{\Delta l}{l(T_0)} = \frac{\langle x \rangle_T - \langle x \rangle_{T_0}}{x_0}; \langle x \rangle_T = \frac{\gamma}{2} T^2 + \frac{3i}{4j^2} [\varepsilon - I\varepsilon^2 - J\varepsilon^3]$$

$$\varepsilon = \left\{ \left( \frac{3}{p_b} \right) 3k_B T \left( \frac{T}{\theta_D} \right)^{\frac{\theta_D}{T}} \int_0^{\frac{\theta_D}{T}} \frac{z^3}{e^z - 1} dz \right\} \quad (5)$$

where  $\gamma$  is the electronic contribution to the average lattice displacement,  $p_b$  is the average number of excited phonon branches over the temperature range,  $\theta_D$  is the Debye temperature and  $i, j, I, J$  are material dependent constants. Applying Eqn. 5 to the experimental data yields Debye temperatures of 180 K, 267 K, and 256 K for  $\text{V}_{0.97}\text{Sb}_2$ ,  $\text{NbSb}_2$ , and  $\text{TaSb}_2$ , respectively. These values are in approximate agreement with the Bloch-Grüneisen fit of the resistivity data, but are somewhat lower than values obtained from specific heat data which, however, reveal marked deviations from a simple Debye model.

Resonant ultrasound spectroscopy (RUS) was employed to derive elastic properties of the  $\{\text{V,Nb,Ta}\}\text{Sb}_2$  compounds at room temperature. RUS data provide direct information on the Young modulus ( $E$ ) and the Poisson ratio ( $\nu$ ). The other elastic properties, such as



shear (G) and bulk (B) moduli (see Table 6) were calculated using the well known equations for isotropic materials, i.e.,

$$G = \frac{E}{2(\nu+1)} \text{ and } B = \frac{E}{3(1-2\nu)} \quad (6).$$

Debye temperatures can also be calculated using Anderson's formulae [57] given by

$$\theta_D = \frac{h\nu_m}{k_B} \sqrt[3]{\frac{3nNd}{4M\pi}}; \quad \text{with} \quad \nu_m = \left[ \frac{1}{3} \left( \frac{2}{\nu_T^3} + \frac{1}{\nu_L^3} \right) \right]^{-\frac{1}{3}} \\ \nu_L = \sqrt{\frac{3B+4G}{3d}} \quad \text{and} \quad \nu_T = \sqrt{\frac{G}{d}} \quad (7)$$

where  $\theta_D$  is the Debye temperature,  $h$  is Planck's constant,  $N$  is Avogadro's number,  $n$  is number of atoms in unit cell,  $M$  is the molecular weight,  $D$  is the density,  $\nu_m$  is the mean sound velocity,  $\nu_L$  is the longitudinal sound velocity and  $\nu_T$  is the transversal sound velocity.

#### 4. Conclusions

The phase diagrams V-Sb and Ta-Sb were constructed for the first time. In the V-Sb system five stable binary phases:  $V_{3+x}Sb_{1-x}$ ,  $\ell T-V_3Sb_2$ ,  $hT-V_{2-x}Sb$ ,  $V_{7.46}Sb_9$ ,  $V_{1-x}Sb_2$  were observed, while in the Ta-Sb system three binary phases exist:  $Ta_{3+x}Sb_{1-x}$ ,  $Ta_5Sb_4$ ,  $TaSb_2$ . Phase relations in the V-Sb system are characterized by various types of transitions. The previously described phases "VSb" and " $V_5Sb_4$ " are likely stabilized by impurity. The existence of carbon in the latter phase was confirmed by X-ray single crystal data of  $V_5Sb_4C_{1-x}$ , the first representative of a filled  $Ti_5Te_4$ -type structure. A re-investigation of the Nb-Sb system proved validity of the Nb-Sb system as presented by Melnyk et al. [1]. The Ta-Sb system resembles the Nb-Sb system both in its compounds as well as their type of formation.

All group-V metal di-antimonides exhibit metallic conductivity over a wide temperature range. They have low resistivity and high thermal conductivity. Low temperature specific heat measurement revealed that  $V_{1-x}Sb_2$  has stronger metallic character compared to  $NbSb_2$  and  $TaSb_2$ . Magnetic fields influence the electrical conductivity of  $NbSb_2$  and  $TaSb_2$  significantly at low temperature, while the effect on  $V_{1-x}Sb_2$  is practically negligible. Various measurement methods were employed to extract the Debye temperature of these

compounds. The thermal expansion coefficient increases from TaSb<sub>2</sub> to V<sub>1-x</sub>Sb<sub>2</sub>, in which the CTE of NbSb<sub>2</sub> is in the range of the average value for Sb-based skutterudites.

Good CTE compatibility and similar shear modulus between {Nb,Ta}Sb<sub>2</sub> and Sb-based skutterudites together with their high thermal stability as well as good thermal and electrical conductivity promote the potential use of Ta and Nb as diffusion barrier and/or hot electrode contact material for Sb-based skutterudite in TE applications.

## 5. Acknowledgements

The research reported herein was supported by the Austrian Federal Ministry of Science and Research (BMWF) under the scholarship scheme: Technology Grant Southeast Asia (Ph.D) in the frame of the ASEA UNINET. The authors are grateful for the support by the OeAD WTZ Austria-Czech Republic CZ12/2013 and by the Ministry of Education, Youth and Sports of the Czech Republic under project 7AMB13AT019. The financial support by "CEITEC – Central European Institute of Technology" (project CZ.1.05/1.1.00/02.0068) from the European Regional Development Fund and by the Grant Agency of the Czech Republic (Project No. GA14-15576S) is gratefully acknowledged by P. Broz.

## 6. References

- [1] G. Melnyk, P. Rogl, R. Skolozdra, D. Maccio, A. Saccone, R. Ferro, J. Phase Equilib. 20 (1999) 475.
- [2] X. Shi, J. Yang, J.R. Salvador, M. Chi, J.Y. Cho, H. Wang, et al., J. Am. Chem. Soc. 133 (2011) 7837.
- [3] G. Rogl, A. Grytsiv, N. Melnychenko-Koblyuk, E. Bauer, S. Laumann, P. Rogl, J. Phys. Condens. Matter 23 (2011) 275601.
- [4] G. Rogl, A. Grytsiv, P. Rogl, E. Bauer, M.B. Kerber, M. Zehetbauer, et al., Intermetallics 18 (2010) 2435.
- [5] G. Rogl, P. Rogl, Sci. Adv. Mat. 3 (2011) 517.
- [6] Y.F. Lomnytska, Y.B. Kuz'ma, J. Alloy. Compd. 413 (2006) 114.
- [7] Pauling File Binary Edition, Version 1.0, Release 2002/1, ASM International, Materials Park, OH, USA, 2002.
- [8] L.F. Myzenkova, V.V. Baron, E.M. Savitskii, Izv. Akad. Nauk, SSSR, Met., 1966, p. 163 (in Russian).
- [9] L. Brattås, J.D. Donaldson, A. Kjekshus, D.G. Nicholson, J.T. Southern, Acta Chem. Scand. (1975), 29a:217.

- [10] S. Furuseth, A. Kjekshus, *Nature* 203 (1964) 512.
- [11] S. Furuseth, K. Selte, A. Kjekshus, *Acta Chem. Scand.* 19 (1965) 95.
- [12] J.D. Donaldson, A. Kjekshus, D.G. Nicholson, T. Rakke, *J. Less-Common Met.* 41 (1975) 255.
- [13] L.D. Dudkin, V.I. Vaidanich, *Vopr. Met. Fiz. Poluprovod., Akad. Nauk. SSSR Trudy 4-Go Soveshchaniya*, Moscow, 1961, p. 113 (in Russian).
- [14] M. Armbrüster, W. Schnelle, U. Schwarz, Y. Grin, *Inorg. Chem.* 46 (2007) 6319.
- [15] K. Wang, D. Graf, L. Li, L. Wang, C. Petrovic, *Sci. Rep.* 4 (2014) 7328.
- [16] J. Bouwma, C.F. van Bruggen, C. Haas, *J. Solid State Chem.* 7 (1973) 255.
- [17] K. Habermehl, *Neue Untersuchungen an Halogeniden des Niobs und Tantal* [Dissertation], Universität zu Köln, 2010 (in German).
- [18] J. Rodriguez-Carvajal, FULLPROF, a Program for Rietveld Refinement and Pattern Matching Analysis, Abstract of the Satellite Meeting on Powder Diffraction of the XV Congress, P. 127. Talence, Int. Union of Crystallography, France, 1990.
- [19] G.M. Sheldrick, *Acta Crystallogr. A.* 64 (2007) 112.
- [20] L.J. Farrugia, *J. Appl. Crystallogr.* 32 (1999) 837.
- [21] G. Schaudy, *Kalorimetrie in hohen Magnetfeldern* [Diploma thesis], Technische Universität Wien, 1990 (in German).
- [22] G. Schaudy, *Kalorimetrie in hohen Magnetfeldern* [Dissertation], Technische Universität Wien, 1995 (in German).
- [23] H. Michor, *Spezifische W€arme Messungen an seltenen Erd Kuprat Verbindungen* [Diploma thesis], Technische Universität Wien, 1993 (in German).
- [24] M. Rotter, H. Müller, E. Gratz, M. Doerr, M. Loewenhaupt, *Rev. Sci. Instrum.* 69 (1998) 2742.
- [25] S. Furuseth, H. Fjellvåg, *Acta Chem. Scand.* 49 (1995) 417.
- [26] V.V. Romaka, L. Romaka, Y. Stadnyk, V. Gvozdetskii, R. Gladyshevskii, N. Skryabina, et al., *Eur. J. Inorg. Chem.* 2012 (2012) 2588.
- [27] H. Meissner, K.Z. Schubert, *Z. Metallkde.* 56 (1965) 475 (in German).
- [28] M. Armbrüster, R.C. Gil, U. Burkhardt, Y. Grin, *Z. Krist. - New Cryst. Struct.* 219 (2004) 209.
- [29] B. Grison, P.A. Beck, *Acta Crystallogr.* 15 (1962) 807.
- [30] D. Eberle, K.Z. Schubert, *Z. Metallkde.* 59 (1968) 306 (in German).
- [31] L. Heyne, T. Igarashi, T. Kanomata, K.-U. Neumann, B. Ouladdiaf, K.R.A. Ziebeck, *J. Phys. Condens. Matter* 17 (2005) 4991.

- [32] P. Villars, K. Cenzual, Pearson's Crystal Data-Crystal structure database for inorganic compounds, release 2014/15, ASM International, Materials Park, OH, USA, 2014.
- [33] J.L. Jorda, J. Muller, *J. Less-Common Met.* 119 (1986) 337.
- [34] M.R. Nadler, C.P. Kempter, *Anal. Chem.* 31 (1959) 1922.
- [35] R.H. Geils, D.I. Potter, *Metall. Trans.* 4 (1973) 1469.
- [36] W. Trzebiatowski, E. Bryjak, *Z. Für. Anorg. Allg. Chem.* 238 (1938) 255 (in German).
- [37] S.S. Kabalkina, T.N. Kolobyanina, L.F. Vereshchagin, *Sov. Phys. JETP* (1970) 31.
- [38] S.E. Rasmussen, R.G. Hazell, *Acta Chem. Scand.* (1978), 32a:785.
- [39] A. Müller, *Z. Naturforsch. Teil A* 24 (1969) 1134 (in German).
- [40] J. Steinmetz, B. Malaman, B. Roques, *C. R. Seances Acad. Sci., Ser. C.* 284 (1977) 499 (in French).
- [41] E.E. Havinga, H. Damsma, P. Hokkeling, *J. Less-Common Met.* 27 (1972) 169.
- [42] M. Armbrüster, Bindungsmodelle für intermetallische Verbindungen mit der Struktur des CuAl<sub>2</sub>-Typs [Dissertation], Technischen Universität Dresden, 2004 (in German).
- [43] E. Teatum, K. Gschneidner, J. Waber, LA-2345, 1960, US Department of Commerce, Washington DC; reproduced in W.B. Pearson, *The Crystal Chemistry and Physics of Metals and Alloys*, Wiley, New York, 1972, p. 151.
- [44] L.M. Gelato, E. Parth\_e, *J. Appl. Crystallogr.* 20 (1987) 139.
- [45] M. Konyk, L. Romaka, P. Demchenko, V.V. Romaka, Y. Stadnyk, A. Horyn, *J. Alloy. Compd.* 589 (2014) 200.
- [46] Z. Zhu, S. Peng, W. Zhu, Q. Xu, M. Chen, F. Yin, *J. Phase. Equilib. Diff.* 36 (2015) 120.
- [47] Y.F. Lomnytska, O.P. Pavliv, *Inorg. Mater.* 43 (2007) 608.
- [48] Y.F. Lomnitska, *Powder. Metall. Met. Ceram.* 46 (2007) 461.
- [49] J.D. Donaldson, A. Kjekshus, D.G. Nicholson, M.J. Tricker, *Acta Chem. Scand.* 26 (1972) 3215.
- [50] J.L. Gómez-Cámer, C. Villevieille, P. Novák, *J. Mater. Chem. A* 1 (2013) 13011.
- [51] M.A. Reddy, U.V. Varadaraju, *J. Power Sources* 159 (2006) 336.
- [52] E.E. Havinga, H. Damsma, J.M. Kanis, *J. Less-Common Met* 27 (1972) 281.
- [53] H. Goldsmid, J. Sharp, *J. Electron. Mater.* 28 (1999) 869.
- [54] A. Junod, T. Jarlborg, J. Muller, *Phys. Rev. B* 27 (1983) 1568.

- [55] A. Junod, J. Muller, H. Rietschel, E. Schneider, J. Phys. Chem. Solids 39 (1978) 317 (in French).
- [56] G.D. Mukherjee, C. Bansal, A. Chatterjee, Phys. Rev. Lett. 76 (1996) 1876.
- [57] O.L. Anderson, J. Phys. Chem. Solids 24 (1963) 909.

**Table 1.** Crystallographic data for unary and binary phases in the {V,Nb,Ta}-Sb systems. (All XRPD data refer to values obtained at room temperature and ambient pressure on alloys quenched from annealing temperature)

Phase; Temperature range (°C)	Space group; Prototype	Lattice parameters (nm)			Comments
		a	b	c	
(V) ≤1910 [7] V <sub>1-x</sub> Sb <sub>x</sub>	<i>Im</i> $\bar{3}m$ W	0.3030  0.3066(1) 0.3046(1) 0.3051(1)	- - - -	- - - -	[33] <sup>a</sup>  x <sub>max</sub> =0.038 at 1200°C [*] x <sub>max</sub> =0.033 at 1100°C [*] x <sub>max</sub> =0.024 at 900°C [*]
(Nb) ≤2469 [7]	<i>Im</i> $\bar{3}m$ W	0.330656(2)	-	-	[34] <sup>a</sup>
(Ta) ≤3020 [7]	<i>Im</i> $\bar{3}m$ W	0.33042	-	-	[35] <sup>a</sup>
(Sb) ≤631 [7]	<i>R</i> $\bar{3}m$ As	0.43000	-	1.1251	[36] <sup>a</sup>
(Sb) hp	<i>P2</i> <sub>1</sub> / <i>m</i> Sb	0.422	0.404 β=94°	0.556	[37] <sup>a</sup> High pressure
V <sub>3</sub> Sb V <sub>3+x</sub> Sb <sub>1-x</sub>	<i>Pm</i> $\bar{3}n$ Cr <sub>3</sub> Si	0.4940(2) 0.4939 0.49440(3) 0.49191(3)	- - - -	- - - -	x=0 [38] <sup>a</sup> x=0.06 [39] <sup>a</sup> x <sub>min</sub> =0.02 at 1100°C [*] x <sub>max</sub> =0.26 at 1100°C [*]
<i>hT</i> -V <sub>2-x</sub> Sb ≤1230±10 [*] ≥815±15 [*]	<i>P6</i> <sub>3</sub> / <i>mmc</i> Ni <sub>2</sub> In  NiAs	0.428 0.4290 0.42903(3) 0.42776(4) 0.42741(4) 0.427	- - - - - -	0.544 0.5447 0.54413(2) 0.5451(1) 0.5453(1) 0.5447	x=0.5, labeled as V <sub>3</sub> Sb <sub>2</sub> (h)[27] x=0.6 [16] x=0.61 at 1000°C [*] x <sub>max</sub> =0.69 at 830°C [*] x <sub>max</sub> =0.68 at 900°C [*] x=1, labeled as VSb [29]
<i>lT</i> -V <sub>3</sub> Sb <sub>2</sub> ≤875±25 [*]	<i>R</i> $\bar{3}m$ Fe <sub>3</sub> Sn <sub>2</sub>	0.5551 0.5565(2) 0.55584 <sup>b</sup>	- - -	2.035 2.0372(6) 2.03363 <sup>b</sup>	[40] <sup>a</sup> [*] labeled as V <sub>6</sub> Sb <sub>5</sub> [27] <sup>a</sup>
V <sub>5</sub> Sb <sub>4</sub> <sup>c</sup>	<i>I4</i> / <i>m</i> Ti <sub>5</sub> Te <sub>4</sub>	0.981 0.9581 0.9851(1)	- - -	0.35 0.3559 0.3535(1)	[27] [31] 900°C [*] for V <sub>5</sub> Sb <sub>4</sub> C <sub>0.56</sub>
V <sub>7.46</sub> Sb <sub>9</sub> ≤939 [25] ≤920±10 [*]	<i>P4</i> / <i>nmm</i> V <sub>7.46</sub> Sb <sub>9</sub>	0.95866(5)  0.9587(1)	- - -	0.70474(5)  0.7041(1)	[25]  800°C [*]
V <sub>1-x</sub> Sb <sub>2</sub> ≤901 [14] ≤869±5 [*]	<i>I4</i> / <i>mcm</i> CuAl <sub>2</sub>	0.65541(4) 0.65542(4) 0.65491(4) 0.6562(5)	- - - -	0.56385(5) 0.5635(1) 0.5637(1) 0.5643(5)	x=0 [12] x ~0.03 [*] x=0.03 [*] x=0.04, XSCD [14]
Nb <sub>3</sub> Sb ≤1750 [8]	<i>Pm</i> $\bar{3}n$ Cr <sub>3</sub> Si	0.52665(5)	-	-	[1]
Nb <sub>5</sub> Sb <sub>4</sub> ≤1320 [1]	<i>I4</i> / <i>m</i> Ti <sub>5</sub> Te <sub>4</sub>	1.03048(24) 1.0312(1)	- -	0.35835(23) 0.3558(1)	[1] [*]
NbSb <sub>2</sub> ≤1080 [1]	<i>C2</i> / <i>m</i> OsGe <sub>2</sub>	1.02379(51)  1.024(1)	0.36315(08) β= 120.04(3)° 0.3633(1) β= 120.04(3)°	0.83326(66)  0.8336(2)	[1]  [*]
Ta <sub>3</sub> Sb	<i>Pm</i> $\bar{3}n$ Cr <sub>3</sub> Si	0.52646 0.52643(2) 0.52692(4)	- - -	- - -	[11] Ta <sub>82.1</sub> Sb <sub>17.9</sub> [*] Ta <sub>81.5</sub> Sb <sub>18.5</sub> [*]
Ta <sub>5</sub> Sb <sub>4</sub>	<i>I4</i> / <i>m</i> Ti <sub>5</sub> Te <sub>4</sub>	1.0248 1.0249(1)	- -	0.3546 0.3549(4)	[11] [*]
TaSb <sub>2</sub> ≤1080 [*]	<i>C2</i> / <i>m</i> OsGe <sub>2</sub>	1.02218  1.0226(5)	0.36447 β= 120.39° 0.36456(3) β=120.39(2)°	0.82915  0.8295(3)	[11]  [*]

\* this work

<sup>a</sup> cited after [7]

<sup>b</sup> recalculated from rhombohedral setting:  $a=0.75$  nm,  $\alpha = 43.5^\circ$

<sup>c</sup> metastable or impurity stabilized phase

**Table 2.** Compositional, crystallographic and DTA data of selected alloys in the V-Sb system. (All XRPD data refer to values obtained at room temperature and ambient pressure on alloys quenched from annealing temperature)

Nominal comp. (at.%)	Ann. temp. (°C)	Phase	Struct. type	Space group	Lattice parameter (nm)		V (at.%)	DTA (°C)	Comments
					a	c			
V5Sb95	600	Overall $V_{1-x}Sb_2$ (Sb)	$CuAl_2$ As	$I4/mcm$ $R\bar{3}m$	0.65497(5) 0.43058(4)	0.5639(1) 1.1269(2)	3.5 32.4 0.3	619 730	Eutectic Liquidus
V15Sb85	600	Overall (Sb) $V_{1-x}Sb_2$	As $CuAl_2$	$R\bar{3}m$ $I4/mcm$	0.43089(1) 0.6549(1)	1.12808(1) 0.5637(1)	14.0 0 32.6	622 870 927	Eutectic Peritectic - $V_{1-x}Sb_2$ Peritectic - $V_{7.46}Sb_9$
V25Sb75	600	Overall $V_{1-x}Sb_2$ (Sb)	$CuAl_2$ As	$I4/mcm$ $R\bar{3}m$	0.65491(4) 0.43056(4)	0.5637(1) 1.1267(2)	23.0 32.7 0.2	622 869 928	Eutectic Peritectic - $V_{1-x}Sb_2$ Peritectic - $V_{7.46}Sb_9$
V40Sb60	800	Overall $V_{7.46}Sb_9$ $V_{1-x}Sb_2$ "V <sub>5</sub> Sb <sub>4</sub> "*	$V_{7.46}Sb_9$ $CuAl_2$ $Ti_5Te_4$	$P4/nmm$ $I4/mcm$ $I4/m$	0.9583(2) 0.65542(4) 0.9847(1)	0.7042(1) 0.5635(1) 0.3538(1)	40.5 45.6 33.3 55.7	855 912	Peritectic - $V_{1-x}Sb_2$ Peritectic - $V_{7.46}Sb_9$
V48Sb52	800	Overall $V_{7.46}Sb_9$ $\ell T-V_3Sb_2$ "V <sub>5</sub> Sb <sub>4</sub> "*	$V_{7.46}Sb_9$ $Fe_3Sn_2$ $Ti_5Te_4$	$P4/nmm$ $R\bar{3}m$ $I4/m$	0.9585(1) 0.5591(1) 0.9856(1)	0.7051(2) 2.0074(1) 0.3533(1)	47.6 46.2 59.5 55.8	853 909	Peritectic - $V_{7.46}Sb_9$ Peritectic - $V_{7.46}Sb_9$
V55Sb45	HP600 600	Overall $\ell T-V_3Sb_2$ $V_{7.46}Sb_9$ $V_{1-x}Sb_2$ * $V_{3+x}Sb_{1-x}$ * "V <sub>5</sub> Sb <sub>4</sub> "*	$Fe_3Sn_2$ $V_{7.46}Sb_9$ $CuAl_2$ $Cr_3Si$ $Ti_5Te_4$	$R\bar{3}m$ $P4/nmm$ $I4/mcm$ $Pm\bar{3}n$ $I4/m$	0.5547(1) 0.9590(2) - 0.4934(3) 0.9820(3)	2.040(3) 0.7043(1) - - 0.3543(1)	55.3 60.0 45.8 - 76.6 -	861 915 1227	Peritectic - $V_{1-x}Sb_2$ Peritectic - $V_{7.46}Sb_9$ Peritectic - $V_{2-x}Sb$
V46Sb54	HP600 600	Overall $V_{7.46}Sb_9$ $V_{1-x}Sb_2$ * $\ell T-V_3Sb_2$ * "V <sub>5</sub> Sb <sub>4</sub> "*	$V_{7.46}Sb_9$ $CuAl_2$ $Fe_3Sn_2$ $Ti_5Te_4$	$P4/nmm$ $I4/mcm$ $R\bar{3}m$ $I4/m$	0.9587(1) 0.6556(1) - 0.9851(3)	0.7041(1) 0.5630(1) - 0.3528(1)	46.9 45.6 33.9 60.0 56.4	850 917	Peritectic - $V_{1-x}Sb_2$ Peritectic - $V_{7.46}Sb_9$
V62Sb38	600	Overall $V_{3+x}Sb_{1-x}$ $V_{7.46}Sb_9$ * (V)* $\ell T-V_3Sb_2$	$Cr_3Si$ $V_{7.46}Sb_9$ W $Fe_3Sn_2$	$Pm\bar{3}n$ $P4/nmm$ $Im\bar{3}m$ $R\bar{3}m$	0.49241(3) 0.9590(1) - 0.56128(1)	- 0.7044(2) - 2.04420(4)	61.3 81.3 - 91.6 60.1	1232	Peritectic - $V_{2-x}Sb$

\*small amounts

**Table 3.** Structural data for  $V_5Sb_4C_{1-x}$  from X-ray single crystal measurement. Filled  $Ti_5Te_4$  type; space group  $I4/m$ ; No. 87.

Parameter/compound	Crystal data
Phase composition (EPMA, at.%)	$V_{48.1}Sb_{37.8}C_{14.1}$
Refinement composition (at.%)	$V_{52.3}Sb_{41.8}C_{5.9}^a$
Structure type	Filled- $Ti_5Te_4$
$\theta$ range (deg)	$5.9 \leq 2\theta \leq 80.5$
Crystal size	$45 \times 50 \times 70 \mu m^3$
$a, b$ [nm]	0.98399(1)
$c$ [nm]	0.354063(5)
Reflections in refinement	$585 \geq 4\sigma(F_o)$ of 603
Number of variables	19
Mosaicity	<0.52
$R_{F2} = \Sigma  F_o^2 - F_c^2  / \Sigma F_o^2$	0.0101
wR2	0.0211
$R_{int}$	0.0243
GOF	1.228
Extinction (Zachariasen)	0.0026(1)
<b>V1</b> in 8h (x,y,0); occ.	x = 0.31787(2); y = 0.38523(2); 1.00(1)
$U_{11}; U_{22}; U_{33}; U_{12}; U_{23}; U_{13}=0$	0.0077(1); 0.0065(1); 0.0086(1); 0.0016(1)
<b>V2</b> in 4e (0,0,z); occ.	z = 0.0696(2); 0.50 <sup>b</sup>
$U_{11}=U_{22}; U_{33}; U_{23}=U_{13}=U_{12}=0$	0.0051(2); 0.0111(4)
<b>Sb1</b> in 8h (x,y,0); occ.	x = 0.06173(1); y = 0.29097(1); 1.00(1)
$U_{11}; U_{22}; U_{33}; U_{23}=U_{13}=0; U_{12}$	0.0063(1); 0.0068(1); 0.0069(1); -0.00072(2)
<b>C1</b> in 2b (0,0,½); occ.	0.56(2)
$U_{iso}$	0.011(1)
Residual electron density; max; min in (electron/nm <sup>3</sup> ) $\times 10^3$	0.83; -0.51

<sup>a</sup> Assumed to be carbon corresponding to  $V_{52.3}Sb_{41.8}C_{5.9}$  (at.%); for oxygen the refined occupancy converged to 0.35(1) O.

<sup>b</sup> Split position from fully occupied site 2a (0,0,0); for explanation see text.

**Table 4.** Interatomic distances ( $d_{1,2}$ ) (in nm) and coordination number (CN) of each site in  $V_5Sb_4C_{1-x}$ . Distances around V2 take care of the split position 4e (V21 and V22,  $d_{V21-V22} = 0.04929$  nm).  $R_V + R_C = 0.212$  nm,  $R_V + R_{Sb} = 0.294$  nm,  $2R_V = 0.269$  nm.

Atom 1	Atom 2	$d_{1,2}$
Sb1 CN=6	V1 (1x)	0.26857
	V1 (2x)	0.27013
	V1 (2x)	0.27466
	V21 (1x)	0.29372
	V22 (1x)	0.29372
V1 CN=10	C1 (1x)	0.21182
	Sb1 (1x)	0.26857
	Sb1 (2x)	0.27013
	Sb1 (2x)	0.27466
	V21 (2x)	0.26094
	V22 (2x)	0.29248
	V1 (2x)	0.29956
V2 CN=14	C1 (1x)	(0.15238)
	C1 (1x)	0.20168
	V1 (4x)	0.26094
	V1 (4x)	0.29248
	Sb1 (4x)	0.29372
C1 CN=6	V21 (2x)	(0.15238)
	V22 (2x)	0.20168
	V1 (4x)	0.21182



**Table 5.** Composition, crystallographic and DTA data of selected alloys in the Ta- Sb system. (All XRPD data refer to values obtained at room temperature and ambient pressure on alloys quenched from annealing temperature)

Nominal comp. (at.%)	Ann. Temp. (°C)	Phase	Struct. type	Space group	Lattice parameter (nm)			Ta (at.%)	DTA (°C)	Comments
					a	b	c			
Ta5Sb95	600 HP 550	Overall TaSb <sub>2</sub> (Sb)	OsGe <sub>2</sub>	$C2/m$	1.0227(2)	0.36468(5)	0.8297(5)	4.3	621	Eutectic $\beta = 120.41(2)^\circ$
			As	$R\bar{3}m$	0.4308(1)	-	1.128(1)	33.4		
Ta15Sb95	600 HP 550	Overall (Sb)	As	$R\bar{3}m$	0.4309(1)	-	1.12815(3)	14.5	613	Eutectic Peritectic - TaSb <sub>2</sub> $\beta = 120.39(2)^\circ$
			OsGe <sub>2</sub>	$C2/m$	1.0226(5)	0.36456(3)	0.8295(3)	0.1		
Ta25Sb75	600 HP 550	Overall (Sb)	As	$R\bar{3}m$	0.4312(2)	-	1.127(2)	22.8	622	Eutectic Peritectic - TaSb <sub>2</sub> $\beta = 120.39(4)^\circ$
			OsGe <sub>2</sub>	$C2/m$	1.0224(3)	0.36455(3)	0.8294(1)	0.1		
Ta35Sb65	900	Overall TaSb <sub>2</sub> Ta <sub>5</sub> Sb <sub>4</sub>	OsGe <sub>2</sub>	$C2/m$	1.0224(2)	0.36454(2)	0.8294(2)	34.2	1084	Peritectic - TaSb <sub>2</sub> $\beta = 120.40(1)^\circ$
			Ti <sub>5</sub> Te <sub>4</sub>	$I4/m$	-	-	-	33.6		
Ta45Sb55	900	Overall TaSb <sub>2</sub> Ta <sub>5</sub> Sb <sub>4</sub>	OsGe <sub>2</sub>	$C2/m$	1.0226(2)	0.36462(2)	0.8295(3)	43.3	1079	Peritectic - TaSb <sub>2</sub> $\beta = 120.39(1)^\circ$
			Ti <sub>5</sub> Te <sub>4</sub>	$I4/m$	1.0249(1)	-	0.3549(4)	33.5		
								55.4		

**Table 6.** Elastic properties and Debye temperatures of {V,Nb,Ta}Sb<sub>2</sub> from various measurements.

	Density (Mg/m <sup>3</sup> )	Relative density	E (GPa)	$\nu$	G (GPa)	B (GPa)	CTE (10 <sup>-6</sup> K <sup>-1</sup> )	$\theta_D$ (K)			
								RUS	C <sub>p</sub>	$\rho$	CTE
V <sub>0.97</sub> Sb <sub>2</sub>	7.92	98%	121.3	0.262	48.1	85.0	14.1	298	269	170	180
NbSb <sub>2</sub>	8.25	99%	186.1	0.217	76.4	110.0	8.4	355	314	267	267
TaSb <sub>2</sub>	10.61	100%	193.4	0.215	79.6	113.1	7.5	321	291	225	256

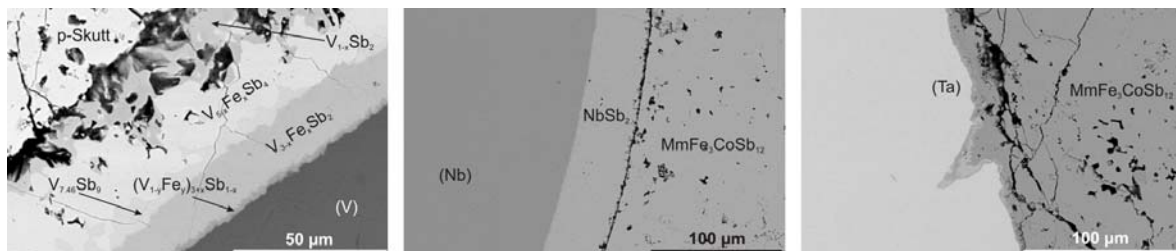


**Figure 1.** Diffusion couples between p-type skutterudite  $\text{MmFe}_3\text{CoSb}_{12}$  (Mm= mischmetal) and group V metals at  $600^\circ\text{C}$ , annealed for 40 days.

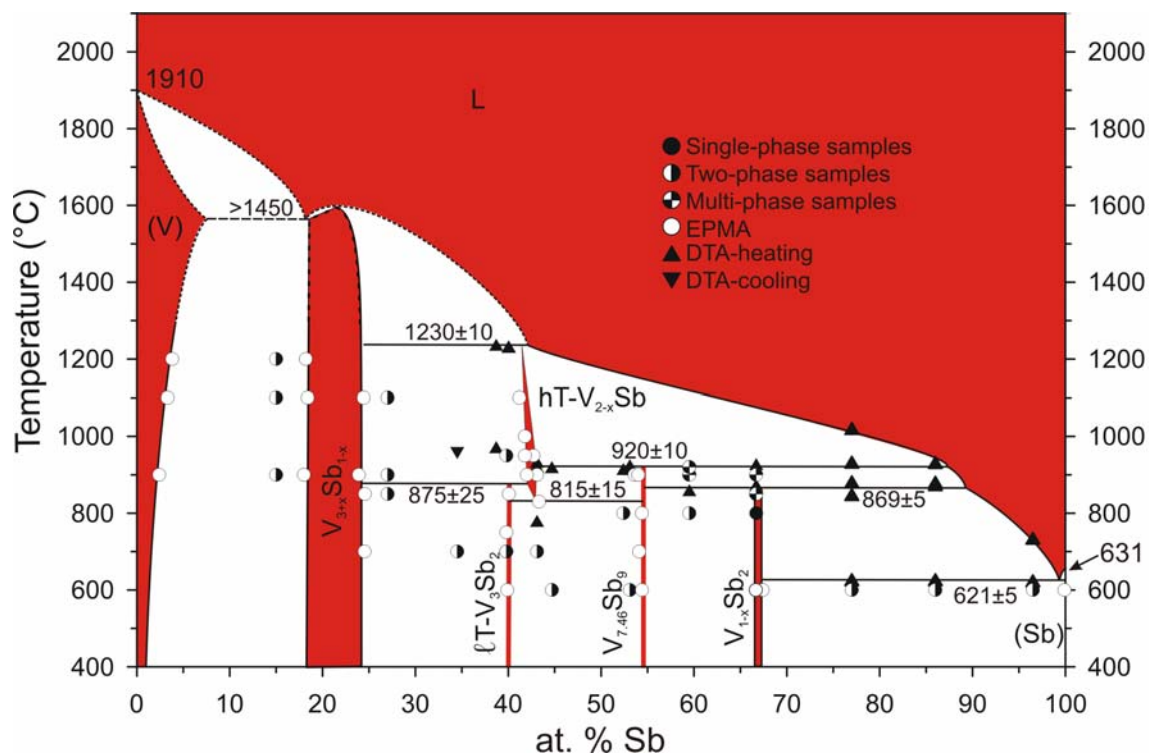


**Figure 2.** The V-Sb phase diagram from this investigation. Filled circles stand for single-phase compositions; (semi)filled circles represent the sample compositions and their type (single, two, or multiphase sample); open circles represent the corresponding phase compositions in two-phase regions (after EPMA), the up-triangles represent the DTA effects recorded on heating, while the down-triangles represent the DTA effects recorded on cooling.

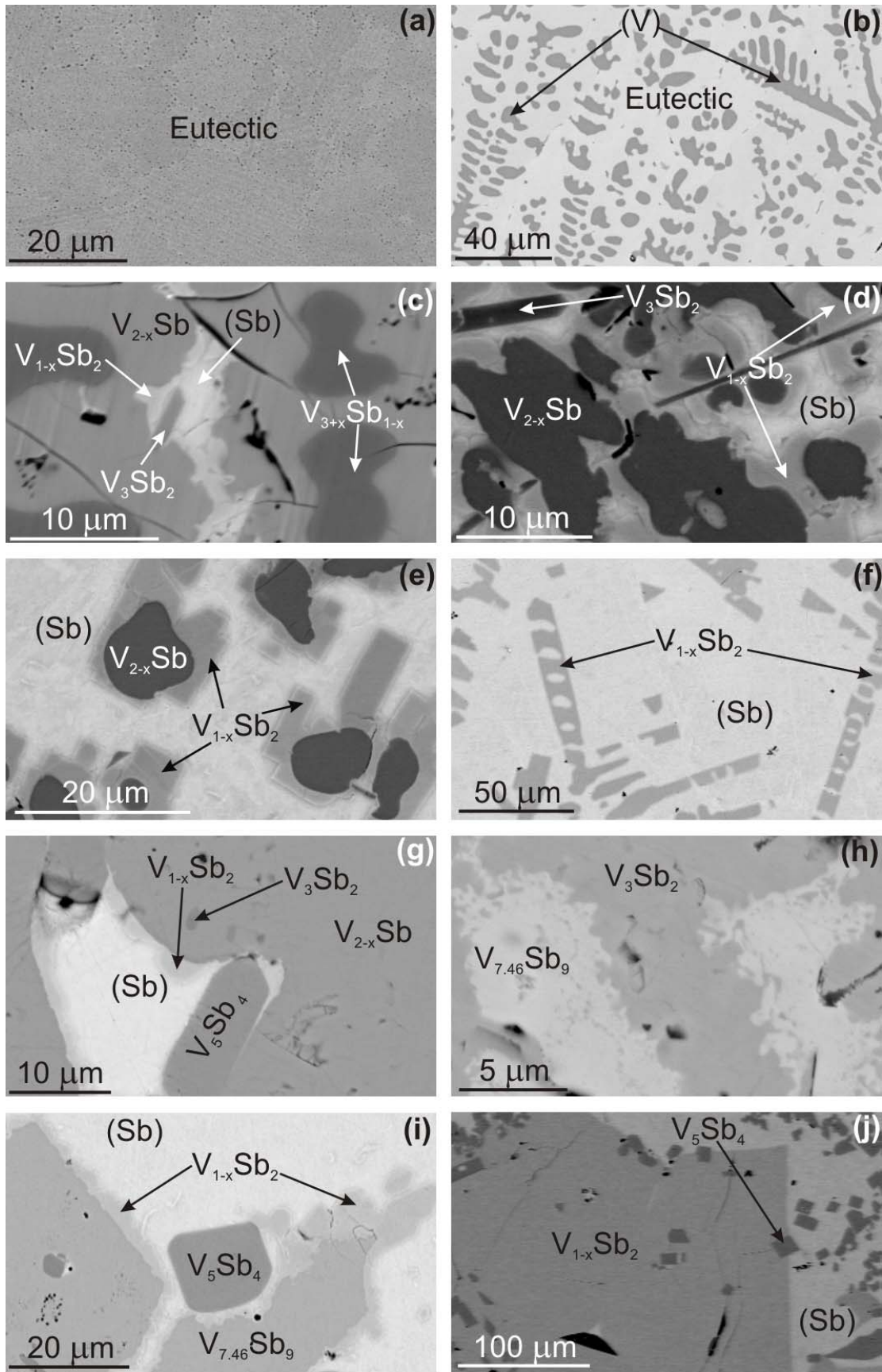


**Figure 3.** Selected micrographs of V-Sb alloys. a) Eutectic V82Sb18, b) Hypoeutectic V85Sb15, c) V63Sb37 as cast, d) V48Sb52 as cast, e) V15Sb85 as cast, f) V10Sb90 as cast, g) V54Sb46 950°C, h) V54Sb46 750°C, i) V40Sb60 900°C, j) V22Sb78 850°C.

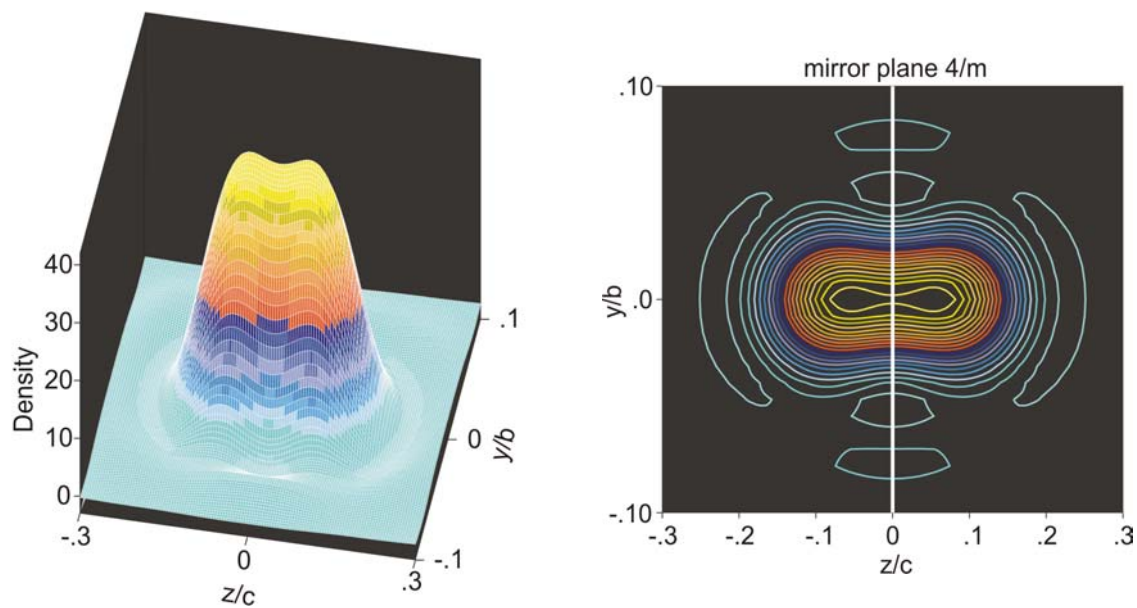


**Figure 4.** Difference Fourier map around V2 atom showing a deviation of V2 position from the mirror plane (white line): 3D (left) and 2D projection on the b-c plane (right).

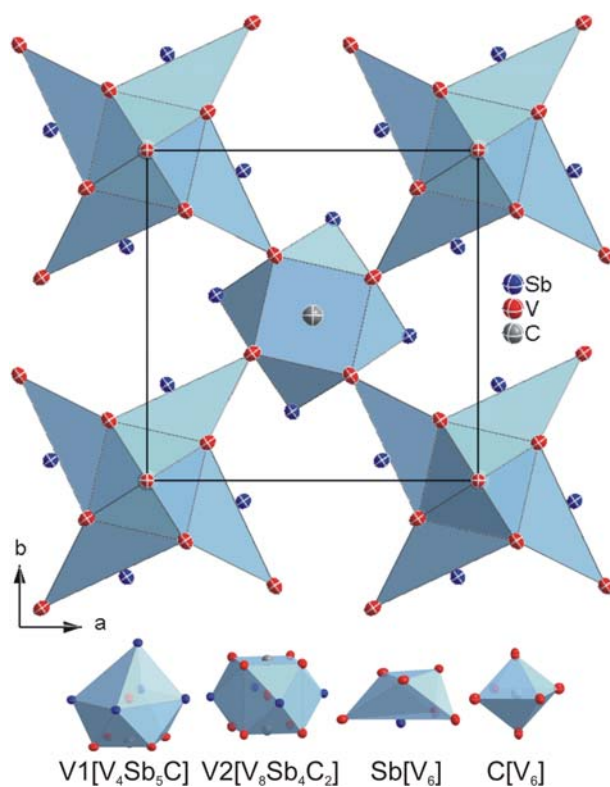


**Figure 5.** Crystal structure of  $V_5Sb_4C_{1-x}$  projected on the  $a$ - $b$  plane and the coordination polyhedra for each atom site. Please note that for the construction of coordination polyhedra only the unsplit V2 position (2a site (0,0,0) is used. Metal atoms are presented with anisotropic displacement parameters, whereas C-atoms are presented with isotropic ADP's from single crystal refinement.

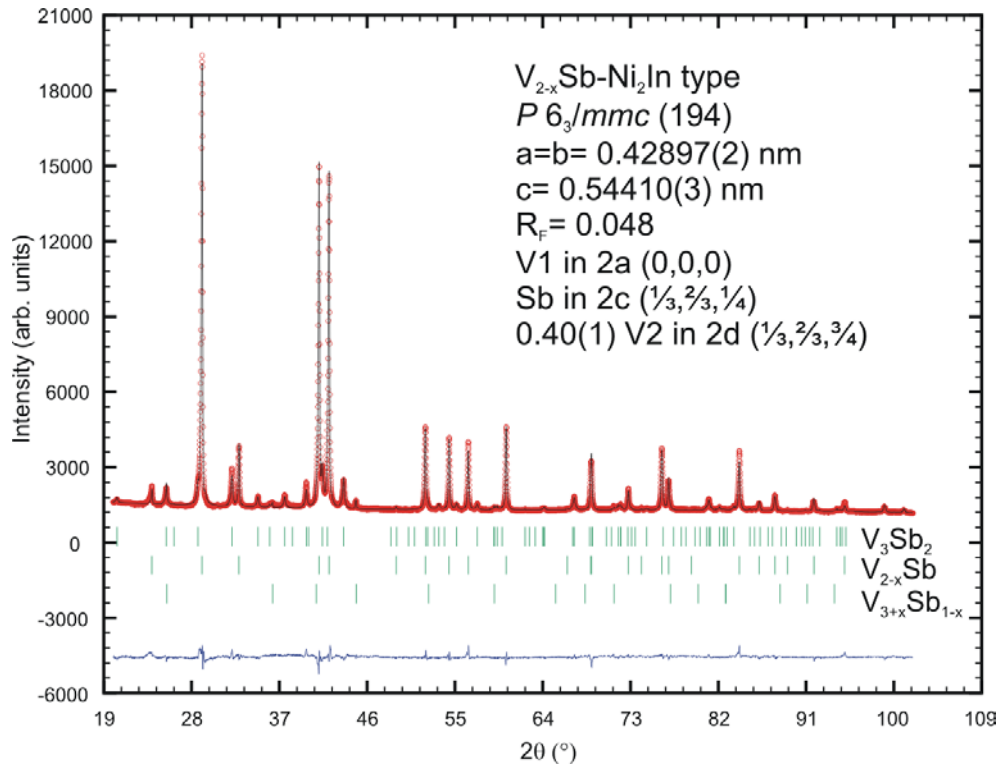


**Figure 6.** Rietveld refinement of sample with composition of V58Sb42 annealed at 950°C, showing hT- $V_{2-x}Sb$  as majority phase with small amounts of  $\ell T-V_3Sb_2$  and  $V_{3+x}Sb_{1-x}$ .

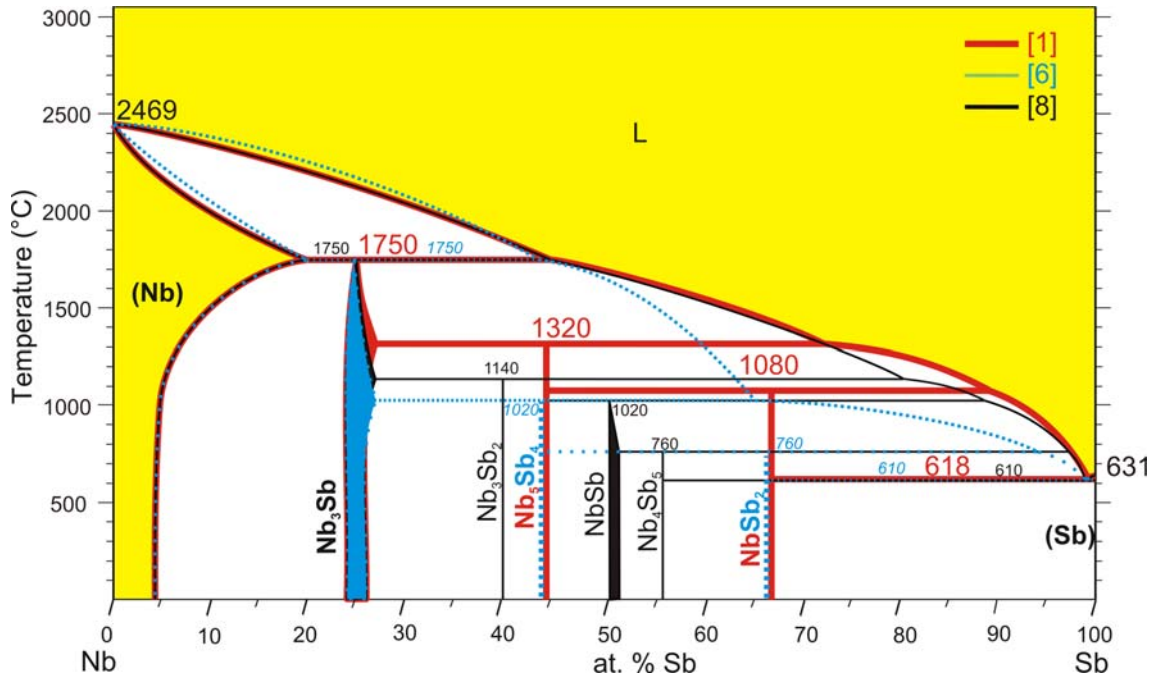


**Figure 7.** Comparison of reported Nb-Sb phase diagrams [1,6,8]. The phase diagram outlined in red is the correct version.



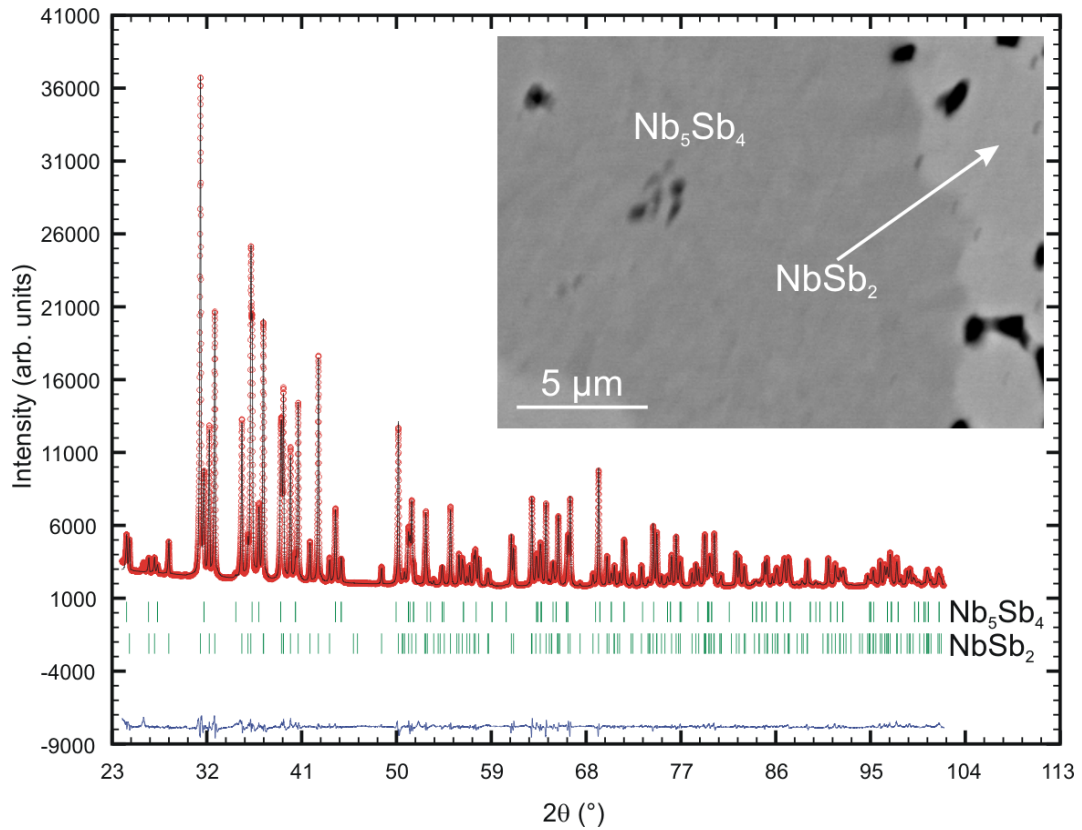


**Figure 8.** Rietveld refinement and micrograph of alloy Nb45Sb55, annealed at 800°C for 2 months (black spots are holes).

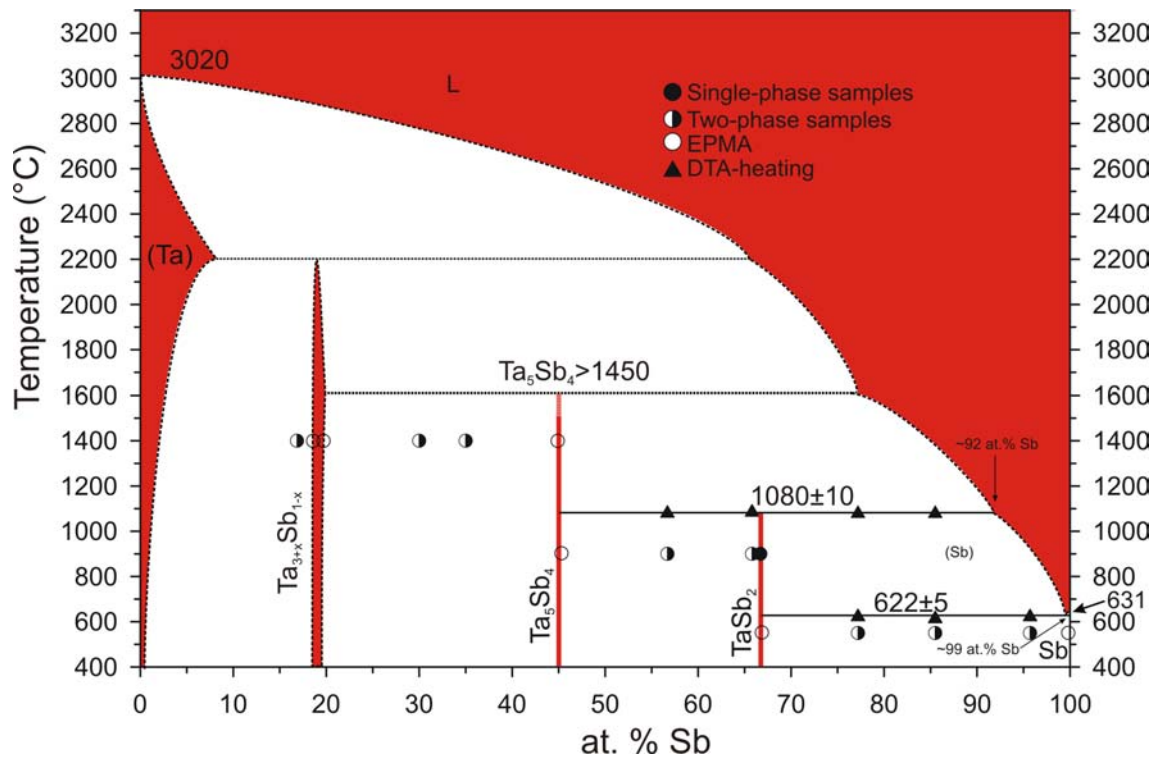


**Figure 9.** The Ta-Sb phase diagram from this investigation. Filled circles stand for single-phase compositions; (semi)filled circles represent the sample compositions and their type (single, two, or multiphase sample); open circles represent the corresponding phase compositions in two-phase regions (after EPMA), the up-triangles represent the DTA effects recorded on heating, while the down-triangles represent the DTA effects recorded on cooling.

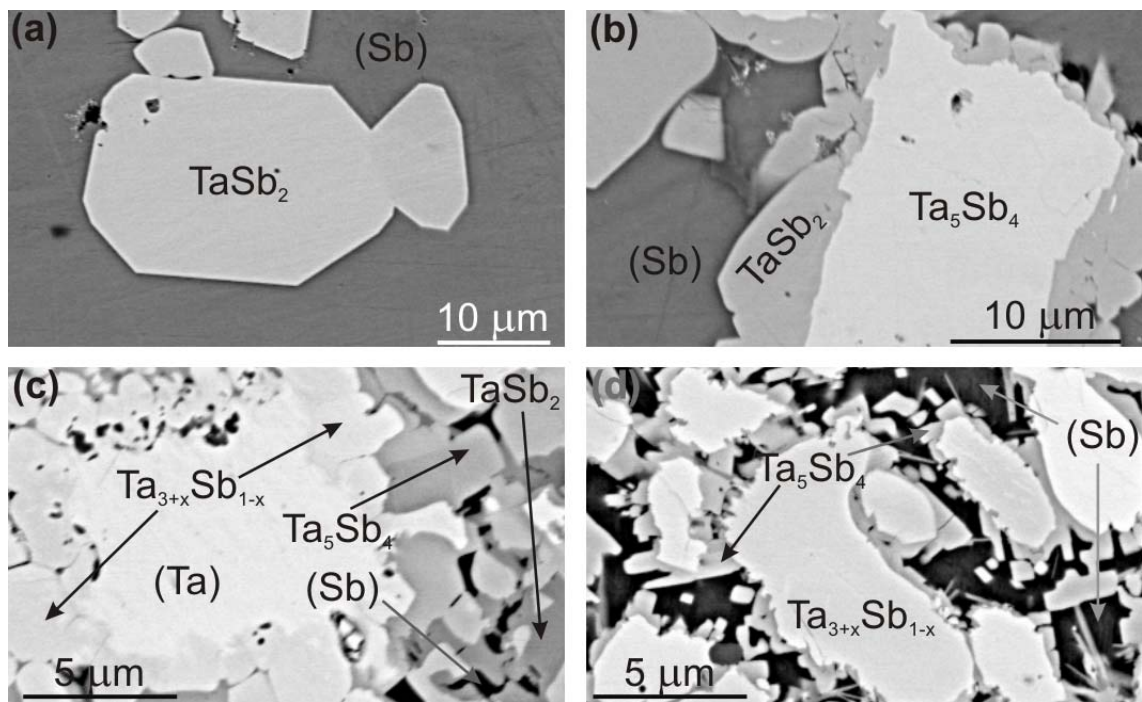


**Figure 10.** Micrographs of selected alloys in the Ta-Sb system. Samples after DTA, Ta5Sb95 (a) and Ta15Sb85 (b). Heterogeneous as cast samples, showing peritectic formation of  $Ta_{3+x}Sb_{1-x}$  (nominal composition Ta45Sb55) (c), and  $Ta_5Sb_4$  (nominal composition Ta35Sb65) (d).

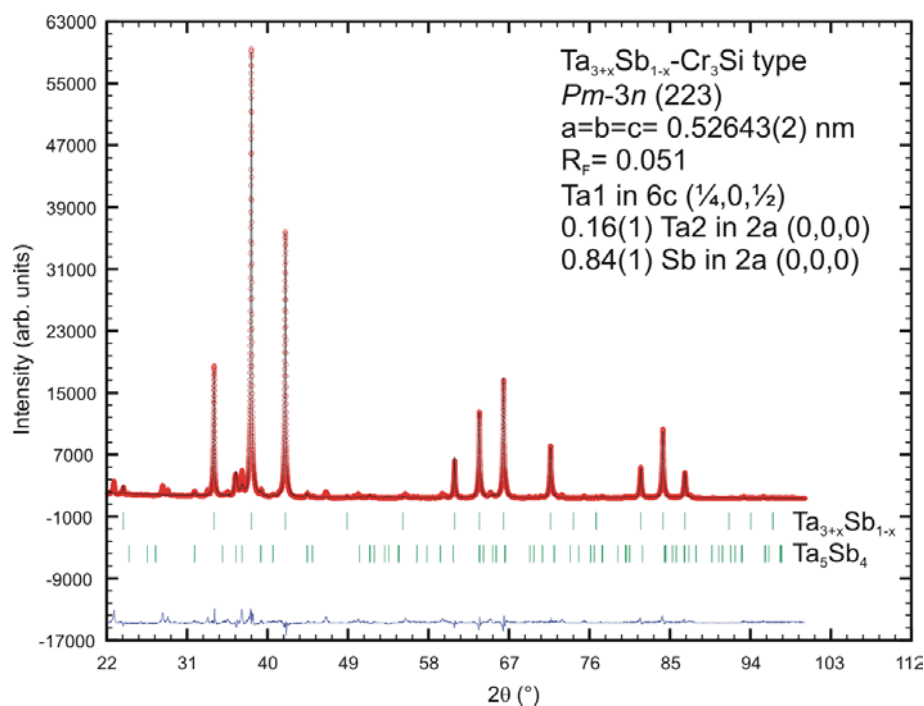


**Figure 11.** Rietveld refinement of alloy Ta80Sb20, hot pressed at 1400°C. The small peaks (unindexed in the graph) correspond to  $Ta_2O_5$  modifications.

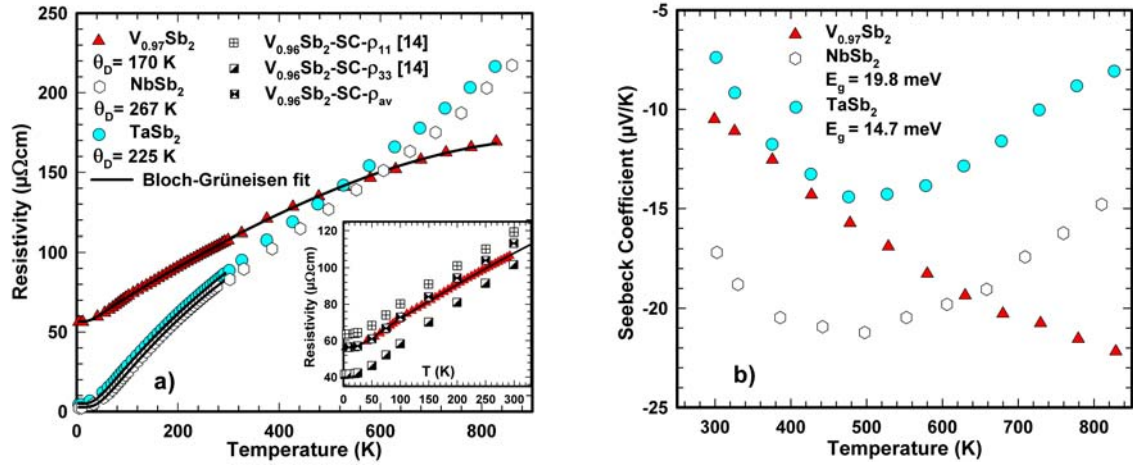


**Figure 12.** Temperature dependent electrical resistivity (left panel) and Seebeck coefficient (right panel) of di-antimonides  $\{\text{V,Nb,Ta}\}\text{Sb}_2$ .

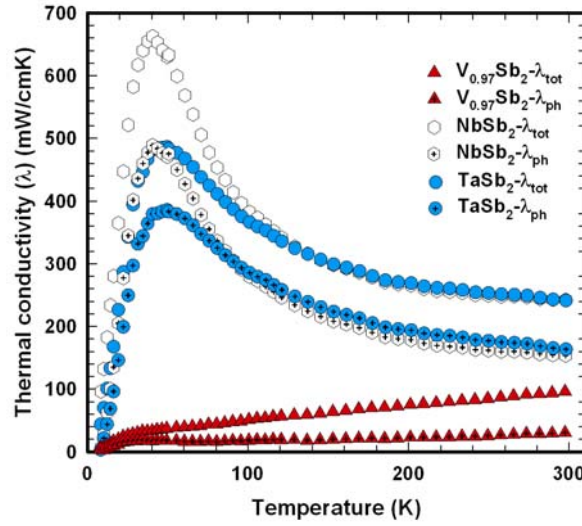


**Figure 13.** Temperature dependent thermal conductivity of  $\{\text{V,Nb,Ta}\}\text{Sb}_2$ .

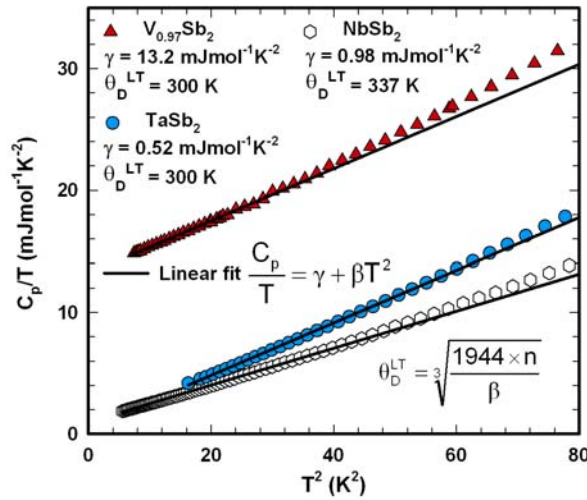


**Figure 14.** Low temperature specific heat ( $< 9$  K) of  $\{\text{V,Nb,Ta}\}\text{Sb}_2$  displayed as  $C/T$  vs.  $T^2$ . The solid lines are fits according to equation 3.



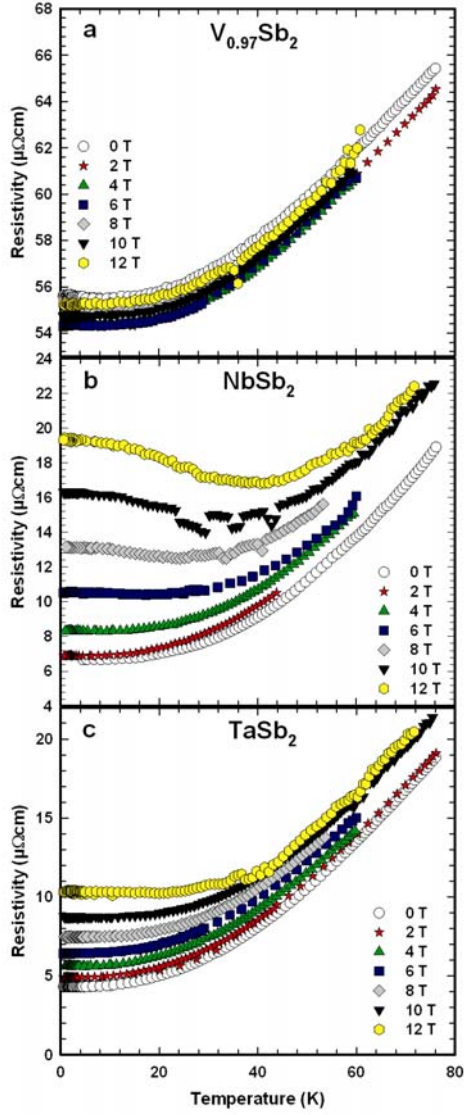


**Figure 15.** Temperature dependent electrical resistivity of  $\{V,Nb,Ta\}Sb_2$  for various externally applied magnetic fields.

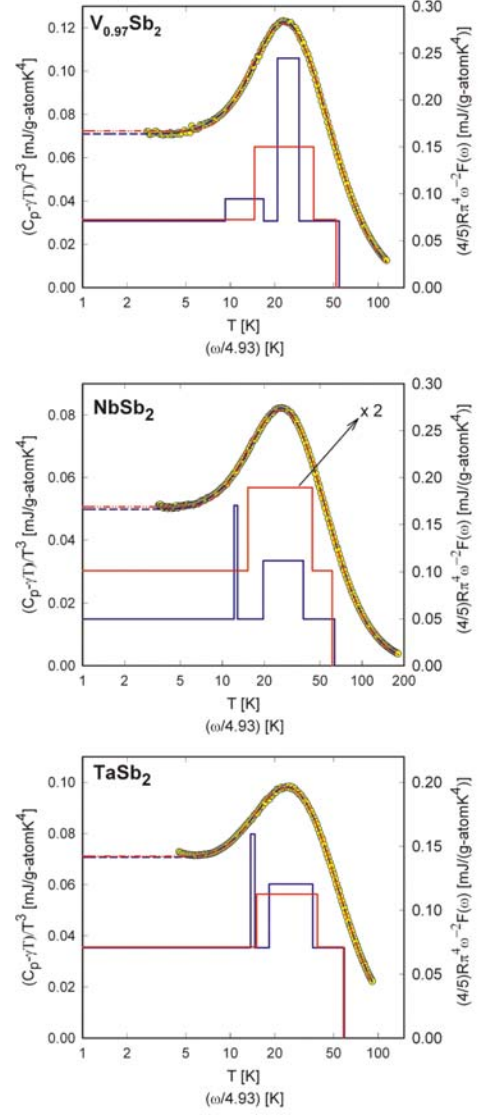


**Figure 16.** Junod fit of the lattice contribution to the specific heat of  $\{V,Nb,Ta\}Sb_2$  and the resulting model PDOS displayed as  $F(\omega)/\omega^2$  (see text for further details).

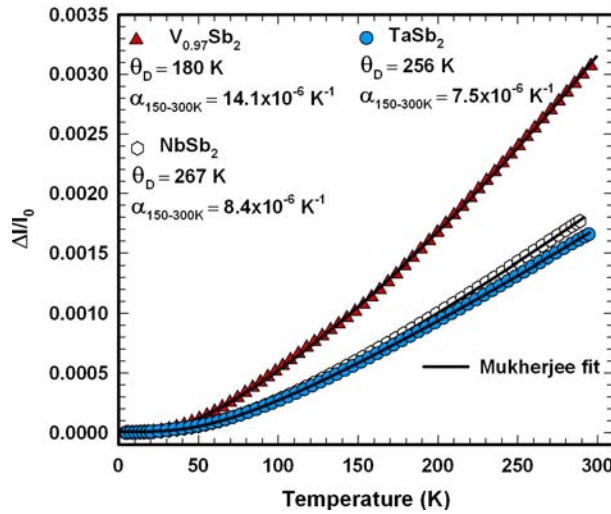


**Figure 17.** Thermal expansion of  $\{V,Nb,Ta\}Sb_2$ . The solid lines are least squares fits according to Eqn. 5.

## **Chapter 4 $\text{Ba}_5\{\text{V},\text{Nb}\}_{12}\text{Sb}_{19+x}$ , Novel Variants of the $\text{Ba}_5\text{Ti}_{12}\text{Sb}_{19+x}$ -type: Crystal Structure and Physical Properties**

F. Failamani<sup>a,b</sup>, A. Grytsiv<sup>a,f</sup>, G. Giester<sup>c</sup>, G. Polt<sup>d</sup>, P. Heinrich<sup>e</sup>, H. Michor<sup>e</sup>, E. Bauer<sup>e,f</sup>, M. Zehetbauer<sup>d</sup>, P. Rogl<sup>a,f</sup>

<sup>a</sup>*Institute of Materials Chemistry and Research, Faculty of Chemistry, University of Vienna, Währingerstraße 42, A-1090 Vienna, Austria*

<sup>b</sup>*Institute of Physical Chemistry, University of Vienna, Währingerstraße 42, A-1090 Vienna, Austria.*

<sup>c</sup>*Institute of Mineralogy and Crystallography, University of Vienna, Althanstraße 14, A-1090 Vienna, Austria.*

<sup>d</sup>*Research Group Physics of Nanostructured Materials, University of Vienna, Boltzmanngasse 5, A-1090 Vienna, Austria.*

<sup>e</sup>*Institute of Solid State Physics, Vienna University of Technology, Wiedner Hauptstraße 8-10, A-1040 Vienna, Austria.*

<sup>f</sup>*Christian Doppler Laboratory for Thermoelectricity, Vienna, Austria.*

(accepted in Physical Chemistry Chemical Physics)

Contributions to this paper:

F. Failamani : samples preparation, transport properties measurements, data evaluation and analysis, writing the paper

A. Grytsiv : diffusion couple experiments, discussions and comments, preliminary single crystal tests, proofreading

G. Giester : single crystal data collections

G. Polt : hardness and elastic moduli measurements, proofreading

P. Heinrich : specific heat and transport properties measurements, discussion, proofreading

H. Michor : specific heat measurements, discussion and comments, proofreading

E. Bauer : transport properties evaluation and analysis, discussions and comments, proofreading

P. Rogl : discussions and comments, proofreading

## Abstract

The novel compounds  $\text{Ba}_5\{\text{V},\text{Nb}\}_{12}\text{Sb}_{19+x}$ , initially found in diffusion zone experiments between Ba-filled skutterudite  $\text{Ba}_{0.3}\text{Co}_4\text{Sb}_{12}$  and group V transition metals (V,Nb,Ta), were synthesized via solid state reaction and were characterized by means of X-ray (single crystal and powder) diffraction, electron probe microanalysis (EPMA), and physical (transport and mechanical) properties measurements.  $\text{Ba}_5\text{V}_{12}\text{Sb}_{19.41}$  ( $a=1.21230(1)$  nm, space group  $P\bar{4}3m$ ;  $R_{F2}=0.0189$ ) and  $\text{Ba}_5\text{Nb}_{12}\text{Sb}_{19.14}$  ( $a=1.24979(2)$  nm, space group  $P\bar{4}3m$ ;  $R_{F2}=0.0219$ ) are the first representatives of the  $\text{Ba}_5\text{Ti}_{12}\text{Sb}_{19+x}$ -type, however, in contrast to the aristotype, the structure of  $\text{Ba}_5\text{V}_{12}\text{Sb}_{19.41}$  shows additional atom disorder. Temperature dependent ADPs and specific heat of  $\text{Ba}_5\text{V}_{12}\text{Sb}_{19.41}$  confirmed the rattling behaviour of Ba<sub>1,2</sub> and Sb<sub>7</sub> atoms within the framework built by V and Sb atoms. Electrical resistivity of both compounds show an upturn at low temperature, and a change from p- to n-type conductivity above 300 K in  $\text{Ba}_{4.9}\text{Nb}_{12}\text{Sb}_{19.4}$ . As expected from the complex crystal structure and the presence of defects and disorder, the thermal conductivity is suppressed and lattice thermal conductivity of  $\sim 0.43 \text{ W m}^{-1}\text{K}^{-1}$  is near values typical for amorphous systems. Vicker's hardness of  $(3.8\pm 0.1)$  GPa (vanadium compound) and  $(3.5\pm 0.2)$  GPa (niobium compound) are comparable to Sb-based filled skutterudites. However, the Young's moduli measured by nanoindentation for these compounds  $E_I(\text{Ba}_{4.9}\text{V}_{12}\text{Sb}_{19.0}) = (85\pm 2)$  GPa and  $E_I(\text{Ba}_{4.9}\text{Nb}_{12}\text{Sb}_{19.4}) = (79\pm 5)$  GPa are significantly smaller than those of skutterudites, which range from about 130 to 145 GPa.

## 1. Introduction

Ternary compounds from the systems EP-M-Sb, combining electropositive elements (EP = alkaline and alkaline earth metals) and early transition metals M, are rare cases among ternary antimonides. Practically complete immiscibility between these two groups of metals<sup>1,2</sup> indicates that bonding interactions are unlikely. The binary immiscibility, together with the high vapor pressure of group I and II metals and antimony also makes preparation routes rather difficult. Hitherto Li and Ba are the only known alkaline and alkaline earth metals that form antimonides with early transition metals. Compounds within the systems Li-M-Sb (M = Ti, V, Zr, Hf) are mostly based on binary Li-Sb phases where the transition metals substitute for Li atoms. Whilst various ternaries Li-M-Sb are known,<sup>2</sup> so far only one compound,  $\text{Ba}_5\text{Ti}_{12}\text{Sb}_{19+x}$ , has been identified among the systems Ba-M-Sb.<sup>3</sup> The crystal structure of  $\text{Ba}_5\text{Ti}_{12}\text{Sb}_{19+x}$  can be considered as a combination of ordered  $\gamma$ -brass

subunits ( $\text{Cu}_9\text{Al}_4$ -type) formed by Ba and Sb atoms and a 3D Ti network. It is interesting to note that this compound crystallizes in a non-centrosymmetric space group,  $P\bar{4}3m$ .

On the other hand, our thermoelectric (TE) research on Ba-filled skutterudites demands also the search for suitable electrode materials and/or diffusion barriers at the hot side of a thermoelectric generator device. Electrode materials should provide good electrical and thermal transport, high mechanical stability and small differences in thermal expansion with the p- and n- type TE materials. For thermoelectric generators in temperature gradients from 300 to 900 K, skutterudites have shown to provide a thermoelectric leg efficiency reaching 15% and device efficiency with commercial TE material of 8 %.<sup>4-11</sup> Long term stability in TE devices, however, requires chemical compatibility of the hot electrode (mainly Ni or Cu) with the thermoelectric material. Severe interaction of n- and p-type skutterudites with late 3d-metal electrodes (formation of antimonides) must be prevented by diffusion barriers. Almost complete immiscibility between early transition metal elements and earth alkaline filler atoms, together with a coefficient of thermal expansion close to the average of filled skutterudites,<sup>12</sup> suggest suitability of early transition metals for such applications. Several reports can be found regarding the use of early transition metal elements (mainly Ti) as diffusion barrier for TE skutterudites and Ni,Cu electrodes.<sup>13,14</sup> In our attempts to explore the potential of group V transition metals (V, Nb, Ta) as barriers, diffusion zone experiments between Ba-filled skutterudite  $\text{Ba}_{0.3}\text{Co}_4\text{Sb}_{12}$  and (V,Nb,Ta) revealed the formation of a novel ternary compound with vanadium, the formula of which being close to a 5-12-20 stoichiometry (see Figure 1; for details on the binary phase diagrams {V,Nb,Ta}-Sb see ref. 15).

The present paper will thus focus on (i) the exploration of phase formation and crystal structure in the ternary systems Ba-{V,Nb,Ta}-Sb particularly for compounds  $\text{Ba}_5\{\text{V,Nb,Ta}\}_{12}\text{Sb}_{19+x}$ , (ii) on the evaluation of their physical properties, and (iii) on the suitability of V, Nb, Ta metals as a diffusion barrier for the hot electrode in a TE-generator based on Ba-filled skutterudites.

## 2. Experimental Methods

Alloys were prepared from Ba rods (Alfa Ventron, 99+, <0.8 mass% Sr), antimony chunks (Alfa Ventron, 99.9%), vanadium pieces (Vanadium Corporation, 99.71%), and niobium/tantalum powders (325 mesh, Sigma Aldrich, 99.9%). First {V,Nb,Ta} $\text{Sb}_x$  master alloys were made either by arc melting (in case of vanadium) or by synthesis from powder mixtures at 900°C in sealed quartz vials (niobium/tantalum). In a second step, barium

pieces were arc melted together with proper amounts of the  $\{V,Nb,Ta\}Sb_x$  master alloys. Due to the high vapor pressure and the highly exothermic interaction between Ba and Sb, and a practically complete immiscibility in the Ba- $\{V,Nb,Ta\}$  systems, it was not possible to reliably assign the weight losses. After several trial and errors single phase bulk samples  $Ba_5\{V,Nb\}_{12}Sb_{19+x}$  for property measurements were obtained by solid state reaction of powder compacts of  $BaSb_3$ , Sb, Nb and powder of a V-rich  $VSb_x$  master alloy. All powders were handled inside an Ar-filled glovebox with  $O_2$  and water vapor levels below 5 ppm.  $BaSb_3$  master alloys were prepared via vapor transport between Ba pieces and Sb pieces at  $500^\circ C$ , while  $VSb_x$  master alloys were prepared by direct arc melting of V and Sb pieces. All master alloys were powderized and sieved below a grain size of  $150\ \mu m$  prior to mixing with other constituents. Stoichiometric blends of these constituents then were ball milled under argon for two hours in a Fritsch vario-planetary mill PULVERISETTE 4 (in tungsten carbide vessels with tungsten carbide balls) in order to increase the surface area and to homogenize the mixtures. Ball milled powders were then loaded within the glove box into graphite dies and hot pressed in a FCT uniaxial hot press system HP W 200/250 2200-200-KS at  $500^\circ C$  for three hours under a pressure of 38 MPa. Each billet was then surface cleaned, vacuum sealed in a quartz ampoule and annealed for 2 weeks at  $700^\circ C$  for V and  $900^\circ C$  for Nb. The annealed alloys were re-powderized and sieved below  $53\ \mu m$  grain size and hot pressed in the same equipment at 50 MPa and the same temperature as for the annealing process. The relative density of the hot pressed sample could only be determined by the Archimedes' method for the Nb compound ( $\sim 96\%$  of the theoretical density). All alloys were analyzed by X-ray powder diffraction with Ge-monochromated  $CuK\alpha_1$ -radiation employing a Guinier-Huber image plate recording system. Rietveld refinements were performed using the program FullProf,<sup>16</sup> while precise lattice parameters were obtained by least squares fit methods with the program STRUKTUR<sup>17</sup> employing Ge/Si as internal standards ( $a_{Ge} = 0.5657906\text{ nm}$ ;  $a_{Si} = 0.5431065\text{ nm}$ ). Quantitative elemental analyses were performed by SEM on a Zeiss Supra 55 VP equipped with an energy dispersive X-ray (EDX) detector operated at 20 kV. Samples for EPMA were prepared by standard metallographic methods. In some cases polishing was performed under glycerine instead of water to avoid oxidation and/or hydrolysis of samples, especially for Ba-rich alloys.

Single crystals of  $Ba_5V_{12}Sb_{19+x}$  suitable for X-ray structure analysis were grown from alloys arc melted under argon with nominal composition of  $Ba_{12}V_{29}Sb_{59}$  (in at.%) in equilibrium with Sb-rich liquid annealed at  $650^\circ C$  for 5 weeks. Single crystals of

$\text{Ba}_5\text{Nb}_{12}\text{Sb}_{19+x}$  were obtained from two alloys (nominal composition: Ba25Nb15Sb60 and Ba30Nb14Sb56) in equilibrium with Ba-rich liquid at 900°C. In all cases rather "spherical" single crystal fragments with "diameters" in the range of 30 to 60  $\mu\text{m}$  were mechanically isolated from the crushed alloys. Inspections on an AXS D8-GADDS texture goniometer assured high crystal quality, unit cell dimensions and Laue symmetry of the single crystal specimens prior to X-ray intensity data collections at various temperatures on a four-circle Nonius Kappa diffractometer equipped with a CCD area detector employing graphite monochromated  $\text{MoK}\alpha$  radiation ( $\lambda = 0.071069 \text{ nm}$ ) whereby constant temperatures for the crystal, mounted with transparent varnish on a glass rod, were assured by a continuous stream of nitrogen gas enclosing the crystal at preset temperature. Orientation matrices and unit cell parameters were derived using the program DENZO.<sup>18</sup> Besides psi-scans no additional absorption corrections were performed because of the rather regular crystal shapes and small dimensions of the investigated specimens. The structures were solved by direct methods (SHELXS-97) and were refined with the SHELXL-97<sup>19</sup> program within the Windows version WinGX.<sup>20</sup> Crystal structure data were standardized using program STRUCTURE-TIDY.<sup>21</sup>

Attempts to adopt the same procedures to produce either single crystals or single-phase  $\text{Ba}_5\text{Ta}_{12}\text{Sb}_{19+x}$  did not yield any significant amount of this phase.

Both samples,  $\text{Ba}_5\{\text{V},\text{Nb}\}_{12}\text{Sb}_{19+x}$ , possess a high degree of brittleness, however, in case of  $\text{Ba}_5\text{Nb}_{12}\text{Sb}_{19+x}$  careful processing of the hot pressed sample allowed us to obtain a specimen large enough for various physical properties measurements. Due to the extreme brittleness of the  $\text{Ba}_5\text{V}_{12}\text{Sb}_{19+x}$  sample, the same procedures did not work, as the hot pressed sample tends to shatter easily during the post hot pressing processes, e.g. removal from die, grinding, and cutting. Therefore only low temperature electrical resistivity, specific heat and hardness measurements could be performed for this compound.

Low temperature resistivity measurements were carried out by a standard four-probe a.c. bridge technique in a home made equipment from 2 - 300 K, whereas the high temperature data (300 - 823 K) together with Seebeck coefficient were measured simultaneously with an ULVAC-ZEM3 instrument. Due to small sample size of  $\text{Ba}_5\text{V}_{12}\text{Sb}_{19+x}$  ( $\sim 3 \text{ mm}$  in length), contacts for electrical resistivity measurement were made using thin gold wire ( $\phi = 50 \mu\text{m}$ ). The spot welded contacts then were coated with silver epoxy in order to improve their mechanical stability. Low temperature thermal conductivity was measured on a rectangular shaped sample in a home made equipment by a steady state heat flow method. Specific heat measurements were performed on a commercial Quantum Design PPMS

calorimeter for  $\text{Ba}_5\text{V}_{12}\text{Sb}_{19+x}$  (~50 mg sample mass) and on a homemade calorimeter with adiabatic step heating technique for  $\text{Ba}_5\text{Nb}_{12}\text{Sb}_{19+x}$  (~1.8 g sample mass).<sup>22–24</sup> Hardness and elastic moduli were obtained by nano-indentation (ASMEC-UNAT) with a Berkovic indenter employing a quasi-continuous stiffness measurement method in a range of loads from 20 to 100 mN.

### 3. Results and Discussion

#### 3.1. Structure solution and refinement

##### 3.1.1. The crystal structure of $\text{Ba}_5\text{V}_{12}\text{Sb}_{19+x}$

Complete indexation of the X-ray single crystal diffraction data prompted a primitive cubic unit cell with lattice parameter  $a=1.21230(1)$  nm. Systematic analysis of extinctions suggested  $Pm\bar{3}m$ ,  $P\bar{4}3m$ ,  $P\bar{4}32$ ,  $Pm\bar{3}$ , and  $P23$  as possible space group types. Searching in the Pearson crystal database<sup>2</sup> for structure types with similar unit cell and Pearson symbol (derived from unit cell and EPMA data) prompted one entry,  $\text{Ba}_5\text{Ti}_{12}\text{Sb}_{19+x}$ , with a similar XRPD pattern as our phase. Indeed structure solution and refinement in the non-centrosymmetric space group  $P\bar{4}3m$  revealed an atomic arrangement as in  $\text{Ba}_5\text{Ti}_{12}\text{Sb}_{19+x}$ , however, with a large electron density of  $\sim 65 \times 10^3 \text{ e}^-/\text{nm}^3$  at  $(\frac{1}{2}, \frac{1}{2}, \frac{1}{2})$ . Taking into account the distance between this peak and the nearest neighbouring atoms, this residual electron density was assigned to a partial occupation of Sb (atom Sb7), which refined to an occupancy  $\text{occ}(\text{Sb7}) \sim 0.5$ . At this stage the residual electron density map (see Figure 2) prompted two further significant electron densities of  $\sim 25 \times 10^3 \text{ e}^-/\text{nm}^3$ , at very close distance ( $\sim 0.04$  nm) to Ba1 ( $\sim 0.18, \frac{1}{2}, \frac{1}{2}$ ) resulting in an ellipsoidal electron density for Ba1, eventually indicating a split position for Ba1. Splitting Ba1 into two positions (assigned as Ba1a ( $\sim 0.17, \frac{1}{2}, \frac{1}{2}$ ) and Ba1b ( $\sim 0.20, \frac{1}{2}, \frac{1}{2}$ ) significantly improved the R-factor ( $R_{F2} = 0.031$ ) and without any constraint the occupancy of each split position refined to almost equal values ( $\text{occ} \sim 0.5$ ), with a slightly smaller value for Ba1a.

At this stage of refinement, a rather small residual electron density of  $\sim 7 \times 10^3 \text{ e}^-/\text{nm}^3$  at ( $\sim 0.46, \sim 0.46, \sim 0.46$ ) was still unassigned, which is very close ( $\sim 0.08$  nm) to the partially occupied Sb7 site. The distances from this peak to the next nearest neighbour atoms Sb5 (0.30 nm) and Ba1b (0.32 nm) correspond very well to the sum of Ba-Sb and Sb-Sb radii<sup>25</sup>. A similar situation was also observed by Bie and Mar<sup>3</sup> in  $\text{Ba}_5\text{Ti}_{12}\text{Sb}_{19+x}$ , where a residual density of  $7.1 \times 10^3 \text{ e}^-/\text{nm}^3$  was observed and was initially thought to be an oxygen atom. Following the arguments from Bie and Mar<sup>3</sup> regarding the interatomic distances of this peak to the nearest neighbours, the residual electron density was finally assigned to a

partial occupation of Sb6 in this position (refined to  $\text{occ}(\text{Sb6}) \sim 0.07$ ). The low occupancies of Sb6 ( $\text{occ} \sim 0.07$ ) and of Sb7 ( $\text{occ} \sim 0.50$ ) may safely rule out that both atoms are simultaneously present in the structure.

The final refinement, assigning anisotropic ADP's to all atoms except Ba1a and Ba1b, resulted in  $R_{F2} = 0.0189$ , now with acceptably low residual electron densities of  $3.83/-1.57 \times 10^3 \text{ e}^-/\text{nm}^3$ . An alternative structural model employing 3 split positions for Ba1 (Ba1a, Ba1b and Ba1c), resulted in only a slightly lower  $R_{F2} = 0.0167$  and smaller residual electron density of  $2.74/-1.16 \times 10^3 \text{ e}^-/\text{nm}^3$  and thus provides no significant improvement. The final formula from refinement,  $\text{Ba}_5\text{V}_{12}\text{Sb}_{19.4}$  ( $\equiv \text{Ba}_{13.4}\text{V}_{33.1}\text{Sb}_{53.5}$ ), agrees well with the composition derived from EPMA ( $\text{Ba}_{13.3}\text{V}_{33.7}\text{Sb}_{53.0}$  in at. %). Results are summarized in Table 1; interatomic distances are presented in Table 2. We want to note here, that for easy comparison we have kept atom labels and site parameters consistent with the standardized description of the parent structure of  $\text{Ba}_5\text{Ti}_{12}\text{Sb}_{19+x}$ .<sup>3</sup> For a detailed description of the crystal structure of  $\text{Ba}_5\text{V}_{12}\text{Sb}_{19.4}$  see Section 3.2.

X-ray powder Rietveld refinement for the sample, which supplied the single crystal, is consistent with the structural model obtained from X-ray single crystal refinement. The disorder, however, could not be reliably extracted, therefore the occupancy values of Ba1a/b, Sb6, and Sb7 were fixed according to the single crystal refinement data. The Flack parameters for all models are close to 0; therefore we may conclude the presence of only one absolute configuration. A test for higher symmetry, employing program PLATON, confirmed that no symmetry is missing for the crystal structure data, in good agreement with the result from the E-test yielding only 31% probability for centrosymmetry.

### 3.1.2. The crystal structure of $\text{Ba}_5\text{Nb}_{12}\text{Sb}_{19+x}$

The discovery of  $\text{Ba}_5\text{V}_{12}\text{Sb}_{19+x}$  led us to search for homologous and isotypic compounds  $\text{Ba}_5\text{M}_{12}\text{Sb}_{19+x}$  with  $\text{M} = \text{Zr}, \text{Hf}, \text{Nb}, \text{Ta}, \text{Cr}, \text{Mo}, \text{W}$ , of which Nb and Ta, indeed, were found to form corresponding phases in alloys annealed at  $700^\circ\text{C}$  for 7 days (see Figure 3; for details on the binary phase diagrams  $\{\text{Nb}, \text{Ta}\}\text{-Sb}$  see ref. 15). The formation of  $\text{Ba}_5\text{Nb}_{12}\text{Sb}_{19+x}$  was confirmed by both XRPD and XRSC data. But we were unable to either synthesize bulk  $\text{Ba}_5\text{Ta}_{12}\text{Sb}_{19+x}$  or to extract suitably sized single crystals for X-ray structure determination.

Despite a single-phase sample  $\text{Ba}_5\text{Nb}_{12}\text{Sb}_{19+x}$  could be obtained by powder metallurgical reaction synthesis, it deemed necessary to provide X-ray single crystal data in order to unambiguously identify atom disorder and partial occupancy as for  $\text{Ba}_5\text{V}_{12}\text{Sb}_{19+x}$ . In



contrast to the single crystal of  $\text{Ba}_5\text{V}_{12}\text{Sb}_{19+x}$ , which was grown from equilibrium with a Sb-rich liquid, such an equilibrium does not exist in the Ba-{Nb,Ta}-Sb ternary systems, neither at 700° nor at 900°C. Therefore a single crystal of  $\text{Ba}_5\text{Nb}_{12}\text{Sb}_{19+x}$  was grown from the equilibrium with a Ba-rich liquid annealing for two weeks at 900°C. EPM analysis proved that no foreign elements were present in the  $\text{Ba}_5\text{Nb}_{12}\text{Sb}_{19+x}$  phase. Diffraction data from a single crystal suitable for X-ray structure determination were completely indexed on a unit cell similar to  $\text{Ba}_5\text{V}_{12}\text{Sb}_{19+x}$ . Considering isotypism, structure solution and refinement were successfully performed in the non-centrosymmetric space group type  $P\bar{4}3m$  with  $\text{Ba}_5\text{Ti}_{12}\text{Sb}_{19+x}$  as initial structure model.

At variance to  $\text{Ba}_5\text{V}_{12}\text{Sb}_{19+x}$ , a difference Fourier map of  $\text{Ba}_5\text{Nb}_{12}\text{Sb}_{19+x}$  at  $z = 0.5$  around Ba1 showed that the shape of electron density for Ba1 became less ellipsoidal (see Figure 4). Weak peaks appear at  $(\frac{1}{2}, \frac{1}{2}, \frac{1}{2})$  (atom site Sb7 in  $\text{Ba}_5\text{V}_{12}\text{Sb}_{19+x}$ ) and  $(0,0,0)$ , which, however, disappeared after the Ba1 atom was added to the refinement. Although a split of this position into two atoms (Ba1a and Ba1b) resulted in a stable refinement without any constraints, the R-factor was not significantly reduced; therefore the Ba1 atom site was kept unsplit. In the final stage of refinement, a small residual electron density of  $\sim 5 \times 10^3 \text{ e}^-/\text{nm}^3$  remained at  $(0,0,0)$  at 0.236 nm from the Sb4 atom. Attempts to assign this electron density to a partial occupancy of antimony or an oxygen atom resulted in unreliable and unstable ADP's. Therefore we conclude that this residual electron density most likely represents Fourier ripples.

The final formula  $\text{Ba}_5\text{Nb}_{12}\text{Sb}_{19.14}$  derived from single crystal refinement,  $\text{Ba}_{13.5}\text{Nb}_{33.5}\text{Sb}_{53.0}$  (in at. %), agrees very well with the phase composition measured by EPMA ( $\text{Ba}_{13.8}\text{Nb}_{33.2}\text{Sb}_{53.0}$ ). Rietveld refinement for a nearly single-phase sample  $\text{Ba}_5\text{Nb}_{12}\text{Sb}_{19+x}$  confirmed the structure model. Similar to its vanadium counterpart, the attempt to search for higher symmetry via PLATON did not reveal any missing symmetry. The Flack parameters are fairly close to zero (0.1) and do not suggest the presence of an inverted structure. Crystallographic data for  $\text{Ba}_5\text{Nb}_{12}\text{Sb}_{19.14}$  are summarized in Table 3; interatomic distances are presented in Table 4. For a closer description of the crystal structure, see section below. Since we could not obtain a single crystal from equilibrium with the Sb-rich liquid, it is not clear whether the absence of Sb7 at  $(\frac{1}{2}, \frac{1}{2}, \frac{1}{2})$  is related to a homogeneity range of  $\text{Ba}_5\text{Nb}_{12}\text{Sb}_{19+x}$ . However, the absence of an electron density at  $(\frac{1}{2}, \frac{1}{2}, \frac{1}{2})$  resembles the structure of  $\text{Ba}_5\text{Ti}_{12}\text{Sb}_{19+x}$ , for which single crystals were obtained under different conditions from the Sb rich part.

### 3.2. Structural chemistry of the phases $\text{Ba}_5\{\text{V},\text{Nb}\}_{12}\text{Sb}_{19+x}$

Following the first structure description of  $\text{Ba}_5\text{Ti}_{12}\text{Sb}_{19+x}$  by Bie and Mar,<sup>3</sup> the crystal structures of  $\text{Ba}_5\{\text{V},\text{Nb}\}_{12}\text{Sb}_{19+x}$  especially the  $\text{Ba}_5\text{Sb}_{19+x}$  substructure can be described in terms of the  $\gamma$ -brass structure (see Figure 5) as a consecutive nesting of polyhedra: an inner tetrahedron, surrounded by an outer tetrahedron, included by an octahedron, finally enclosed by a distorted cuboctahedron. The distortion in the cuboctahedron is due to rectangular faces instead of squares.

There are two types of such polyhedra per unit cell, one located at the corner of the unit cell and one in the center of unit cell. For the corner of unit cell, the inner tetrahedron, outer tetrahedron, octahedron, and the distorted cuboctahedron are formed by Sb4, Ba2, Sb3, and Sb2, respectively, while the nested polyhedra at the centre of the unit cell are formed by Sb6, Sb5, Ba1, and Sb1, respectively. Note that the cuboctahedron in the centre of unit cell is more distorted due to the larger difference between the two Sb1-Sb1 distances forming the cuboctahedron (0.41534 and 0.57207 nm). For  $\text{Ba}_5\text{V}_{12}\text{Sb}_{19+x}$  atom site Sb7 resides inside the innermost tetrahedron at the centre of the unit cell.

Alternatively, the structure can be described as a combination of tetrahedrally arranged distorted icosahedra formed by  $\text{Ba}_2[\text{Sb}_{12}]$  and nearly planar group-V metal nets. The metal nets are sandwiched between trigonal antiprisms (distorted octahedra) formed by  $\text{Sb}_4[\text{Ba}_3\text{V}_3]$  and distorted heptahedra formed by  $\text{Sb}_5[\text{Ba}_3\text{V}_3\text{Sb}_4]$  along the body diagonal (see Figure 6).

There are three main differences between the crystal structure of  $\text{Ba}_5\{\text{V},\text{Nb}\}_{12}\text{Sb}_{19+x}$  and the parent compound  $\text{Ba}_5\text{Ti}_{12}\text{Sb}_{19+x}$ : (i) the disorder in site Ba1 (in case of  $\text{Ba}_5\text{V}_{12}\text{Sb}_{19+x}$ ), (ii) the partial filling of Sb7 in site 1b (in case of  $\text{Ba}_5\text{V}_{12}\text{Sb}_{19+x}$ ), and (iii) the extremely short distances between Sb6 atoms. The disorder in the Ba1 site seems to be inferred by the nature of the group-V elements forming this compound, since the same feature was not encountered in  $\text{Ba}_5\text{Ti}_{12}\text{Sb}_{19+x}$ . This disorder could also be related to point (iii) where the partial filling of  $\sim 7.5\%$  of Sb6 results in extremely short distances among Sb6 atoms. This holds true for  $\text{Ba}_5\text{V}_{12}\text{Sb}_{19+x}$ , where the site 1b is also partially filled by Sb7 atoms. Note, that in case of  $\text{Ba}_5\text{Nb}_{12}\text{Sb}_{19+x}$ , despite the electron density around Ba1 is rather spherical, the displacement parameter Ba1- $U_{11}$  in direction towards Sb6 is still twice as big as for Ba1- $U_{22,33}$ . The same partial filling of this site was also observed in  $\text{Ba}_5\text{Ti}_{12}\text{Sb}_{19+x}$ , however, in that case the position of Sb6 is much further away from the centre of the unit cell and therefore the distance between Sb6 atoms is not so short ( $d_{\text{Sb6-Sb6}} = 0.4757$  nm). The short distance between Sb6 atoms in  $\text{Ba}_5\{\text{V},\text{Nb}\}_{12}\text{Sb}_{19+x}$  implies that this site cannot

be fully occupied. This was confirmed by DFT calculations for  $\text{Ba}_5\text{Ti}_{12}\text{Sb}_{19+x}$  where a full occupancy of Sb6 creates a rather short Sb1-Sb6 bonding distance of 2.8 Å and thereby reduces the Ti-Ti and Ti-Sb bonding stability.<sup>3</sup>

As mentioned in the previous section, the presence of Sb7 in site 1b ( $\frac{1}{2}, \frac{1}{2}, \frac{1}{2}$ ) seems to increase the degree of disorder in the Ba1 site. However, since the Sb7 position is located just ~0.085 nm from the Sb6 position, both sites cannot be simultaneously filled. Reassuringly both sites are not capable of maintaining full occupancy, i.e. Sb6 and Sb7 sites show 7.5% and 50% occupancy.

Bond distance analyses for Ba1 split positions and partially occupied sites Sb6 and Sb7 (see Figure 7) revealed little correspondence with the occupancy, since both Ba1 split positions have similar occupancy. The distance between Ba1b (occupancy = 51%) and Sb7 corresponds much better to the sum of atomic radii<sup>25</sup> than the distance between Ba1a (occupancy = 46%) and Sb7. While the distance between Ba1b and Sb6 (0.30347 nm) is too short for a Ba-Sb contact, the distance between Ba1a and Sb6 shows good correspondence with the sum of atomic radii. Nevertheless, the higher occupancy of Ba1b corresponds to the Sb site with the higher occupancy (Sb7).

Similarly short Ba-Sb distances (<0.32 nm) can only be found in  $\text{BaSb}_2\text{F}_{12}$  ( $d_{\text{Ba-Sb}}=0.2951$  nm).<sup>2</sup> The combination of electropositive elements such as Ba and highly electronegative F (electronegativity=3.98) may suggest a strong ionic character of Ba, thus reducing the radii and consequently the interatomic distances.

It is interesting to note that a small vacancy level (~0.03) exists in  $\text{Ba}_5\text{V}_{12}\text{Sb}_{19.41}$  for the Ba1 site. The vacancy is still present even when no splitting with anisotropic ADPs was applied. On the other hand, the Ba1 site in  $\text{Ba}_5\text{Nb}_{12}\text{Sb}_{19.14}$  prefers to retain full occupancy even without anisotropic ADPs.

### 3.3. Physical properties

#### 3.3.1. Lattice dynamics

Temperature dependent ADPs in  $\text{Ba}_5\text{V}_{12}\text{Sb}_{19+x}$  (see Figure 8) for the framework atoms V and Sb (except Sb6 and Sb7) reveal a significantly smaller slope than for the Ba atoms. Treating the framework atoms as Debye oscillators according to Eqn. (1)

$$U_{\text{eq}} = \frac{3\hbar^2 T}{mk_B \theta_D^2} \left[ \frac{T}{\theta_D} \int_0^{\theta_D/T} \frac{x}{e^x - 1} dx + \frac{\theta_D}{4T} \right] + d^2 \quad (1)$$

where  $U_{\text{eq}}$  is calculated from the anisotropic thermal displacement parameters ( $U_{ii}$ ),  $U_{\text{eq}} =$

$(U_{11}+U_{22}+U_{33})/3$ ,  $\hbar$  is the reduced Planck's constant,  $k_B$  is the Boltzmann constant,  $m$  is the weighted average mass of the framework atoms (based on the site multiplicity), the Debye temperature  $\theta_D$  can be extracted, together with the static disorder parameter  $d^2$ . Since the framework consists of two V and five Sb atoms, the value of  $U_{av}$  is taken from the weighted average of  $U_{eq}$  of V and Sb atoms. The Debye temperature obtained from this fit is  $\theta_{D,av} = 229$  K.

The two Ba atoms and Sb7 show large ADPs (rattling behaviour) and thus, can be treated as Einstein oscillators,

$$U_{ii} = \frac{\hbar^2}{2mk_B\theta_{Eii}} \coth\left(\frac{\theta_{Eii}}{2T}\right) + d^2 \quad (2)$$

where  $\theta_{Eii}$  is the corresponding Einstein temperature to the  $U_{ii}$ .

Despite having similar behaviour as Sb7, atom Sb6 was not included in the calculation due to its small occupancy (less than 10%). Because of the site symmetry constraint  $U_{11}=U_{22}=U_{33}$  for Ba2 and Sb7, only one Einstein temperature of 81.8 K and 67.9 K could be extracted from the fitting process, respectively. However, for unsplit Ba1, two Einstein temperatures,  $\theta_{E11} = 73.2$  K and  $\theta_{E22,33} = 89.6$  K were determined. The disorder at the Ba1 site, caused by the presence of the Sb7 atom, can be clearly seen from the ellipsoid's direction towards Sb7, which corresponds to  $\theta_{E11}$  (see Figure 8). The separation distance between the split Ba1 atoms (0.0371 nm) corresponds very well with the disorder parameter ( $d^2=0.21 \times 10^{-2}$  nm<sup>2</sup>) obtained from the fitting process.

Similar to  $Ba_5V_{12}Sb_{19.41}$ , Nb and Sb atoms (except Sb6) form the framework structure in  $Ba_5Nb_{12}Sb_{19.14}$  (see Figure 9). The corresponding Debye temperature obtained from a fit to equation (1) is  $\theta_D=206$  K, which is somewhat lower than that of  $Ba_5V_{12}Sb_{19.4}$ . Such a trend is in good agreement with the simple vibrational spring approximation, in which the Debye temperature (frequency) is inversely proportional to the square root of atom mass. Since Sb7 is not present, Ba atoms are the only remaining rattlers in  $Ba_5Nb_{12}Sb_{19.14}$ . The Einstein temperatures related to these two atom sites are  $\theta_{E11} = 66.3$  K and  $\theta_{E22,33} = 78.3$  K for Ba1 and  $\theta_E = 72.5$  K for Ba2.

To get additional information on the lattice dynamics of  $Ba_5\{V,Nb\}_{12}Sb_{19+x}$ , heat capacity measurements were carried out. For non-magnetic materials the specific heat ( $C_p$ ) can be described as the sum of the electronic ( $C_{el}$ ) and the lattice ( $C_{lat}$ ) contribution. The electronic contribution at low temperatures varies linearly with temperature according to the Sommerfeld approximation, whilst at sufficiently low temperature ( $T \ll \theta_D$ ) the lattice part

can be approximated with the Debye  $T^3$  law, i.e.,

$$C_p = C_{el} + C_{lat} = \gamma T + \beta T^3; \beta = \frac{12R\pi^4 n}{5\theta_D^3} \quad (3).$$

Here,  $\gamma$  and  $\beta$  are the coefficients of the electron and the lattice contribution, respectively,  $R$  is the gas constant and  $n$  is number of atoms in the formula unit.

The analysis of the low temperature specific heat of polycrystalline  $Ba_{4.9}V_{12}Sb_{19.0}$  (presented in Figure 10) according to Eqn. 3 yields a Sommerfeld coefficient,  $\gamma = 74.7 \text{ mJ mol}^{-1} \text{ K}^{-2}$ , ( $2.08 \text{ mJ g-at}^{-1} \text{ K}^{-2}$ ) which refers to a large value of the electronic density of states at the Fermi energy ( $N(E_F)$ ). The Debye temperature,  $\theta_D = 247 \text{ K}$ , extracted via Eqn. (3) is in good agreement with the value obtained from the ADPs ( $229 \text{ K}$ ). The specific heat data of  $Ba_{4.9}Nb_{12}Sb_{19.4}$ , on the other hand, show a lower Sommerfeld coefficient of  $\gamma = 47.1 \text{ mJ mol}^{-1} \text{ K}^{-2}$  ( $1.29 \text{ mJ g-at}^{-1} \text{ K}^{-2}$ ), which indicates a metallic state with a smaller electronic density of states at the Fermi energy as compared to  $Ba_{4.9}V_{12}Sb_{19.0}$ .

The obvious deviations of the experimental specific heat data of both compounds in Figure 10 from the simple Debye approximation of Eqn. 3 starting already above about  $10 \text{ K}^2$  are indicative for the presence of Einstein modes with rather low energies. Accordingly, we perform a more detailed analysis of the lattice contribution to the specific heat via a so-called Junod fit<sup>26</sup> (Figure 11) providing a reasonable parameterization of the experimental data for both compounds with two narrow Einstein modes,  $\theta_{E1} \sim 40 \text{ K}$  and  $\theta_{E2} \sim 70 \text{ K}$  with similar width of  $\sim 1 \text{ K}$ . The value of  $\theta_{E2}$  is very close to the values of  $\theta_{E,Sb7}$  and  $\theta_{E,Ba(1,2)}$  obtained from the analysis of the ADPs. Note that the chemical formula of the vanadium compound derived from EPMA ( $Ba_{4.9}V_{12}Sb_{19.0}$ ) does not show any extra antimony either as Sb6 or Sb7, however, since the contributions of those sites to the overall composition are small, they may fall within the error of the EPMA measurement ( $\pm 0.5 \text{ at. \%}$ ).

From the practically linear temperature dependent lattice parameters, coefficients of thermal expansion,  $\alpha = 14.9 \times 10^{-6} \text{ K}^{-1}$  and  $15.8 \times 10^{-6} \text{ K}^{-1}$ , were obtained from the fit between  $100\text{--}300 \text{ K}$  for  $Ba_5Nb_{12}Sb_{19+x}$  and  $Ba_5V_{12}Sb_{19+x}$ , respectively. Such large values of  $\alpha$  exceed the maximum value reported for p-type Sb-based skutterudites,<sup>12</sup> but lie in range of some type-I clathrates.<sup>27</sup>

The previously derived Debye temperatures can be used to approximate the speed of sound

$$v_s = \frac{\theta_D k_B}{\hbar} \sqrt[3]{6\pi^2 \frac{n}{V}} \quad (4),$$

where  $n$  is the number of atom in the unit cell and  $V$  is the unit cell volume.

The resulting values of  $\sim 2235$  and  $\sim 2076 \text{ m s}^{-1}$  for  $\text{Ba}_5\text{V}_{12}\text{Sb}_{19+x}$  and  $\text{Ba}_5\text{Nb}_{12}\text{Sb}_{19+x}$ , respectively, are lower than those of filled skutterudites,<sup>12</sup> suggesting a lower lattice thermal conductivity,  $\lambda_{\text{ph}}$ ,

$$\lambda_{\text{ph}} = \frac{1}{3} v_s \ell_{\text{ph}} C_v \quad (5),$$

where  $\ell_{\text{ph}}$  is the phonon mean free path and  $C_v$  is the specific heat at constant volume. The phonon mean free path can be estimated from the distance between rattler atoms.<sup>28</sup> By neglecting Sb7 atoms, the average distance between Ba atoms in  $\text{Ba}_5\{\text{Nb},\text{V}\}_{12}\text{Sb}_{19+x}$  is  $<0.6 \text{ nm}$ ; this is lower than the distance between filler atoms in Sb based skutterudites ( $>0.7 \text{ nm}$ )<sup>2</sup>. Using the afore mentioned values, together with the measured specific heat of  $\text{Ba}_5\text{V}_{12}\text{Sb}_{19+x}$  at 300 K ( $\sim 800 \text{ J mol}^{-1} \text{ K}^{-1}$ ), the estimated lattice thermal conductivity is in the order of  $\sim 1 \text{ W m}^{-1} \text{ K}^{-1}$ .

Measurements of the thermal conductivity of  $\text{Ba}_{4.9}\text{Nb}_{12}\text{Sb}_{19.4}$  seem to confirm the prediction mentioned above, due to its glass-like behaviour, and the low measured value near room temperature ( $\sim 5 \text{ W m}^{-1} \text{ K}^{-1}$ , see Figure 12). As expected from the presence of defects and disorder, the frequently observed maximum of  $\lambda_{\text{ph}}$  (as typical for almost defect free materials) at low temperatures is suppressed. Attempts to extract and analyze the lattice contribution to the overall thermal conductivity in terms of Callaway's model<sup>29–31</sup> did not result in reliable outcomes. This is likely due to the dominant contribution of the electronic part to the overall thermal conductivity as a consequence of the relatively low electrical resistivity of this compound (see below). Indeed the electronic contribution calculated via the Wiedemann Franz law, using the Lorenz number ( $L_0$ ) for a free electron system,  $L_0 = 2.45 \times 10^{-8} \text{ W } \Omega \text{ K}^{-2}$  (see Figure 12), covers most of the overall measured thermal conductivity up to  $\sim 100 \text{ K}$ . Assuming the minimum lattice thermal conductivity as proposed by Cahill and Pohl,<sup>32</sup> the difference between the measured data and the sum of the lattice and electronic thermal conductivity could be well approximated, together with radiation losses  $\sim AT^3$ . At room temperature, the latter amounts to about  $\sim 2.5 \text{ W m}^{-1} \text{ K}^{-1}$ , typically for the measurement set-up used in this study.

### 3.3.2. *Electrical resistivity*

Due to the brittleness of the  $\text{Ba}_{4.9}\text{V}_{12}\text{Sb}_{19.0}$ , the sample specimen (a cuboid of  $\sim 8 \times 2 \times 2 \text{ mm}^3$ ) contained a significant amount of cracks, yielding a rather high resistivity at room temperature,  $\rho \sim 40 \text{ } \mu\Omega \text{ m}$ . To reduce the influence of cracks, a smaller piece ( $\sim 3 \text{ mm}$

length) was used for electrical resistivity measurements with spot welded Au contacts, revealing a significantly lower room temperature resistivity ( $\sim 18 \mu\Omega \text{ m}$ ). However, the absolute value of  $\rho$  of  $\text{Ba}_{4.9}\text{V}_{12}\text{Sb}_{19.0}$  could not be measured with confidence, and thus  $\rho$  is presented as normalized electrical resistivity ( $\rho/\rho_{\text{RT}}$ ). On the other hand, the  $\text{Ba}_{4.9}\text{Nb}_{12}\text{Sb}_{19.4}$  sample shows better mechanical stability; therefore the absolute value of electrical resistivity could be reliably measured and analyzed.

Below room temperature, both compounds exhibit a metallic like temperature dependent electrical resistivity (Figure 13), reaching a minimum at  $\sim 10 \text{ K}$ , followed by a slight increase of  $\rho(T)$  towards lower temperatures. Above room temperature,  $\rho(T)$  features a transition from a metallic to a more semiconducting behaviour. This holds true in case of  $\text{Ba}_{4.9}\text{Nb}_{12}\text{Sb}_{19.4}$ , while for  $\text{Ba}_{4.9}\text{V}_{12}\text{Sb}_{19.0}$  the electrical resistivity seems to reach saturation near room temperature, presumably being the beginning of the transition towards a semiconducting behaviour.

In order to describe the temperature dependent electrical resistivity of both samples, various scattering mechanisms are considered, and additionally, a temperature dependent charge carrier density,  $n_{\text{ch}}$ , is introduced. The former can be accounted for in terms of independent relaxation times ( $\tau_i$ ), describing scattering of electrons by defects and impurities, by phonons and by other electrons. Quantitatively, for simple metallic systems, scattering on static imperfections is assumed to be temperature independent (residual resistivity  $\rho_0$ ), while the electron phonon interaction is accounted for by a modified Bloch-Grüneisen model taking into account both acoustic and optical phonon scattering<sup>33</sup>, i.e.,

$$\rho(T) = \rho_0 + \rho_{ph}(T) \quad (6), \text{ with}$$

$$\rho_{ph} = \Re_A \left( \frac{T}{\theta_D} \right)^5 \int_0^{\frac{\theta_D}{T}} \frac{z^5}{(e^z - 1)(1 - e^{-z})} dz + \frac{\Re_O \theta_E^2}{T(e^x - 1)(1 - e^{-x})}; x = \frac{\theta_E}{T} \quad (7),$$

$\rho_{ph}$  is the resistivity arising from electron-phonon scattering,  $\Re_A$  and  $\Re_O$  are the electron acoustic phonon and the electron optical phonon interaction constants, respectively.  $\theta_D$  and  $\theta_E$  are the Debye and the Einstein temperatures, respectively. Electron – electron scattering is omitted here; this term is of importance only at very low temperatures and/or in systems with strong correlations among electrons. Combining Eqn. 6 and 7 reveals a constant value for  $T \rightarrow 0$ , a  $T^5$  term at low and a linear temperature dependence at elevated temperatures. Obviously, both compounds (see Figure 13) do not follow that simple metallic scenario; rather the maximum and the drop of the resistivity at high temperatures as observed for the

Ba-Nb-Sb system indicates some activated behaviour due to the presence of a gap in the electronic density of states near to the Fermi energy  $E_F$ . In order to describe such a scenario, we have developed a model using a box-like density of state with height  $N(E)$ , where the valence and the conduction bands are separated by a gap with width  $E_g$ ; the Fermi energy can be located either in the valence band, below the band edge ( $E_l$ ) of this band, or in the conduction band, above the respective band edge (compare, inset, Fig. 13 (left panel)). This simple band structure allows to analytically derive the charge carrier concentration of both holes,  $n_h$ , and electrons,  $n_e$ , with  $n_{ch}(T) = \sqrt{n_e(T)n_h(T)} + n_{ch}^0$ . Calculations have to be done employing the Fermi-Dirac distribution function. In addition, this model allows for in-gap states as well, as sketched in the inset of Figure 13 (left panel). Eqn. 6 then modifies to

$$\rho(T) = \frac{n_{ch}^0 (\rho_0 + \rho_{ph}(T))}{n_{ch}(T)} \quad (8),$$

$n_{ch}^0$  is a residual charge carrier density (see ref. 34 and the supporting information for detailed descriptions).

Applying Eqns. 7 and 8 to the experimental data reveals excellent agreement (solid lines in Figure 13) for the whole temperature range studied. Relevant parameters describing our model are indicated in both figures. Since the measurement of  $Ba_{4.9}V_{12}Sb_{19.0}$  is restricted to temperatures below 300 K, we started the fit procedure with the  $Ba_{4.9}Nb_{12}Sb_{19.4}$  sample and used those fit parameters as starting values to account for  $Ba_{4.9}V_{12}Sb_{19.0}$  as well. Reasonable values of the various material parameters are revealed, e.g., the narrow gaps in the electronic density of states.

The present band model provides a large variation of temperature dependencies of the electrical resistivity, without involving scattering processes others than electron-static impurity and electron-phonon interaction. The overall resistivity behaviour as observed experimentally is thus a balance of an increasing contribution due to electron scattering by phonons with respect to the temperature dependent variation of the charge carrier concentration. Subtle changes of the various parameters involved in this model can cause dramatic changes of  $\rho(T)$ . Focusing e.g., on the negative slope of the resistivity at very low temperatures observed in both present compounds, does not require a description based on the Kondo effect or weak localisation due to disorder in the crystal; rather, a stronger increase of  $n_{ch}(T)$  in relation to the initial increase of  $\rho_{ph}(T)$  results in a low temperature



decrease of the electrical resistivity as the temperature raises. In other words, thermodynamics outweighs standard scattering scenarios in systems, which are near to a metal-to-insulator transition.

The resistivity change from metal towards semiconducting behaviour in  $\text{Ba}_{4.9}\text{Nb}_{12}\text{Sb}_{19.4}$  is in line with the occurrence of a maximum in the Seebeck coefficient vs temperature (see inset Figure 13 (right panel)). A crossover from p- to n-type conductivity is also observed in  $\text{Ba}_{4.9}\text{Nb}_{12}\text{Sb}_{19.4}$  at  $\sim 680$  K, which is usually accompanied by a large value of electrical resistivity. However in this case the existence of a small energy gap ( $\sim 50$  meV) obtained from the resistivity fit could explain the low resistivity value of this compound. The small difference between the Fermi level and the valence band edge ( $\sim 4$  meV) together with the small energy gap may be responsible for the crossover from p- to n-type.

### 3.3.3. *Mechanical properties*

Hardness measurement on a polished surface of  $\text{Ba}_{4.9}\text{V}_{12}\text{Sb}_{19.0}$  and  $\text{Ba}_{4.9}\text{Nb}_{12}\text{Sb}_{19.4}$  employing a nano-indenter resulted in a hardness value of  $(3.8 \pm 0.1)$  GPa equivalent to  $\text{HV} = 391$  and  $(3.5 \pm 0.2)$  GPa equivalent to  $\text{HV} = 355$ , respectively.

Load dependent hardness measurements (see Figure 14) clearly show saturation yielding the true hardness value for loads of more than 50 mN. The hardness measured is in the range of filled Sb-based skutterudites,<sup>12</sup> which suggests a similar type of bonding. An estimate for Young's modulus ( $E_I$ ) was derived from the nano-indentation experiment assuming a Poisson's ratio ( $\nu$ ) as for  $\text{V}_{1-x}\text{Sb}_2$  ( $\nu = 0.26$ ).<sup>15</sup> This yields  $E_I = (85 \pm 2)$  GPa, a value much smaller than that for filled skutterudites. Details on the hardness and Young's modulus measurement via nanoindentation can be found in ref. 35 and from references therein.

For isotropic materials, the shear (G) and bulk (B) moduli can be calculated employing Eqn. 9 (see Table 5 for the results):

$$G = \frac{E}{2(\nu + 1)} \text{ and } B = \frac{E}{3(1 - 2\nu)} \quad (9)$$

For isotropic materials the mean sound velocity estimated from Anderson's formulae<sup>36</sup> (Eqn. 10) could be used to calculate the Debye temperature:

$$\theta_D = \frac{h\nu_m}{k_B} \sqrt[3]{\frac{3nN_A D}{4M\pi}}; \quad \text{with} \quad \nu_m = \left[ \frac{1}{3} \left( \frac{2}{\nu_T^3} + \frac{1}{\nu_L^3} \right) \right]^{-\frac{1}{3}} \quad (10)$$

$$\nu_L = \sqrt{\frac{3B + 4G}{3D}} \quad \text{and} \quad \nu_T = \sqrt{\frac{G}{D}}$$

where  $N_A$  is Avogadro's number,  $n$  is the number of atoms in the unit cell,  $M$  is the molecular weight,  $D$  is the density,  $\nu_m$  is the mean sound velocity,  $\nu_L$  is the longitudinal sound velocity and  $\nu_T$  is the transversal sound velocity. The resulting values are listed in Table 5. Similar values of Young's moduli of  $(87 \pm 2)$  GPa and  $(80 \pm 5)$  GPa were also obtained for  $\text{Ba}_{4.9}\text{V}_{12}\text{Sb}_{19.0}$  and  $\text{Ba}_{4.9}\text{Nb}_{12}\text{Sb}_{19.4}$ , respectively, if we take the Poisson's ratio of 0.22 from  $\{\text{Nb}, \text{Ta}\}\text{Sb}_2$ .<sup>15</sup> In that case the corresponding Debye temperatures calculated from Anderson's formulae are slightly higher (260 and 237 K).

#### 4. Conclusions

This paper summarizes crystal structure analyses as well as the characterization of transport and mechanical properties of two novel compounds  $\text{Ba}_5\{\text{V}, \text{Nb}\}_{12}\text{Sb}_{19+x}$ . These compounds are variants of the stuffed  $\gamma$ -brass structure  $\text{Ba}_5\text{Ti}_{12}\text{Sb}_{19+x}$ . The disorder in these compounds leads to complicated and high values of electrical resistivity. Hardness measurements employing a nano-indenter revealed hardness values similar to filled Sb-based skutterudites, however, yield remarkably smaller Young's moduli of  $\sim 80$  GPa. The atomic displacement parameters show rattling behavior for both Ba atoms in the V(Nb)-Sb framework, and (in case of  $\text{Ba}_5\text{V}_{12}\text{Sb}_{19+x}$ ) additionally Sb7 in the octahedral cage formed by Ba1 atoms. The rattling behaviour in these compounds is reflected in various physical properties such as electrical resistivity, specific heat, and low thermal conductivity.  $\text{Ba}_5\text{Nb}_{12}\text{Sb}_{19+x}$  possesses an extremely low lattice thermal conductivity, presumably close to the minimum thermal conductivity. A resistivity upturn at low temperatures occurs in both compounds, as well as a change from p- to n-type conductivity in  $\text{Ba}_5\text{Nb}_{12}\text{Sb}_{19+x}$  above 300 K, suggesting the existence of a narrow gap in close proximity of the Fermi level.

Incompatibility of  $\text{Ba}_5\{\text{V}, \text{Nb}\}_{12}\text{Sb}_{19+x}$  with Ba-filled Sb-based skutterudites with respect to a high coefficient of thermal expansion and dissimilar shear moduli together with the low thermal and electrical conductivity highly recommends to avoid formation of these phases in a hot contact zone between V, Nb electrodes and the skutterudite material.

## 5. Acknowledgement

The research reported herein was supported by the Austrian Federal Ministry of Science and Research (BMWF) under the scholarship scheme: Technology Grant Southeast Asia (Ph.D.) in the frame of the ASEA UNINET. The work was supported in part by the Christian Doppler Laboratory for Thermoelectricity.

## 6. References

- 1 *Pauling File Binary Edition, Version 1.0, Release 2002/1*, ASM International, Materials Park, OH, USA, 2002.
- 2 P. Villars and K. Cenzual, *Pearson's Crystal Data—Crystal Structure Database for Inorganic Compounds, release 2014/15*, ASM International, Materials Park, OH, USA, 2014.
- 3 H. Bie and A. Mar, *J. Solid State Chem.*, 2009, **182**, 3131–3137.
- 4 G. Rogl, A. Grytsiv, K. Yubuta, S. Puchegger, E. Bauer, C. Raju, R. C. Mallik and P. Rogl, *Acta Mater.*, 2015, **95**, 201–211.
- 5 G. Schierning, R. Chavez, R. Schmechel, B. Balke, G. Rogl and P. Rogl, *Transl. Mater. Res.*, 2015, **2**, 025001.
- 6 G. Rogl, A. Grytsiv, P. Rogl, N. Peranio, E. Bauer, M. Zehetbauer and O. Eibl, *Acta Mater.*, 2014, **63**, 30–43.
- 7 G. Rogl, A. Grytsiv, P. Rogl, E. Bauer, M. Hohenhofer, R. Anbalagan, R. C. Mallik and E. Schafner, *Acta Mater.*, 2014, **76**, 434–448.
- 8 G. Rogl, A. Grytsiv, P. Heinrich, E. Bauer, P. Kumar, N. Peranio, O. Eibl, J. Horky, M. Zehetbauer and P. Rogl, *Acta Mater.*, 2015, **91**, 227–238.
- 9 G. J. Snyder and T. S. Ursell, *Phys. Rev. Lett.*, 2003, **91**, 148301.
- 10 X. Shi, J. Yang, J. R. Salvador, M. Chi, J. Y. Cho, H. Wang, S. Bai, J. Yang, W. Zhang and L. Chen, *J. Am. Chem. Soc.*, 2011, **133**, 7837–7846.
- 11 K. Bartholomé, *Thermoelectric modules built with new high-temperature materials*, IAV-Berlin, 2014.
- 12 G. Rogl and P. Rogl, *Sci. Adv. Mater.*, 2011, **3**, 517–538.
- 13 X. C. Fan, M. Gu, X. Shi, L. D. Chen, S. Q. Bai and R. Nunna, *Ceram. Int.*, 2015, **41**, 7590–7595.
- 14 D. Zhao, H. Geng and X. Teng, *J. Alloys Compd.*, 2012, **517**, 198–203.

- 15 F. Failamani, P. Broz, D. Macciò, S. Puchegger, H. Müller, L. Salamakha, H. Michor, A. Grytsiv, A. Saccone, E. Bauer, G. Giester and P. Rogl, *Intermetallics*, 2015, **65**, 94–110.
- 16 J. Rodriguez-Carvajal, *FULLPROF, a program for Rietveld refinement and pattern matching analysis*, *Abstract of the satellite meeting on powder diffraction of the XV congress*, p. 127, Int. Union of Crystallography, Talence, France, 1990.
- 17 W. Wacha, Diploma thesis, Technische Universität Wien, 1989.
- 18 *Nonius Kappa CCD Program Package COLLECT, DENZO, SCALEPACK, SORTAV*, Nonius Delft, The Netherlands, 1998.
- 19 G. M. Sheldrick, *Acta Crystallogr. A*, 2007, **64**, 112–122.
- 20 L. J. Farrugia, *J. Appl. Crystallogr.*, 1999, **32**, 837–838.
- 21 L. M. Gelato and E. Parthé, *J. Appl. Crystallogr.*, 1987, **20**, 139–143.
- 22 G. Schaudy, Diploma thesis, Technische Universität Wien, 1990.
- 23 G. Schaudy, PhD thesis, Technische Universität Wien, 1995.
- 24 L. Leber, Diploma thesis, Technische Universität Wien, 2012.
- 25 L. Pauling and B. Kamb, *Proc. Natl. Acad. Sci. U. S. A.*, 1986, **83**, 3569–3571.
- 26 A. Junod, T. Jarlborg and J. Muller, *Phys. Rev. B*, 1983, **27**, 1568–1585.
- 27 M. Falmbigl, G. Rogl, P. Rogl, M. Kriegisch, H. Müller, E. Bauer, M. Reinecker and W. Schranz, *J. Appl. Phys.*, 2010, **108**, 043529.
- 28 M. Christensen, S. Johnsen and B. B. Iversen, *Dalton Trans.*, 2010, **39**, 978.
- 29 J. Callaway and H. C. von Baeyer, *Phys. Rev.*, 1960, **120**, 1149–1154.
- 30 J. Callaway, *Phys. Rev.*, 1959, **113**, 1046–1051.
- 31 J. Callaway, *Phys. Rev.*, 1961, **122**, 787–790.
- 32 D. G. Cahill, S. K. Watson and R. O. Pohl, *Phys. Rev. B*, 1992, **46**, 6131–6140.
- 33 A. I. Golovashkin, A. V. Gudenko, L. N. Zherikhina, M. L. Norton and A. M. Tskhovrebov, *J. Exp. Theor. Phys.*, 1994, **79**, 163–168.
- 34 S. Berger, PhD thesis, Technische Universität Wien, 2003.
- 35 T. Chudoba, in *Nanostructured Coatings*, eds. A. Cavaleiro and J. T. M. D. Hosson, Springer New York, 2006, pp. 216–260.
- 36 O. L. Anderson, *J. Phys. Chem. Solids*, 1963, **24**, 909–917.

**Table 1.** Crystallographic data for Ba<sub>5</sub>V<sub>12</sub>Sb<sub>19+x</sub>, x = 0.41; for comparison all atom labels and site parameters were kept consistent with the description of the parent crystal structure of Ba<sub>5</sub>Ti<sub>12</sub>Sb<sub>19+x</sub> (standardized).

Parameter/compound	300 K	200 K	100 K
Phase composition (EPMA, at.%)	Ba <sub>13.3</sub> V <sub>33.7</sub> Sb <sub>53.0</sub>	Ba <sub>13.3</sub> V <sub>33.7</sub> Sb <sub>53.0</sub>	Ba <sub>13.3</sub> V <sub>33.7</sub> Sb <sub>53.0</sub>
Refinement composition (at.%)	Ba <sub>13.4</sub> V <sub>33.1</sub> Sb <sub>53.5</sub>	Ba <sub>13.4</sub> V <sub>33.1</sub> Sb <sub>53.5</sub>	Ba <sub>13.4</sub> V <sub>33.1</sub> Sb <sub>53.5</sub>
Structure type	disordered-Ba <sub>5</sub> Ti <sub>12</sub> Sb <sub>19+x</sub>	disordered-Ba <sub>5</sub> Ti <sub>12</sub> Sb <sub>19+x</sub>	disordered-Ba <sub>5</sub> Ti <sub>12</sub> Sb <sub>19+x</sub>
$\theta$ range (deg)	4.75 ≤ 2 $\theta$ ≤ 72.61	4.76 ≤ 2 $\theta$ ≤ 72.53	4.76 ≤ 2 $\theta$ ≤ 72.62
$a=b=c$ [nm] (from Kappa CCD)	1.21230(1)	1.21039(1)	1.20914(1)
$a$ [nm] (from Guinier, Si-standard)	1.21391(5)	-	-
Reflections in refinement	1673 ≥ 4 $\sigma$ (F <sub>o</sub> ) of 1675	1670 ≥ 4 $\sigma$ (F <sub>o</sub> ) of 1671	1670 ≥ 4 $\sigma$ (F <sub>o</sub> ) of 1671
Number of variables	50	50	50
R <sub>F2</sub> = $\Sigma F_o^2 - F_c^2 /\Sigma F_o^2$	0.0189	0.0181	0.0184
wR2	0.0421	0.0403	0.0420
R <sub>int</sub>	0.0380	0.0325	0.0326
GOF	1.295	1.350	1.392
Extinction (Zachariasen)	0.00040(1)	0.00034(2)	0.00029(1)
<b>Ba1a</b> in 6g (x, 1/2, 1/2); occ.	x = 0.1723(2); 0.46(1)	x = 0.1720(2); 0.46(1)	x = 0.1717(2); 0.46(1)
U <sub>11</sub> ; U <sub>22</sub> =U <sub>33</sub> ; U <sub>23</sub> ; U <sub>13</sub> =U <sub>12</sub> =0 <sup>1</sup>	0.0644(5); 0.0121(2); -0.0015(2)	0.0586(5); 0.0078(2); -0.0011(2)	0.0514(5); 0.0035(2); -0.0008(2)
	U <sub>equiv</sub> = U <sub>iso</sub> = 0.0115(4)	U <sub>equiv</sub> = 0.0075(4)	U <sub>equiv</sub> = 0.0036(4)
<b>Ba1b</b> in 6g (x, 1/2, 1/2); occ.	x = 0.2028(2); 0.51(1)	x = 0.2022(2); 0.50(1)	x = 0.2014(2); 0.50(1)
U <sub>11</sub> ; U <sub>22</sub> =U <sub>33</sub> ; U <sub>23</sub> ; U <sub>13</sub> =U <sub>12</sub> =0 <sup>1</sup>	U <sub>equiv</sub> = U <sub>iso</sub> = 0.0143(4)	U <sub>equiv</sub> = 0.0095(3)	U <sub>equiv</sub> = 0.0045(3)
<b>Ba2</b> in 4e (x, x, x); occ.	x = 0.83405(4); 1.00(1)	x = 0.83401(3); 1.00(1)	x = 0.83395(3); 1.00(1)
U <sub>11</sub> =U <sub>22</sub> =U <sub>33</sub> ; U <sub>23</sub> =U <sub>13</sub> =U <sub>12</sub>	0.0150(1); -0.0010(1)	0.0100(1); -0.0008(1)	0.0046(1); -0.0004(1)
<b>V1</b> in 12i (x, x, z); occ.	x = 0.1576(1); z = 0.3252(1); 1.00(1)	x = 0.1577(1); z = 0.3250(1); 1.00(1)	x = 0.1578(1); z = 0.3249(1); 1.00(1)
U <sub>11</sub> =U <sub>22</sub> ; U <sub>33</sub> ; U <sub>23</sub> =U <sub>13</sub> ; U <sub>12</sub>	0.0074(2); 0.0094(4); 0.0009(2); 0.0003(3)	0.0050(2); 0.0065(4); 0.0005(2); 0.0004(3)	0.0025(2); 0.0034(4); 0.0004(2); 0.0004(3)
<b>V2</b> in 12h (x, 1/2, 0); occ.	x = 0.1867(1); 1.00(1)	x = 0.1869(1); 1.00(1)	x = 0.1870(1); 1.00(1)
U <sub>11</sub> ; U <sub>22</sub> ; U <sub>33</sub> ; U <sub>23</sub> ; U <sub>13</sub> =U <sub>12</sub> =0	0.0059(3); 0.0063(3); 0.074(3); 0.0012(3)	0.0038(3); 0.0042(3); 0.048(3); 0.0009(3)	0.0014(3); 0.0018(3); 0.023(3); 0.0005(3)
<b>Sb1</b> in 12i (x, x, z); occ.	x = 0.21683(2); z = 0.54221(3); 1.00(1)	x = 0.21697(2); z = 0.54215(3); 1.00(1)	x = 0.21712(2); z = 0.54205(3); 1.00(1)
U <sub>11</sub> =U <sub>22</sub> ; U <sub>33</sub> ; U <sub>23</sub> =U <sub>13</sub> ; U <sub>12</sub>	0.0087(1); 0.0104(1); -0.0011(1); -0.0011(1)	0.0057(1); 0.0069(1); -0.0008(1); -0.0008(1)	0.0025(1); 0.0030(1); -0.0005(1); -0.0004(1)
<b>Sb2</b> in 12i (x, x, z); occ.	x = 0.33272(2); z = 0.01344(3); 1.00(1)	x = 0.33265(2); z = 0.01325(3); 1.00(1)	x = 0.33259(2); z = 0.01306(3); 1.00(1)
U <sub>11</sub> =U <sub>22</sub> ; U <sub>33</sub> ; U <sub>23</sub> =U <sub>13</sub> ; U <sub>12</sub>	0.0071(1); 0.0093(2); 0.0018(1); 0.0021(1)	0.0047(1); 0.0062(1); 0.0013(1); 0.0014(1)	0.0020(1); 0.0030(1); 0.0008(1); 0.0009(1)
<b>Sb3</b> in 6f (x, 0, 0); occ.	x = 0.36550(4); 1.00	x = 0.36558(4); 1.00(1)	x = 0.36562(4); 1.00(1)
U <sub>11</sub> ; U <sub>22</sub> =U <sub>33</sub> ; U <sub>23</sub> ; U <sub>13</sub> =U <sub>12</sub> =0	0.0056(2); 0.0060(1); -0.0011(2)	0.0036(2); 0.0038(1); -0.0008(1)	0.0011(2); 0.0015(1); -0.0006(2)
<b>Sb4</b> in 4e (x, x, x); occ.	x = 0.11037(3); 1.00(1)	x = 0.11008(3); 1.00(1)	x = 0.10977(3); 1.00(1)
U <sub>11</sub> =U <sub>22</sub> =U <sub>33</sub> ; U <sub>23</sub> =U <sub>13</sub> =U <sub>12</sub>	0.0095(1); -0.0004(1)	0.0063(1); -0.0001(1)	0.0028(1); -0.0001(1)
<b>Sb5</b> in 4e (x, x, x); occ.	x = 0.31626(3); 1.00(1)	x = 0.31647(3); 1.00(1)	x = 0.31671(3); 1.00(1)
U <sub>11</sub> =U <sub>22</sub> =U <sub>33</sub> ; U <sub>23</sub> =U <sub>13</sub> =U <sub>12</sub>	0.0082(1); 0.0005(1)	0.0055(1); 0.0006(1)	0.0027(1); 0.0008(1)
<b>Sb6</b> in 4e (x, x, x); occ.	x = 0.460(1); 0.073(5)	x = 0.458(1); 0.075(5)	x = 0.4568(4); 0.079(4)
U <sub>11</sub> =U <sub>22</sub> =U <sub>33</sub> ; U <sub>23</sub> =U <sub>13</sub> =U <sub>12</sub>	0.025(4); -0.003(3)	0.017(3); -0.002(2)	0.007(2); -0.002(2)
<b>Sb7</b> in 1b (1/2, 1/2, 1/2); occ.	0.53(1)	0.52(1)	0.49(1)
U <sub>11</sub> =U <sub>22</sub> =U <sub>33</sub> ; U <sub>23</sub> =U <sub>13</sub> =U <sub>12</sub> =0	0.030(2)	0.020(1)	0.011(1)
Residual electron density; max; min (electron/nm <sup>3</sup> ) × 10 <sup>3</sup>	3.83; -1.57	4.00; -1.41	3.95; -1.33
Flack parameter	0.02(6)	0.01(6)	0.01(6)

<sup>1</sup> Independent refinement was also performed for unsplit Ba1 with anisotropic ADPs to extract U<sub>ij</sub> for analysis in Figure 8.

**Table 2.** Interatomic distances  $d$  in [nm] for  $\text{Ba}_5\text{V}_{12}\text{Sb}_{19+x}$  ( $x=0.41$ ). The coordination number, CN, is given for unsplit Ba1.

Atom 1	Atom 2	d [nm]	Atom 1	Atom 2	d [nm]	Atom 1	Atom 2	d [nm]
Ba1a CN=13	Sb2 (2x)	0.34542	V2 CN=8	Sb2 (2x)	0.26969	Sb3 CN=11	V1 (2x)	0.27451
	Sb1 (4x)	0.35126		Sb1 (2x)	0.27028		V2 (4x)	0.27894
	Sb6 (2x)	0.35511		Sb3 (2x)	0.27894		Sb3 (1x)	0.32612
	Sb5 (2x)	0.36016		V1 (2x)	0.28751		Sb4 (2x)	0.36258
	Sb2 (2x)	0.36459					Ba2 (2x)	0.37346
Ba1b CN=13	Sb6 (2x)	0.31882	Sb1 CN=9	V2 (2x)	0.27028	Sb4 CN=6	V1 (3x)	0.27265
	Sb5 (2x)	0.34372		V1 (1x)	0.28209		Ba2 (3x)	0.34828
	Sb1 (4x)	0.34749		Sb5 (1x)	0.32263	Sb5 CN=10	V1(3x)	0.27231
	Sb7(1x)	0.36024		Sb2 (2x)	0.34736		Sb6 (1x)	0.30083
	Sb2 (2x)	0.36739		Ba1b (2x)	0.34749		Sb1(3x)	0.32263
	Sb2 (2x)	0.38859		Ba1a (2x)	0.35126		Ba1b (3x)	0.34372
Ba2 CN=12	Sb4 (3x)	0.34828	Sb2 CN=9	Ba2 (1x)	0.36439		Ba1a(3x)	0.36016
	Sb2 (3x)	0.35923		V2 (2x)	0.26969	Sb6 CN=4 <sup>1</sup>	Sb7 (1x)	0.08499
	Sb1 (3x)	0.36439		V1 (2x)	0.27514		Sb6 (3x)	0.13878
	Sb3(3x)	0.37346		Ba1a (1x)	0.34542		Sb5 (1x)	0.30083
V1 CN=10	Sb5(1x)	0.27231		Sb1 (2x)	0.34736		Ba1b (3x)	0.31882
	Sb4 (1x)	0.27265		Ba2 (1x)	0.35923		Ba1a (3x)	0.35511
	Sb3 (1x)	0.27451		Ba1a (1x)	0.36459	Sb7 CN=6 <sup>1</sup>	Sb6(4x)	0.08499
	Sb2 (2x)	0.27514		Ba1b (1x)	0.36739		Ba1b (6x)	0.36024
	Sb1(1x)	0.28209		Sb5 (1x)	0.36819		Sb5 (4x)	0.38582
	V1 (2x)	0.28733		Sb1 (2x)	0.38083		Ba1a (6x)	0.39733
	V2 (2x)	0.28751		Ba1b (1x)	0.38859			

<sup>1</sup> Sb6 and Sb7 are excluded from the coordination polyhedra due to their short distance and small occupancy of Sb6, while Sb5 is located outside the polyhedra if unsplit Ba1 is considered.

**Table 3.** Crystallographic data for Ba<sub>5</sub>Nb<sub>12</sub>Sb<sub>19+x</sub>, x = 0.14; for comparison all atom labels and site parameters were kept consistent with the description of the parent crystal structure of Ba<sub>5</sub>Ti<sub>12</sub>Sb<sub>19+x</sub> (standardized).

Parameter/compound	300 K	200 K	100 K
Phase composition (EPMA, at.%)	Ba <sub>13.5</sub> Nb <sub>33.5</sub> Sb <sub>53.0</sub>	Ba <sub>13.5</sub> Nb <sub>33.5</sub> Sb <sub>53.0</sub>	Ba <sub>13.5</sub> Nb <sub>33.5</sub> Sb <sub>53.0</sub>
Refinement composition (at.%)	Ba <sub>13.8</sub> Nb <sub>33.2</sub> Sb <sub>53.0</sub>	Ba <sub>13.8</sub> Nb <sub>33.2</sub> Sb <sub>53.0</sub>	Ba <sub>13.8</sub> Nb <sub>33.2</sub> Sb <sub>53.0</sub>
Structure type	Ba <sub>5</sub> Ti <sub>12</sub> Sb <sub>19+x</sub>	Ba <sub>5</sub> Ti <sub>12</sub> Sb <sub>19+x</sub>	Ba <sub>5</sub> Ti <sub>12</sub> Sb <sub>19+x</sub>
$\theta$ range (deg)	$2 \leq 2\theta \leq 72.55$	$2 \leq 2\theta \leq 72.55$	$2 \leq 2\theta \leq 72.45$
$a=b=c$ [nm] (from Kappa CCD)	1.24979(2)	1.24827(2)	1.24691(2)
$a$ [nm] (from Guinier, Si-standard)	1.2501(3)	-	-
Reflections in refinement	$1623 \geq 4\sigma(F_o)$ of 1758	$1701 \geq 4\sigma(F_o)$ of 1787	$1721 \geq 4\sigma(F_o)$ of 1786
Number of variables	46	46	46
$R_{F2} = \sum  F_o^2 - F_c^2  / \sum F_o^2$	0.0219	0.0202	0.0184
wR2	0.0449	0.0401	0.0355
$R_{int}$	0.0176	0.0149	0.0143
GOOF	1.137	1.121	1.118
Extinction (Zachariasen)	0.00021(1)	0.00020(1)	0.00018(1)
<b>Ba1</b> in 6g (x, $\frac{1}{2}$ , $\frac{1}{2}$ ); occ.	x = 0.17161(5); 1.00(1)	x = 0.17138(4); 1.00(1)	x = 0.17111(4); 1.00(1)
U <sub>11</sub> ; U <sub>22</sub> =U <sub>33</sub> ; U <sub>23</sub> ; U <sub>13</sub> =U <sub>12</sub> =0	0.0311(3); 0.0181(1); 0.0003(2)	0.0235(2); 0.0127(1); 0.0003(2)	0.0159(2); 0.0072(1); -0.0001(2)
<b>Ba2</b> in 4e (x,x,x); occ.	x = 0.83454(4); 1.00(1)	x = 0.83456(3); 1.00(1)	x = 0.83457(3); 1.00(1)
U <sub>11</sub> =U <sub>22</sub> =U <sub>33</sub> ; U <sub>23</sub> =U <sub>13</sub> =U <sub>12</sub>	0.0213(1); -0.0021(1)	0.0151(1); -0.0015(1)	0.0086(1); -0.0009(1)
<b>Nb1</b> in 12i (x,x,z); occ.	x = 0.16023(3); z = 0.32652(4); 1.00(1)	x = 0.16022(2); z = 0.32641(4); 1.00(1)	x = 0.16017(2); z = 0.32633(4); 1.00(1)
U <sub>11</sub> =U <sub>22</sub> ; U <sub>33</sub> ; U <sub>23</sub> =U <sub>13</sub> ; U <sub>12</sub>	0.0089(1); 0.0091(2); 0.0015(2); 0.001(2)	0.0066(1); 0.0069(2); 0.0010(1); 0.007(1)	0.0042(1); 0.0044(2); 0.0005(1); 0.0004(1)
<b>Nb2</b> in 12h (x, $\frac{1}{2}$ , 0); occ.	x = 0.18670(4); 1.00(1)	x = 0.18686(3); 1.00(1)	x = 0.18699(3); 1.00(1)
U <sub>11</sub> ; U <sub>22</sub> ; U <sub>33</sub> ; U <sub>23</sub> ; U <sub>13</sub> =U <sub>12</sub> =0	0.0087(2); 0.0080(2); 0.0094(2); 0.0016(2)	0.0066(2); 0.0060(2); 0.0070(2); 0.0009(2)	0.0041(2); 0.0039(2); 0.0042(2); 0.0005(2)
<b>Sb1</b> in 12i (x,x,z); occ.	x = 0.22067(2); z = 0.54434(3); 1.00(1)	x = 0.22079(2); z = 0.54429(3); 1.00(1)	x = 0.22093(2); z = 0.54423(2); 1.00(1)
U <sub>11</sub> =U <sub>22</sub> ; U <sub>33</sub> ; U <sub>23</sub> =U <sub>13</sub> ; U <sub>12</sub>	0.0117(1); 0.0141(2); -0.0014(1); -0.0007(1);	0.0084(1); 0.0102(1); -0.0010(1); -0.0005(1);	0.0049(1); 0.0061(1); -0.0005(1); -0.0002(1);
<b>Sb2</b> in 12i (x,x,z); occ.	x = 0.33233(2); z = 0.00887(3); 1.00(1)	x = 0.33226(2); z = 0.00868(3); 1.00(1)	x = 0.33221(2); z = 0.00849(3); 1.00(1)
U <sub>11</sub> =U <sub>22</sub> ; U <sub>33</sub> ; U <sub>23</sub> =U <sub>13</sub> ; U <sub>12</sub>	0.0096(1); 0.0111(2); 0.0022(1); 0.0022(1)	0.0070(1); 0.0081(1); 0.0014(1); 0.0016(1)	0.0042(1); 0.0048(1); 0.0008(1); 0.0009(1)
<b>Sb3</b> in 6f (x, 0, 0); occ.	x = 0.36280(4); 1.00(1)	x = 0.36293(4); 1.00(1)	x = 0.36302(4); 1.00(1)
U <sub>11</sub> ; U <sub>22</sub> =U <sub>33</sub> ; U <sub>23</sub> ; U <sub>13</sub> =U <sub>12</sub> =0	0.0089(2); 0.0082(1); -0.0005(2)	0.0068(2); 0.0059(1); -0.0005(2)	0.0043(2); 0.0036(1); -0.0002(2)
<b>Sb4</b> in 4e (x,x,x); occ.	x = 0.10884(3); 1.00(1)	x = 0.10853(3); 1.00(1)	x = 0.10829(3); 1.00(1)
U <sub>11</sub> =U <sub>22</sub> =U <sub>33</sub> ; U <sub>23</sub> =U <sub>13</sub> =U <sub>12</sub>	0.0122(1); -0.0008(1);	0.0089(1); -0.0004(1);	0.0054(1); -0.0001(1);
<b>Sb5</b> in 4e (x,x,x); occ.	x = 0.32277(3); 1.00(1)	x = 0.32283(3); 1.00(1)	x = 0.32290(3); 1.00(1)
U <sub>11</sub> =U <sub>22</sub> =U <sub>33</sub> ; U <sub>23</sub> =U <sub>13</sub> =U <sub>12</sub>	0.0115(1); -0.0005(1);	0.0083(1); -0.0002(1);	0.0049(1); 0.0001(1);
<b>Sb6</b> in 4e (x,x,x); occ.	x = 0.4521(6); 0.067(4)	x = 0.4515(4); 0.077(3)	x = 0.4515(4); 0.074(3)
U <sub>11</sub> =U <sub>22</sub> =U <sub>33</sub> ; U <sub>23</sub> =U <sub>13</sub> =U <sub>12</sub>	U <sub>iso</sub> = 0.020(3)	U <sub>iso</sub> = 0.016(2)	U <sub>iso</sub> = 0.008(2)
Residual electron density; max; min in (electron/nm <sup>3</sup> ) × 10 <sup>3</sup>	5.02; -2.26	5.65; -1.82	5.35; -1.32
Flack parameter	0.10(3)	0.10(2)	0.24(2)

**Table 4.** Interatomic distances  $d$  in [nm] for  $\text{Ba}_5\text{Nb}_{12}\text{Sb}_{19+x}$ .

Atom 1	Atom 2	$d$ [nm]	Atom 1	Atom 2	$d$ [nm]	Atom 1	Atom 2	$d$ [nm]
Ba1 CN=12	Sb1 (4x)	0.35875	Nb2 CN=10	Sb2 (2x)	0.27778	Sb3 CN=11	Nb1 (2x)	0.28681
	Sb2 (2x)	0.35943		Sb1 (2x)	0.28449		Nb2 (4x)	0.28956
	Sb6 (2x)	0.36059		Sb3 (2x)	0.28956		Sb3 (1x)	0.34295
	Sb5 (2x)	0.36581		Nb1 (2x)	0.29699		Sb4 (2x)	0.37114
	Sb2 (2x)	0.37243		Nb2 (2x)	0.32998		Ba2 (2x)	0.38256
Ba2 CN=12	Sb4 (3x)	0.35713	Sb1 CN=9	Nb2 (2x)	0.28449	Sb4 CN=6	Nb1 (3x)	0.28682
	Sb2 (3x)	0.36668		Nb1 (1x)	0.29243		Ba2 (3x)	0.35713
	Sb1 (3x)	0.37558		Sb5 (1x)	0.33052	Sb5 CN=10	Sb6 (1x)	0.27984
	Sb3 (3x)	0.38256		Sb2 (2x)	0.35431		Nb1 (3x)	0.28732
Nb1 CN=10	Sb2 (2x)	0.28653		Ba1 (2x)	0.35875		Sb1 (3x)	0.33052
	Sb3 (1x)	0.28681		Ba2 (1x)	0.37558		Ba1 (3x)	0.36581
	Sb4 (1x)	0.28682	Sb2 CN=9	Nb2 (2x)	0.27778	Sb6 CN=4 <sup>1</sup>	Sb6 (3x)	0.16953
	Sb5 (1x)	0.28732		Nb1 (2x)	0.28653		Sb5 (1x)	0.27984
	Sb1 (1x)	0.29243		Sb1 (2x)	0.35431		Ba1 (3x)	0.36059
	Nb1 (2x)	0.29392		Ba1 (1x)	0.35943			
	Nb2 (2x)	0.29699		Ba2 (1x)	0.36668			
				Ba1 (1x)	0.37243			

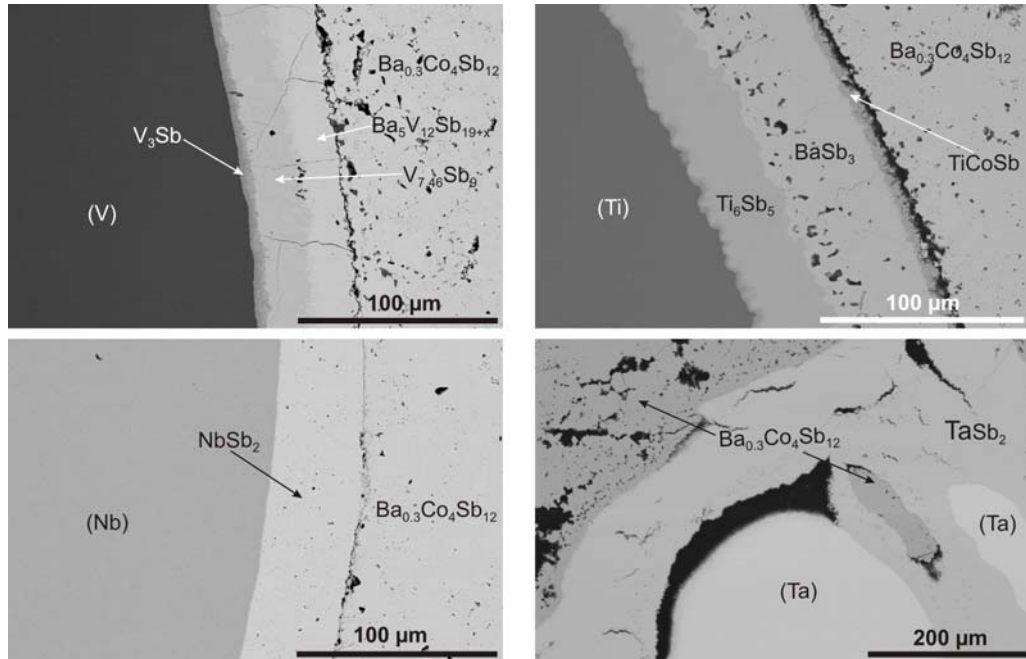
<sup>1</sup> Sb6 is excluded from the coordination polyhedra due to its short distance and small occupancy.

**Table 5.** Elastic properties and Debye temperatures of  $\text{Ba}_5\{\text{V},\text{Nb}\}_{12}\text{Sb}_{19+x}$  and comparison of data obtained from different measurements.

	$H_V$ [GPa]	$E_I$ [GPa]	$\nu^*$	$G$ [GPa]	$B$ [GPa]	CTE <sup>s</sup>	$\theta_D$ [K]				$\theta_E$ [K]					
							ADP	$C_p$	$\rho$	$E_I$	ADP				$C_p$	
											Ba1 <sub>11</sub>	Ba1 <sub>22,33</sub>	Ba2	Sb7	$\theta_{E1}$	$\theta_{E2}$
$\text{Ba}_5\text{V}_{12}\text{Sb}_{19+x}$	3.8	85	0.26	33.7	59.0	15.8	229	247	247	254	73.2	89.6	81.8	67.9	72	40
$\text{Ba}_5\text{Nb}_{12}\text{Sb}_{19+x}$	3.5	79	0.26	31.3	54.9	14.9	206	235	235	233	66.3	78.3	72.5	-	70	41

\*Taken from  $\text{V}_{1-x}\text{Sb}_2$ .<sup>15</sup>

<sup>s</sup> Given in  $10^{-6}\text{K}^{-1}$

**Figure 1.** Diffusion zones formed between n-type  $\text{Ba}_{0.3}\text{Co}_4\text{Sb}_{12}$  and group-V metals (V,Nb,Ta) and Ti at 600°C annealed for 40 days.



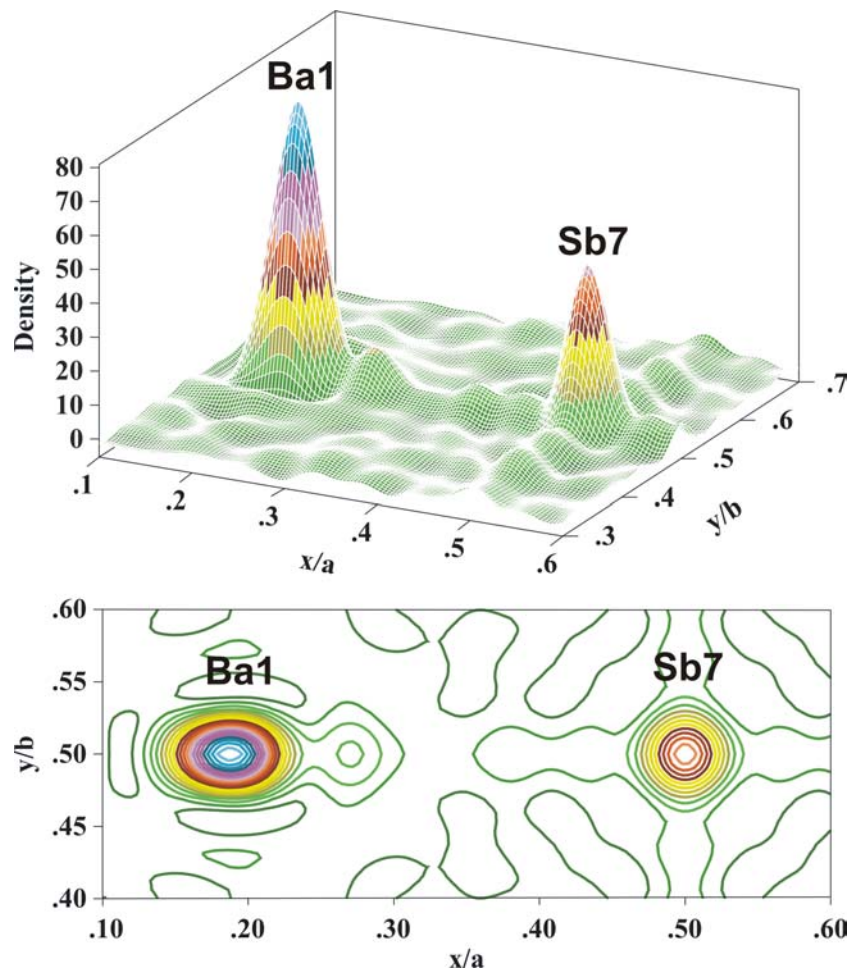


**Figure 2.** Difference Fourier map of  $\text{Ba}_5\text{V}_{12}\text{Sb}_{19+x}$  at  $z=0.5$  around Ba1 from data measured at 100 K.

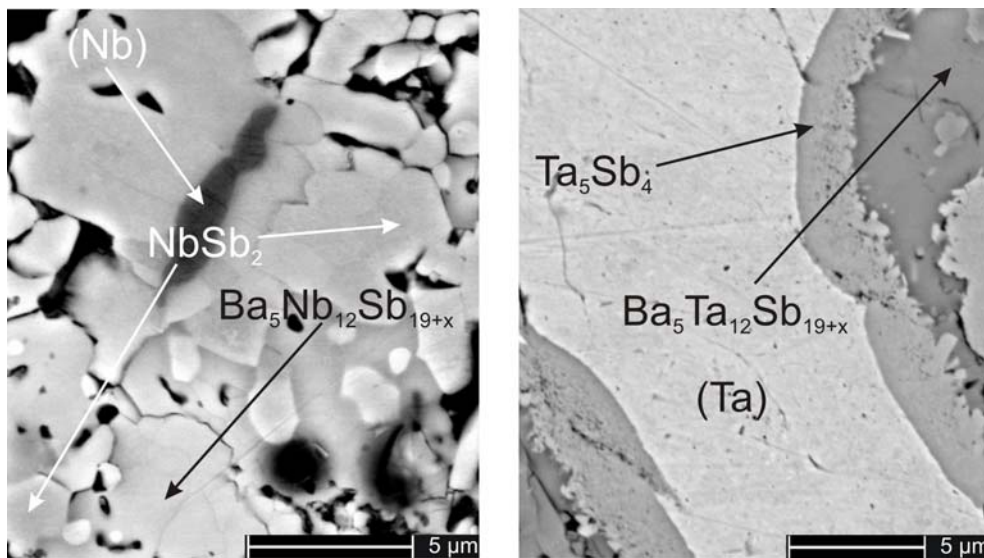


**Figure 3.**  $\text{Ba}_5\{\text{Nb,Ta}\}_{12}\text{Sb}_{19+x}$  phases formed at 700°C.

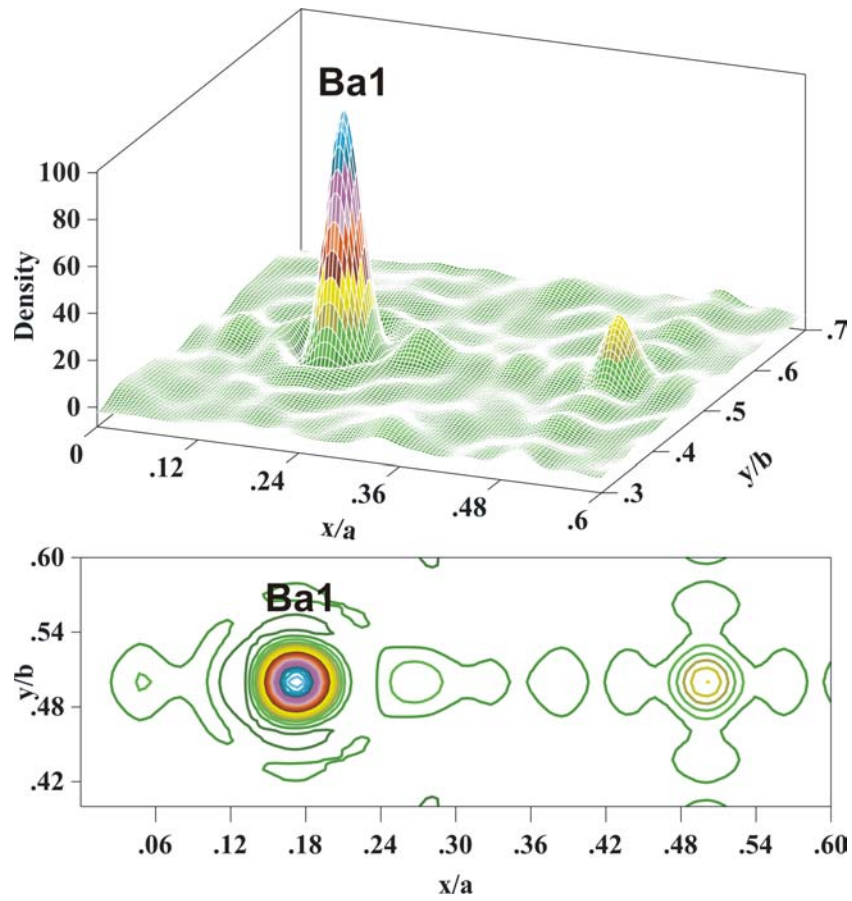


**Figure 4.** Difference Fourier map of  $\text{Ba}_5\text{Nb}_{12}\text{Sb}_{19+x}$  at  $z = 0.5$  around Ba1 from data measured at 100 K.

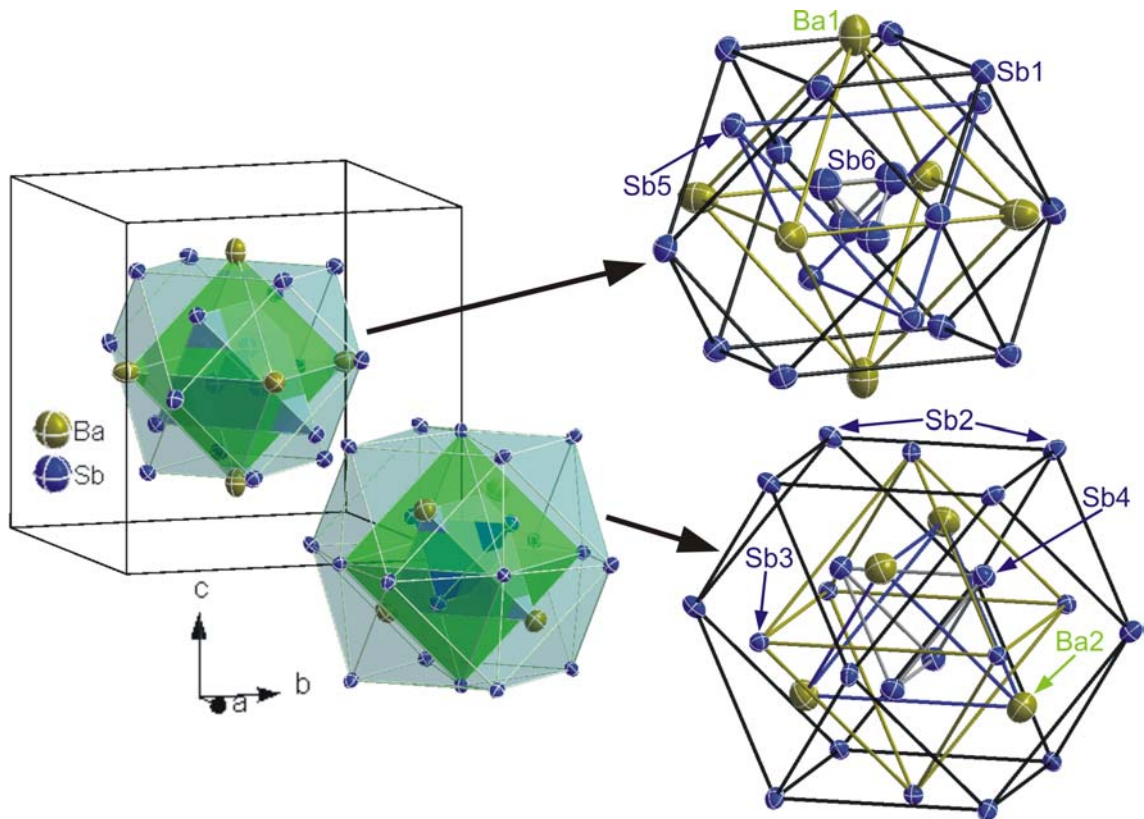


**Figure 5.**  $\gamma$ -brass cluster representation of  $\text{Ba}_5\{\text{Nb},\text{V}\}_{12}\text{Sb}_{19+x}$  with ADPs from SC refinement for  $\text{Ba}_5\text{Nb}_{12}\text{Sb}_{19+x}$  at RT.

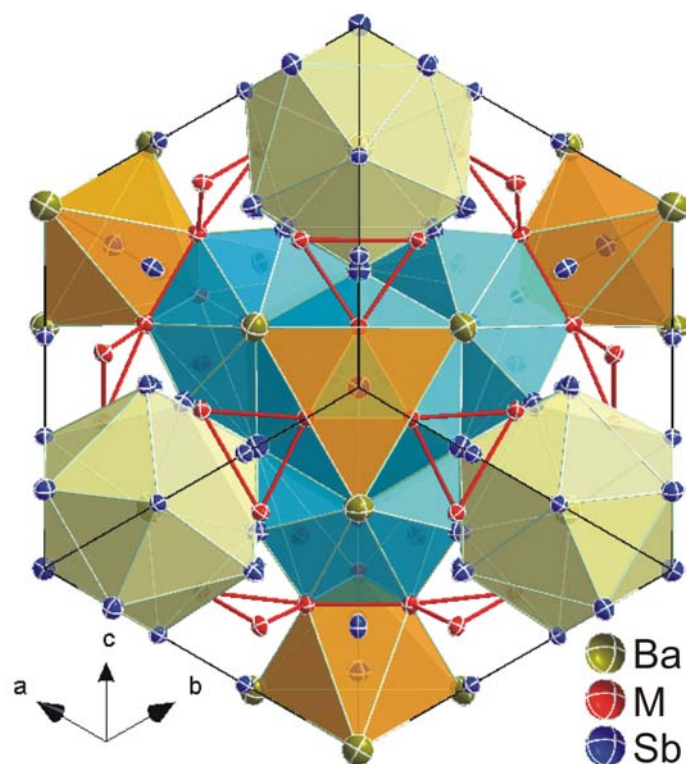


**Figure 6.** Projection of  $\text{Ba}_5\text{M}_{12}\text{Sb}_{19+x}$  along  $\langle 111 \rangle$  direction.

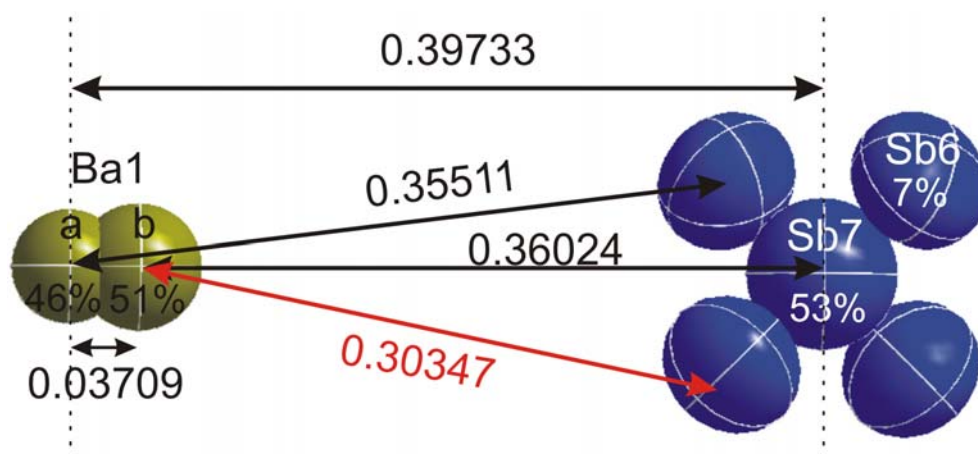


**Figure 7.** Bond distance (in nm) analysis between split Ba1, Sb6 and Sb7.

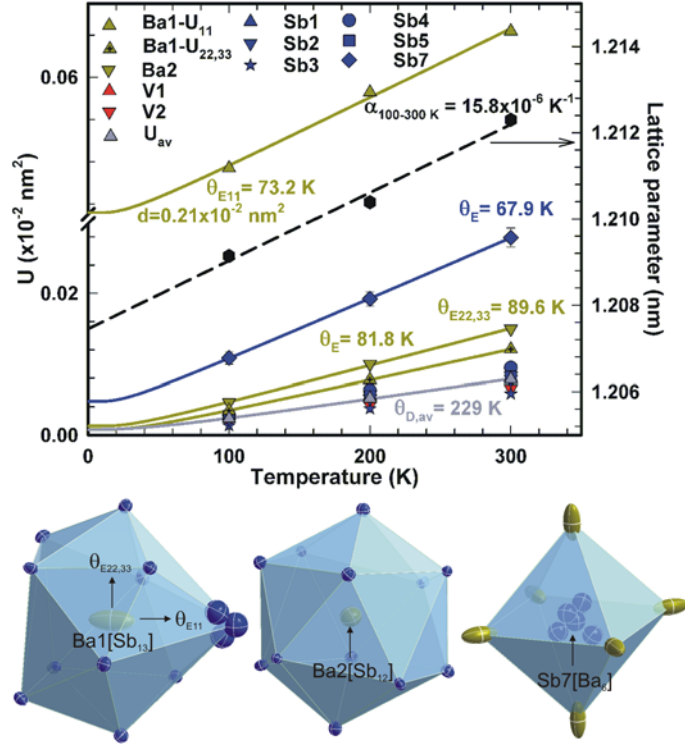


**Figure 8.** Upper panel: temperature dependent lattice parameters and ADPs ( $U_{\text{eq}}$ ) for  $\text{Ba}_5\text{V}_{12}\text{Sb}_{19.41}$ . The solid lines represent the fit for the ADPs according to Eqn. (1) and (2), while the dashed line is the linear fit for the lattice parameters. Lower panel: atom coordination around atoms Ba1, Ba2 and Sb7 with ADPs from the SC refinement at RT.

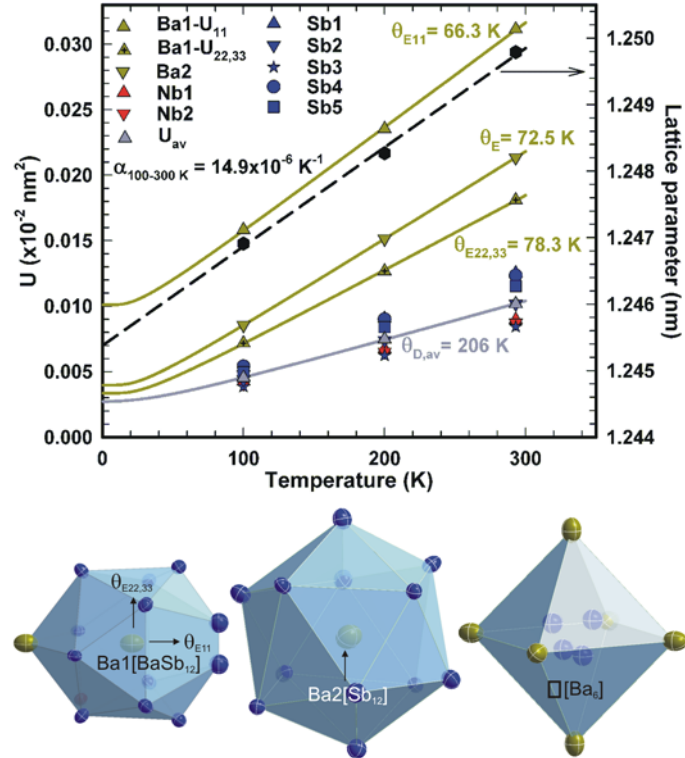


**Figure 9.** Upper panel: temperature dependent lattice parameters and ADPs ( $U_{\text{eq}}$ ) for  $\text{Ba}_5\text{Nb}_{12}\text{Sb}_{19.14}$ . The solid lines represent the fit for the ADPs according to Eqn. (1) and (2), while the dashed line is the linear fit for the lattice parameters. Lower panel: atom coordination around atoms Ba1, Ba2 and Sb7 with ADPs from the SC refinement at RT. The open square symbol represents the vacancy in the 1b site.



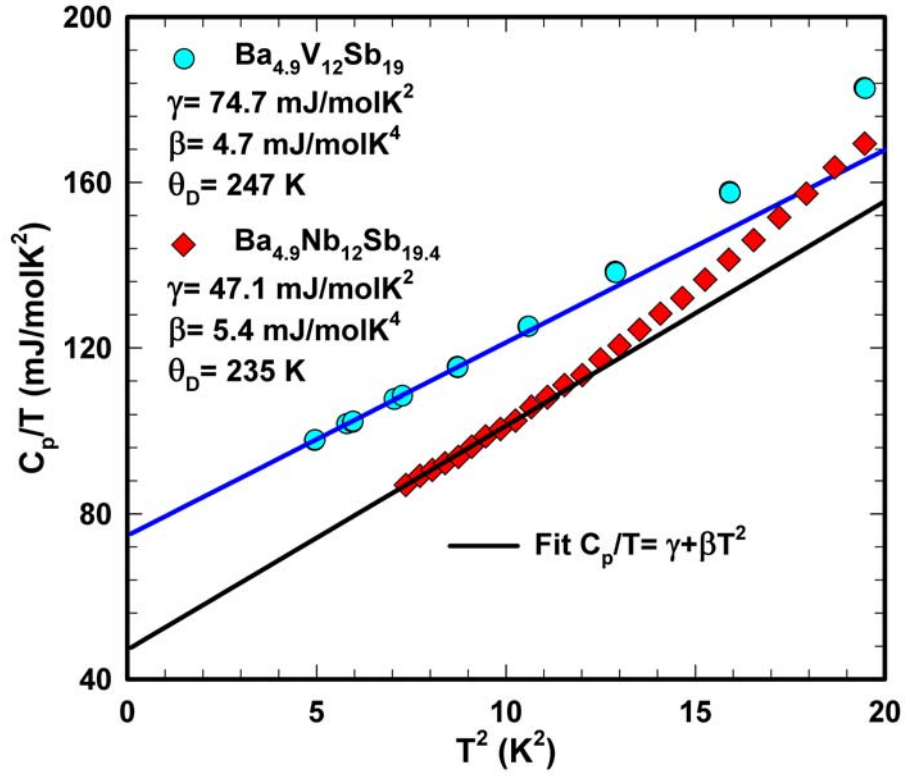


**Figure 10.** Low temperature specific heat  $C_p/T$  vs.  $T^2$  of polycrystalline  $Ba_5\{V,Nb\}_{12}Sb_{19+x}$  (composition from EPMA).

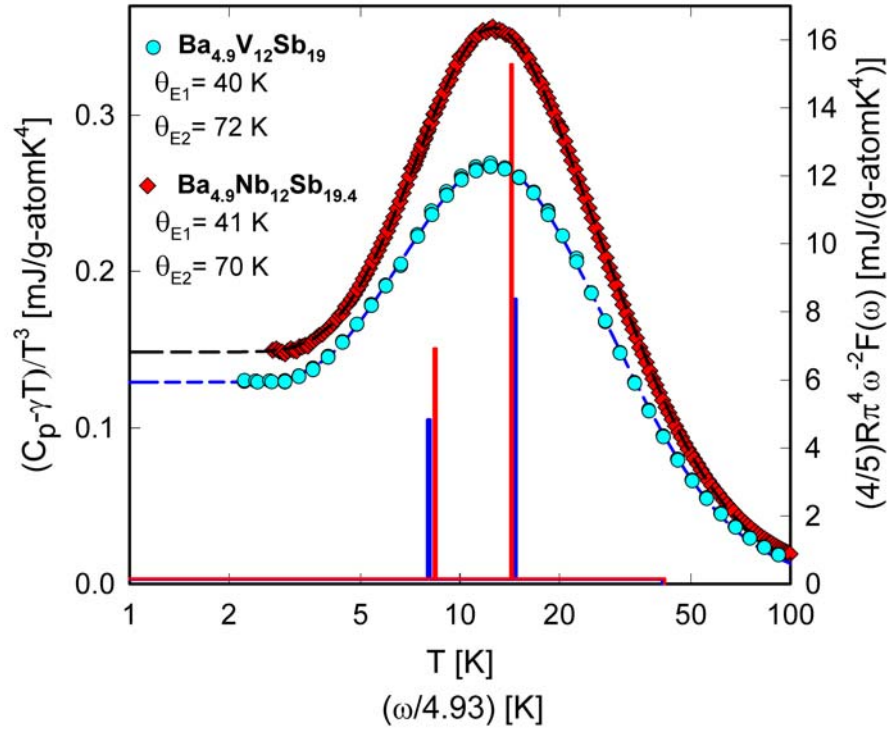


**Figure 11.** Junod fit (dashed lines) for the lattice contribution to the specific heat and the phonon density of states (solid lines) displayed as  $F(\omega)/\omega^2$  of  $Ba_5\{V,Nb\}_{12}Sb_{19+x}$  (composition from EPMA).

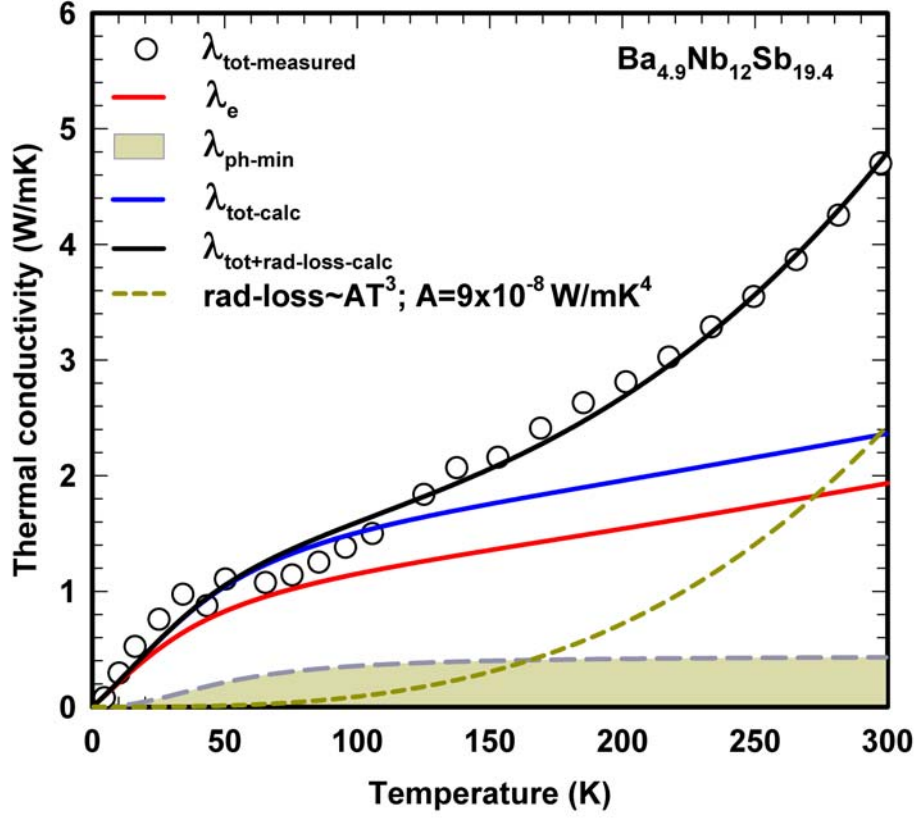


**Figure 12.** Temperature dependent thermal conductivity of  $\text{Ba}_{4.9}\text{Nb}_{12}\text{Sb}_{19.4}$ . The solid and the dashed lines are model curves as explained in the text.

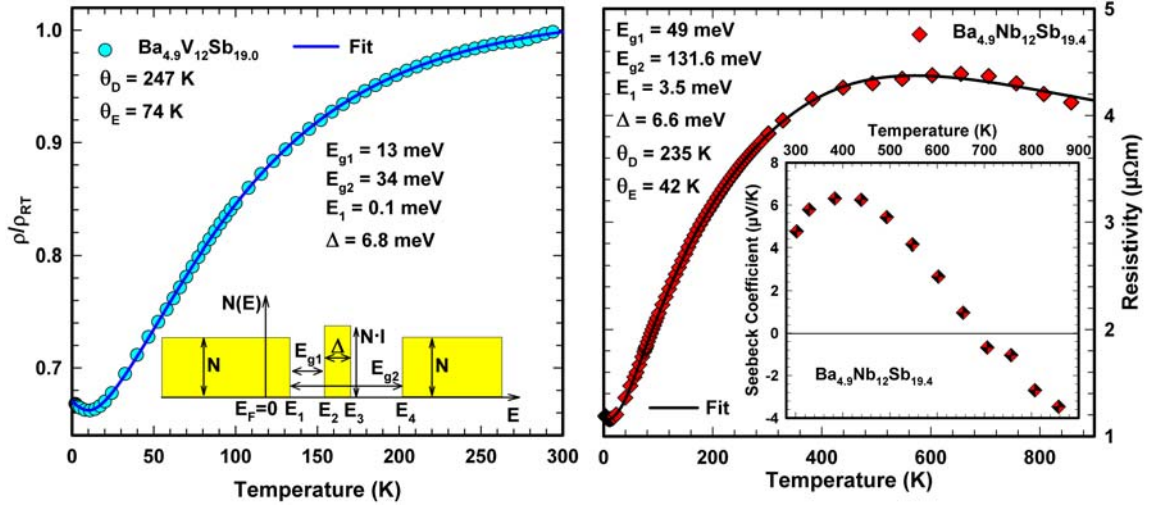


**Figure 13.** Temperature dependent electrical resistivity of  $\text{Ba}_5(\text{V},\text{Nb})_{12}\text{Sb}_{19+x}$  and high temperature Seebeck coefficient of  $\text{Ba}_{4.9}\text{Nb}_{12}\text{Sb}_{19.4}$ . Solid lines represent the least squares fit according to Eqn. 7 and Eqn. 8.

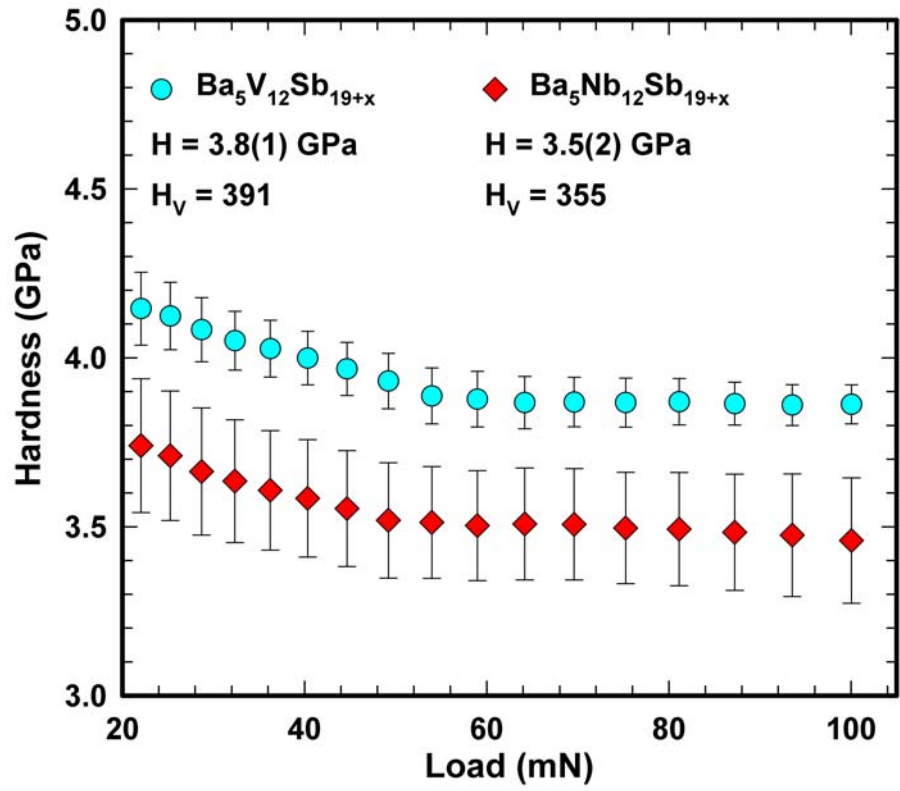
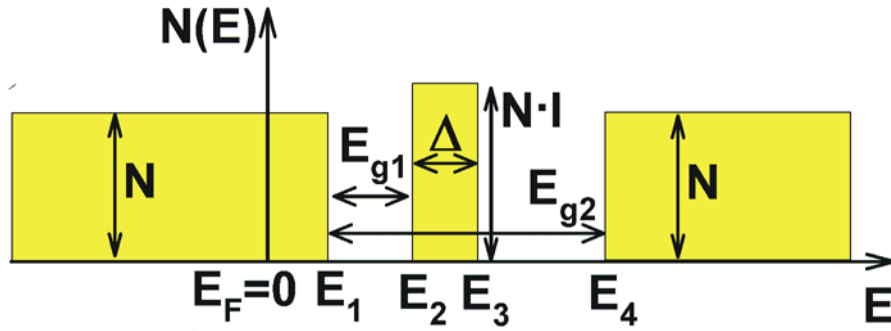


Figure 14. Load dependent hardness of  $\text{Ba}_5(\text{V},\text{Nb})_{12}\text{Sb}_{19+x}$ .

## Supplementary

### Derivation of model used for the electrical resistivity



$$N(E) = \begin{cases} N & E \leq E_1 \\ 0 & E_1 < E < E_2 \\ N \cdot I & E_2 \leq E \leq E_3 \\ 0 & E_3 < E < E_4 \\ N & E \geq E_4 \end{cases} \quad \begin{aligned} E_2 &= E_1 + E_{g1} \\ E_3 &= E_1 + E_{g1} + \Delta \\ E_4 &= E_1 + E_{g2} \end{aligned} \quad f(E) = \left[ 1 + \exp\left(\frac{E - E_F}{k_B T}\right) \right]^{-1}$$

$$n_e(T) = \int_{E_F=0}^{\infty} N(E) f(E) dE = N \left[ \int_{E_F=0}^{E_1} f(E) dE + \int_{E_4}^{\infty} f(E) dE + I \int_{E_2}^{E_3} f(E) dE \right]$$

$$= N \left[ \begin{aligned} & \left[ -E_{g2} - k_B T \ln \left( \exp \left( \frac{E_1}{k_B T} \right) + 1 \right) + k_B T \ln 2 + k_B T \ln \left( \exp \left( \frac{E_1 + E_{g2}}{k_B T} \right) + 1 \right) \right] \\ & + I \left[ \Delta + k_B T \ln \left( \exp \left( \frac{E_1 + E_{g1}}{k_B T} \right) + 1 \right) - k_B T \ln \left( \exp \left( \frac{E_1 + E_{g1} + \Delta}{k_B T} \right) + 1 \right) \right] \end{aligned} \right]$$

$$\begin{aligned} n_h(T) &= \int_{-\infty}^{E_F=0} N(E)(1-f(E))dE = N \int_{-\infty}^{E_F=0} (1-f(E))dE \\ &= N k_B T \ln 2 \end{aligned}$$

$$n_{ch}(T) = \sqrt{n_e(T)n_h(T)} + n_{ch}^0$$

$$\rho(T) = \frac{n_{ch}^0 (\rho_0 + \rho_{ph}(T))}{n_{ch}(T)}$$



## Chapter 5 The System Ce-Zn-Si for <33.3 at.% Ce: Phase Relations, Crystal Structures and Physical Properties

F. Failamani<sup>a</sup>, A. Grytsiv<sup>a,f</sup>, R. Podloucky<sup>a</sup>, H. Michor<sup>b</sup>, E. Bauer<sup>b,f</sup>, P. Broz<sup>c,d</sup>, G. Giester<sup>e</sup>,  
Peter Rogl<sup>a,f</sup>

<sup>a</sup>*Institute of Physical Chemistry, University of Vienna, Währingerstraße 42, A-1090 Vienna, Austria*

<sup>b</sup>*Institute of Solid State Physics, Vienna University of Technology, Wiedner Hauptstraße 8-10, A-1040 Vienna, Austria.*

<sup>c</sup>*Masaryk University, Faculty of Science, Department of Chemistry, Kotlarska 2, Brno 61137, Czech Republic.*

<sup>d</sup>*Masaryk University, Central European Institute of Technology, CEITEC, Kamenice 753/5, Brno 62500, Czech Republic.*

<sup>e</sup>*Institute of Mineralogy and Crystallography, University of Vienna, Althanstraße 14, A-1090 Vienna, Austria.*

<sup>f</sup>*Christian Doppler Laboratory for Thermoelectricity, Vienna University of Technology, Wiedner Hauptstraße 8-10, A-1040 Vienna, Austria.*

(RSC Advances (2015), 5(46), 36480-36497)

Contributions to this paper:

- F. Failamani : samples preparation and characterization, transport properties measurements and analysis, writing the paper
- A. Grytsiv : discussions, preliminary single crystal test, comments, proofreading
- R. Podloucky : DFT calculations, analysis and evaluation, comments, proofreading
- H. Michor : specific heat and magnetic susceptibility measurement and analysis, discussions, comments, proofreading
- P. Broz : DTA measurements in quartz crucible, discussions, proofreading
- G. Giester : single crystal data collection
- E. Bauer and P. Rogl: discussions, comments, proofreading

## Abstract

Phase equilibria of the system Ce-Zn-Si have been determined for the isothermal section at 600° for <33.3 at.% Ce by XRPD and EPMA. This partial section is characterized by the formation of five ternary compounds with homogeneity regions at constant Ce-content and partial substitution of Zn/Si:  $\tau_1$ -Ce<sub>7</sub>Zn<sub>21</sub>(Zn<sub>1-x</sub>Si<sub>x</sub>)<sub>2</sub> (unique type; 0.45≤x≤0.99),  $\tau_2$ -Ce(Si<sub>1-x</sub>Zn<sub>x</sub>)<sub>2</sub> (AlB<sub>2</sub>-type; 0.36≤x≤0.73),  $\tau_5$ -CeZn(Zn<sub>1-x</sub>Si<sub>x</sub>)<sub>2</sub> (CeNiSi<sub>2</sub>-type; 0.68≤x≤0.76),  $\tau_6$ -CeZn<sub>2</sub>(Si<sub>1-x</sub>Zn<sub>x</sub>)<sub>2</sub> (ThCr<sub>2</sub>Si<sub>2</sub>-type; 0.25≤x≤0.30) and  $\tau_7$ -Ce<sub>37</sub>Zn<sub>48</sub>Si<sub>15</sub> (structure unknown). Whereas  $\tau_1$ ,  $\tau_2$  and  $\tau_5$  are stable at 600 and 800 °C, the phases  $\tau_6$ ,  $\tau_7$  are unstable at 800°C. Atom site distribution in the crystal structures of  $\tau_5$ ,  $\tau_6$  and the {La,Ce}<sub>7</sub>Zn<sub>21</sub>(Zn<sub>1-x</sub>Ge<sub>x</sub>)<sub>2</sub> have been elucidated from X-ray intensity refinements on single crystals. The small amounts of the stabilizing tetravalent element in {La,Ce}<sub>7</sub>Zn<sub>21</sub>[Zn<sub>1-x</sub>Si(Ge)<sub>x</sub>]<sub>2</sub> suggest a hypothetical binary phase “{La,Ce}<sub>7</sub>Zn<sub>23</sub>”. The stabilizing effect of Ge in Ce<sub>7</sub>Zn<sub>23-x</sub>Ge<sub>x</sub> has been elucidated from density functional theory (DFT) calculations discussing the electronic structure in terms of the density of states (DOS) and defining enthalpies of formation for Ce<sub>7</sub>Zn<sub>23-x</sub>Ge<sub>x</sub> (x=0, 0.5, 2) as well as for several neighbouring binary Ce-Zn phases. A Schultze-Scheil diagram for the solidification behaviour in the (Zn,Si)-rich part of the diagram was constructed from DTA measurements in closed silica crucibles along with partial isothermal sections determined in the temperature range from 400 to 900°C. The phases  $\tau_5$  and  $\tau_6$  both form in degenerate ternary peritectic reactions: L + CeSi<sub>2</sub>,β-Ce<sub>2</sub>Zn<sub>17</sub> ⇌  $\tau_5$  at 865±5°C and L +  $\tau_5$ ,CeZn<sub>11</sub> ⇌  $\tau_6$  at 695±5°C, respectively. Magnetic susceptibility, specific heat and resistivity measurements of  $\tau_5$ -CeZn(Zn<sub>1-x</sub>Si<sub>x</sub>)<sub>2</sub> revealed Kondo lattice behavior with ferromagnetic ordering below T<sub>C</sub>=4.4 K, whereas susceptibility and specific heat studies of  $\tau_6$ -CeZn<sub>2</sub>(Zn<sub>0.28</sub>Si<sub>0.72</sub>)<sub>2</sub> revealed Curie-Weiss paramagnetic behaviour down to 3 K. The effective paramagnetic moments of Ce obtained from Curie-Weiss fits of  $\tau_5$  (2.50 μ<sub>B</sub>) and  $\tau_6$  (2.34 μ<sub>B</sub>) reveal a ground state close to trivalent Ce.

## 1. Introduction

Ternary compounds Ce-T-Si (T is one of the late transition metals) have been known for their interesting physical properties, such as heavy fermion and unconventional superconductors,<sup>1,2</sup> Kondo-behaviour and quantum criticalities,<sup>3</sup> intermediate valency,<sup>4</sup> thermoelectric features,<sup>5</sup> etc. Most ternary Ce-T-Si systems have been explored,<sup>6</sup> except for group 12 elements (Zn, Cd, Hg). The high vapor pressure of these metals complicates sample preparation, and requests careful control of compositions. Therefore conventional

preparation methods such as arc melting or induction melting in open crucibles cannot be used. However, a few investigations were already concerned with the Ce-Zn-Si system. Kido et al.<sup>7</sup> reported paramagnetism and metallic behavior of REZnSi compounds (RE = Ce, Nd, Sm, Gd, Tb, Ho) in the temperature range of 77-300 K. Recently, phase equilibria for the Ce-Zn-Si system have been derived at 800°C by Malik et al.<sup>8</sup> and revealed the existence of 4 ternary compounds, labeled as  $\tau_1$  to  $\tau_4$ . Whilst the crystal structures of  $\tau_1$  and  $\tau_2$  and their La-homologues have been elucidated from single crystal X-ray data, the crystal structures of the other compounds remained unresolved. A recent study of RE<sub>7</sub>Zn<sub>21</sub>Tt<sub>2</sub>-phases (Tt is a tetrel element) by Nian-Tzu Suen and Bobev<sup>9</sup>, prompted among other rare earth elements (La-Nd) the formation of novel cerium compounds Ce<sub>7</sub>Zn<sub>21</sub>{Ge,Sn,Pb}<sub>2</sub> crystallizing with the structure type first determined by Malik et al.<sup>8</sup> for {La,Ce}<sub>7</sub>Zn<sub>21</sub>(Zn<sub>1-x</sub>Si<sub>x</sub>)<sub>2</sub>. In their latest publication, they also investigated the single crystals of {Ce-Pr}<sub>7</sub>Zn<sub>21</sub>(Zn<sub>1-x</sub>Si<sub>x</sub>)<sub>2</sub> and their magnetic properties.<sup>10</sup> Their result, especially on the crystal structure of Ce<sub>7</sub>Zn<sub>21.95</sub>Si<sub>1.05</sub> confirms the work of Malik et al.<sup>8</sup>

The absence of ternary compounds in the Ce-poor part (< 33 at.% Ce) of the isothermal section Ce-Zn-Si seems unusual, particularly ternary compounds with ThCr<sub>2</sub>Si<sub>2</sub> structure or derivative types are encountered in most Ce-T-Si systems (T is a transition metal from Cr to Cu).<sup>11</sup> Therefore also the possibility of compound formation at lower temperature needs to be explored. Indeed the investigation of the Zn/Si-rich part of the Ce-Zn-Si phase diagram at 800°C<sup>8</sup> revealed hints for a ternary compound (labelled as  $\tau_5$ ) with composition close to Ce(Zn<sub>1-x</sub>Si<sub>x</sub>)<sub>3</sub>; x $\approx$ 0.5. Our further attempts to investigate this phase at 700°C prompted another ternary compound (labelled as  $\tau_6$ ) with composition of Ce<sub>20</sub>Zn<sub>53</sub>Si<sub>27</sub>, which is also formed from the melt. An electron count on  $\tau_5$ -CeZn<sub>1.5</sub>Si<sub>1.5</sub>, considering the valencies of Ce = +3, Zn = +2 and Si = -4 yields balanced electronic charges suggesting a Zintl behaviour interesting for thermoelectric application.

Therefore this work focuses on the investigation of phase equilibria and crystal structures of  $\tau_5$  and  $\tau_6$ , as well as their mechanism of formation and stability. Furthermore the magnetic ground state of cerium in these compounds was of interest. Particularly the small amount of tetrel elements (Tt) to stabilize {La,Ce}<sub>7</sub>Zn<sub>21</sub>(Zn<sub>1-x</sub>Tt<sub>x</sub>)<sub>2</sub> was investigated by DFT calculations for Tt=Ge to get insight into the electronic DOS, bonding behavior and ground state energies of hypothetical binary Ce<sub>7</sub>Zn<sub>23</sub> in comparison with ternary Ce<sub>7</sub>Zn<sub>23-x</sub>Ge<sub>x</sub> (x=0.5, 2).

## 2. Experimental Methods and Density Functional Theory Calculation

Most samples were prepared by mixing and cold pressing proper blends of ball milled powders of  $\text{CeSi}_x$  master alloys with Zn filings inside an Ar filled glove box. Master alloys  $\text{CeSi}_x$  were prepared by argon arc melting of Ce and Si pieces on a water-cooled copper hearth with a tungsten electrode, while Zn filings were prepared from purified Zn drops. Samples in the Zn-rich corner were then sealed under vacuum or argon and annealed at 600°C for 4 to 14 days. Samples with low Si(Ge) content (close to binary Ce-Zn) were prepared in a different way. Ce filings, Zn filings, and Si(Ge) powder were mixed in proper ratio, cold pressed, sealed and then subjected to the same heat treatment. All starting materials had a purity of better than 99.9 mass%.

After heat treatment, samples were quenched by submersing the quartz capsules in cold water and analyzed by X-ray powder diffraction with Ge-monochromated  $\text{CuK}\alpha_1$ -radiation employing a Guinier-Huber image plate recording system. X-ray powder diffraction analyses were performed via Rietveld refinement using the FULLPROF program.<sup>12</sup> Precise lattice parameters were determined referring to Ge as internal standard ( $a_{\text{Ge}} = 0.565791$  nm). Special treatments were needed to prepare samples for Electron Probe Microanalysis (EPMA) due to their powder-like consistency. Coarse powders of samples were mixed and cold pressed with fine powders of conductive resin in a small steel die (5-6 mm in diameter) prior to hot compacting them together into a coarse powder/granule of conductive resin. Samples were ground and polished under glycerin in order to avoid oxidation and/or hydrolysis. Microstructures and compositions were examined by light optical microscopy (LOM) and scanning electron microscopy (SEM) and EPMA on a Zeiss Supra 55 VP equipped with an energy dispersive X-ray analysis (EDX) detector operated at 20 kV.

Single crystals of  $\tau_5$  and  $\tau_6$  were grown from Zn flux. Powders of a multiphase alloy with nominal composition  $\text{Ce}_{20}\text{Zn}_{50}\text{Si}_{30}$  were mixed and cold pressed with Zn filings in a weight ratio of 1:45 and 1:57 for  $\tau_5$  and  $\tau_6$ , respectively. The sample billets were sealed under vacuum in quartz capsules, heated to 800°C, kept at this temperature for 1 hour, and were then slowly cooled with a rate of 6°C/h to 735°C and 670°C for  $\tau_5$  and  $\tau_6$ , respectively. After quenching in cold water, the Zn flux matrix was dissolved in cold diluted HCl. No reaction of the single crystal material with HCl was observed during leaching.

Single crystals of  $\{\text{La,Ce}\}_7\text{Zn}_{21}(\text{Zn}_{1-x}\text{Ge}_x)_2$  were prepared from cold pressed mixtures of La/Ce filings, Zn filings and Ge powder with nominal composition of  $\text{La}_{25}\text{Zn}_{73}\text{Ge}_2$  and

Ce<sub>25</sub>Zn<sub>70</sub>Ge<sub>5</sub>, respectively. The Ce-containing pellet was sealed under vacuum into a quartz ampoule, heated to 600°C with a rate of 60°C/h, kept at this temperature for 12 hrs, further heated to 1050°C at 600°C/h, and then slowly cooled to 800°C with a rate of 10°C/h. A slightly different heat treatment was performed to grow single crystals of La<sub>7</sub>Zn<sub>21</sub>(Zn<sub>1-x</sub>Ge<sub>x</sub>)<sub>2</sub> heating the pellet to 600°C at 60°C/h, keeping this temperature for 12 hrs, followed by further heating to 900°C at a rate of 600°C/h, resting at this temperature for 30 minutes, and then slowly cooling to 800°C at a rate of 6°C/h. Single crystals were then mechanically isolated and selected from the crushed regulus.

Inspections on an AXS D8-GADDS texture goniometer assured high crystal quality, unit cell dimensions and Laue symmetry of the single crystal specimens prior to X-ray intensity data collections at room temperature on a Bruker APEXII diffractometer equipped with a CCD area detector and an Incoatec Microfocus Source I $\mu$ S (30 W, multilayer mirror, Mo-K $\alpha$ ,  $\lambda$  = 0.071069 nm). Orientation matrices and unit cell parameters were derived using the Bruker APEXII software suite.<sup>13</sup> No additional absorption corrections were performed because of the rather regular crystal shapes and small dimensions of the investigated specimens. The structures were solved by direct methods (SHELXS-97) and were refined with the SHELXL-97<sup>14</sup> program within the Windows version WINGX.<sup>15</sup> Crystal structure data were standardized using program STRUCTURE-TIDY.<sup>16</sup>

In order to investigate the thermal stability of  $\tau_5$  and  $\tau_6$  and to determine the corresponding ternary reaction isotherms, DTA measurements were performed using a Netzsch STA 409 CD/3/403/5/G apparatus. Due to the high vapor pressure of Zn, measurements were performed in closed thin-walled quartz crucibles. Single-phase material of  $\tau_5$  and  $\tau_6$  was measured from room temperature to 900°C with a heating/cooling rate of 5°C/min. Isothermal annealing served to confirm the phase fields related to the four-phase reactions observed in DTA: for this purpose two alloys in the Zn rich part with nominal compositions, Ce<sub>5.9</sub>Zn<sub>59.8</sub>Si<sub>34.3</sub> and Ce<sub>7.6</sub>Zn<sub>78.4</sub>Si<sub>14</sub>, were prepared from powders of CeSi<sub>x</sub> and Zn filings and annealed at 500°C for 4 days. After first reaction, the alloys were powderized to a grain size below 53  $\mu$ m inside the glove box and were then cold compacted in a steel die (diameter=10 mm). The pellets were dry-cut into several pieces and sealed in quartz tubes under about 300 mbar Ar and annealed at 400°C, 650°C, 710°C, 750°C, 770°C, 790°C, 810°C, 850°C, 860°C, 870°C, 880°C and 900°C for 1 day each. Single phase samples of  $\tau_5$  and  $\tau_6$  were prepared in a similar way. The second annealing temperature was 700 and 600 °C for  $\tau_5$  and  $\tau_6$ , respectively. The furnaces were calibrated with standard thermocouples and Sb (melting point = 631°C).

Dc magnetic susceptibility measurements were performed with a SQUID magnetometer for  $\tau_5$  and  $\tau_6$  from 2-300 K with various magnetic fields from 0.006 to 6 T on freely rotating single crystals with a total mass of 0.80 mg (individual crystals with a typical mass of 100  $\mu$ g) and on sintered polycrystalline samples of about 20 mg. Ac susceptibility measurements were carried out on sintered polycrystalline samples of about 200 mg with a Lakeshore 7000 ac susceptometer applying an ac-field with amplitude of 325 A/m and a frequency of 100 Hz. Specific heat measurements were performed on a commercial Quantum Design PPMS calorimeter on a sintered  $\tau_6$  sample and on  $\tau_5$  single crystals. Parts of a sintered sample of  $\tau_5$  were also used for resistivity and Seebeck coefficient measurements. Resistivity measurements were performed from 2-300 K in a home-made equipment using the ac bridge resistance technique, while the high temperature part (300-673 K) was measured simultaneously with the Seebeck coefficient in a ZEM-3 ULVAC. The density functional theory (DFT) calculations were performed by using the Vienna ab initio simulation package (VASP)<sup>17,18</sup> and applying the pseudopotential construction according to the projector-augmented-wave method.<sup>19</sup> For the exchange-correlation functional the generalized gradient approximation according to Perdew et al. (PBE)<sup>20</sup> was chosen. The VASP calculations were done with high precision using the predefined/default values as provided by the VASP package. The energy cutoff was chosen at 350 eV. Spin polarized calculations were done assuming ferro/ferrimagnetic ordering. For the  $\mathbf{k}$  space integration the Gaussian smearing method with a value for  $\sigma$  of 0.1 eV was taken.  $\mathbf{k}$  space grids were constructed by the method outlined in Ref. 21, namely 11 $\times$ 11 $\times$ 11 for CeZn; 7 $\times$ 5 $\times$ 5 for Ce<sub>4</sub>Zn<sub>8</sub> (CeZn<sub>2</sub>); 7 $\times$ 3 $\times$ 5 for Ce<sub>4</sub>Zn<sub>12</sub> (CeZn<sub>3</sub>); 3 $\times$ 3 $\times$ 7 for Ce<sub>14</sub>Zn<sub>46</sub> (Ce<sub>7</sub>Zn<sub>23</sub>) and related compounds; 7 $\times$ 3 $\times$ 2 for Ce<sub>6</sub>Zn<sub>22</sub> (Ce<sub>3</sub>Zn<sub>11</sub>). No additional many-body treatment was made for the localized character of the f-like states of Ce, since the compounds under study are all in a metallic state with f-occupation of  $\sim 1$  per Ce atom. PBE is considered to reasonably capture the localization properties in terms of spin-polarization as it does for 3d transition metals. Assuming the experimental structure as starting point for all cases, the atomic positions as well as the unit cell parameters were fully relaxed. The Ge substitution was made according to Table 3 at the experimentally defined M1 sites.

### 3. Results and Discussions

#### 3.1. Binary boundary systems

The Zn-Si system (calculated) and the Ce-Zn system were accepted after Massalski<sup>22</sup> taking also into account a more recent investigation on the low temperature modification of  $\alpha\text{Ce}_2\text{Zn}_{17}$  ( $\alpha\text{Ce}_{1-x}\text{Zn}_{5+2x}$ ) with TbCu<sub>7</sub>-type.<sup>23</sup> For the Ce-Si system we rely on the version of Malik et al.,<sup>8</sup> which essentially is based on the investigation by Bulanova et al.<sup>24</sup> but also includes further phases such as  $\text{Ce}_2\text{Si}_{3-x}$ <sup>25</sup> and the high pressure phases  $\text{CeSi}_5$  and  $\text{Ce}_2\text{Si}_7$ .<sup>26</sup> The La-Zn system was taken from the latest experimental investigation by Berche et al.<sup>27</sup> with recent data on the crystal structure of  $\text{LaZn}_4$ .<sup>28</sup> Detailed crystallographic data for unary and binary boundary phases are summarized in Table S1 (Supporting Information), those for ternary compounds are listed in Table 1, respectively.

#### 3.2. Crystal structure of ternary compounds in the Ce-Zn-Si system

##### 3.2.1. Crystal structure of $\tau_5\text{-CeZn}(\text{Zn}_{1-x}\text{Si}_x)_2$ , $x = 0.71$

The X-ray diffraction pattern of a suitable flux grown single crystal of  $\tau_5$  was fully indexed in orthorhombic symmetry ( $a = 0.42079(1)$ ,  $b = 1.76522(3)$ ,  $c = 0.41619(1)$  nm). Analysis of systematic extinctions suggested three possible space group types  $Cmcm$ ,  $Cmc2_1$ ,  $C2cm$  (non-standard setting) and consequently structure solution employing direct methods was attempted in the space group type  $Cmcm$  of highest symmetry (see Table 2). In order to find mixed Zn/Si sites, refinements were first performed with Ce and Zn only. Two of the three Zn sites (M1, M2) were found to have an unusually high atomic displacement parameter (ADP), indicating partial substitution by Si atoms.

Further refinement with anisotropic ADPs for all atoms converged to  $R_F = 0.020$  and residual electron densities smaller than  $\pm 3.04 \text{ e}^-/\text{\AA}^3$ . The final formula obtained,  $\text{CeZn}(\text{Zn}_{1-x}\text{Si}_x)_2$  with  $x = 0.71$  corresponds to the composition  $\text{Ce}_{25.0}\text{Zn}_{39.7}\text{Si}_{35.3}$  (in at.%), which perfectly fits to the value derived from EPMA ( $\text{Ce}_{24.9}\text{Zn}_{39.6}\text{Si}_{35.5}$ ). Details on crystal data along with ADPs are summarized in Table 2. A Rietveld X-ray powder diffraction refinement confirms the structure model for  $\tau_5$ . Furthermore, lattice parameters, crystal symmetry, and Wyckoff positions proved that this compound is isotypic with the structure type of  $\text{CeNiSi}_2$  (see Figure 1).

Interatomic distances are given in Table S2 (Supporting Information). Comparing atom distances with the sum of atomic radii, direct bonding is neither revealed between M1-Zn3 nor for M2-M2. However, stronger bonding is inferred from the distances among M1-M1, M1-M2 and M2-Zn3 atoms, particularly taking into account the Zn/Si random occupancy.

At 600°C the phase  $\tau_5\text{-CeZn}(\text{Zn}_{1-x}\text{Si}_x)_2$  exhibits a compositional range,  $0.68 \leq x \leq 0.76$ , excluding any stoichiometric composition (for details see section 3.4).

Compounds with the  $\text{CeNiSi}_2$  type are known in many Ce-T-Si systems (T = Fe to Cu, Rh, Ir, Pt, and Sn) and exist in both stoichiometric and non-stoichiometric forms.<sup>11</sup> For  $\tau_5\text{-CeZn}(\text{Zn}_{1-x}\text{Si}_x)_2$ , however, only the non-stoichiometric composition could be found, whereas the Ce-Cu-Si system,<sup>29</sup> which is the closest homologous system, contains two individual phases of same symmetry (isotypic with  $\text{CeNiSi}_2$ ), namely  $\text{CeCu}_{1.6}\text{Si}_{1.4}$  ( $\equiv \text{CeCu}(\text{Cu}_{0.6}\text{Si}_{0.4})\text{Si}$ ) and stoichiometric  $\text{CeCu}_2\text{Si}_2$ , both separated by a two-phase equilibrium:  $\text{Ce}(\text{Cu}_{1-x}\text{Si}_{1+x})_2$  ( $\text{AlB}_2$ -type) +  $\text{CeCu}_2\text{Si}_2$ . It should be noted that the atom preference in the mixed sites in  $\tau_5\text{-CeZn}(\text{Zn}_{0.26}\text{Si}_{0.74})(\text{Zn}_{0.31}\text{Si}_{0.69})$  - where Zn/Si randomly fill two 4c-sites with  $y=0.03338(5)$  and  $y=0.16921(5)$  - differs from non-stoichiometric  $\text{CeCu}(\text{Cu}_{0.6}\text{Si}_{0.4})\text{Si}$  where Cu and Si atoms only share the 4c-site with  $y=0.038$ . However, we have to note here that the reliability of the X-ray single crystal study on photographs for  $\text{CeCu}_{1.6}\text{Si}_{1.4}$  is low, as  $R_F$  was only 17.7%.<sup>30</sup> The discussion on  $\text{TbFe}_{0.5}\text{Si}_2$  being a site exchange variant of the  $\text{CeNiSi}_2$ -type has been solved from neutron diffraction data on  $\text{HoFe}_{0.5}\text{Si}_2$ ,<sup>31</sup> which clearly revealed isotypism with the  $\text{CeNiSi}_2$ -type. From the good correspondence of the composition refined from X-ray data with the composition derived from EDX, we can safely conclude that the structure of  $\tau_5\text{-CeZn}(\text{Zn}_{1-x}\text{Si}_x)_2$  does not contain any defect sites like  $\text{HoFe}_{0.5}\text{Si}_2$ .

### 3.2.2. Crystal structure of $\tau_6\text{-CeZn}_2(\text{Si}_{1-x}\text{Zn}_x)_2$ , $x = 0.3$

Complete indexation of the X-ray single crystal diffraction data for  $\tau_6$  prompted a tetragonal unit cell. The systematic analysis of extinctions suggested  $I4$ ,  $I\bar{4}$ ,  $I4/m$ ,  $I422$ ,  $I4mm$ ,  $I\bar{4}2m$ ,  $I\bar{4}m2$  and  $I4/mmm$ , as possible space group types. Structure solution and refinement employing direct methods in the highest symmetry space group type  $I4/mmm$  converged to  $R_F = 0.008$  with residual electron densities smaller than  $\pm 0.81 \text{ e}^-/\text{\AA}^3$ . Details on crystal data along with ADPs are summarized in Table 2. Unit cell parameters, crystal symmetry, and Wyckoff sites confirm isotypism with the  $\text{ThCr}_2\text{Si}_2$  structure type (see Figure 2).

The final structure formula,  $\text{CeZn}_2(\text{Si}_{1-x}\text{Zn}_x)_2$  with  $x=0.30$ , reveals one Zn/Si mixed atom site ( $M = 0.30\text{Zn}_2 + 0.70 \text{ Si}$  in  $4e$ ;  $0,0,z$ ), which in many cases provides close contacts among the tetrel elements (dumbbell formation).<sup>32</sup> The formula ( $\text{Ce}_{20.1}\text{Zn}_{51.8}\text{Si}_{28.1}$ , in at.%) perfectly fits to the value derived from EDX:  $\text{Ce}_{20.0}\text{Zn}_{52.0}\text{Si}_{28.0}$ .



Interatomic distances are given in Table S2 (Supporting Information). As the M-site is mainly occupied by Si, distances M-M and M-Zn1 are much smaller than distances Zn1-Zn1. Taking into account the random occupancy Zn/Si in the 4e site, the M-M distance is smaller than the sum of radii<sup>33</sup> and is a good indication for dumbbell formation. Comparing the M-M and M-Zn1 distances with those in  $\text{YbZn}_2(\text{Si}_{1-x}\text{Zn}_x)_2$ ;  $x=0.25$ ,<sup>34</sup> which is hitherto the only far off-stoichiometric  $\text{REZn}_2\text{Si}_2$  crystallizing in the  $\text{ThCr}_2\text{Si}_2$  type, no significant difference can be found. Consistent with the mixed atom site,  $\tau_6\text{-CeZn}_2(\text{Si}_{1-x}\text{Zn}_x)_2$  exists at 600°C in a small homogeneity range  $0.25 \leq x \leq 0.30$  (for details see section 3.4). Similar to  $\tau_5$  also the phase  $\tau_6$  does not include the stoichiometric composition  $\text{CeZn}_2\text{Si}_2$ , although first row transition metals mostly form ordered, stoichiometric compounds  $\text{CeT}_2\text{Si}_2$  ( $T = \text{Cr to Cu}$ ), some with only a small deviation from 1:2:2 stoichiometry.

### 3.2.3. Crystal structures of $\text{Ce}_7\text{Zn}_{21}(\text{Zn}_{1-x}\text{Ge}_x)_2$ $x = 0.75$ and $\text{La}_7\text{Zn}_{21}(\text{Zn}_{1-x}\text{Ge}_x)_2$ , $x = 0.10$

In a previous investigation Malik *et al.*<sup>8</sup> found that a surprisingly small amount of only 2 at.% Si was able to stabilize the ternary compound  $\tau_1\text{-Ce}_7\text{Zn}_{21}(\text{Zn}_{1-x}\text{Si}_x)_2$  ( $x=0.28$ , unique structure type) at 800 °C. X-ray single crystal analysis proved  $\text{La}_7\text{Zn}_{21}(\text{Zn}_{1-x}\text{Si}_x)_2$  ( $x=0.27$ ) to be isotypic.<sup>8</sup> Some controversy exists between the recently reported formation of  $\text{Ce}_7\text{Zn}_{21.3}\text{Ge}_{1.7}$ <sup>9</sup> (isotypic with  $\text{Ce}_7\text{Zn}_{21}(\text{Zn}_{1-x}\text{Si}_x)_2$ ) and the investigation of the isothermal section of the homologous system Ce-Zn-Ge at 470 K by Opainich,<sup>35</sup> who did not observe any compound near a composition  $\text{Ce}_7\text{Zn}_{21}\text{Ge}_2$ . In order to dissolve the controversy it seemed of interest to test the formation of Ge-homologues  $\{\text{La,Ce}\}_7\text{Zn}_{21}(\text{Zn}_{1-x}\text{Ge}_x)_2$  as well as the extent of their homogeneity regions. Indeed microprobe analyses confirmed that in both systems  $\{\text{La,Ce}\}\text{-Zn-Ge}$  a phase exists with composition close to the RE-Zn boundary:  $\text{La}_{23.3}\text{Zn}_{71.6}\text{Ge}_{5.1}$  and  $\text{Ce}_{23.3}\text{Zn}_{71.7}\text{Ge}_{5.0}$  (in at.%; see Figure 3 b,c).

Indexing of the X-ray diffraction data from a suitable single crystal of  $\text{Ce}_7\text{Zn}_{21}(\text{Zn}_{1-x}\text{Ge}_x)_2$  was complete for an orthorhombic unit cell corresponding to the structure type of  $\text{Ce}_7\text{Zn}_{21}(\text{Zn}_{1-x}\text{Si}_x)_2$ . The structure solution, employing direct methods in space group  $Pbam$  with the highest symmetry, compatible with the set of systematic extinctions, resulted in the same atom arrangement as for  $\text{Ce}_7\text{Zn}_{21}(\text{Zn}_{1-x}\text{Si}_x)_2$ . Despite the small difference in the X-ray scattering power of Zn and Ge atoms, one mixed Zn/Ge site could unambiguously be identified from the rest of the fully occupied Zn sites. It is the same site as in the parent

$\text{Ce}_7\text{Zn}_{21}(\text{Zn}_{1-x}\text{Si}_x)_2$  type revealing a slightly smaller ADP and thus requests the presence of an atom with a slightly higher scattering power.

Even though it was possible to refine the occupancy of Zn/Ge (yielding 0.45(5)  $\text{Zn}_{1+0.55(5)}\text{Ge}_1$ ), the ratio Zn/Ge was fixed in accord with the composition obtained from EPMA (0.25  $\text{Zn}_{1+0.75}\text{Ge}_1$ ). A final refinement with anisotropic ADPs converged to  $R_F = 0.0215$  with a residual electron density less than  $1.7 \text{ e}/\text{\AA}^3$ . Detailed crystal data and atomic displacement parameters are summarized in Table 3. The structure refinement essentially confirmed the data obtained by Suen et al.<sup>9</sup> but here for an even lower Ge-content.

Although EPM analyses in the La-Zn-Ge system prompted a phase with composition of  $\text{La}_{23.3}\text{Zn}_{71.6}\text{Ge}_{5.1}$  (see Figure 3b), attempts to grow a single crystal with this Ge content were unsuccessful. However, for lower Ge-contents a suitable single crystal could be obtained (see Figure 3a). Following the same steps and arguments as for  $\text{Ce}_7\text{Zn}_{21}(\text{Zn}_{1-x}\text{Ge}_x)_2$ , structure solution and refinement of the single crystal data clearly showed isotypism with  $\text{Ce}_7\text{Zn}_{21}(\text{Zn}_{1-x}\text{Si}_x)_2$ . However, due to the low amount of Ge atoms in the unit cell, it was not possible to identify the Zn/Ge mixed site from the rest of the Zn sites. Therefore Ge atoms were placed at the corresponding Si-site as in  $\text{Ce}_7\text{Zn}_{21}(\text{Zn}_{1-x}\text{Si}_x)_2$  with the occupancy taken from EPMA ( $\text{La}_{23.3}\text{Zn}_{76.0}\text{Ge}_{0.7}$  in at.%).

Detailed crystal data and atomic displacement parameters are listed in Table 3. As expected from the isotypism with  $\text{Ce}_7\text{Zn}_{21}(\text{Zn}_{1-x}\text{Si}_x)_2$ , the atomic arrangement in  $\{\text{La,Ce}\}_7\text{Zn}_{21}(\text{Zn}_{1-x}\text{Ge}_x)_2$  also gives a similar zig-zag chain of distorted  $\text{AuCu}_3$  and  $\text{BaAl}_4$  blocks along the b-axis (see Figure 4). This arrangement is similar to  $\text{Ce}_3\text{Zn}_{11}$  with  $\text{La}_3\text{Al}_{11}$ -type, which is the neighbouring phase of  $\text{Ce}_7\text{Zn}_{21}(\text{Zn}_{1-x}\text{Ge}_x)_2$ . Due to the comparable size of Zn and Ge atoms, no significant difference could be found in the interatomic distances between fully occupied Zn and mixed Zn/Ge sites.

The amount of Ge necessary to stabilize the ternary compounds  $\{\text{La,Ce}\}_7\text{Zn}_{21}(\text{Zn}_{1-x}\text{Ge}_x)_2$  is even less than for isotypic  $\{\text{La,Ce}\}_7\text{Zn}_{21}(\text{Zn}_{1-x}\text{Si}_x)_2$  and with less than 1 atom percent of Ge infers a rather small degree of thermodynamic instability for the hypothetical binary phases “ $\text{La}_7\text{Zn}_{23}$ ” and “ $\text{Ce}_7\text{Zn}_{23}$ ”.

### 3.3. Phase stability of $\text{Ce}_7\text{Zn}_{23-x}\text{Ge}_x$

#### 3.3.1. DFT phase stabilities

The enthalpy of formation  $\Delta H_{\text{DFT}}$  at  $T=0 \text{ K}$  was derived from the DFT total energies  $E_{\text{DFT}}^{\text{tot}}$  as obtained from VASP according to:

$$\Delta H_{\text{DFT}}(\text{Ce}_x\text{Zn}_{1-x}) = E_{\text{DFT}}^{\text{tot}}(\text{Ce}_x\text{Zn}_{1-x}) - (xE_{\text{DFT}}^{\text{ref}}(\text{Ce}) + (1-x)E_{\text{DFT}}^{\text{ref}}(\text{Zn})) \quad (1)$$

As reference energies of the pure phases we defined:

$$E_{\text{DFT}}^{\text{ref}}(\text{Ce}) = E_{\text{DFT}}^{\text{tot}}(\text{Ce}) - E_{\text{adj}}(\text{Ce}), \text{ and } E_{\text{DFT}}^{\text{ref}}(\text{Zn}) = E_{\text{DFT}}^{\text{tot}}(\text{Zn}) - E_{\text{adj}}(\text{Zn}) \quad (2)$$

The DFT energies for the pure phases were calculated for solid nonmagnetic  $\alpha$ -fcc-Ce and solid hcp-Zn. It was necessary to adjust the reference energies by  $E_{\text{adj}}(\text{Ce})$  and  $E_{\text{adj}}(\text{Zn})$  for a direct comparison with the results of the thermodynamic modeling of Wang et al.,<sup>36</sup> and experimental work by Chiotti et al.<sup>37</sup> and Johnson et al.,<sup>38</sup> because of the choice of different reference ground states. Then the values for  $E_{\text{adj}}$  were extracted by linearly fitting the DFT results (column DFT in Table 4) to the thermodynamic modeling data (column "model") for the four given compounds, and by that  $E_{\text{adj}}(\text{Ce}) = 27.87$  and  $E_{\text{adj}}(\text{Zn}) = 4.38 \text{ kJ mol}^{-1}$  were obtained.

Table 4 summarizes results of the DFT calculations. The DFT derived adjusted enthalpy of formation compares very well with data of the thermodynamic modelling by Wang et al.<sup>36</sup> Concerning magnetic properties, as taken from the listed magnetic moments, CeZn does not spin polarize, whereas for the other listed compounds  $\text{Ce}_x\text{Zn}_{1-x}$  the magnetic moment per Ce atom decreases with decreasing Ce content, starting with CeZn<sub>2</sub> which has the largest local moment per Ce atom of  $0.71 \mu_B$ . For (hypothetical) Ce<sub>14</sub>Zn<sub>46</sub> ( $x=0.23$ ) the local moment is still sizeable amounting to  $4.06 \mu_B$  for the total magnetic moment of the unit cell. Replacing Zn by Ge in Ce<sub>14</sub>Zn<sub>46-x</sub>Ge<sub>x</sub> strongly reduces the magnetic moment to less than  $0.07 \mu_B$  for  $x=1$ . The gain in spin-polarization energy is very small being about  $0.01 \text{ kJ/mol}$  /per Ce atom, which hints at a spin fluctuation system. If  $x=4$  than there is no spin polarization anymore.

The enthalpy of formation for  $\text{Ce}_x(\text{Ge,Zn})_{1-x}$  compounds was derived similarly to the procedure described above. As a reference, solid Ge was taken in its ground state in the diamond structure. Most noticeable for our study is the stability for the Ge-doped compounds. Even for one Ge atom per formula unit, Ce<sub>14</sub>Zn<sub>45</sub>Ge<sub>1</sub>,  $\Delta H_{\text{DFT}}$  is below the tie-line connecting neighboring Zn-compounds. Here we assume, that in fact the ternary system can be approximately described as a binary one (see Figure 5). Why Ge stabilizes the compound is analyzed in the following discussing the electronic structure in terms of the density of states (DOS).

### 3.3.2. DFT phase stabilities for $\text{Ce}_7\text{Zn}_{23-x}\text{Ge}_x$ ( $Z=2$ )

Panel (a) of Figure 6 presents the total and atom projected local DOS for  $\text{Ce}_{14}\text{Zn}_{45}\text{Ge}_1$ . The Fermi energy falls into a sharp uprise of the DOS, which clearly is attributed to the f-states of Ce. At lower energies the DOS is a mixture of Zn and Ce states depending on the energy region. The Ge-DOS features in the range  $-2.7 < E < -1 \text{ eV}$  indicate a more covalent bonding as compared to Zn, which is more pronounced in panel (b) of Figure 6 showing the local DOS per atom. There the Zn-like DOS is more uniformly spread out in the energy region shown.

The stabilization property of Ge-substitution can be understood by inspecting Figure 7 showing a reduction of the total DOS at Fermi energy when one Zn is replaced by Ge. This is mainly due to the reduction of the f-like DOS for  $\text{Ce}_{14}\text{Zn}_{45}\text{Ge}_1$ . The corresponding  $\gamma$  values of the electronic specific heat are 3.43 (DOS at  $E_F = 87.3$  states per eV for  $\text{Ce}_{14}\text{Zn}_{46}$ ) and 3.25  $\text{mJ mol}^{-1} \text{K}^{-2}$  (DOS at  $E_F = 82.7$  states per eV for  $\text{Ce}_{14}\text{Zn}_{45}\text{Ge}_1$ ) indicating poor metals. Analyzing the Ce-f states it turns out that the magnetic moments break down upon Ge substitution, which is responsible for the DOS reduction. The reduction is due to the destruction of the magnetic moment of Ce atoms in the 2c position, because these states are predominant at the Fermi energy for spin polarized  $\text{Ce}_{14}\text{Zn}_{46}$ . They carry the largest magnetic moment of all Ce atoms and are therefore the most localized f-states with the largest uprise of all f-DOSes and therefore the largest value at Fermi energy. For  $\text{Ce}_{14}\text{Zn}_{46}$  the local f-moments are 0.27, 0.21, and 0  $\mu_B$  for the 4-fold coordinated atoms, and 0.74  $\mu_B$  for the Ce atoms in the 2c position. The breakdown of the magnetic moment upon substitution indicates also a weaker localization and consequently the DOS at Fermi energy is lowered: this leads to the reduction of the total DOS and indicates the thermodynamic stabilization of  $\text{Ce}_{14}\text{Zn}_{45}\text{Ge}_1$ . Summarizing, the more pronounced covalent bonding between Ce and Ge seems to be the main factor for the stabilization. By substituting 4 Ge atoms the stabilization with respect to the tie-line is considerably enhanced.

### 3.4. Partial isothermal section at 600°C for less than 33.3 at% Ce

The partial isothermal section at 600°C in the Ce-poor part of the ternary system Ce-Zn-Si was established from EPMA and X-ray powder diffraction of about 45 alloys (see Figure 8). Considering the high stability of the phase  $\text{Ce}(\text{Si}_{1-x}\text{Zn}_x)_2$  with the  $\alpha\text{ThSi}_2$  type and the relatively slow reaction kinetic at 600°C (diffusion in cast alloys) the samples were prepared by powder metallurgical techniques i.e. via isothermal reaction synthesis starting

from compacts of powder/filings in order to ensure establishment of true phase relations at this temperature.

In addition to the ternary compounds  $\tau_1$ -Ce<sub>7</sub>Zn<sub>21</sub>(Zn<sub>1-x</sub>Si<sub>x</sub>)<sub>2</sub>,  $0.45 \leq x \leq 0.99$  and  $\tau_2$ -Ce(Si<sub>1-x</sub>Zn<sub>x</sub>)<sub>2</sub>,  $0.36 \leq x \leq 0.73$ , both established previously in the 800°C isothermal section (for details see ref. 8), three new phases, which previously were not encountered at 800°C<sup>8</sup>, were found to exist at 600°C:  $\tau_5$ -CeZn(Zn<sub>1-x</sub>Si<sub>x</sub>)<sub>2</sub>,  $\tau_6$ -CeZn<sub>2</sub>(Si<sub>1-x</sub>Zn<sub>x</sub>)<sub>2</sub>, and  $\tau_7$ -Ce<sub>37</sub>Zn<sub>48</sub>Si<sub>15</sub>. Moreover binary CeZn<sub>11</sub> enters the phase equilibria at 600°C. Similar to 800°C, solubility of Si is negligible for all binary compounds CeZn<sub>x</sub> with  $x > 2$ . Extended homogeneity regions were established for  $\tau_1$  and  $\tau_2$ , as well as for  $\tau_5$  and  $\tau_6$  (Table 1 for details see Table 5). The homogeneity range of  $\tau_1$ -Ce<sub>7</sub>Zn<sub>21</sub>(Zn<sub>1-x</sub>Si<sub>x</sub>)<sub>2</sub> becomes slightly smaller at 600°C as compared to 800°C. The maximum concentration of Si in this phase practically remained the same, while the minimum amount of Si required to stabilize this phase slightly increased from  $x = 0.28$  (1.9 at. % Si) at 800°C to  $x = 0.45$  (3.0 at. % Si) at 600°C. The homogeneity range of  $\tau_1$  at 800°C, studied by combination of XRPD, XRSC, and EPMA contradicts the claim of Hoos et al.<sup>10</sup> regarding 3.5 at.% Si as minimum amount of Si in this phase. The three-phase regions involving binary Ce-Zn phases with more than 75 at. % Zn at 600°C resemble those observed at 800°C.

Despite all these three-phase equilibrium triangles are narrow, we were able to prepare corresponding samples and to define by EPMA the composition of the equilibrium phases involved. Ternary phases Ce(Si<sub>1-x</sub>Zn<sub>x</sub>)<sub>2</sub> ( $\alpha$ -ThSi<sub>2</sub> type),  $\tau_2$ , and  $\tau_5$  that coexist in three-phase equilibria with binary CeZn<sub>x</sub> ( $x \geq 5$ ) crystallized in fine microstructures, which made quantitative analyses by EPMA unreliable. The fine grains could not be agglomerated even with longer annealing time (more than two weeks). Therefore the ternary phases Ce(Si<sub>1-x</sub>Zn<sub>x</sub>)<sub>2</sub> with  $\alpha$ -ThSi<sub>2</sub> type,  $\tau_2$ , and  $\tau_5$ , and their composition were determined via Rietveld refinement in combination with the compositional dependence of lattice parameters presented in Figure 9.

Microstructures of selected three-phase equilibria are given in Figure 10. Alloys in equilibrium with Si, which were prepared from CeSi<sub>x</sub> master alloys containing CeSi<sub>2</sub>, did not reach complete equilibrium even after re-powderization followed by hot pressing and/or long term annealing. Ce(Si<sub>1-x</sub>Zn<sub>x</sub>)<sub>2</sub>,  $x \leq 0.25$ , with  $\alpha$ -ThSi<sub>2</sub> type was always observed in those alloys. Moreover, long term annealing generally shifted the overall alloy composition due to unavoidable evaporation of Zn, especially for alloys in the Zn-rich corner. However, equilibrated samples were easily obtained in case binary Ce-Si precursors with Ce content above 40 at.% were used.

Table 5 summarizes data on composition and lattice parameters of all phases coexisting in equilibrium at 600°C. The only uncertainty concerns the maximal solubility of Si in binary CeZn<sub>2</sub>. Our various attempts to prepare samples in the corresponding three-phase region  $\tau_7 + \text{CeZn}_2 + \tau_1$  resulted in non-equilibrium alloys with about 5 at. % Si in the CeZn<sub>2</sub>-phase. It is noteworthy that the phase triangulation in this part of the phase diagram at 600°C is different from that established at 800°C<sup>8</sup> and this is essentially due to the formation of  $\tau_7$ . Thus, two three-phase regions:  $\text{Ce}(\text{Zn}_{1-x}\text{Si}_x)_2(\text{CeCu}_2\text{-type}) + \tau_2 + \tau_1$  and  $\text{Ce}(\text{Zn}_{1-x}\text{Si}_x)_2(\text{CeCu}_2\text{-type}) + \tau_2 + \tau_4$ , which were observed at 800°C are now changed into two three-phase regions:  $\tau_7 + \tau_2 + \tau_1$  and  $\tau_7 + \text{Ce}(\text{Zn}_{1-x}\text{Si}_x)_2(\text{CeCu}_2\text{-type}) + \tau_1$ , possibly due to the peritectoid formation of  $\tau_7$  ( $\tau_2 + \tau_4 + \text{Ce}(\text{Zn}_{1-x}\text{Si}_x)_2 \Leftrightarrow \tau_7$ ), and a U-type reaction ( $\tau_2 + \text{Ce}(\text{Zn}_{1-x}\text{Si}_x)_2 \Leftrightarrow \tau_1 + \tau_7$ ) in the temperature interval 600°C < T < 800°C.

### 3.5. Formation of $\tau_5$ and $\tau_6$ and partial Schulz-Scheil diagram

Due to the high melting point of cerium silicides  $\text{Ce}(\text{Si}_{1-x}\text{Zn}_x)_2$  and the high vapour pressure of Zn at elevated temperatures, it is difficult to obtain homogeneous cast alloys for the determination of the crystallization behaviour of alloys. On the other hand, the established isothermal section at 600°C shows that three-phase regions involved in equilibria with binary Ce-Zn compounds are very narrow and our attempts to equilibrate the samples at higher temperature resulted in a significant change of the overall compositions. Filling the ampoules with argon slightly suppressed the Zn losses, but even in this case samples were heterogeneous, which at first did not allow us to reliably determine the change in phase equilibria via annealing at different temperatures. This shift of the compositions during thermal treatment also hinders the interpretation of DTA. For instance, DTA measurements on single-phase  $\tau_5$  and  $\tau_6$  resulted in a sequence of several thermal effects that are difficult to reconcile with the phase triangulation. Investigation of the specimens after DTA by SEM/EDX showed that samples became heterogeneous and contained regions with different phases (see Figure 11). Reliable temperatures for isothermal reactions were only obtained for wide three-phase regions:  $\text{CeSi}_2 + \tau_5 + (\text{Si})$ ,  $\tau_5 + \tau_6 + (\text{Si})$ ,  $\tau_6 + \text{CeZn}_{11} + (\text{Si})$ ,  $\text{CeZn}_{11} + (\text{Zn}) + (\text{Si})$ . The temperatures of invariant reactions that correspond to these fields were derived as follows: 727°C, 634°C, 561°C and 412°C, respectively. These four isothermal reaction temperatures were confirmed by DTA from the Zn-rich sample that contains  $\tau_6$ , (Si), and  $\text{CeZn}_{11}$  (close to the tie line (Si) +  $\text{CeZn}_{11}$ ) (see Figure 12). After three DTA runs the sample contains additionally  $\tau_5$ , (Zn), and  $\text{CeSi}_2$ , which suggests incongruent formation of both  $\tau_5$  and  $\tau_6$ .

All invariant reactions determined are summarized in the Scheil reaction scheme in Figure 13 along with the partial isothermal sections (Figure 14) at temperatures between the thermal effects established by DTA. Selected microstructures of alloys are presented in Figure 15 and Figure 16. Comparing the phase equilibria at 500°C (Figure 14a) with those observed at 600°C (Figure 14b) we conclude on the existence of a transition type reaction  $U_1$  (561°C after DTA):  $L + \tau_6 \rightleftharpoons \text{CeZn}_{11} + (\text{Si})$ .

The characterization of sample  $\text{Ce}_{5.9}\text{Zn}_{59.8}\text{Si}_{34.3}$  shows that  $\tau_6$  coexists in equilibrium with (Si) and L(Zn) at 600°C (Figure 15a), however after annealing at 650°C  $\tau_6$  was not observed in this sample, instead  $\tau_5$  enters the equilibrium with L(Zn) and silicon (Figure 14c and Figure 15b). Such a change of phase equilibria requests another transition type reaction  $U_2$ :  $L + \tau_5 \rightleftharpoons \tau_6 + (\text{Si})$  to occur between 600 and 650°C (634° after DTA).

Although  $\tau_6$  was observed in the sample  $\text{Ce}_{7.6}\text{Zn}_{78.4}\text{Si}_{14}$  annealed at this temperature,  $\tau_6$  does not participate in the equilibria at 710°C (Figure 14d). It has to be noted that the microstructure of this sample contains four phases ( $\tau_6$ ,  $\tau_5$ ,  $\text{CeZn}_{11}$ , and L(Zn)), see Figure 16b) and one of these phases has to be considered as non-equilibrium phase. Comparing this microstructure with the three-phase structure ( $\tau_5$ ,  $\text{CeZn}_{11}$  and L(Zn)) obtained for this sample annealed at 750°C (Figure 16c) we may safely conclude that  $\tau_6$  is the non-equilibrium phase that forms during quenching from 710°C. On the other hand, the same sample annealed at 690°C showed only 3 phases ( $\tau_6$ ,  $\text{CeZn}_{11}$  and L(Zn)). Based on these observations, the invariant reaction for the formation of  $\tau_6$  is supposed to occur in the temperature range between 690 and 700°C (see Figure 13).

Three peritectic-type reactions may be responsible for the formation of this phase: (i)  $L + \tau_5 \rightleftharpoons \tau_6$ , (ii)  $L + \tau_5 + \text{CeZn}_{11} \rightleftharpoons \tau_6$  and (iii)  $L + \tau_5 + (\text{Si}) \rightleftharpoons \tau_6$ . The latter reaction requests the existence of a three-phase field  $\tau_5 + \tau_6 + (\text{Si})$  at a temperature just below this invariant reaction. However, this three-phase field is not observed at 650°C (see Figure 14c), and thus rules out reaction (iii). Rietveld analysis of a sample with composition of  $\text{Ce}_{24.5}\text{Zn}_{37.5}\text{Si}_{38.0}$  annealed at 650°C showed three phases: L(Zn) +  $\tau_5 + \tau_6$ . However due to porosity of the sample it was not possible to reliably analyze the microstructure. Due to a strong degeneracy of the three-phase field L(Zn) +  $\tau_5 + \tau_6$  (compositions of these phases lie almost on one line; (see Figure 14c), the two remaining possible invariant reactions (i) and (ii) are almost identical from a thermodynamic point of view.

The existence of a maximum on the solidus in the two-phase field  $\tau_5 + \tau_6$  would infer a three-phase invariant peritectic  $L + \tau_5 \rightleftharpoons \tau_6$ , but due to the difficulties in the interpretation of DTA we cannot provide such evidence. Thus the type of this reaction remains uncertain

and is therefore denoted as a degenerated peritectic:  $L + \tau_5, \text{CeZn}_{11} \rightleftharpoons \tau_6$  in the temperature range  $690 \leq T \leq 700^\circ\text{C}$  ( $P_{D1}$  : Figure 13). The invariant reaction recorded by DTA at  $727^\circ\text{C}$  (Figure 12) is defined as transition type reaction  $U_3$ ,  $L + \text{CeSi}_2 \rightleftharpoons \tau_5 + (\text{Si})$ . Confirmation is available from a comparison of the isothermal sections and microstructures of the alloys annealed at 710 (the micrograph is not shown due to its similarity to  $650^\circ\text{C}$ ) and  $750^\circ\text{C}$  (Figure 14d,e and Figure 15b,c). Similar to the narrow three-phase field  $L(\text{Zn}) + \tau_5 + \tau_6$ , Rietveld analysis of sample  $\text{Ce}_{22.7}\text{Zn}_{42.9}\text{Si}_{34.4}$  annealed at  $750^\circ\text{C}$  revealed three phase constituents:  $L(\text{Zn})$ ,  $\tau_5$ , and  $\text{CeSi}_2$  consistent with the three-phase field  $L(\text{Zn}) + \tau_5 + \text{CeSi}_2$ .

The previously reported isothermal section at  $800^\circ\text{C}$  <sup>8</sup> suggested that  $\tau_5$  is unstable at this temperature and decomposes into  $\text{Ce}(\text{Si}_{1-x}\text{Zn}_x)_2$  with  $\alpha\text{-ThSi}_2$  type,  $L(\text{Zn})$ , and possibly  $\text{CeZn}_{11}$  or  $\beta\text{-Ce}_2\text{Zn}_{17}$ . Indeed DTA runs of sample  $\text{Ce}_{7.6}\text{Zn}_{78.4}\text{Si}_{14}$  up to  $850^\circ\text{C}$  gave two signals between  $780\text{-}790^\circ\text{C}$ . Surprisingly EPM analysis of this sample after three DTA runs did not show any trace of  $\text{Ce}(\text{Si}_{1-x}\text{Zn}_x)_2$ . In order to confirm these observations the remaining pieces of  $\text{Ce}_{7.6}\text{Zn}_{78.4}\text{Si}_{14}$  alloys were heat treated at  $770, 790, 810, 850, 860, 870, 880$  and  $900^\circ\text{C}$ .

Rietveld refinement and EPM analysis clearly showed that  $\tau_5$  is still stable up to  $850^\circ\text{C}$  and is in equilibrium with  $L(\text{Zn})$  and  $\beta\text{-Ce}_2\text{Zn}_{17}$ , while at  $900^\circ\text{C}$  it disappears completely yielding a three-phase field  $L(\text{Zn}) + \beta\text{-Ce}_2\text{Zn}_{17} + \tau_2$ . Such a peritectic reaction involving  $\tau_2$  is not compatible with the existence of the three-phase field  $\tau_2 + \text{CeSi}_2 + \beta\text{-Ce}_2\text{Zn}_{17}$ . Careful heat treatment between  $850\text{-}900^\circ\text{C}$  followed by XRPD and EPM analysis showed that an alloy annealed at  $860^\circ\text{C}$  gives the same phase constituents as in  $850^\circ\text{C}$ , while at  $870^\circ\text{C}$   $\text{Ce}(\text{Si}_{1-x}\text{Zn}_x)_2$  with  $\alpha\text{-ThSi}_2$  type is additionally present in this sample. This fact narrows down the decomposition temperature of  $\tau_5$  to  $865 \pm 5^\circ\text{C}$ , and confirms the participation of  $\text{Ce}(\text{Si}_{1-x}\text{Zn}_x)_2$  with  $\alpha\text{-ThSi}_2$  type in the peritectic formation of  $\tau_5$ . Taking into consideration similar arguments, as discussed above for the formation of  $\tau_6$ , a degenerated invariant reaction of peritectic type  $P_{D2}$ :  $L + \text{CeSi}_2, \beta\text{-Ce}_2\text{Zn}_{17} \rightleftharpoons \tau_5$  is assigned. The equilibria observed at  $900^\circ\text{C}$  could be explained by a transition type reaction  $U_5$ :  $L + \tau_2 \rightleftharpoons \text{CeSi}_2 + \beta\text{-Ce}_2\text{Zn}_{17}$  that occurs at  $890 \pm 10^\circ\text{C}$ .

One of the afore-mentioned thermal effects observed between  $780\text{-}790^\circ\text{C}$  could be attributed to a transition type reaction  $U_4$ :  $L + \beta\text{-Ce}_2\text{Zn}_{17} \rightleftharpoons \tau_5 + \text{CeZn}_{11}$ . The phase field  $L(\text{Zn}) + \tau_5 + \text{CeZn}_{11}$  was still observed up to  $770^\circ\text{C}$ , while at  $790^\circ\text{C}$  it changed to  $L(\text{Zn}) + \tau_5 + \beta\text{-Ce}_2\text{Zn}_{17}$ . Note that in some samples  $\text{CeZn}_{11}$  and/or  $\tau_6$  were observed as the



fourth or fifth phase. Based on the amount and morphology, those phases were considered to be formed during the quenching process.

The stability of  $\tau_5$  at 800°C has been incorporated in the new isothermal section shown in Figure 17. It supersedes the older version by Malik *et al.*<sup>8</sup> In addition to the three-phase field  $L(\text{Zn})+\tau_5+\beta\text{-Ce}_2\text{Zn}_{17}$ , two narrow three-phase fields are required to complete the section:  $\text{CeSi}_2+\tau_5+\beta\text{-Ce}_2\text{Zn}_{17}$  and  $L(\text{Zn})+\tau_5+\text{CeSi}_2$ . Note that the three-phase field  $L(\text{Zn})+\text{CeSi}_2+(\text{Si})$  is still stable up to 900°C. Such narrow phase fields are complicated to investigate, and without careful control of the overall sample composition it may earlier have led to a wrong conclusion regarding the stability of  $\tau_5$ .

The results on the phase equilibria are consistent (i) with the single crystal growth experiments, which reveal a large crystallization field of the  $\alpha\text{ThSi}_2$ -type phase  $\text{Ce}(\text{Si}_{1-x}\text{Zn}_x)_2$  extending far into the Zn-rich corner (up to 95 at. % Zn), and consequently (ii) with a rather steep liquidus surface in the Zn-rich region, which infers a high degeneracy in the isothermal reactions involving the Zn-rich liquid.

### 3.6. Physical Properties of $\tau_5\text{-CeZn}(\text{Zn}_{1-x}\text{Si}_x)_2$ and $\tau_6\text{-CeZn}_2(\text{Zn}_{0.28}\text{Si}_{0.72})_2$

Ac magnetic susceptibility measurements on a polycrystalline sample of  $\tau_5$   $\text{CeZn}(\text{Zn}_{0.32}\text{Si}_{0.68})_2$  revealed a  $\delta$ -shape magnetic anomaly near  $T_C \sim 5$  K (see Figure 18) which is indicative of a ferromagnetic transition. Accordingly, we performed dc magnetisation and dc susceptibility measurements on a few freely rotating, flux-grown single crystals of  $\tau_5$  (with a total mass of 0.8 mg). Field dependent isothermal (see Figure 19) as well as temperature dependent magnetisation (Figure 20) measurements confirm ferromagnetic ordering below about 4.4 K with a saturation moment near  $1 \mu_B$  at 1.9 K and 6 T. The slightly lower  $T_C$  of the flux-grown single crystals as compared to the polycrystalline bulk samples relates to slightly different compositions of  $\tau_5$  bulk samples as compared to flux grown  $\tau_5$  crystals  $\text{CeZn}(\text{Zn}_{0.29}\text{Si}_{0.71})_2$ .

The ferromagnetic phase transition at  $T_C \sim 4.4$  K is corroborated by distinct anomalies of the specific heat and electrical resistivity in Figure 21 and Figure 22, respectively.

The analysis of the inverse dc magnetic susceptibility in terms of a modified Curie-Weiss fit,  $\chi(T) = \chi_0 + C/(T - \Theta_p)$ , in Figure 20 reveals an effective paramagnetic moment of Ce near  $2.5 \mu_B$  which is close to the effective moment of free  $\text{Ce}^{3+}$  ( $2.54 \mu_B$ ). The negative value of the paramagnetic Curie temperature of  $-10$  K obtained from analysing the data of freely rotating crystals refers to Kondo correlations rather than to a specific type of magnetic coupling (whether antiferro- or ferromagnetic). The relevance of Kondo

correlations for  $\tau_5$  is further revealed by the temperature dependence of the electrical resistivity in Figure 22, showing typical Kondo lattice features, and by the specific heat data in Figure 21. The magnitude of the specific heat anomaly at  $T_C$  of  $\tau_5$ - $\text{CeZn}(\text{Zn}_{0.29}\text{Si}_{0.71})_2$  single crystals is significantly reduced as compared to the value expected from a basic local moment mean-field approach. We thus analyse the temperature dependence and magnitude of the magnetic specific heat contribution in terms of a simple model for a ferromagnetic Kondo lattice system based on the resonant level model by Schotte and Schotte.<sup>39,40</sup> The details of this model calculations are explained e.g. in ref. 41. The corresponding fit to the experimental data, indicated as solid line in Figure 21, yields a ferromagnetic exchange coupling  $J = 14.6$  K and a Kondo temperature  $T_K = 5$  K, thus, suggesting a ferromagnetic Kondo lattice ground state of  $\tau_5$ - $\text{CeZn}(\text{Zn}_{0.32}\text{Si}_{0.68})_2$ . The largest deviation between the applied model and the experimental data is observed right above the ferromagnetic phase transition and relates to short range order and phonon contributions which are not included in the model. Using the same values for  $J$  and  $T_K$  and an effective Landé factor  $g = 2$  to adjust the model for the unknown  $4f$  wave function of the crystal field ground state doublet, we calculated the temperature and field dependent magnetisation displayed as solid lines in Figure 19. The approximate agreement with the experimental data further supports the validity of a ferromagnetic Kondo model.

The magnetic ground state properties of polycrystalline bulk samples of  $\tau_6$ - $\text{CeZn}_2(\text{Zn}_{0.28}\text{Si}_{0.72})_2$  were studied by means of specific heat as well as dc and ac magnetic susceptibility measurements at temperatures down to 3 K. Within the experimental temperature range the  $\tau_6$  phase displays a Curie-Weiss type paramagnetic behaviour as demonstrated by the dc magnetic susceptibility depicted in Figure 23. A modified Curie-Weiss fit of the inverse susceptibility in the temperature interval 80-300 K is indicated as solid line in Figure 23 and yields a temperature independent Pauli component  $\chi_0 = 1.0 \times 10^{-4}$  emu/mol, a paramagnetic Curie-Weiss temperature  $\Theta_p = -0.5$  K being indicative for weak antiferromagnetic or very weak Kondo correlations. Via the Curie constant of this fit an effective paramagnetic moment  $\mu_{\text{eff}} = 2.34 \mu_B$  is calculated, which is markedly reduced as compared to the  $\text{Ce}^{3+}$  free ion value ( $2.54 \mu_B$ ). The heat capacity data of  $\tau_6$ - $\text{CeZn}_2(\text{Zn}_{0.28}\text{Si}_{0.72})_2$  in Figure 21 display an upturn at lowest temperatures, which may either refer to short range correlations above a magnetic phase transition taking place below 3K or refer to Kondo correlations with a rather small characteristic energy of the order of one Kelvin.

Consistent with the small Seebeck coefficient (see top left inset in Figure 22) electrical resistivity of  $\tau_5$  indicates metallic type behaviour ruling out any thermoelectrically interesting behaviour.

#### 4. Conclusions

As the Ce-Zn-Si system is an important part of multinary Mg-based Mg-Zn-Mn-RE-(Si) high strength lightweight alloys for automotive applications, we have explored the constitution of the Ce-Zn-Si subsystem and particularly have determined in this work the phase equilibria for the isothermal section at 600°C in the region with <33.3 at.% Ce. Five ternary compounds ( $\tau_1$ ,  $\tau_2$ ,  $\tau_5$  to  $\tau_7$ ) exist at the investigated region at 600°C. Several four-phase reactions in the Zn rich corner were detected by DTA, including the peritectic decomposition temperatures of  $\tau_5$  and  $\tau_6$  at 865±5°C and 695±5°C, respectively. To provide details on the solidification of Ce-poor alloys, a Schultze-Scheil diagram was constructed from DTA measurements and partial isothermal sections determined at various temperatures. The crystal structures of  $\tau_5$  (CeNiSi<sub>2</sub>-type, *Cmcm*, *a*= 0.42079(1), *b*= 1.76522(3), *c*= 0.41619(1) nm), and  $\tau_6$  (ThCr<sub>2</sub>Si<sub>2</sub>-type, *I4/mmm*, *a*=0.41757(1), *c*= 1.05073(2) nm) were solved from X-ray single crystal diffraction data. An interesting case was met in the stabilization by extremely small amounts of Ge (less than ~2 atom percent of Ge) of the ternary phases {La,Ce}<sub>7</sub>Zn<sub>21</sub>(Zn<sub>1-x</sub>Ge<sub>x</sub>)<sub>2</sub>, both isotypic with the structure of Ce<sub>7</sub>Zn<sub>21</sub>(Zn<sub>1-x</sub>Si<sub>x</sub>)<sub>2</sub>. DFT calculations elucidated the extent and nature of the stabilizing effect of Ge in Ce<sub>7</sub>Zn<sub>23-x</sub>Ge<sub>x</sub> discussing the electronic structure in terms of the density of states (DOS) and determining enthalpies of formation for Ce<sub>7</sub>Zn<sub>23-x</sub>Ge<sub>x</sub> (*x*=0, 0.5, 2) as well as for several neighbouring binary Ce-Zn phases.

Physical property measurements document that neither  $\tau_5$  nor  $\tau_6$  are near a metal to insulator transition and thus exhibit rather metallic than semiconducting (thermoelectric) behaviour. Magnetic measurements as well as specific heat and electrical resistivity data reveal interesting ferromagnetic Kondo lattice behavior for  $\tau_5$ -CeZn(Zn<sub>1-x</sub>Si<sub>x</sub>)<sub>2</sub> with a Curie temperature *T<sub>C</sub>* = 4.4 K, whereas  $\tau_6$  displays Curie-Weiss type paramagnetic behavior down to 3 K. The effective paramagnetic moments of Ce obtained from Curie-Weiss fit of  $\tau_5$  (2.50  $\mu_B$ ) and  $\tau_6$  (2.34  $\mu_B$ ) suggest that the ground state of Ce-ions in these compounds is trivalent or close to 3+.

## 5. Acknowledgements

The research reported herein was supported by the Austrian Federal Ministry of Science and Research (BMWF) under the scholarship scheme: Technology Grant Southeast Asia (Ph.D) in the frame of the ASEA UNINET. DFT calculations were done on the facilities of the Vienna Scientific Cluster (VSC). The authors are also grateful for the support by the OeAD WTZ Austria-Czech Republic CZ12/2013 and by the Ministry of Education, Youth and Sports of the Czech Republic under the project 7AMB13AT019. The financial support by the project "CEITEC – Central European Institute of Technology" (CZ.1.05/1.1.00/02.0068) from the European Regional Development Fund and by the Grant Agency of the Czech Republic (Project No. GA14-15576S) is gratefully acknowledged by P. Broz.

## 6. References

- 1 E. Bauer, G. Hilscher, H. Michor, C. Paul, E. W. Scheidt, A. Griбанov, Y. Seropegin, H. Noël, M. Sigrist and P. Rogl, *Phys. Rev. Lett.*, 2004, **92**, 027003.
- 2 E. Bauer and P. Rogl, in *Non-Centrosymmetric Superconductors*, eds. E. Bauer and M. Sigrist, Springer Berlin Heidelberg, 2012, pp. 3–33.
- 3 R. K  chler, P. Gegenwart, C. Geibel and F. Steglich, *Sci. Technol. Adv. Mater.*, 2007, **8**, 428.
- 4 B. Chevalier, P. Rogl, K. Hiebl, J. Etourneau, *J. Solid State Chem.*, 1993, **107(2)**, 327-331.
- 5 A. Amato and J. Sierro, *J. Magn. Magn. Mater.*, 1985, **47–48**, 526–528.
- 6 P. Rogl, in *Handbook on the Physics and Chemistry of Rare Earths*, ed. K. A. Gschneidner Jr and L. Eyring, Elsevier, 1984, vol. 7, pp. 1–264.
- 7 H. Kido, T. Hoshikawa, M. Shimada and M. Koizumi, *Phys. Status Solidi A*, 1983, **80**, 601–605.
- 8 Z. Malik, A. Grytsiv, P. Rogl and G. Giester, *Intermetallics*, 2013, **36**, 118–126.
- 9 N.-T. Suen and S. Bobev, *Inorg. Chem.*, 2013, **52**, 12731–12740.
- 10 J. Hoos, N.-T. Suen and S. Bobev, *Acta Crystallogr. Sect. C Struct. Chem.*, 2014, **70**, 945–948.
- 11 P. Villars and K. Cenzual, *Pearson’s Crystal Data–Crystal Structure Database for Inorganic Compounds, release 2014/15*, ASM International, Materials Park, OH, USA, 2014.

- 12 J. Rodriguez-Carvajal, *Satellite Meeting on Powder Diffraction of the XV Congress of the IUCR*, Toulouse, France, 1990.
- 13 *APEXII Software Suite*, Bruker AXS Inc., Madison, Wisconsin, USA, 2005.
- 14 G. M. Sheldrick, *Acta Crystallogr. A*, 2007, **64**, 112–122.
- 15 L. J. Farrugia, *J. Appl. Crystallogr.*, 1999, **32**, 837–838.
- 16 L. M. Gelato and E. Parthé, *J. Appl. Crystallogr.*, 1987, **20**, 139–143.
- 17 G. Kresse and J. Furthmüller, *Phys. Rev. B*, 1996, **54**, 11169–11186.
- 18 G. Kresse and D. Joubert, *Phys. Rev. B*, 1999, **59**, 1758–1775.
- 19 P. Blöchl, *Phys. Rev. B*, 1994, **50**, 17953–17979.
- 20 J. Perdew, K. Burke and M. Ernzerhof, *Phys. Rev. Lett.*, 1996, **77**, 3865–3868.
- 21 H. Monkhorst and J. Pack, *Phys. Rev. B*, 1976, **13**, 5188–5192.
- 22 *Pauling File Binary Edition, Version 1.0, Release 2002/1*, ASM international, Materials Park, OH, USA, 2002.
- 23 Z. Malik, O. Sologub, G. Giester and P. Rogl, *J. Solid State Chem.*, 2011, **184**, 2840–2848.
- 24 M. V. Bulanova, P. N. Zheltov, K. A. Meleshevich, P. A. Saltykov and G. Effenberg, *J. Alloys Compd.*, 2002, **345**, 110–115.
- 25 P. Schobinger-Papamantellos and K. H. J. Buschow, *J. Alloys Compd.*, 1993, **198**, 47–50.
- 26 A. Wosylus, K. Meier, Y. Prots, W. Schnelle, H. Rosner, U. Schwarz and Y. Grin, *Angew. Chem.*, 2010, **122**, 9187–9191.
- 27 A. Berche, P. Benigni, J. Rogez and M. C. Record, *Thermochim. Acta*, 2011, **523**, 70–78.
- 28 I. Oshchapovsky, V. Pavlyuk, G. Dmytriv and A. Griffin, *Acta Crystallogr. C*, 2012, **68**, i37–i40.
- 29 O. I. Bodak, Y. M. Kalychak and E. I. Gladyshevskii, *Izv. Akad. Nauk SSSR Neorganicheskie Mater.*, 1974, **10**, 450–5.
- 30 O.I. Bodak, E.I. Gladyshevskii and Y.M. Kalychak, *Tezisy Dokl. Vses. Konf. Kristallokhim. Internet. Soeden. (1st)*, 1971.
- 31 N. M. Norlidah, G. Venturini, B. Malaman and E. Ressouche, *J. Alloys Compd.*, 1998, **265**, 77–80.
- 32 A. Grytsiv, D. Kaczorowski, A. Leithe-Jasper, P. Rogl, C. Godart, M. Potel and H. Noël, *J. Solid State Chem.*, 2002, **163**, 37–43.
- 33 L. Pauling and B. Kamb, *Proc. Natl. Acad. Sci. U. S. A.*, 1986, **83**, 3569–3571.

- 34 A. Grytsiv, A. Leithe-Jasper, H. Flandorfer, P. Rogl, K. Hiebl, C. Godart and T. Velikanova, *J. Alloys Compd.*, 1998, **266**, 7–12.
- 35 I.M. Opainich, Ph.D. Thesis (in Ukrainian), University of L'viv, 1996.
- 36 C. P. Wang, X. Chen, X. J. Liu, F. S. Pan and K. Ishida, *J. Alloys Compd.*, 2008, **458**, 166–173.
- 37 P. Chiotti and J. T. Mason, *Trans. Am. Inst. Min. Metall. Pet. Eng.*, 1965, **233**, 786–95.
- 38 I. Johnson and R. M. Yonco, *Metall. Trans.*, 1970, **1**, 905–10.
- 39 K. D. Schotte and U. Schotte, *Phys. Lett. A*, 1975, **55**, 38–40.
- 40 C. D. Bredl, F. Steglich and K. D. Schotte, *Z. f. Phys. B Condens. Matter*, 1978, **29**, 327–340.
- 41 L. Peyker, C. Gold, E.-W. Scheidt, W. Scherer, J. G. Donath, P. Gegenwart, F. Mayr, T. Unruh, V. Eyert, E. Bauer and H. Michor, *J. Phys. Condens. Matter*, 2009, **21**, 235604.

**Table 1.** Crystallographic data of ternary solid phases of the system Ce-Zn-Si.

Phase Temperature range (°C)	Space group, Prototype	Lattice parameters (nm)			Comments
		a	b	c	
$\tau_1$ -Ce <sub>7</sub> Zn <sub>21</sub> (Zn <sub>1-x</sub> Si <sub>x</sub> ) <sub>2</sub>	<i>Pbam</i> Ce <sub>7</sub> Zn <sub>21</sub> (Zn <sub>1-x</sub> Si <sub>x</sub> ) <sub>2</sub>	1.55722(3) - -	1.71942(3)	0.44772(1)	x=0.28 SC (ref. 8) 0.28≤x≤0.98 at 800°C (ref. 8) 0.45≤x≤0.99 at 600°C [this work]
$\tau_2$ -Ce(Si <sub>1-x</sub> Zn <sub>x</sub> ) <sub>2</sub>	<i>P6/mmm</i> AlB <sub>2</sub>	0.4223 0.41827(2) 0.4421(2) 0.42206(5)	- - - -	0.4238 0.42747(2) 0.38960(3) 0.42334(6)	x=0.50 (ref. 7) SC at x=0.44 (ref. 8) 0.36≤x≤0.76 at 800°C (ref. 8) x=0.75 (ref. 8) 0.36≤x≤0.73 at 600°C [this work] x=0.47 [This work]
$\tau_3$ -Ce(Zn <sub>x</sub> Si <sub>1-x</sub> )	unknown	-	-	-	0.17<x<0.23 at 800°C <sup>8</sup>
$\tau_4$ -Ce <sub>40</sub> Zn <sub>37</sub> Si <sub>23</sub>	unknown	-	-	-	at. % (ref. 8)
$\tau_5$ -CeZn(Zn <sub>1-x</sub> Si <sub>x</sub> ) <sub>2</sub> <865±5 [this work]	<i>Cmcm</i> CeNiSi <sub>2</sub>	0.42079(1)	1.76522(3)	0.41619(1)	x=0.71 SC [this work] 0.68≤x≤0.76 at 600°C [this work]
$\tau_6$ -CeZn <sub>2</sub> (Si <sub>1-x</sub> Zn <sub>x</sub> ) <sub>2</sub> <695±5 [this work]	<i>I4/mmm</i> ThCr <sub>2</sub> Si <sub>2</sub>	0.41757(1)	-	1.05073(2)	x=0.30 SC [This work] 0.25≤x≤0.30 at 600°C [This work]
$\tau_7$ -Ce <sub>37</sub> Zn <sub>48</sub> Si <sub>15</sub> <800	unknown	-	-	-	[This work]

**Table 2.** X-ray single crystal data for  $\tau_5$ -CeZn(Zn<sub>1-x</sub>Si<sub>x</sub>)<sub>2</sub>, x = 0.71; space group *Cmcm*, No. 63 and for  $\tau_6$ -CeZn<sub>2</sub>(Si<sub>1-x</sub>Zn<sub>x</sub>)<sub>2</sub>, x = 0.30; space group *I4/mmm*, No. 139.

Parameter/compound	$\tau_5$ -CeZn(Zn <sub>1-x</sub> Si <sub>x</sub> ) <sub>2</sub> , x=0.71	$\tau_6$ -CeZn <sub>2</sub> (Si <sub>1-x</sub> Zn <sub>x</sub> ) <sub>2</sub> , x=0.30
Phase composition (EPMA, at.%)	Ce <sub>24.9</sub> Zn <sub>39.6</sub> Si <sub>35.5</sub>	Ce <sub>20.1</sub> Zn <sub>51.8</sub> Si <sub>28.1</sub>
Refinement composition (at.%)	Ce <sub>25.0</sub> Zn <sub>39.7</sub> Si <sub>35.3</sub>	Ce <sub>20.0</sub> Zn <sub>52.0</sub> Si <sub>28.0</sub>
Structure type	CeNiSi <sub>2</sub>	ThCr <sub>2</sub> Si <sub>2</sub>
2θ range (deg)	4.62≤2θ≤80.32	7.76≤2θ≤72.72
a[nm]	0.42079(1)	0.41757(1)
b[nm]	1.76522(3)	0.41757(1)
c [nm]	0.41619(1)	1.05073(2)
Reflections in refinement	537 ≥ 4σ(F <sub>o</sub> ) of 556	157 ≥ 4σ(F <sub>o</sub> ) of 157
Mosaicity	0.55	0.48
Number of variables	20	11
R <sub>F2</sub> = Σ F <sub>o</sub> <sup>2</sup> -F <sub>c</sub> <sup>2</sup>  /ΣF <sub>o</sub> <sup>2</sup>	0.0203	0.0077
wR2	0.0402	0.0197
R <sub>int</sub>	0.0432	0.0311
GOF	1.349	1.370
Extinction (Zachariasen)	0.0059(3)	0.034(1)
Ce; occ.	4c (0,y,¼), y = 0.39888(1); 1.00(-)	2a (0,0,0); 1.00(-)
U <sub>11</sub> ;U <sub>22</sub> ;U <sub>33</sub> ;U <sub>23</sub> ;U <sub>13</sub> ;U <sub>12</sub>	0.0052(1); 0.0073(1); 0.0038(1); 0; 0; 0	0.00567(9); 0.00567(9); 0.0096(1); 0; 0; 0
M1; occ.	4c (0,y,¼), y = 0.03338(5); 0.26(1) Zn1 + 0.74 Si1	4d (0,½,¼); 1.00(-) Zn1.
U <sub>11</sub> ;U <sub>22</sub> ;U <sub>33</sub> ; U <sub>23</sub> ;U <sub>13</sub> ;U <sub>12</sub>	0.0137(4); 0.0062(4); 0.0050(4); 0; 0; 0	0.0101(1); 0.0101(1); 0.0090(1); 0; 0; 0
M2; occ.	4c (0,y,¼), y = 0.16921(5); 0.31(1) Zn2 + 0.69 Si2	4e (0,0,z); z = 0.38507(5); 0.30(1) Zn2+0.70(1) Si1
U <sub>11</sub> ;U <sub>22</sub> ;U <sub>33</sub> ; U <sub>23</sub> ;U <sub>13</sub> ;U <sub>12</sub>	0.0087(4); 0.0080(4); 0.0064(4); 0; 0; 0	0.0087(2); 0.0087(2); 0.0090(2); 0; 0; 0
Zn3; occ.	4c (0,y,¼), y = 0.74962(3); 1.00 Zn3	
U <sub>11</sub> ;U <sub>22</sub> ;U <sub>33</sub> ; U <sub>23</sub> ;U <sub>13</sub> ;U <sub>12</sub>	0.0099(2); 0.0082(2); 0.0080(2); 0; 0; 0	
Residual electron density; max; min in (electron/nm <sup>3</sup> ) × 10 <sup>3</sup>	2.61; -3.04	0.32; -0.81

**Table 3.** X-ray single crystal data for  $\text{Ce}_7\text{Zn}_{21}(\text{Zn}_{1-x}\text{Ge}_x)_2$ ,  $x = 0.75$  and  $\text{La}_7\text{Zn}_{21}(\text{Zn}_{1-x}\text{Ge}_x)_2$ ,  $x = 0.10$ ; space group *Pbam*, No. 55. Standardized<sup>a</sup> with program Structure Tidy.<sup>16</sup>

Parameter/compound	$\text{Ce}_7\text{Zn}_{21}(\text{Zn}_{1-x}\text{Ge}_x)_2$ , $x = 0.75$	$\text{La}_7\text{Zn}_{21}(\text{Zn}_{1-x}\text{Ge}_x)_2$ , $x = 0.10$
Phase composition (EPMA, at.%)	$\text{Ce}_{23.2}\text{Zn}_{71.9}\text{Ge}_{5.0}$	$\text{La}_{23.5}\text{Zn}_{75.9}\text{Ge}_{0.6}$
Refinement composition (at.%)	$\text{Ce}_{23.3}\text{Zn}_{71.7}\text{Ge}_{5.0}$	$\text{La}_{23.3}\text{Zn}_{76.0}\text{Ge}_{0.7}$
Structure type	$\text{Ce}_7\text{Zn}_{21}(\text{Zn}_{1-x}\text{Si}_x)_2$	$\text{Ce}_7\text{Zn}_{21}(\text{Zn}_{1-x}\text{Si}_x)_2$
2 $\theta$ range (°)	4.75 ≤ 2 $\theta$ ≤ 72.58	5.19 ≤ 2 $\theta$ ≤ 72.64
a [nm]	1.55215(2)	1.57043(2)
b [nm]	1.71447(2)	1.73321(3)
c [nm]	0.44836(1)	0.45076(1)
Reflections in refinement	2706 ≥ 4 $\sigma$ (F <sub>o</sub> ) of 3103	2732 ≥ 4 $\sigma$ (F <sub>o</sub> ) of 3196
Mosaicity	0.45	0.50
Number of variables	94	94
R <sub>F2</sub> = $\sum  F_o^2 - F_c^2  / \sum F_o^2$	0.0215	0.0330
wR2	0.0532	0.0609
R <sub>int</sub>	0.0147	0.0147
GOF	0.774	1.325
Extinction (Zachariasen)	0.00094(4)	0.00028(3)
RE1 in 4h (x,y,½); occ.	x = 0.16459(2); y = 0.04538(1); 1.00(-)	x = 0.16342(2); y = 0.04474(2); 1.00(-)
U <sub>11</sub> ;U <sub>22</sub> ;U <sub>33</sub> ;U <sub>23</sub> =U <sub>13</sub> =0;U <sub>12</sub>	0.0093(1); 0.0094(1); 0.0076(1); -0.0004(1)	0.0099(1); 0.0084(2); 0.0067(1); -0.0003(1)
RE2 in 4g (x,y,0); occ.	x = 0.16580(2); y = 0.31940(1); 1.00(-)	x = 0.16739(2); y = 0.31848(2); 1.00(-)
U <sub>11</sub> ;U <sub>22</sub> ;U <sub>33</sub> ;U <sub>23</sub> =U <sub>13</sub> =0;U <sub>12</sub>	0.0086(1); 0.0087(1); 0.0076(1); -0.00002(7)	0.0096(1); 0.0091(2); 0.0072(1); -0.0005(1)
RE3 in 4g (x,y,0); occ.	x = 0.41826(2); y = 0.24008(3); 1.00(-)	X = 0.41760(2); y = 0.24148(3); 1.00(-)
U <sub>11</sub> ;U <sub>22</sub> ;U <sub>33</sub> ;U <sub>23</sub> =U <sub>13</sub> =0;U <sub>12</sub>	0.0093(1); 0.0195(1); 0.0118(1); -0.0019(1)	0.0104(2); 0.0269(2); 0.0125(2); 0.0037(1)
RE4 in 2c (0,½,0); occ.	1.00(-)	1.00(-)
U <sub>11</sub> ;U <sub>22</sub> ;U <sub>33</sub> ;U <sub>23</sub> =U <sub>13</sub> =0;U <sub>12</sub>	0.0103(1); 0.0143(2); 0.0115(2); -0.0030(1)	0.0137(2); 0.0166(3); 0.01304(2); 0.0056(2)
M1 in 4h (x,y,½); occ. <sup>b</sup>	x = 0.02039(3); y = 0.35860(3); 0.25 Zn1+0.75 Ge1 <sup>b</sup>	x = 0.02098(5); y = 0.35861(4); 0.90 Zn1+ 0.10 Ge1 <sup>b</sup>
U <sub>11</sub> ;U <sub>22</sub> ;U <sub>33</sub> ;U <sub>23</sub> =U <sub>13</sub> =0;U <sub>12</sub>	0.0091(2); 0.0104(2); 0.0131(2); 0.0001(2)	0.0108(3); 0.0107(4); 0.0165(3); 0.0001(3)
Zn2 in 4h (x,y,½); occ.	x = 0.07520(4); y = 0.21623(3); 1.00(-)	x = 0.07441(5); y = 0.21634(4); 1.00(-)
U <sub>11</sub> ;U <sub>22</sub> ;U <sub>33</sub> ;U <sub>23</sub> =U <sub>13</sub> =0;U <sub>12</sub>	0.0143(2); 0.0097(2); 0.0110(2); -0.0008(2)	0.01500(3); 0.0093(3); 0.0102(3); -0.0005(3)
Zn3 in 4h (x,y,½); occ.	x = 0.15224(4); y = 0.44824(3); 1.00(-)	x = 0.15203(5); y = 0.44898(5); 1.00(-)
U <sub>11</sub> ;U <sub>22</sub> ;U <sub>33</sub> ;U <sub>23</sub> =U <sub>13</sub> =0;U <sub>12</sub>	0.0128(2); 0.0102(2); 0.0102(2); -0.0019(2)	0.01432(3); 0.01062(4); 0.0096(3); -0.0023(3)
Zn4 in 4h (x,y,½); occ.	x = 0.25707(4); y = 0.21844(3); 1.00(-)	x = 0.25851(5); y = 0.21716(4); 1.00(-)
U <sub>11</sub> ;U <sub>22</sub> ;U <sub>33</sub> ;U <sub>23</sub> =U <sub>13</sub> =0;U <sub>12</sub>	0.0134(2); 0.0096(2); 0.0105(2); 0.0005(2)	0.0166(3); 0.0085(3); 0.0093(3); 0.0001(3)
Zn5 in 4h (x,y,½); occ.	x = 0.30414(4); y = 0.35837(3); 1.00(-)	x = 0.30569(5); y = 0.35746(4); 1.00(-)
U <sub>11</sub> ;U <sub>22</sub> ;U <sub>33</sub> ;U <sub>23</sub> =U <sub>13</sub> =0;U <sub>12</sub>	0.0128(2); 0.0120(2); 0.0115(2); -0.0032(2)	0.0132(3); 0.0114(4); 0.0107(3); -0.0037(3)
Zn6 in 4h (x,y,½); occ.	x = 0.36349(4); y = 0.09927(3); 1.00(-)	x = 0.36446(5); y = 0.09913(5); 1.00(-)
U <sub>11</sub> ;U <sub>22</sub> ;U <sub>33</sub> ;U <sub>23</sub> =U <sub>13</sub> =0;U <sub>12</sub>	0.0105(2); 0.0111(2); 0.0200(3); -0.0005(2)	0.0114(3); 0.0124(4); 0.0223(4); -0.0011(3)
Zn7 in 4h (x,y,½); occ.	x = 0.46584(4); y = 0.40147(4); 1.00(-)	x = 0.46662(5); y = 0.40073(5); 1.00(-)
U <sub>11</sub> ;U <sub>22</sub> ;U <sub>33</sub> ;U <sub>23</sub> =U <sub>13</sub> =0;U <sub>12</sub>	0.0103(2); 0.0179(3); 0.0172(3); 0.0029(2)	0.0106(3); 0.0176(4); 0.0178(4); 0.0030(3)
Zn8 in 4g (x,y,0); occ.	x = 0.07303(4); y = 0.14088(3); 1.00(-)	x = 0.07359(6); y = 0.14124(5); 1.00(-)
U <sub>11</sub> ;U <sub>22</sub> ;U <sub>33</sub> ;U <sub>23</sub> =U <sub>13</sub> =0;U <sub>12</sub>	0.0217(3); 0.0141(2); 0.0104(2); 0.0043(2)	0.0260(4); 0.0144(4); 0.0096(3); 0.0046(3)
Zn9 in 4g (x,y,0); occ.	x = 0.24865(4); y = 0.14674(3); 1.00(-)	x = 0.24920(6); y = 0.14602(5); 1.00(-)
U <sub>11</sub> ;U <sub>22</sub> ;U <sub>33</sub> ;U <sub>23</sub> =U <sub>13</sub> =0;U <sub>12</sub>	0.0226 (3); 0.0119(2); 0.0109(2); -0.0050(2)	0.0295(4); 0.0123(4); 0.0099(3); -0.0079(3)
Zn10 in 4g (x,y,0); occ.	x = 0.29957(4); y = 0.00600(4); 1.00(-)	x = 0.29942(5); y = 0.00570(5); 1.00(-)
U <sub>11</sub> ;U <sub>22</sub> ;U <sub>33</sub> ;U <sub>23</sub> =U <sub>13</sub> =0;U <sub>12</sub>	0.0144(3); 0.0197(3); 0.0106(2); 0.0067(2)	0.0166(4); 0.0240(4); 0.0100(3); 0.0099(3)
Zn11 in 4g (x,y,0); occ.	x = 0.35248(4); y = 0.41919(3); 1.00(-)	x = 0.35252(6); y = 0.41889(5); 1.00(-)
U <sub>11</sub> ;U <sub>22</sub> ;U <sub>33</sub> ;U <sub>23</sub> =U <sub>13</sub> =0;U <sub>12</sub>	0.0223(3); 0.0135(2); 0.0100(2); -0.0021(2)	0.0250(4); 0.0134(4); 0.0093(3); -0.0031(3)
Zn12 in 2a (0,0,0); occ.	1.00(-)	1.00(-)
U <sub>11</sub> ;U <sub>22</sub> ;U <sub>33</sub> ;U <sub>23</sub> =U <sub>13</sub> =0;U <sub>12</sub>	0.0147(4); 0.0175(4); 0.0178(4); -0.0010(3)	0.0139(5); 0.0205(6); 0.0172(5); -0.0020(4)
Residual electron density; max; min in (electron/nm <sup>3</sup> ) × 10 <sup>3</sup>	1.59; -1.70	1.71; -2.13

<sup>a</sup>The earlier data sets for single crystal  $\text{Ce}_7\text{Zn}_{21}(\text{Zn}_{1-x}\text{Si}_x)_2$ ,  $x = 0.28$ <sup>8</sup> and for isotypic  $\text{La}_7\text{Zn}_{21}(\text{Zn}_{1-x}\text{Si}_x)_2$ ,  $x = 0.27$ ,<sup>8</sup> as well as the sets for  $\{\text{La-Nd}\}_7\text{Zn}_{21+x}(\text{Ti})_{2-x}$ <sup>9,10</sup> were not standardized correctly.

<sup>b</sup>The occupancy value is fixed after EPMA



**Table 4.** DFT derived equilibrium heat of formation (DFT) for  $T = 0$  K (in kJ/mol) for  $\text{Ce}_x(\text{Ge,Zn})_{1-x}$  as a function of Ce concentration  $x$ , in comparison to the adjusted DFT values (DFT-adj, see text) and  $T=0$  extrapolation of the thermodynamic modeling (model) of Wang et al.<sup>36</sup>. For Ce the  $\alpha$ -phase was taken as reference. Local magnetic moment per Ce-atom  $m_{\text{loc}}$  (in  $\mu_B$ ) and the equilibrium volume per atom  $V_0$  (in  $\text{\AA}^3$ ) are also given.

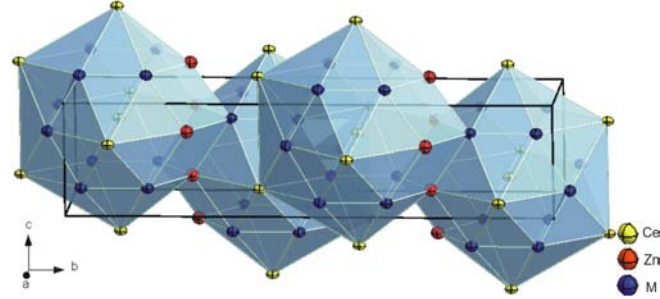
Compound	$x_{\text{Ce}}$	DFT	DFT-adj	Model	$m_{\text{loc}}$	$V_0$
CeZn	0.50	-17.81	-33.94	-34.04	0	23.72
CeZn <sub>2</sub>	0.333	-28.16	-40.37	-40.06	0.71	21.22
CeZn <sub>3</sub>	0.25	-28.00	-38.25	-38.47	0.25	19.23
Ce <sub>14</sub> Zn <sub>46</sub>	0.233	-26.76	-36.62	-	0.29	19.29
Ce <sub>14</sub> Zn <sub>42</sub> Ge <sub>4</sub>	0.233	-34.16	-43.73	-	0.19	19.16
Ce <sub>14</sub> Zn <sub>45</sub> Ge	0.233	-28.47	-38.33	-	0.08	19.16
Tie-line	0.233	-27.75	-37.61	-		
Ce <sub>3</sub> Zn <sub>11</sub>	0.214	-27.47	-36.89	-36.88	0.65	18.66

**Table 5.** Three phase equilibria and lattice parameters of alloys annealed at 600°C.

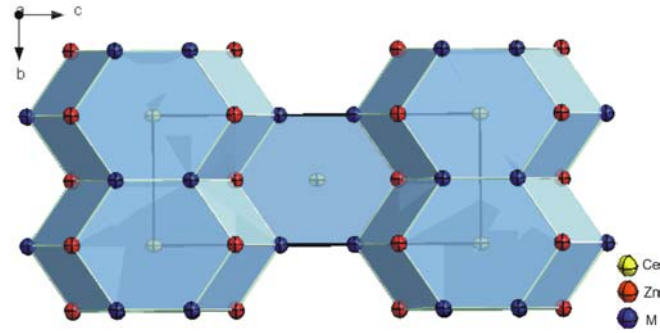
Phase region	Phases	Structure type	EPMA (at%)			Lattice parameters (nm)		
			Ce	Zn	Si	a	b	c
$\tau_5 + \tau_6 + \text{Si}$	$\tau_5$	CeNiSi <sub>2</sub>	25	36.8	38.2	0.4209(1)	1.7662(5)	0.4177(1)
	$\tau_6$	ThCr <sub>2</sub> Si <sub>2</sub>	20.5	49.8	29.7	0.41881(6)	-	1.0560(4)
	Si	C <sub>diamond</sub>	-	-	-	0.54297(5)	-	-
CeSi <sub>2</sub> + $\tau_5$ + Si	CeSi <sub>2</sub>	ThSi <sub>2</sub>	33.0	15.2	51.8	0.42025(3)	-	1.4172(4)
	$\tau_5$	CeNiSi <sub>2</sub>	24.8	38.1	37.1	0.42046(7)	1.7699(3)	0.41713(3)
	Si	C <sub>diamond</sub>	0.3	0.5	99.2	-	-	-
$\tau_6 + \text{L}(\text{Zn}) + \text{Si}$	$\tau_6$	ThCr <sub>2</sub> Si <sub>2</sub>	19.9	52.0	28.1	0.41848(3)	-	1.05615(6)
	L(Zn)	Mg	-	-	-	-	-	-
	Si	C <sub>diamond</sub>	0.0	0.4	99.6	0.54298(4)	-	-
$\tau_6 + \text{L}(\text{Zn}) + \text{CeZn}_{11}$	$\tau_6$	ThCr <sub>2</sub> Si <sub>2</sub>	19.8	51.9	28.3	0.41830(6)	-	1.0558(3)
	L(Zn)	Mg	0.4	99.3	0.3	-	-	-
	CeZn <sub>11</sub>	BaCd <sub>11</sub>	8.6	91.1	0.3	1.0662(1)	-	0.6866(1)
$\tau_5 + \text{CeZn}_{11} + \text{Ce}_2\text{Zn}_{17}$	$\tau_5$	CeNiSi <sub>2</sub>	-	-	-	0.4210(1)	1.767(1)	0.4165(1)
	CeZn <sub>11</sub>	BaCd <sub>11</sub>	-	-	-	1.0661(1)	-	0.6865(1)
	$\alpha$ Ce <sub>2</sub> Zn <sub>17</sub>	TbCu <sub>7</sub>	10.8	88.8	0.4	0.5253(1)	-	0.4433(1)
$\tau_5 + \tau_6 + \text{CeZn}_{11}$	$\tau_5$	CeNiSi <sub>2</sub>	-	-	-	0.42173(1)	1.75258(2)	0.41738(1)
	$\tau_6$	ThCr <sub>2</sub> Si <sub>2</sub>	-	-	-	0.41872(7)	-	1.0558(1)
	CeZn <sub>11</sub>	BaCd <sub>11</sub>	-	-	-	1.0662(1)	-	0.6868(2)
$\tau_2 + \text{CeSi}_2 + \text{Ce}_2\text{Zn}_{17}$	$\tau_2$	AlB <sub>2</sub>	33.3	25.6	41.1 <sup>a</sup>	0.41365(5)	-	0.42967(5)
	CeSi <sub>2</sub>	ThSi <sub>2</sub>	33.3	19.4	47.3 <sup>a</sup>	0.42029(6)	-	1.4258(4)
	$\alpha$ Ce <sub>2</sub> Zn <sub>17</sub>	TbCu <sub>7</sub>	-	-	-	0.52571(3)	-	0.44397(7)
$\tau_2 + \text{Ce}_3\text{Zn}_{22} + \text{Ce}_2\text{Zn}_{17}$	$\tau_2$	AlB <sub>2</sub>	33.3	28.8	37.9 <sup>a</sup>	0.41816(1)	-	0.42592(2)
	Ce <sub>3</sub> Zn <sub>22</sub>	Ce <sub>3</sub> Zn <sub>22</sub>	12.1	87.7	0.2	0.89375(2)	-	2.13790(2)
	$\alpha$ Ce <sub>2</sub> Zn <sub>17</sub>	TbCu <sub>7</sub>	10.7	89.0	0.3	0.52482(6)	-	0.44295(2)
$\tau_2 + \text{CeZn}_5 + \text{Ce}_3\text{Zn}_{22}$	$\tau_2$	AlB <sub>2</sub>	33.3	28.9	37.8 <sup>a</sup>	0.41857(7)	-	0.4260(2)
	CeZn <sub>5</sub>	CaCu <sub>5</sub>	16.7	82.8	0.5	-	-	-
	Ce <sub>3</sub> Zn <sub>22</sub>	Ce <sub>3</sub> Zn <sub>22</sub>	12.2	87.4	0.4	0.8937(4)	-	2.138(1)
$\tau_2 + \text{CeZn}_5 + \tau_1$	$\tau_2$	AlB <sub>2</sub>	33.3	31.3	35.4 <sup>a</sup>	0.42206(5)	-	0.42334(6)
	CeZn <sub>5</sub>	CaCu <sub>5</sub>	-	-	-	0.54236(4)	-	0.42553(5)
	$\tau_1$	Ce <sub>7</sub> Zn <sub>23-x</sub>	22.8	70.6	6.6	-	-	-
$\tau_1 + \text{CeZn}_5 + \text{Ce}_{13}\text{Zn}_{58}$	$\tau_1$	Ce <sub>7</sub> Zn <sub>23-x</sub>	23.1	70.8	6.1	1.4882(2)	1.7238(4)	0.4491(1)
	CeZn <sub>5</sub>	CaCu <sub>5</sub>	16.6	83.3	0.1	0.54256(9)	-	0.42542(8)
	Ce <sub>13</sub> Zn <sub>58</sub>	Gd <sub>13</sub> Zn <sub>58</sub>	18.0	81.9	0.1	1.4622(2)	-	1.4178(3)
$\tau_1 + \text{Ce}_{13}\text{Zn}_{58} + \text{Ce}_3\text{Zn}_{11}$	$\tau_1$	Ce <sub>7</sub> Zn <sub>23-x</sub>	23.1	72.4	4.4	-	-	-
	Ce <sub>13</sub> Zn <sub>58</sub>	Gd <sub>13</sub> Zn <sub>58</sub>	17.9	81.9	0.2	-	-	-
	Ce <sub>3</sub> Zn <sub>11</sub>	La <sub>3</sub> Al <sub>11</sub>	21.5	78.3	0.2	-	-	-
$\tau_1 + \text{Ce}_3\text{Zn}_{11} + \text{CeZn}_3$	$\tau_1$	Ce <sub>7</sub> Zn <sub>23-x</sub>	23.1	73.6	3.3	-	-	-
	Ce <sub>3</sub> Zn <sub>11</sub>	La <sub>3</sub> Al <sub>11</sub>	21.4	78.4	0.2	0.4514(1)	0.8879(2)	1.3463(3)
	CeZn <sub>3</sub>	CeZn <sub>3</sub>	24.7	75.1	0.2	-	-	-
$\tau_1 + \text{CeZn}_2 + \text{CeZn}_3$	$\tau_1$	Ce <sub>7</sub> Zn <sub>23-x</sub>	23.3	72.8	4.0	1.5498(4)	1.7107(4)	0.4502(1)
	CeZn <sub>3</sub>	CeZn <sub>3</sub>	25.2	74.5	0.3	0.46254(6)	1.0448(5)	0.6641(1)
	CeZn <sub>2</sub>	CeCu <sub>2</sub>	32.9	63.8	3.3	0.46417(6)	0.7596(7)	0.7508(1)

$\tau_1 + \tau_7 + \tau_2$	$\tau_1$	$\text{Ce}_7\text{Zn}_{23-x}$	23.3	71.1	5.6	-	-	-
	$\tau_2$	$\text{AlB}_2$	33.3	48.4	18.3	0.4388(1)	-	0.39738(7)
	$\tau_7$	unknown	36.9	48.5	14.6	-	-	-

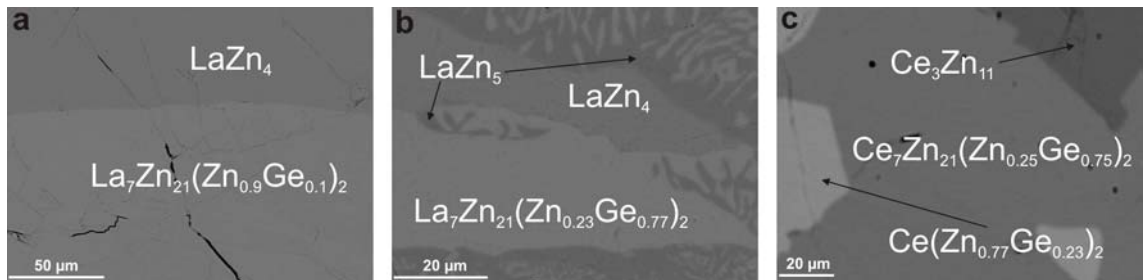
<sup>a</sup> The values are calculated from compositional dependence of corresponding lattice parameters (Figure 9).



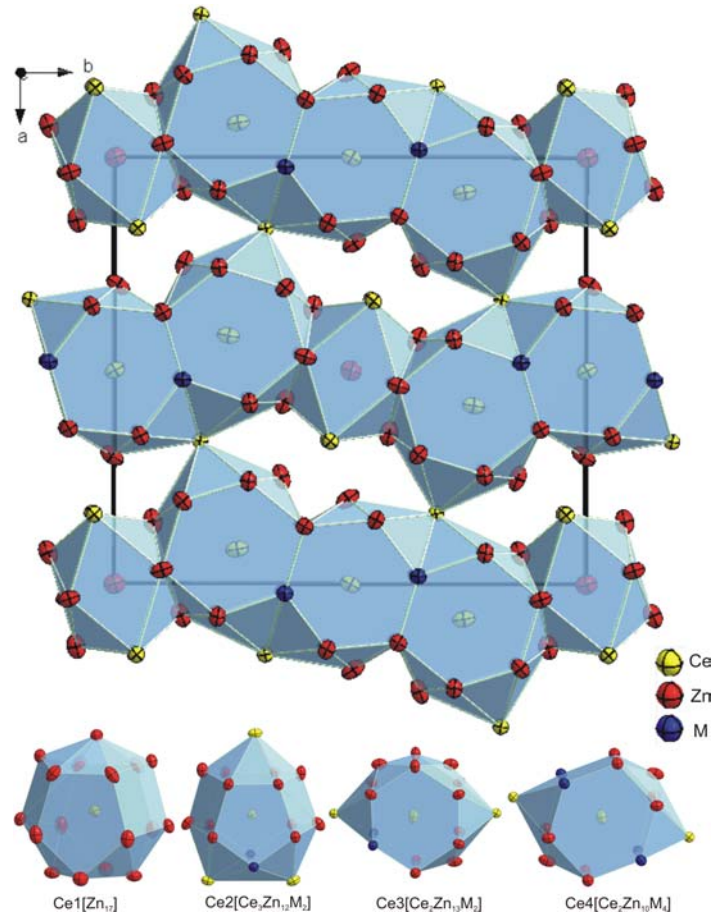
**Figure 1.** Crystal structure of  $\tau_5\text{-CeZn}(\text{Zn}_{1-x}\text{Si}_x)_2$ ,  $x = 0.71$  showing atoms with anisotropic displacement parameters from X-ray single crystal refinement.



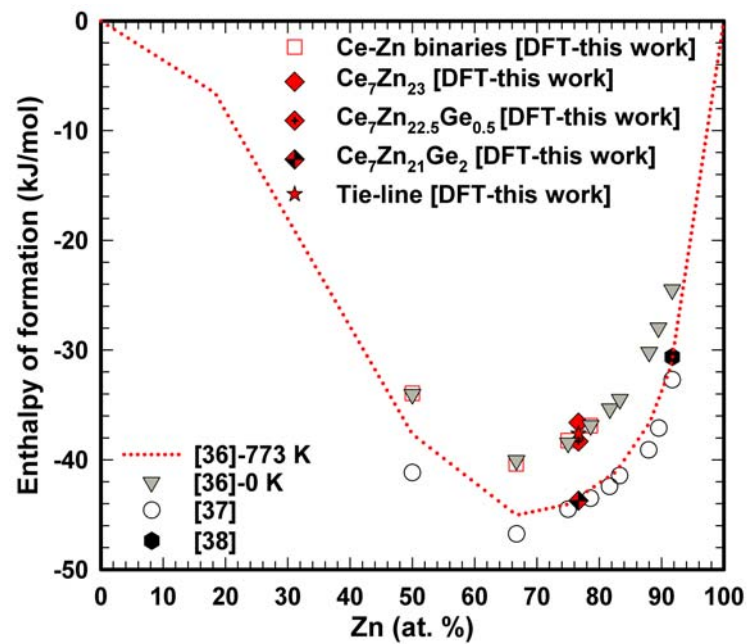
**Figure 2.** Crystal structure of  $\tau_6\text{-CeZn}_2(\text{Si}_{1-x}\text{Zn}_x)_2$ ,  $x = 0.30$  showing atoms with anisotropic displacement parameters from X-ray single crystal refinement.



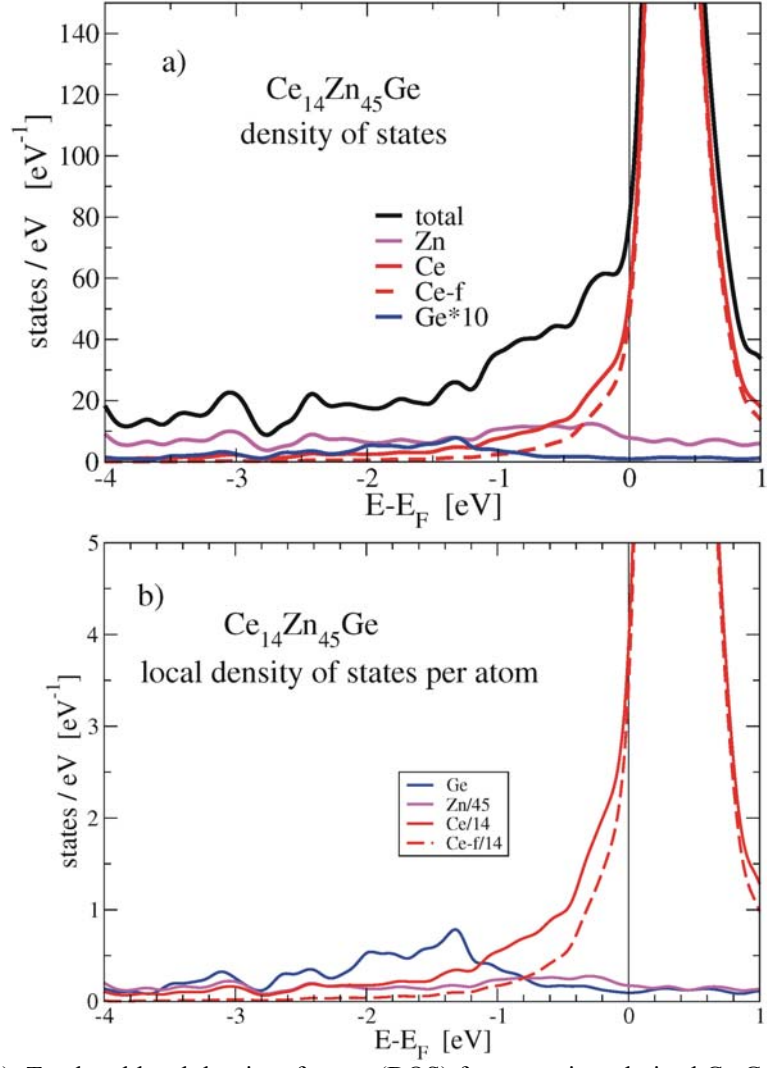
**Figure 3.** Micrographs of samples revealing the phase  $\{\text{La,Ce}\}_7\text{Zn}_{21}(\text{Zn}_{1-x}\text{Ge}_x)_2$  in contact with binary phases from the systems  $\{\text{La,Ce}\}\text{-Zn}$ .



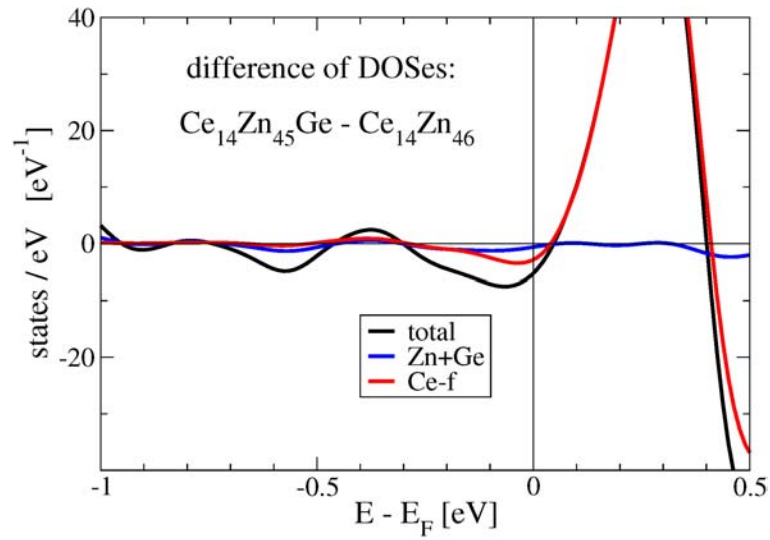
**Figure 4.** Crystal structure of  $\text{Ce}_7\text{Zn}_{21}(\text{Zn}_{1-x}\text{Ge}_x)_2$ ,  $x = 0.75$  projected along the  $c$ -axis and the coordination polyhedra for the Ce atoms. Atoms are drawn with anisotropic displacement parameters from X-ray single crystal refinement. Please note that (with respect to the previously incorrect standardization of  $\text{Ce}_7\text{Zn}_{21}(\text{Zn}_{1-x}\text{Si}_x)_2$ ) the origin of the unit cell is now shifted by  $(\frac{1}{2} \ 0 \ 0)$ .



**Figure 5.** Comparison between experimental and DFT derived adjusted calculated enthalpies of formation for Ce-Zn binaries and  $\text{Ce}_7\text{Zn}_{23-x}\text{Ge}_x$ .

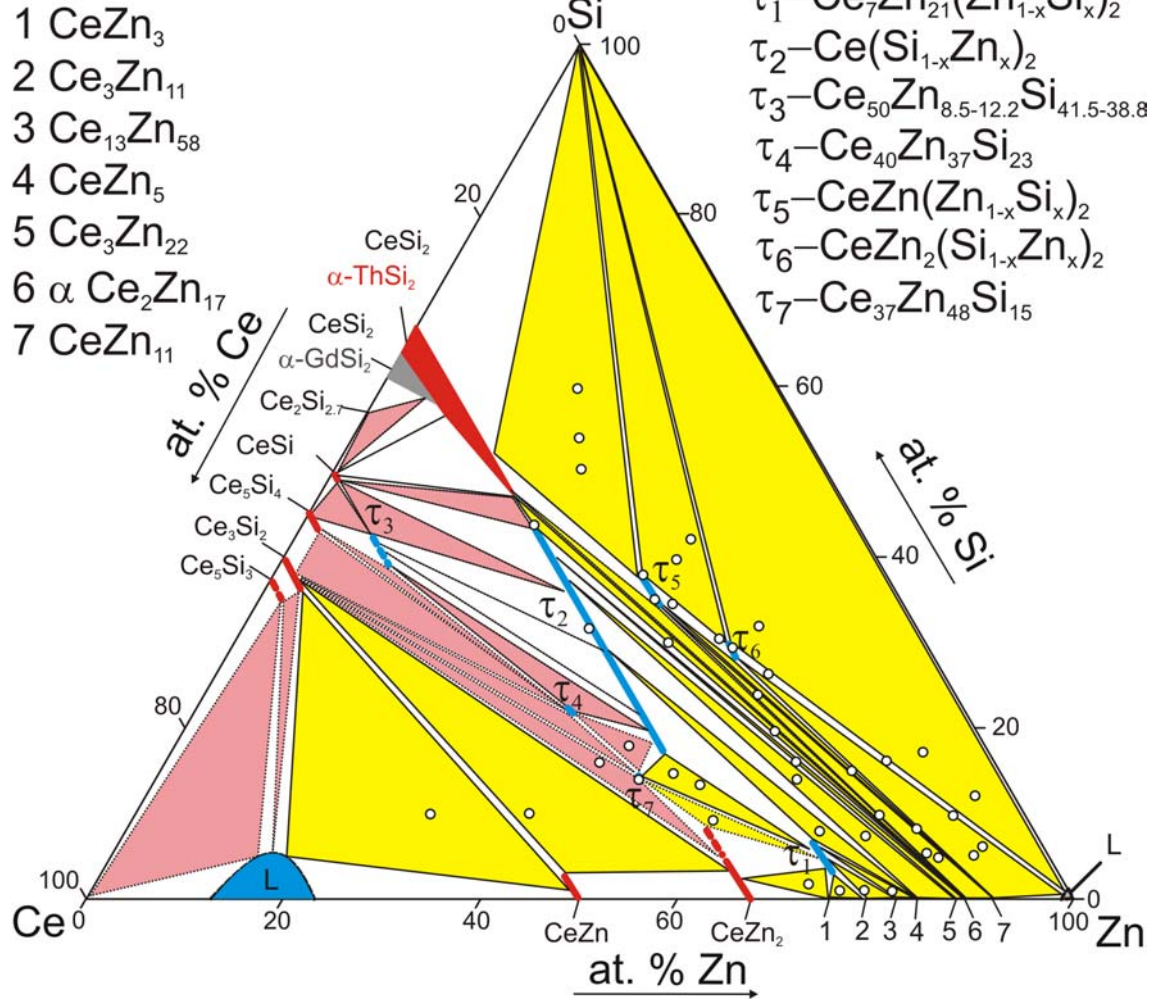


**Figure 6.** Panel (a): Total and local density of states (DOS) for non spin-polarized  $\text{Ce}_7\text{Ge}_{0.5}\text{Zn}_{22.5}$ . panel (b): local DOS per atom. For better visibility, the local DOS for Ge is multiplied by a factor of 10.

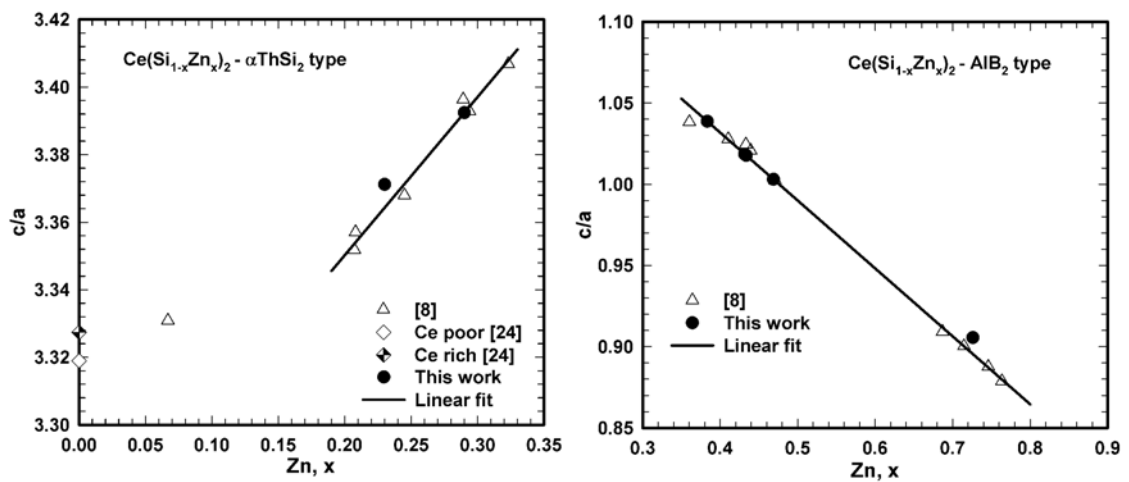


**Figure 7.** Differences of total and local density of states,  $\text{Ce}_7\text{Ge}_{0.5}\text{Zn}_{22.5}$  minus  $\text{Ce}_7\text{Zn}_{23}$ .

# Ce-Zn-Si 600°C

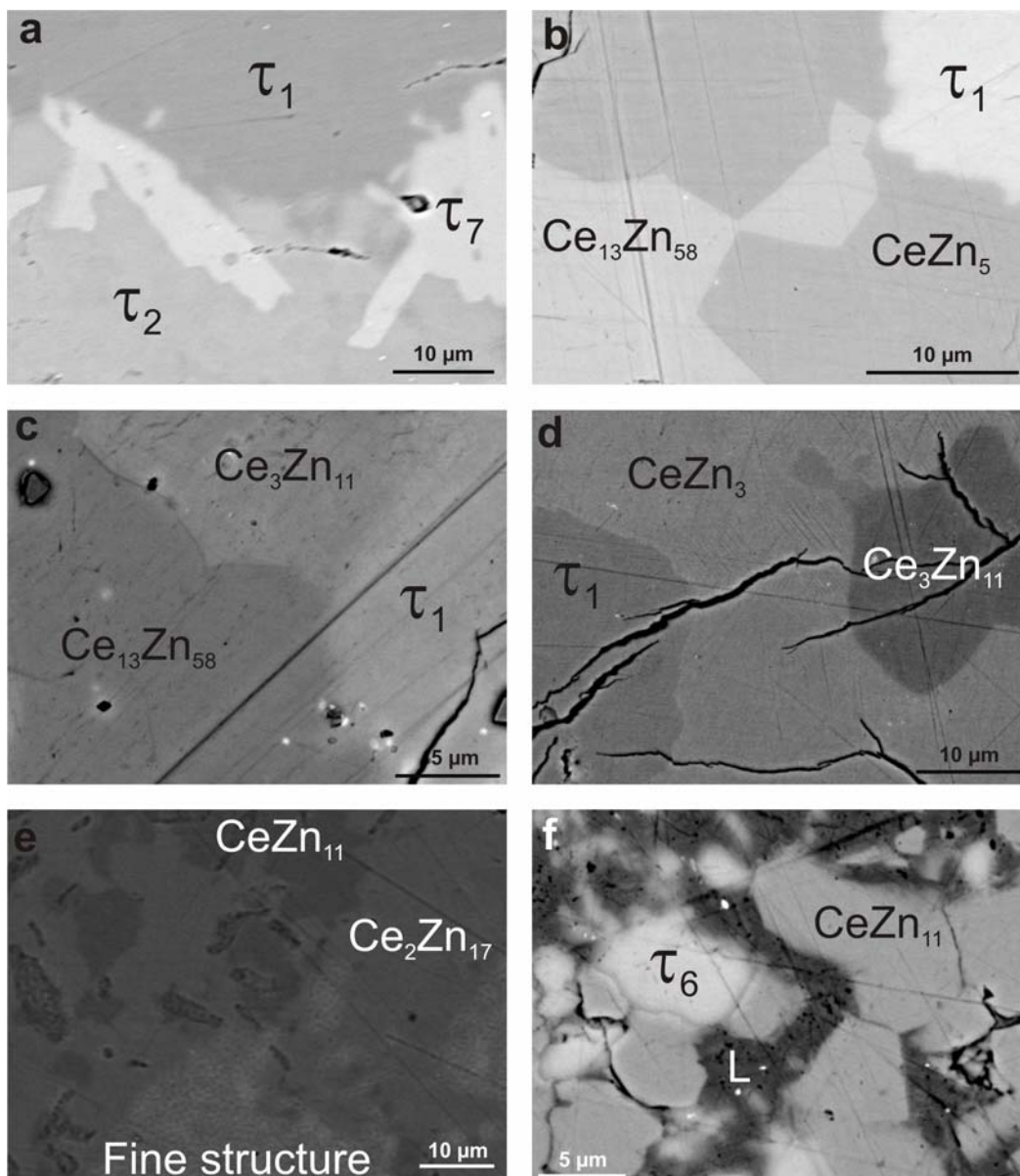


**Figure 8.** Partial isothermal section at 600°C (<33.3 at. % Ce). The circles represent nominal compositions of alloys. The pink three phase fields are taken from Ref. 8.

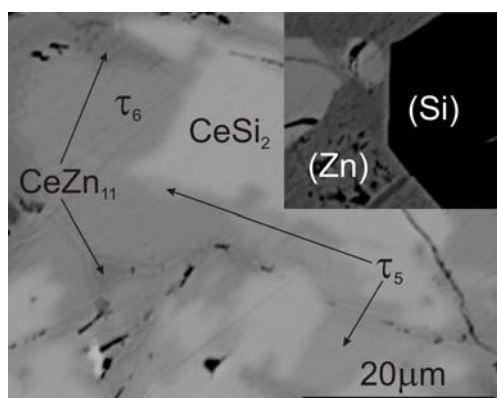


**Figure 9.** Compositional dependence of c/a ratio for  $\text{Ce}(\text{Si}_{1-x}\text{Zn}_x)_2$  with  $\alpha\text{ThSi}_2$  (left) and  $\text{AlB}_2$  (right) type.

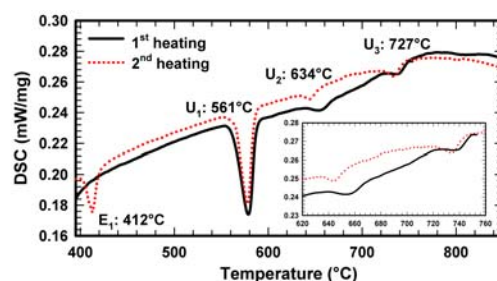




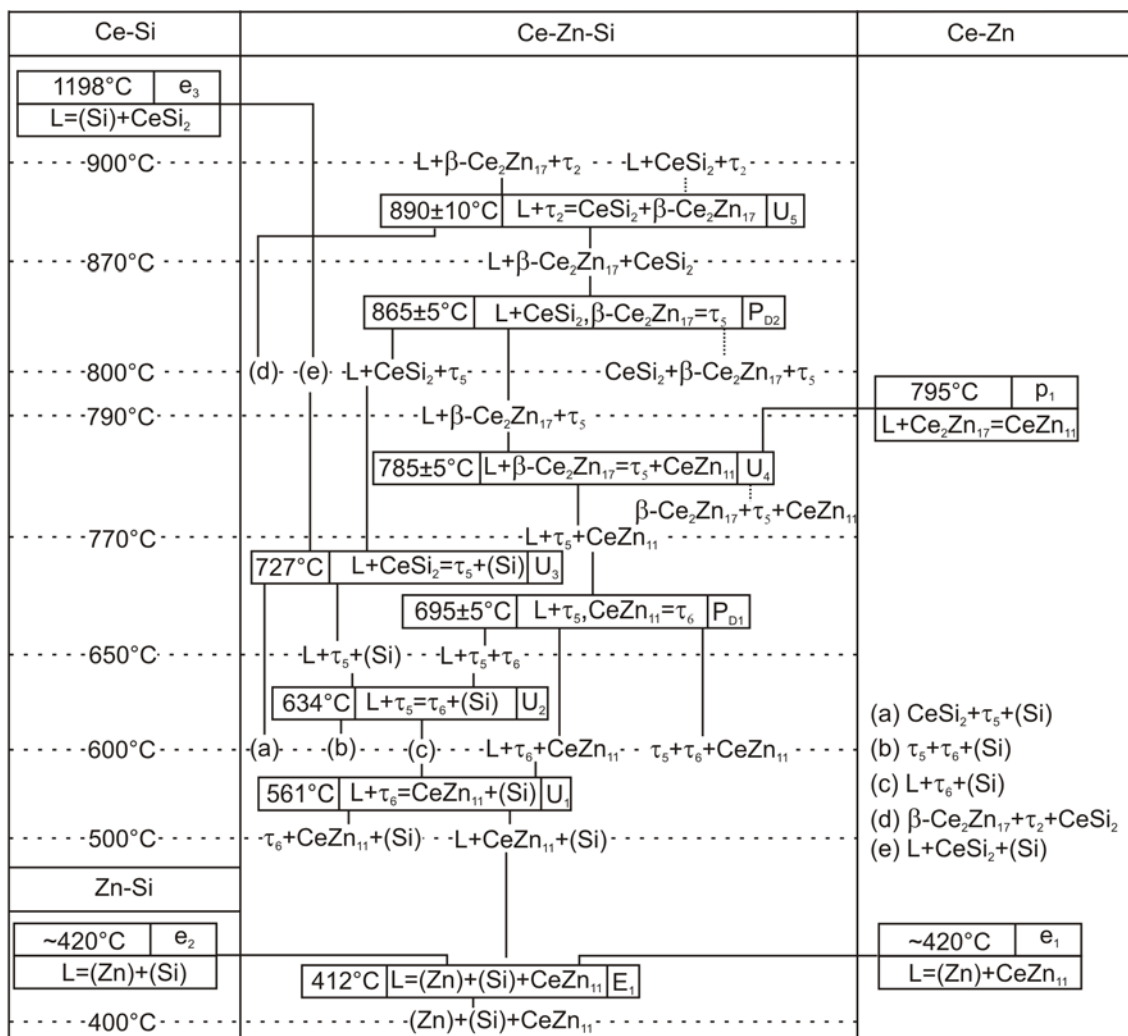
**Figure 10.** Selected micrograph of Ce-Zn-Si alloys annealed at 600°C: (a)  $\text{Ce}_{32}\text{Zn}_{54}\text{Si}_{14}$ , (b)  $\text{Ce}_{18}\text{Zn}_{81}\text{Si}_1$ , (c)  $\text{Ce}_{21}\text{Zn}_{78}\text{Si}_1$ , (d)  $\text{Ce}_{23}\text{Zn}_{76}\text{Si}_1$ , (e) diffusion couple  $\text{Ce}_{70}\text{Si}_{30}\text{-Zn}$  (12 hours), and (f) diffusion couple  $\text{Ce}_{50}\text{Si}_{50}\text{-Zn}$  (12 hours) (nominal composition in at. %).



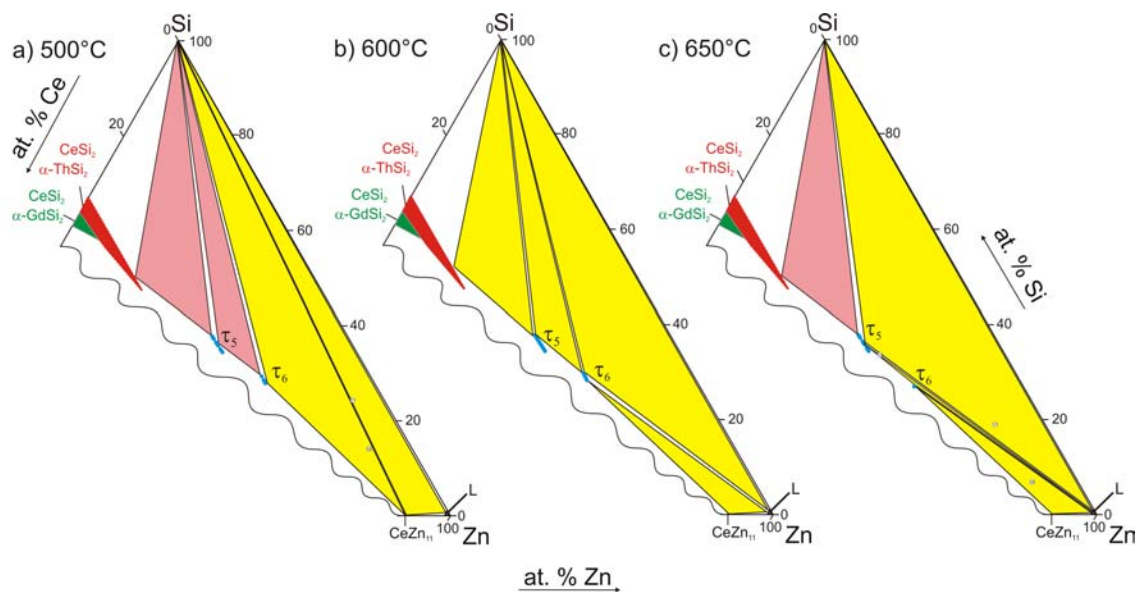
**Figure 11.** Micrograph of  $\tau_5$  after DTA, showing sequence of crystallization:  $\text{CeSi}_2\text{-}\tau_5\text{-}\tau_6$ .



**Figure 12.** DTA curve of alloy  $\text{Ce}_{5.9}\text{Zn}_{59.8}\text{Si}_{34.3}$ .



**Figure 13.** Scheil diagram for the Zn-rich corner



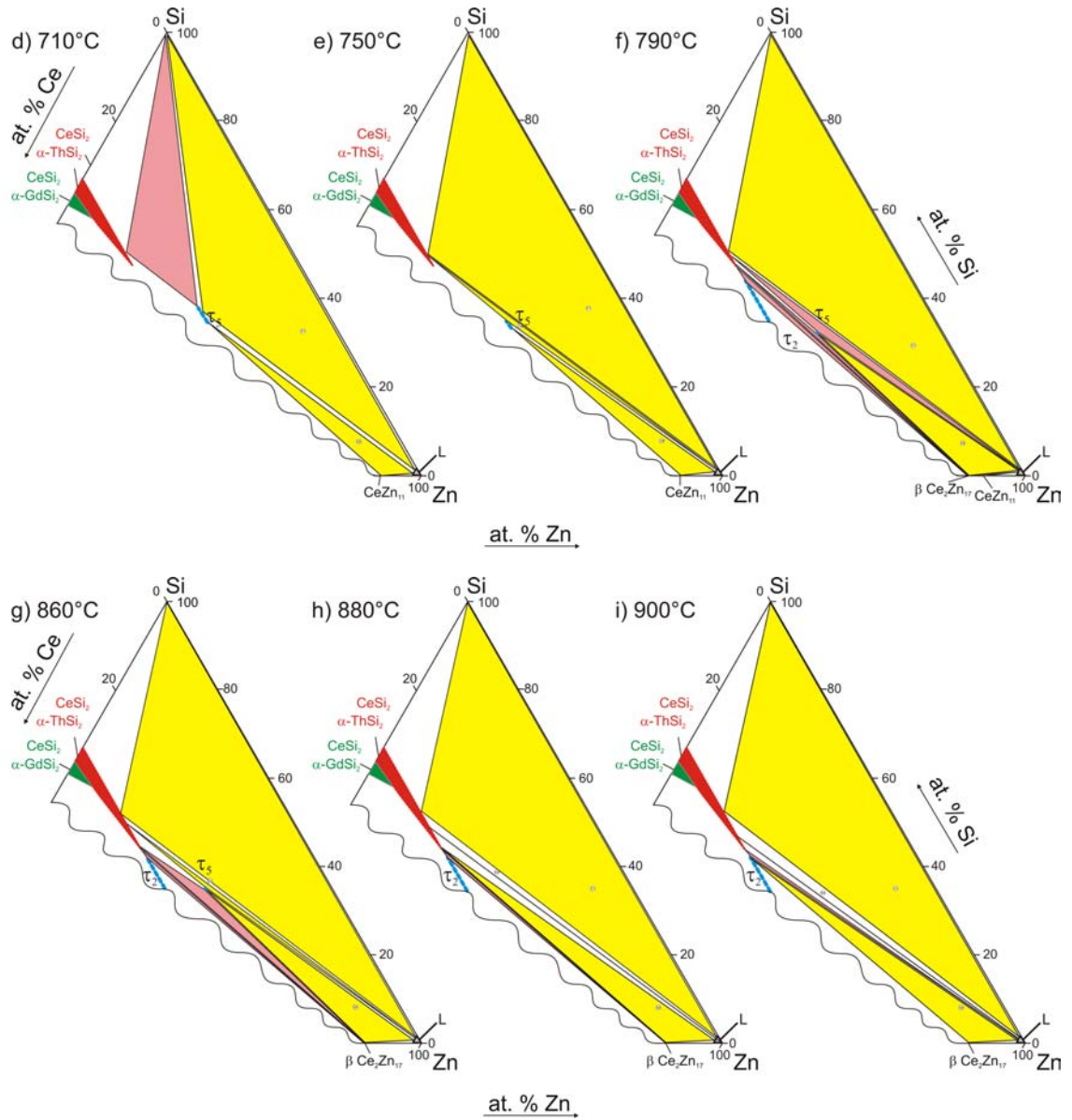


**Figure 14.** Partial isothermal sections in the Zn-corner at various temperatures..

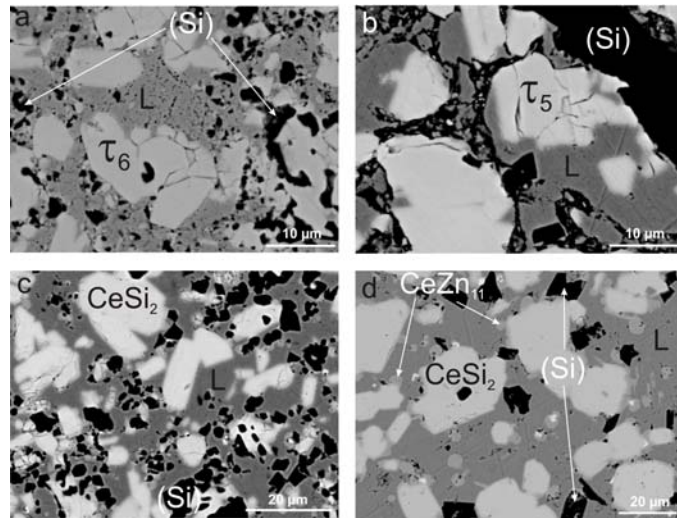


**Figure 15.** Microstructure of alloy  $\text{Ce}_{5.9}\text{Zn}_{59.8}\text{Si}_{34.3}$  annealed at different temperatures: (a) 600°C, (b) 650°C, (c) 750°C, (d) 900°C for one day each under Argon.



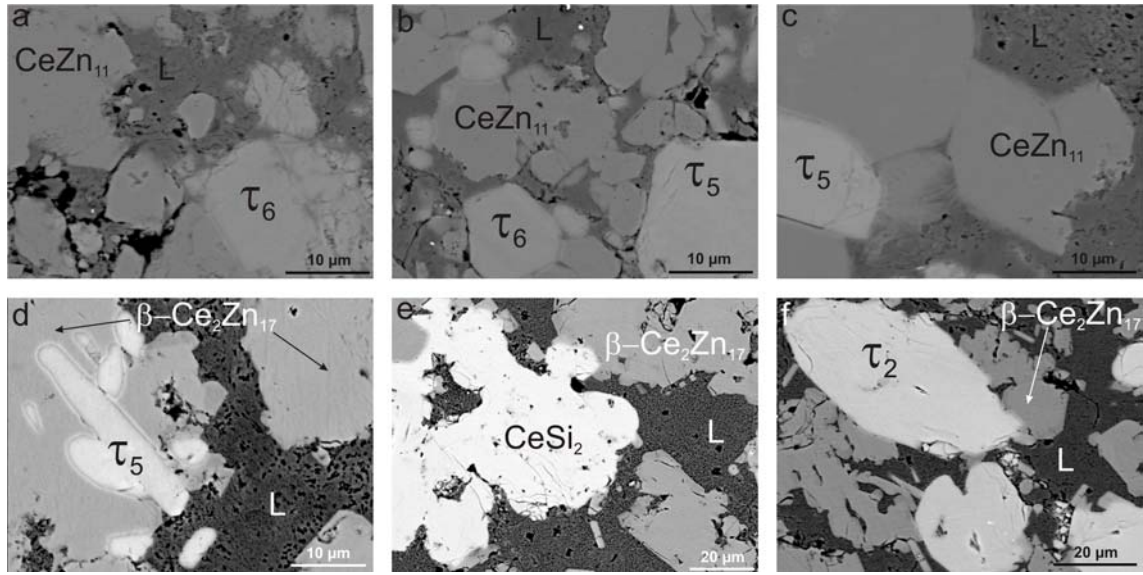


**Figure 16.** Microstructure of alloy  $\text{Ce}_{7.6}\text{Zn}_{78.4}\text{Si}_{14}$  annealed at different temperatures: (a) 650°C, (b) 710°C, (c) 750°C, (d) 790°C, (e) 880°C, and (f) 900°C for one day each under Argon.

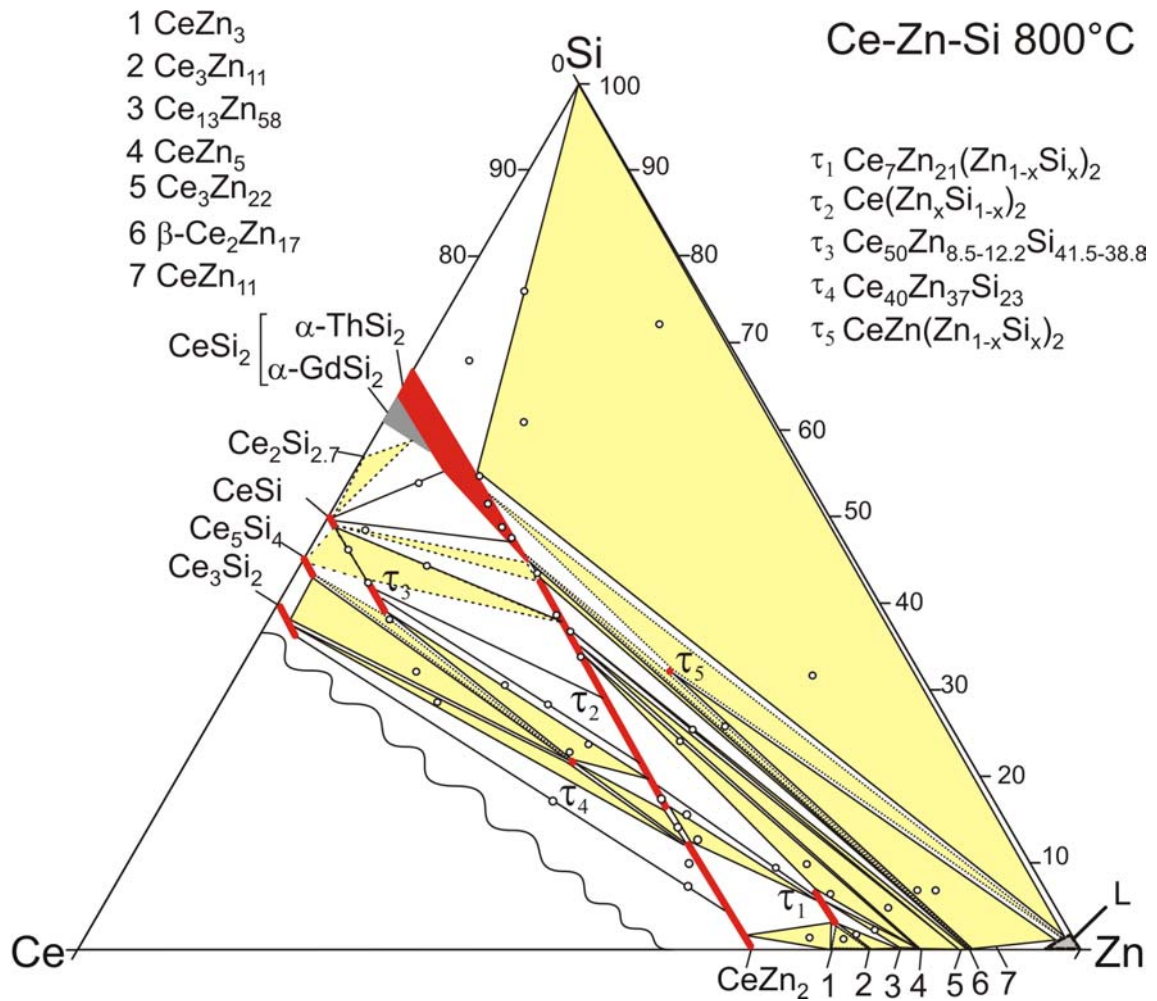


**Figure 17.** Isothermal section at 800°C (modified after ref. 8; see text).

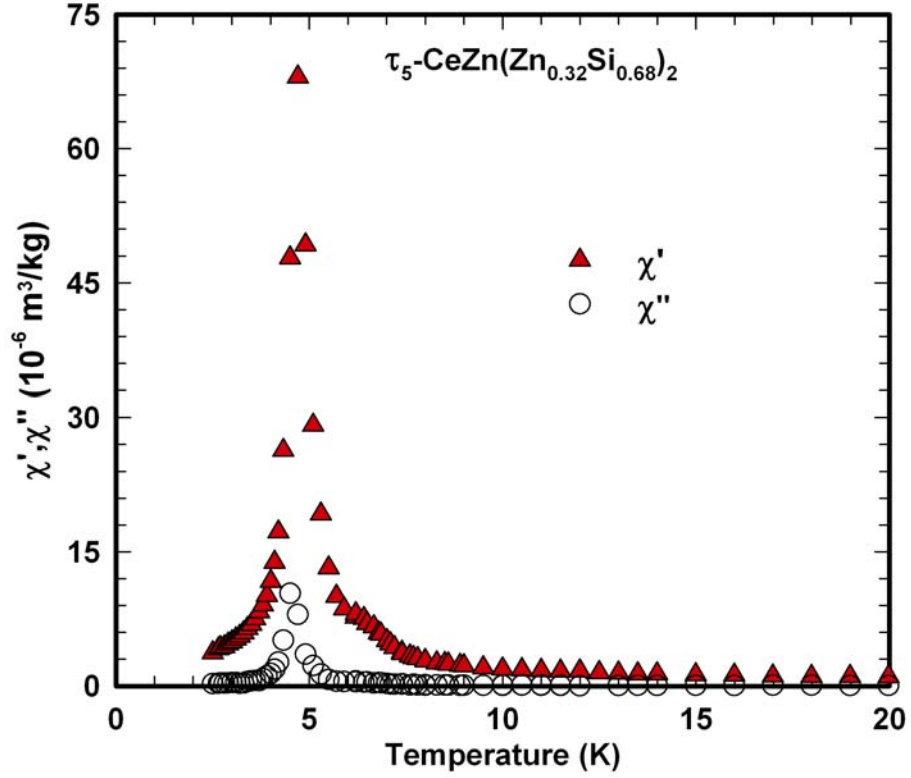


**Figure 18.** Temperature dependent in-phase and out-of-phase ac susceptibility components,  $\chi'$  and  $\chi''$ , measured on polycrystalline  $\tau_5$ -CeZn(Zn<sub>0.32</sub>Si<sub>0.68</sub>)<sub>2</sub> with a field amplitude of 325 A/m and frequency of 100 Hz.

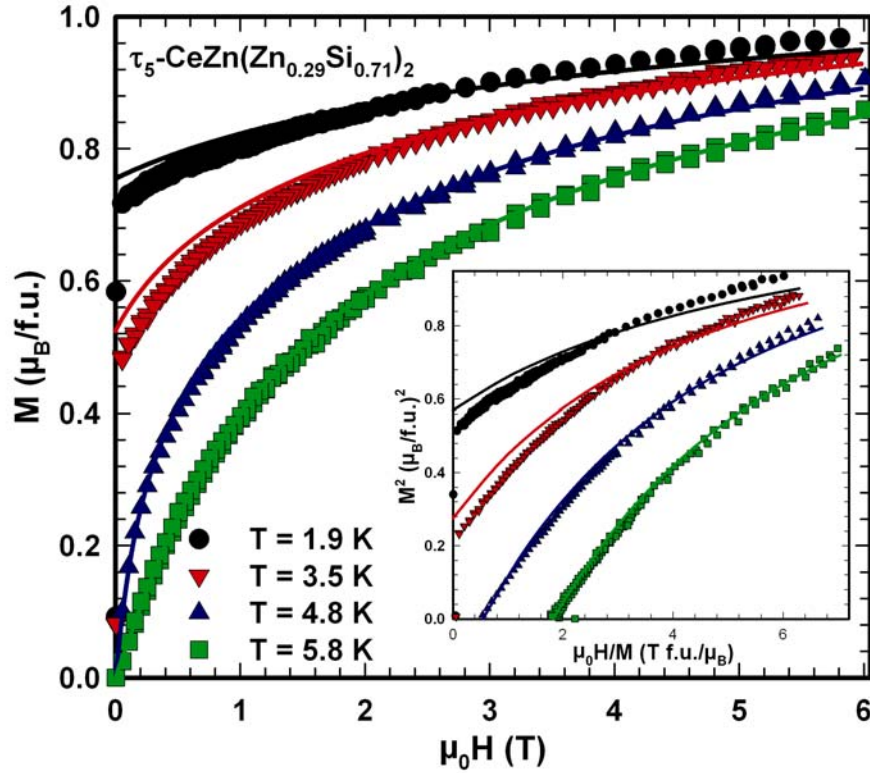


**Figure 19.** Isothermal magnetisation measurements of single crystalline  $\tau_5$ -CeZn(Zn<sub>0.29</sub>Si<sub>0.71</sub>)<sub>2</sub>; the inset shows the corresponding Arrott plot,  $M^2$  vs.  $H/M$ . The solid lines display a model calculation in terms of the resonant level model by Schotte and Schotte.

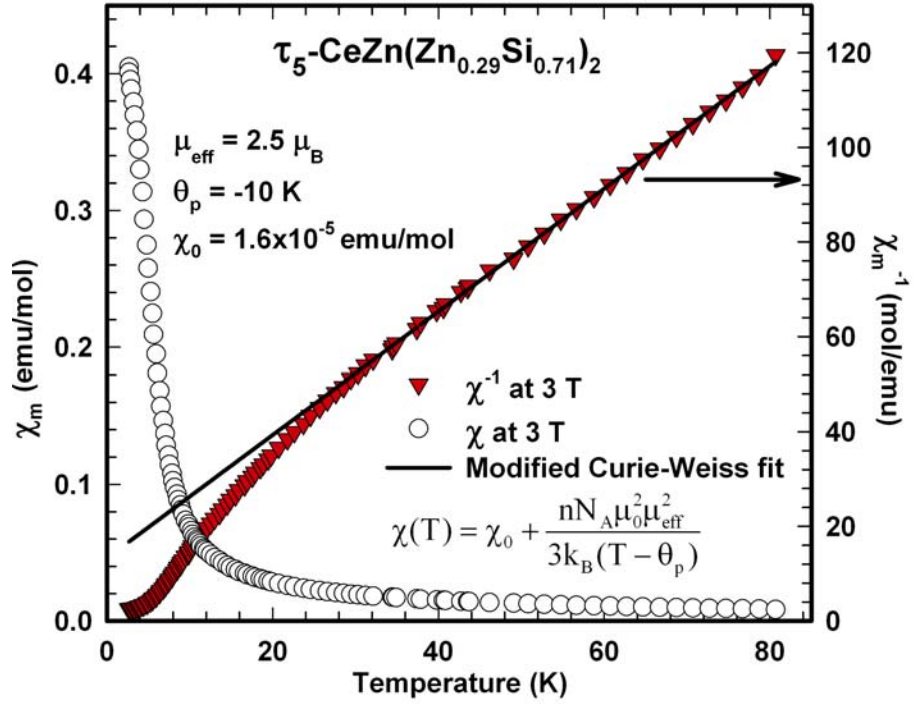


**Figure 20.** Temperature dependent dc magnetic susceptibility,  $\chi(T)$  at left axis, and inverse magnetic susceptibility,  $1/\chi(T)$  at right axis, of freely rotating  $\tau_5$ -CeZn(Zn<sub>0.29</sub>Si<sub>0.71</sub>)<sub>2</sub> single crystals measured at 3 T; the solid line displays a modified Curie-Weiss fit of the inverse susceptibility.

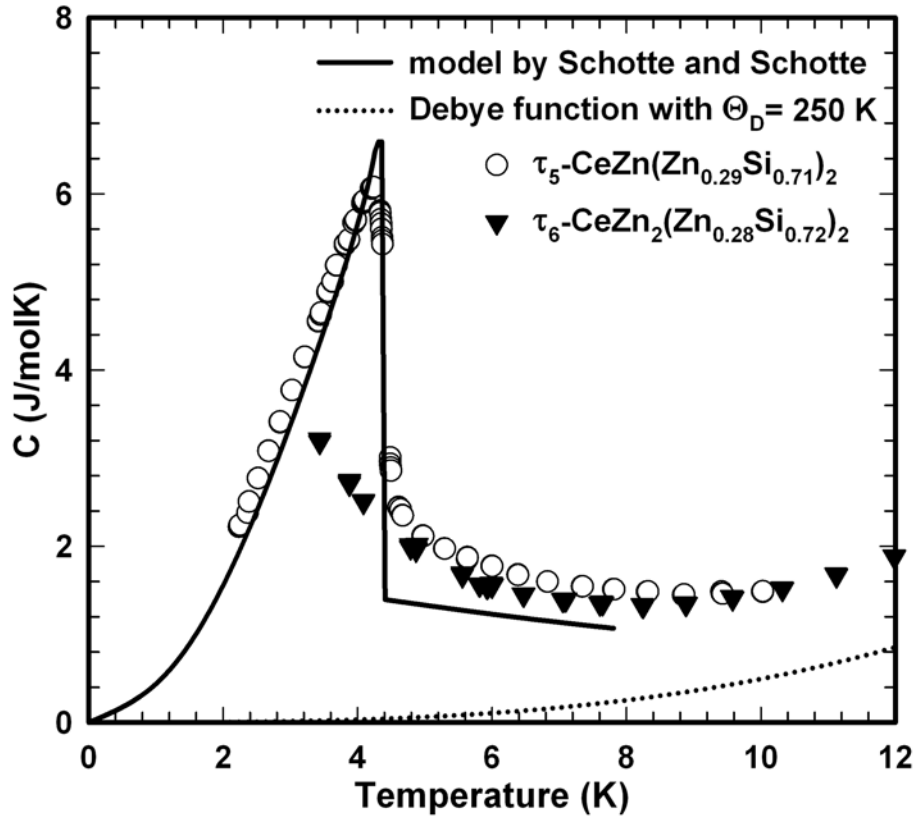


**Figure 21.** Temperature dependent specific heat of  $\tau_5$ -CeZn(Zn<sub>0.29</sub>Si<sub>0.71</sub>)<sub>2</sub> single crystals and polycrystalline  $\tau_6$ -CeZn<sub>2</sub>(Zn<sub>0.28</sub>Si<sub>0.72</sub>)<sub>2</sub>; the solid and dotted lines refer to the analysis of  $\tau_5$  data in terms of the resonant level model by Schotte and Schotte and a tentative phonon contribution represented by a Debye function, respectively.

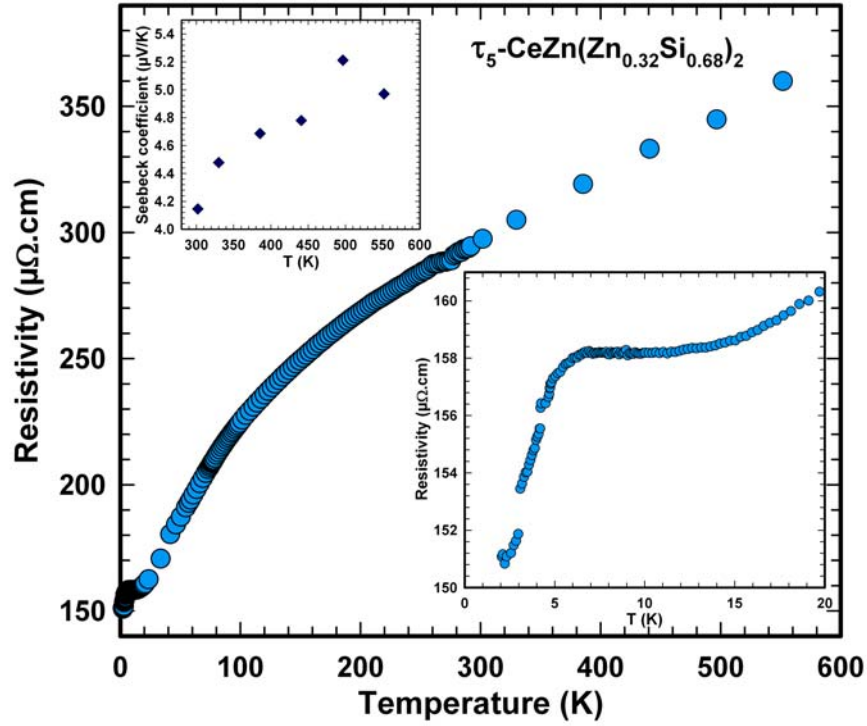


**Figure 22.** Temperature dependent electrical resistivity of polycrystalline  $\tau_5$ -CeZn(Zn<sub>0.32</sub>Si<sub>0.68</sub>)<sub>2</sub>. Bottom right inset shows the kink at the ordering temperature; top left inset shows the Seebeck coefficient above room temperature.

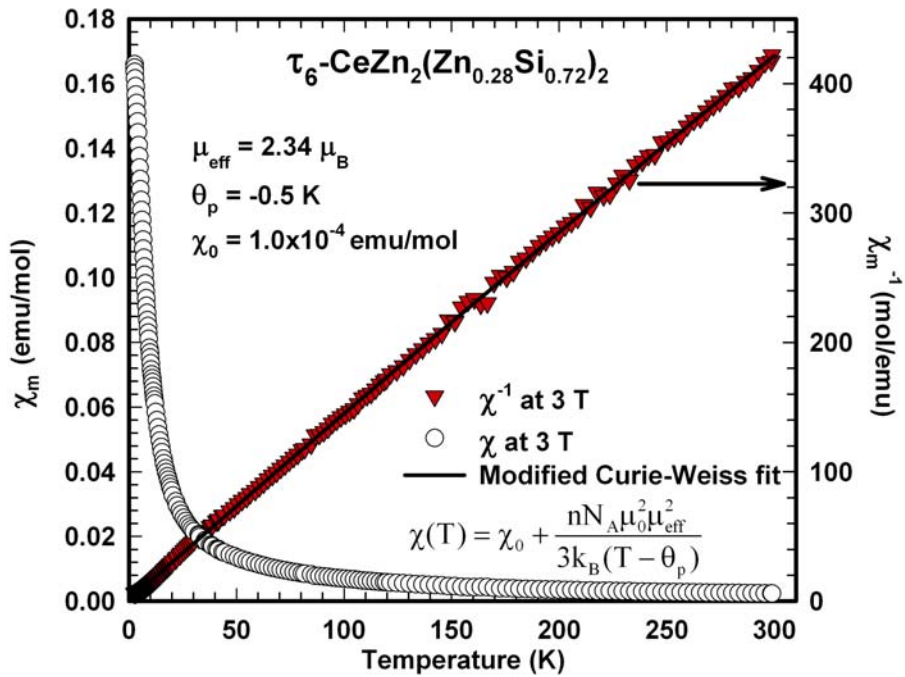


**Figure 23.** Temperature dependent dc magnetic susceptibility,  $\chi(T)$  at left axis, and inverse magnetic susceptibility,  $1/\chi(T)$  at right axis, of polycrystalline  $\tau_6$ -CeZn<sub>2</sub>(Zn<sub>0.28</sub>Si<sub>0.72</sub>)<sub>2</sub> measured at 3T; the solid line displays a modified Curie-Weiss fit of the inverse susceptibility.

## Supplementary

**Table S1.** Crystallographic data of unary and binary boundary solid phases of the system Ce-Zn-Si.

Phase Temperature range (°C)	Space group, Prototype	Lattice parameters (nm)			Comments
		a	b	c	
(δCe) 798-700 <sup>1</sup>	$Im\bar{3}m$ W	0.412	-	-	<sup>1</sup> -
(γCe) <726 <sup>1</sup>	$Fm\bar{3}m$ Cu	0.51610	-	-	<sup>1</sup>
(Zn) <420 <sup>1</sup>	$P6_3/mmc$	0.2665	-	0.4947	<sup>1</sup> -
(Si) <1414 <sup>1</sup>	$Fd\bar{3}m$ C (Diamond)	0.543110	-	-	<sup>2</sup>
CeSi <sub>2</sub> <1725 <sup>3</sup>	$Imma$ $\alpha$ GdSi <sub>2</sub>	0.4189(1)	-	0.4109(1)	Ce <sub>37.4</sub> Si <sub>62.6</sub> <sup>3</sup>
CeSi <sub>2</sub> ~1575 <sup>3</sup> Ce(Zn <sub>x</sub> Si <sub>1-x</sub> ) <sub>2</sub>	$I4_1/amd$ O2 $\alpha$ ThSi <sub>2</sub>	0.4192(1) 0.4201(1) 0.42029(6)	-	1.3913(5) 1.4312(7) 1.4258(4)	Ce <sub>33.3</sub> Si <sub>66.7</sub> <sup>3</sup> $x_{\max}=0.32$ at 800°C <sup>4</sup> $x_{\max}=0.30$ , at 600°C [this work]
CeSi <1630 <sup>3</sup>	$Pnma$ FeB	0.8298(4)	-	0.3961(2)	Ce <sub>49.9</sub> Si <sub>50.1</sub> <sup>3</sup>
Ce <sub>5</sub> Si <sub>4</sub> <1500 <sup>3</sup>	$P4_12_12$ Zr <sub>5</sub> Si <sub>4</sub>	0.7936(1)	-	1.5029(5)	Ce <sub>55.6</sub> Si <sub>44.4</sub> <sup>3</sup>
Ce <sub>3</sub> Si <sub>2</sub> <1335 <sup>3</sup>	$P4/mbm$ U <sub>3</sub> Si <sub>2</sub>	0.7780(6)	-	0.4367(6)	<sup>3</sup>
Ce <sub>5</sub> Si <sub>3</sub> <1260 <sup>3</sup>	$I4/mcm$ Cr <sub>5</sub> B <sub>3</sub>	0.7878(4)	-	1.067(1)	<sup>3</sup>
Ce <sub>2</sub> Si <sub>3-x</sub>	$Cmcm$ V <sub>2</sub> B <sub>3</sub>	0.44035	2.48389	0.39517	$x=0.3$ <sup>5</sup>
CeSi <sub>5</sub> <827	$Immm$ LaGe <sub>5</sub>	0.37774839	0.60189(4)	0.92979(6)	<sup>6</sup> high pressure phase; 10GPa
Ce <sub>2</sub> Si <sub>7</sub> <1127	$Cmmm$ Ce <sub>2</sub> Si <sub>7</sub>	0.70893(7)	0.99644(7)	0.44868(4)	<sup>6</sup> high pressure phase; 10GPa
CeZn <825 <sup>1</sup>	$Pm\bar{3}m$ CsCl	0.3704(1) 0.37059(2)	-	-	<sup>7</sup> <sup>8</sup>
CeZn <sub>2</sub> <875 <sup>1</sup> Ce(Zn <sub>1-x</sub> Si <sub>x</sub> ) <sub>2</sub>	$Imma$ CeCu <sub>2</sub>	0.46393(8) 0.4583(3) 0.46417(6)	0.7544(1) 0.7568(5) 0.7596(7)	0.7506(1) 0.759(5) 0.7508(1)	<sup>8</sup> $x_{\max}=0.18$ <sup>4</sup> $x=0.05$ at 600°C [this work]
CeZn <sub>3</sub> <820 <sup>1</sup>	$Cmcm$ CeZn <sub>3</sub>	0.4620(5) 0.46324(5)	1.0440(5) 1.0452(1)	0.6640(5) 0.66557(6)	<sup>7</sup> <sup>8</sup>
Ce <sub>3</sub> Zn <sub>11</sub> <840 <sup>1</sup>	$Immm$ La <sub>3</sub> Al <sub>11</sub>	0.45215 0.45242(2)	0.88855 0.88942(3)	1.3463 1.34754(4)	<sup>7</sup> SC <sup>8</sup>
Ce <sub>13</sub> Zn <sub>58</sub> <870 <sup>1</sup>	$P6_3/mmc$ Gd <sub>13</sub> Zn <sub>58</sub>	1.4638(1) 1.4616(1)	-	1.4158(1) 1.4173(1)	<sup>9</sup> <sup>8</sup>
CeZn <sub>5</sub> <885 <sup>1</sup> CeZn <sub>5+y</sub>	$P6/mmm$ CaCu <sub>5</sub>	0.54163(5) 0.54082(1) 0.54163(5)	-	0.42647(5) 0.42798(1) 0.42647(5)	<sup>7</sup> <sup>8</sup> 0.017≤y≤0.046 <885°C <sup>10</sup>
Ce <sub>3</sub> Zn <sub>22</sub> <960 <sup>1</sup>	$I4_1/amd$ Ce <sub>3</sub> Zn <sub>22</sub>	0.897(1) 0.8936(2)	-	2.133(5) 2.1380(5)	<sup>11</sup> SC <sup>8</sup>
β Ce <sub>2</sub> Zn <sub>17</sub> <980 <sup>1</sup> 980~750 <sup>8</sup>	$R\bar{3}m$ Th <sub>2</sub> Zn <sub>17</sub>	0.9090(5) 0.90916(4)	-	1.32844(7) 1.32861(1)	<sup>7</sup> <sup>8</sup>
α Ce <sub>2</sub> Zn <sub>17</sub> α Ce <sub>1+x</sub> Zn <sub>5+2x</sub> <~750 <sup>8</sup>	$P6_3/mmc$ TbCu <sub>7</sub>	0.9088(4) 0.52424(2)	-	0.8856(5) 0.44274(1)	<sup>12</sup> $x=0.33$ <sup>8</sup>
CeZn <sub>11</sub> <795 <sup>1</sup>	$I4_1/amd$ BaCd <sub>11</sub>	1.0658(6) 1.06630(1)	-	0.6862(8) 0.686644(7)	<sup>13</sup> <sup>8</sup>

**Table S2.** Interatomic distances (<0.421 nm) in  $\tau_5$ -CeZn(Zn<sub>1-x</sub>Si<sub>x</sub>)<sub>2</sub>, x = 0.71 and  $\tau_6$ -CeZn<sub>2</sub>(Si<sub>1-x</sub>Zn<sub>x</sub>)<sub>2</sub>, x = 0.30).

$\tau_5$ -CeZn(Zn <sub>1-x</sub> Si <sub>x</sub> ) <sub>2</sub> , x = 0.71						$\tau_6$ -CeZn <sub>2</sub> (Si <sub>1-x</sub> Zn <sub>x</sub> ) <sub>2</sub> , x = 0.30		
Atom 1	Atom 2	Distance	Atom 1	Atom 2	Distance	Atom 1	Atom 2	Distance
Ce CN=21	M1 (2x)	0.31726		Ce (2x)	0.31726	Ce CN=22	M (8x)	0.31901
	M1 (4x)	0.31916		Ce (4x)	0.31916		Zn1 (8x)	0.33555
	M2 (4x)	0.31940					M (2x) <sup>a</sup>	(0.40460)
	Zn3 (2x)	0.33470	M2 CN=9	M1 (1x)	0.23975		Ce (4x) <sup>a</sup>	(0.41757)
	Zn3 (2x)	0.33714		Zn3 (2x)	0.25263	Zn1 CN=12	M (4x)	0.25245
	M2 (1x) <sup>a</sup>	(0.40539)		Zn3 (2x)	0.25381		Zn1 (4x)	0.29527
	Ce (2x) <sup>a</sup>	(0.41324)	Zn3 CN=16	Ce (4x)	0.31940		Ce (4x)	0.33555
	Ce (2x) <sup>a</sup>	(0.41619)		M2 (2x)	0.25263	M CN=9	M (1x)	0.24152
	Ce (2x) <sup>a</sup>	(0.42079)		M2 (2x)	0.25381		Zn1 (4x)	0.25245
M1 CN=9	M1 (2x)	0.23917		Zn3 (4x)	0.29592		Ce (4x)	0.31901
	M2 (1x)	0.23975		Ce (2x)	0.33470			
				Ce (2x)	0.33714			

<sup>a</sup> Contribution of these atoms to the Dirichlet domain is less than 2%, which indicates rather weak bonding.

## References

- 1 *Pauling File Binary Edition, Version 1.0, Release 2002/1*, ASM international, Materials Park, OH, USA, 2002.
- 2 G. Celotti, D. Nobili and P. Ostojica, *J. Mater. Sci.*, 1974, **9**, 821–828.
- 3 M. V. Bulanova, P. N. Zheltov, K. A. Meleshevich, P. A. Saltykov and G. Effenberg, *J. Alloys Compd.*, 2002, **345**, 110–115.
- 4 Z. Malik, A. Grytsiv, P. Rogl and G. Giester, *Intermetallics*, 2013, **36**, 118–126.
- 5 P. Schobinger-Papamantellos and K. H. J. Buschow, *J. Alloys Compd.*, 1993, **198**, 47–50.
- 6 A. Wosylus, K. Meier, Y. Prots, W. Schnelle, H. Rosner, U. Schwarz and Y. Grin, *Angew. Chem.*, 2010, **122**, 9187–9191.
- 7 P. Villars and K. Cenzual, *Pearson's Crystal Data–Crystal Structure Database for Inorganic Compounds, release 2014/15*, ASM International, Materials Park, OH, USA, 2014.
- 8 Z. Malik, O. Sologub, G. Giester and P. Rogl, *J. Solid State Chem.*, 2011, **184**, 2840–2848.
- 9 S. Piao, C. P. Gómez and S. Lidin, *Z. Krist.*, 2006, **221**, 391–401.
- 10 B. G. Lott and P. Chiotti, *Acta Crystallogr.*, 1966, **20**, 733–738.
- 11 P. I. Kripyakevich, Y. B. Kuz'ma and N. S. Ugrin, *J. Struct. Chem.*, 1968, **8**, 632–633.
- 12 A. Iandelli and A. Palenzona, *J. -Common Met.*, 1967, **12**, 333–343.
- 13 O. Zelinska, M. Conrad and B. Harbrecht, *Z. Krist. - New Cryst. Struct.*, 2004, **219**, 357–358.



## Chapter 6 BaAl<sub>4</sub> Derivative Phases in the Sections {La,Ce}Ni<sub>2</sub>Si<sub>2</sub>- {La,Ce}Zn<sub>2</sub>Si<sub>2</sub>: Phase Relations, Crystal Structures and Physical Properties

F. Failamani<sup>a,b</sup>, Z. Malik<sup>b</sup>, F. Kneidinger<sup>c</sup>, A. Grytsiv<sup>a,d</sup>, H. Michor<sup>c</sup>, L. Salamakha<sup>c</sup>, E. Bauer<sup>c,d</sup>, P. Rogl<sup>a,d</sup> and G. Giester<sup>e</sup>

<sup>a</sup>*Institute of Materials Chemistry and Research, University of Vienna, Währingerstrasse 42, A-1090 Vienna, Austria*

<sup>b</sup>*Institute of Physical Chemistry, University of Vienna, Währingerstrasse 42, A-1090 Vienna, Austria*

<sup>c</sup>*Institute of Solid State Physics, Vienna University of Technology, Wiedner Hauptstrasse 8-10, A-1040 Vienna, Austria*

<sup>d</sup>*Christian Doppler Laboratory for Thermoelectricity, Vienna, Austria*

<sup>e</sup>*Institute of Mineralogy and Crystallography, University of Vienna, Althanstrasse 14, A-1090 Vienna, Austria*

(to be submitted)

Contributions to this paper:

- F. Failamani : samples preparation, characterization and analysis, writing the paper  
Z. Malik : initial single crystal and phase equilibria study in the quaternary {La,Ce}-(Ni,Zn)-Si system  
F. Kneidinger : resistivity and specific heat measurements  
A. Grytsiv : discussions, preliminary single crystal test, comments, proofreading  
H. Michor : specific heat and magnetic susceptibility measurement and analysis, discussions, comments, proofreading  
L. Salamakha : resistivity measurements  
E. Bauer : physical properties data analysis, discussions, comments, proofreading  
P. Rogl : discussions, comments, proofreading  
G. Giester : single crystal data collections

## Abstract

Phase relations and crystal structures have been evaluated within the sections  $\text{LaNi}_2\text{Si}_2$ - $\text{LaZn}_2\text{Si}_2$  and  $\text{CeNi}_2\text{Si}_2$ - $\text{CeZn}_2\text{Si}_2$  at  $800^\circ\text{C}$  using electron microprobe analysis and X-ray powder and single crystal structure analyses. Although the systems  $\text{La-Zn-Si}$  and  $\text{Ce-Zn-Si}$  at  $800^\circ\text{C}$  do not reveal compounds such as “ $\text{LaZn}_2\text{Si}_2$ ” or “ $\text{CeZn}_2\text{Si}_2$ ”, solid solutions  $\{\text{La,Ce}\}(\text{Ni}_{1-x}\text{Zn}_x)_2\text{Si}_2$  exist with  $\text{Ni/Zn}$  substitution starting from  $\{\text{La,Ce}\}\text{Ni}_2\text{Si}_2$  ( $\text{ThCr}_2\text{Si}_2$ -type) up to  $0 \leq x \leq 0.18$ . For higher Zn-contents  $0.22 \leq x \leq 0.55$  the solutions adopt the  $\text{CaBe}_2\text{Ge}_2$ -type. The investigations are backed by single crystal X-ray diffraction data for both  $\text{Ce}(\text{Ni}_{0.61}\text{Zn}_{0.39})_2\text{Si}_2$  ( $P4/nmm$ ;  $a=0.41022(1)$  nm,  $c=0.98146(4)$  nm;  $R_F=0.012$ ) and for  $\text{La}(\text{Ni}_{1-x}\text{Zn}_x)_2\text{Si}_2$  ( $x=0.44$ ;  $P4/nmm$ ;  $a=0.41680(6)$  nm,  $c=0.99364(4)$  nm;  $R_F=0.043$ ). Interestingly, the  $\text{Ce-Zn-Si}$  system contains a ternary phase  $\text{CeZn}_2(\text{Si}_{1-x}\text{Zn}_x)_2$  with  $\text{ThCr}_2\text{Si}_2$  structure type ( $0.25 \leq x \leq 0.30$  at  $600^\circ\text{C}$ ), which forms peritectically at  $T=695^\circ\text{C}$  but does not include the stoichiometric composition 1:2:2. The primitive high temperature tetragonal phase with  $\text{CaBe}_2\text{Ge}_2$ -type has also been observed for the first time in the  $\text{Ce-Ni-Si}$  system at  $\text{CeNi}_{2+x}\text{Si}_{2-x}$ ,  $x=0.26$  (single crystal data,  $P4/nmm$ ;  $a=0.40150(2)$  nm,  $c=0.95210(2)$  nm;  $R_F=0.012$ ).

Physical properties (400 mK to 300 K) including specific heat, electrical resistivity and magnetic susceptibility have been elucidated for  $\text{Ce}(\text{Ni}_{0.61}\text{Zn}_{0.39})_2\text{Si}_2$  and  $\text{La}(\text{Ni}_{0.56}\text{Zn}_{0.44})_2\text{Si}_2$ .  $\text{Ce}(\text{Ni}_{0.61}\text{Zn}_{0.39})_2\text{Si}_2$  exhibits a long range magnetic order below 2 K and a Kondo-type interaction. Low temperature specific heat data of  $\text{La}(\text{Ni}_{0.56}\text{Zn}_{0.44})_2\text{Si}_2$  suggests spin fluctuations behavior, whereas the resistivity shows a hopping-type conductivity below 25 K.

*Keywords:* isopleths  $\{\text{La,Ce}\}\text{Ni}_2\text{Si}_2$ - $\{\text{La,Ce}\}(\text{NiZn})_2\text{Si}_2$ , crystal structure, magnetic ordering, spin fluctuation, Kondo effect, hopping conductivity.

## 1. Introduction

Since its discovery in 1935 by Andress and Alberti [1] the  $\text{BaAl}_4$  structure type and its derivatives are found in more than 200 intermetallic compounds, particularly the three tetragonal ternary variants:  $\text{ThCr}_2\text{Si}_2$ -type by Ban and Sikirica [2] (or  $\text{CeAl}_2\text{Ga}_2$ -type discovered independently by Zarechnyuk et al. [3] in the same year),  $\text{CaBe}_2\text{Ge}_2$  by Eisenmann et al. [4] and the non-centrosymmetric variant  $\text{BaNiSn}_3$  by Dörrscheidt and Schäfer [5]. The  $\text{BaAl}_4$  structure type furthermore is one of the building blocks of various structure types, such as  $\text{U}_3\text{Ni}_4\text{Si}_4$ ,  $\text{CeNiSi}_2$ , (in combination with  $\text{AlB}_2$ -type slabs) and many others [6].



Despite phase equilibria in the Ce-Ni-Si system have been investigated in the 70s by Bodak et al. [7,8], more ternary phases were discovered afterwards:  $\text{Ce}_2\text{Ni}_3\text{Si}_5$  ( $\text{U}_2\text{Co}_3\text{Si}_5$ -type, orthorhombic superstructure variant of  $\text{BaAl}_4$ ) [9],  $\text{Ce}_{14}\text{Ni}_6\text{Si}_{11}$  [10],  $\text{Ce}_3\text{NiSi}_3$  [11], etc. Being the last member of the first row of transition metals, Zn containing ternary rare earth silicon systems had been one of the least investigated systems. Only several reports on the formation of ternary compounds could be found in the literature [12]. Recently our report on the Ce-Zn-Si system at 800°C [13] revealed formation of several ternary phases. Surprisingly neither  $\text{BaAl}_4$  nor its derivative structure could be found in the system at 800°C, instead a far off-stoichiometric  $\text{ThCr}_2\text{Si}_2$ -type  $\text{CeZn}_{2+x}\text{Si}_{2-x}$  ( $x \sim 0.5$ , labeled as  $\tau_6$ ) was found to be stable at temperatures below  $695 \pm 5^\circ\text{C}$  [14].

Compounds crystallizing in the  $\text{BaAl}_4$  type or its derivatives are often associated with various exotic superconducting phenomena, starting with the discovery of heavy fermion superconductivity in  $\text{CeCu}_2\text{Si}_2$  by Steglich et al. in 1979 [15], which breaks the previous belief of non-coexistence between magnetism and superconductivity. Spin density wave transition was found in  $\text{BaFe}_2\text{As}_2$  [16], followed by the discovery of superconductivity in K-doped [17] and Co-doped [18]  $\text{BaFe}_2\text{As}_2$ . More recently, BCS-like superconductivity was found in non-centrosymmetric  $\text{BaPtSi}_3$  ( $\text{BaNiSn}_3$ -type) [19] and isotypes [20].

In cerium and actinide compounds the hybridization of the Ce-f electrons with the conduction band gives rise to various kinds of interesting physical phenomena. Systematic studies of transport, magnetic and calorimetric properties and Ce  $L_{\text{III}}$  X-ray absorption spectra and XPS measurements characterized  $\text{CeNi}_2\text{Si}_2$  as an intermediate valent (valence fluctuation) system with a characteristic Kondo-lattice temperature  $T^* \sim 600$  K [21–26]. The positive Seebeck coefficient, decreasing with Si content in  $\text{CeNi}_{2-x}\text{Si}_{2+x}$  was taken as a decrease of the electronic DOS particularly of the Ni-3d-states at the Fermi level concomitant with a narrowing of the Ce-4f level and a decreasing Ce-valence [27]. Replacing of Ni by Pd, Cu, Au drives the Ce from an intermediate valence to a non-IV ground state [21–26]. Probably because of the non-existence of compounds " $\text{LaZn}_2\text{Si}_2$ " and " $\text{CeZn}_2\text{Si}_2$ ", the corresponding isopleths  $\{\text{La,Ce}\}\text{Ni}_2\text{Si}_2$ - $\{\text{La,Ce}\}\text{Zn}_2\text{Si}_2$  have not attracted interest.

Therefore the present work intends to provide detailed information on the phase equilibria, crystal structures and physical properties of the novel  $\text{BaAl}_4$ -derivative phases in the systems  $\{\text{La,Ce}\}$ -Ni-Si as well as in the isopleths  $\{\text{La,Ce}\}\text{Ni}_2\text{Si}_2$  -  $\{\text{La,Ce}\}\text{Zn}_2\text{Si}_2$ .

## 2. Experimental Methods

Samples were prepared from cerium ingots (Alfa Aesar, purity >99.9 mass%), lanthanum ingots (Auer Remy, 99.9 mass %) zinc granules (Alfa Aesar, >99.9 mass%), Ni foil (Alfa Aesar, >99.8 mass%) and silicon pieces (Alfa Aesar, 6N). Zinc drops were purified in an evacuated quartz tube by heating them at ~800°C, below the boiling point of Zn (907°C). Cerium and lanthanum ingots were mechanically surface cleaned before use.

Polycrystalline bulk samples for the analysis of the quaternary isopleths  $\{La,Ce\}(Ni_{1-x}Zn_x)_2Si_2$  and for physical property studies were prepared from intimate blends of powders of arc melted master alloys  $\{La,Ce\}Ni_{2-x}Si_2$  (various  $x$ ; powdered under cyclohexane) and fine Zn-filings in proper compositional ratios. These blends were cold compacted in a steel die without lubricants, vacuum-sealed in quartz tubes, heated from 420°C to 800°C at the rate of 1°C/min and then annealed at this temperature for 7 days. After water quenching the samples were re-powderized under Argon inside an oxygen (< 2 Torr) and water-vapour (<5 Torr) controlled glove box in order to ensure homogeneity. The samples were loaded into 10 mm diameter graphite dies for hot pressing under Ar in an uniaxial hot press system (HP W 200/250-2200-200-KS) at 800°C for 1 hour employing a pressure of 56 MPa. Densities of the samples have been calculated from their dimensions and mass after removing a 0.5 mm thick surface layer (grinding with SiC paper).

X-ray powder diffraction data were collected from each alloy employing a Guinier-Huber image plate system with monochromatic  $CuK_{\alpha 1}$  radiation ( $8^\circ < 2\theta < 100^\circ$ ). Precise lattice parameters were calculated by least squares fits to the indexed  $2\theta$  values calibrated with Ge as internal standard ( $a_{Ge} = 0.565791$  nm). Quantitative Rietveld refinements of the X-ray powder diffraction data were performed with the FULLPROF program [28].

Single crystals from the systems  $\{La,Ce\}$ -Ni-Si were picked from crushed reguli. Quaternary single crystals were grown from Zn flux starting from a cold compacted pellet ( $Ce_2Ni_4Si_8 + Zn\text{-filings} = Ce_2Ni_4Si_8Zn_{86}$  (in at. %)), which was heated to 900 °C at the rate of 1°C/min and then cooled to 800°C at the same rate. After annealing for 4 days at this temperature the sample was subsequently quenched in water and then boiled with 15% aqueous solution of HCl in a water bath in order to dissolve the extra Zn. Crystals were carefully washed with distilled water and dried.

Inspections on an AXS-GADDS texture goniometer assured high crystal quality, unit cell dimensions and Laue symmetry of the specimens prior to the X-ray intensity data collections on a four-circle Nonius Kappa diffractometer equipped with a CCD area

detector employing graphite monochromated MoK $\alpha$  radiation ( $\lambda=0.071069$  nm). Orientation matrices and unit cell parameters were derived using the program DENZO [29]. No additional absorption corrections were performed because of the rather regular crystal shapes and small dimensions of the investigated specimens. The structures were solved by direct methods and were refined with the SHELXL-97 program [30] within the Windows version WinGX [31].

After reaction during annealing the samples had almost powder-like consistency, too soft to be polished by standard procedures. This problem was overcome by casting the sample powder along with conducting glue into a cylindrical mould of  $\sim 5$  mm diameter. After hardening several of the powder cylinders were hot compacted in conductive resin and were ground and polished under glycerine instead of water in order to avoid oxidation of the samples. Microstructures and compositions were examined by light optical microscopy (LOM) and scanning electron microscopy (SEM) via Electron Probe Micro-Analyses (EPMA) on a Zeiss Supra 55 VP equipped with an EDX system operated at 20 kV.

### 3. Results and Discussion

#### 3.1. The BaAl<sub>4</sub>-type derivative phases in the systems La-Ni-Si and Ce-Ni-Si

The system Ce-Ni-Si relevant to this work was investigated by Bodak and coworkers [7]. The isothermal section of La-Ni-Si at 400°C was established much later by Zhou et al. [32]. Both systems contain a compound {La,Ce}Ni<sub>2</sub>Si<sub>2</sub> which was reported to crystallize in the ThCr<sub>2</sub>Si<sub>2</sub> type [33] with practically negligible homogeneity range. A thorough check on these findings prompted us to prepare samples with nominal composition {La,Ce}20Ni40Si40 (in at.%). As cast alloys as well as samples annealed at 800°C for 4 days revealed nearly single phase condition with ThCr<sub>2</sub>Si<sub>2</sub> type, thus suggesting a congruent or a degenerate peritectic formation of these phases, and furthermore confirmed the crystal structure data from Bodak et al. [33]. Levin et al. [27] studied the homogeneity range of CeNi<sub>2</sub>Si<sub>2</sub> (ThCr<sub>2</sub>Si<sub>2</sub>-type) at a relatively low temperature of 727°C and discovered a rather large homogeneity range of 8 at. % ranging from 36 to 44 at.% Si. Our reinvestigation of the phase relations around CeNi<sub>2</sub>Si<sub>2</sub> at 800°C reveals a smaller homogeneity range for the ThCr<sub>2</sub>Si<sub>2</sub> type of  $\sim 4$  at. % from 38.3 to 42.3 at. % Si. Our lattice parameters (see Figure 1), however, agree well with the result of Levin et al. In general the Ni/Si substitution does not affect much the *a* axis, however one can see that the *c* axis decreases almost linearly with increasing of the Ni content.

In an attempt to investigate the crystal structure of CeNi<sub>4</sub>Si [34] we discovered a Ni-rich phase CeNi<sub>2+x</sub>Si<sub>2-x</sub> (x~0.3). EPM analysis of an as cast alloy with slightly higher Ni-content (Ce<sub>20</sub>Ni<sub>43</sub>Si<sub>37</sub>) showed primary crystallization of Ce<sub>20</sub>Ni<sub>41</sub>Si<sub>39</sub> followed by a peritectic-like formation of a thin layer of Ce<sub>20</sub>Ni<sub>46</sub>Si<sub>34</sub> (see Figure 2). The remaining liquid crystallized as CeNi<sub>4</sub>Si and a novel phase Ce(Ni<sub>1-x</sub>Si<sub>x</sub>)<sub>3</sub>. Beside the main reflections arising from ThCr<sub>2</sub>Si<sub>2</sub>-type Ce<sub>20</sub>Ni<sub>41</sub>Si<sub>39</sub>, the X-ray powder spectrum revealed a set of weak satellite reflections that correspond to a tetragonal lattice similar to ThCr<sub>2</sub>Si<sub>2</sub> with shorter *c* axis. At this point, it was not clear whether the Ni-rich phase Ce<sub>20</sub>Ni<sub>46</sub>Si<sub>34</sub> represents a new phase or the Ni-rich end of a homogeneity range of ThCr<sub>2</sub>Si<sub>2</sub>-type CeNi<sub>2</sub>Si<sub>2</sub>. The amount of the Ni-rich phase Ce<sub>20</sub>Ni<sub>46</sub>Si<sub>34</sub> in the as cast state increases as the alloy composition shifts towards the Ni-rich side at constant Ce content, where at alloy composition of Ce<sub>20</sub>Ni<sub>60</sub>Si<sub>20</sub> a single crystal suitable for X-ray structure analysis (see below) was selected.

### 3.1.1. The crystal structure of CeNi<sub>2+x</sub>Si<sub>2-x</sub>, x=0.33 with CaBe<sub>2</sub>Ge<sub>2</sub>-type

A single crystal, extracted from an as cast alloy with nominal composition of Ce<sub>20</sub>Ni<sub>60</sub>Si<sub>20</sub> revealed unit cell parameters (*a*=0.40150(2) and *c*=0.95210(2) nm) consistent at first glance with a body centered ThCr<sub>2</sub>Si<sub>2</sub> type, but additional weak reflections could be satisfactorily indexed on the basis of a primitive Bravais cell. Systematic extinctions suggested space group type *P4/nmm* for the highest crystal symmetry. Direct methods prompted Ce, Ni, Si atoms in positions typical for the CaBe<sub>2</sub>Ge<sub>2</sub>-type, where the electropositive atom occupies the 2c site (1/4, 1/4, ~0.75), the transition metal atoms occupy a 2c site (1/4, 1/4, ~0.1) and 2b site, and the tetrel atoms occupy the sites 2c (1/4, 1/4, ~0.35) and 2a. Refinement with anisotropic atom displacement parameters (ADPs) converged to *R<sub>F</sub>*=0.0163 and residual electron densities smaller than ±1.53 e<sup>-</sup>/Å<sup>3</sup> with fully occupied metal sites but for a statistical occupation of 0.33Ni+0.67Si, in site 2a of *P4/nmm*, which was fixed after the EPMA value. Thus, a structure formula CeNi<sub>2+x</sub>Si<sub>2-x</sub>, x=0.33, results, which corresponds to a composition Ce<sub>20</sub>Ni<sub>46.5</sub>Si<sub>33.5</sub> close to the ThCr<sub>2</sub>Si<sub>2</sub>-type phase. Crystal data for CeNi<sub>2+x</sub>Si<sub>2-x</sub> along with the ADPs are summarized in Table 1. Although attempts to refine the Ni/Si ratio in the 2a site yield lower *R<sub>F</sub>* and residual electron density of 0.011 and less than 0.87 e<sup>-</sup>/Å<sup>3</sup>, respectively, the resulting Ni content (0.22(1)Ni+0.78(Si)) corresponds to the composition Ce<sub>20</sub>Ni<sub>44.5</sub>Si<sub>35.5</sub> deviating significantly from the EPMA derived composition. Thus we prefer the EPMA value and the corresponding formula CeNi<sub>2+x</sub>Si<sub>2-x</sub>, x=0.33.

It is worth mentioning that despite the primitive reflections in  $\text{CaBe}_2\text{Ge}_2$ -type  $\text{CeNi}_{2+x}\text{Si}_{2-x}$  are relatively small, they are still visible in the single phase powder diffraction spectra. Interestingly, neither a Ni-rich composition nor primitive reflections could be observed at  $800^\circ\text{C}$  in alloys at the Ni-rich side of the 1:2:2 stoichiometry. This strongly suggests that the primitive  $\text{CaBe}_2\text{Ge}_2$ -type phase  $\text{CeNi}_{2+x}\text{Si}_{2-x}$  is a high temperature phase.

Alloys at the Ni-rich side of 1:2:2 annealed at  $1000^\circ\text{C}$  indeed show the Ni-rich composition  $\text{Ce}_{20}\text{Ni}_{46}\text{Si}_{34}$  in equilibrium with  $\text{CeNi}_4\text{Si}$  and  $\text{Ce}(\text{Ni}_{1-x}\text{Si}_x)_3$ . Consequently, the X-ray powder diffraction spectra show two sets of  $\text{BaAl}_4$ -type reflections (see Figure 2). As the sample is multiphase, it is rather difficult to identify the primitive peaks, however, the lattice parameters of one of the  $\text{BaAl}_4$  derivative phases shows a shorter  $c$  axis, which is closer to the value of  $\text{CeNi}_{2+x}\text{Si}_{2-x}$  with primitive  $\text{CaBe}_2\text{Ge}_2$ -type as obtained from the single crystal data. The other set of  $\text{BaAl}_4$  derivative reflections give similar unit cell parameters as for  $\text{CeNi}_2\text{Si}_2$  with the  $\text{ThCr}_2\text{Si}_2$ -type. These observations, together with the fact that the single crystal was obtained from an as cast alloy led us to conclude that  $\text{CeNi}_{2+x}\text{Si}_{2-x}$  with the primitive  $\text{CaBe}_2\text{Ge}_2$ -type is a high temperature phase ( $1000^\circ\text{C} \leq T_{\text{stability}} < 1615^\circ\text{C}$  [37]).

Polymorphism between  $\text{ThCr}_2\text{Si}_2$ - and  $\text{CaBe}_2\text{Ge}_2$ -types is often encountered in various systems, particularly for ternary rare earth silicides containing Ir and Pt [12]. In some cases, e.g. in the La-Ir-Si system [38], the  $\text{CaBe}_2\text{Ge}_2$ -type is the high temperature form, whilst the  $\text{ThCr}_2\text{Si}_2$ -type is stable at lower temperature. Therefore  $\text{CeNi}_{2+x}\text{Si}_{2-x}$  with the primitive  $\text{CaBe}_2\text{Ge}_2$ -type is hitherto the first example of  $\text{ThCr}_2\text{Si}_2$  -  $\text{CaBe}_2\text{Ge}_2$  polymorphism found in ternary rare earth silicides with 3d transition metal elements. The slight flattening of the unit cell, i.e. the shorter length of  $c$ -axis observed in  $\text{CeNi}_{2+x}\text{Si}_{2-x}$  ( $\text{CaBe}_2\text{Ge}_2$ -type), is also commonly found in many systems exhibiting such polymorphism [12].

Besides the temperature effect, the substitution of Si by Ni in the  $2a$ -site may act as the driving force for the structural change from a body centered to a primitive atom arrangement in terms of a group-subgroup relation. This idea comes from the fact that an alloy with stoichiometric composition  $\text{CeNi}_2\text{Si}_2$  does not show any changes in the powder diffraction spectra in as cast state, and after annealing at  $1000^\circ\text{C}$  for 4 days. An example of structural evolution at a constant temperature can be found in the Sr-Au-Ge system [39] where at  $700^\circ\text{C}$ , increasing Ge content in  $\text{SrAu}_{2-x}\text{Ge}_{2+x}$  led to a series of structural changes from  $\text{ThCr}_2\text{Si}_2$ -type to  $\text{BaCu}_2\text{Sb}_2$ -type and finally to  $\text{CaBe}_2\text{Ge}_2$ -type, where all structure types are variants of the  $\text{BaAl}_4$ -type.

### 3.2. The quaternary solution phases $\text{La}(\text{Ni}_{1-x}\text{Zn}_x)_2\text{Si}_2$ and $\text{Ce}(\text{Ni}_{1-x}\text{Zn}_x)_2\text{Si}_2$

As neither stoichiometric  $\text{CeZn}_2\text{Si}_2$  nor off-stoichiometric  $\text{CeZn}_{2+x}\text{Si}_{2-x}$  ( $x \sim 0.5$ ) exist in the Ce-Zn-Si system at 800°C, it is interesting to investigate the extent of solubility of Zn in the 1:2:2 phase at 800°C. Stoichiometric body centered  $\text{CeNi}_2\text{Si}_2$  is found to solve up to 18% Zn substituting in the Ni site, i.e.  $\text{Ce}(\text{Ni}_{1-x}\text{Zn}_x)_2\text{Si}_2$ ;  $x=0.18$ . The substitution of Zn for Ni is also reflected in the gradual increase of the unit cell parameters (Figure 3). For further Zn substitution the Bravais lattice changes from body centered to primitive, as indicated by the appearance of additional weak reflections that violate the systematic extinction of a body-centered cell. The samples remain single phase up to  $x=0.55$  at 800°C. On further Zn substitution the samples became multiphase, indicating that the solubility limit has been reached.

Since the primitive  $\text{CaBe}_2\text{Ge}_2$ -type phase also exists in the Ce-Ni-Si end member system at high temperature in the Ni-rich side, and the body centered  $\text{ThCr}_2\text{Si}_2$ -type phase extends slightly to both the Ni- and Si-rich side at 800°C, we suspected that a slight deviation from stoichiometric 1:2:2 composition could stabilize/destabilize one of these structure types with the incorporation of Zn. Such a situation is often found in various systems, e.g. in the Ce-Zn-Si system at 800°C [13] or Ce-Ag-Si at 500°C [40] where two compositional polymorphic modifications of  $\text{CeSi}_2$  with  $\alpha\text{-ThSi}_2$  type and  $\alpha\text{-GdSi}_2$  type solve transition metal elements, however, the  $\alpha\text{-GdSi}_2$ -based solid solutions end prematurely with transition metal incorporation while the others extend further up to ~20 at.% transition metal content.

In order to check the possibility of such a scenario we prepared several alloys with off-stoichiometric compositions. Despite the nominal compositions deviate far (~5 at.%) from the 1:2:2 composition, only a small variation ( $\pm 1$  at.%) in the homogeneity range could be observed in the quaternary 122 phase. Variation of unit cell parameters of alloys in both the Si- poor and rich part of 122 stoichiometry shows good agreement with those from the stoichiometric 122 alloys. This suggests that there is no parallel solid solution running beside the one shown in Figure 3.

#### 3.2.1. The crystal structures of $\{\text{La}, \text{Ce}\}(\text{Ni}_{1-x}\text{Zn}_x)_2\text{Si}_2$ with $\text{CaBe}_2\text{Ge}_2$ -type

In order to get details on the primitive unit cell, a single crystal has been selected from the flux residuals of an alloy with composition  $\text{Ce}_2\text{Ni}_4\text{Si}_8\text{Zn}_{86}$  (in at.%), slowly cooled from 900°C. A SEM analysis performed directly on the crystals separated from the flux (shown in Figure 4), defined the composition as  $\text{Ce}_{19.4}\text{Ni}_{25.3}\text{Zn}_{16.1}\text{Si}_{39.2}$  (at. %). Unit cell, systematic

extinctions (indicating  $P4/nmm$  as the space group type of highest symmetry) as well as the X-ray intensity pattern confirmed a structure solution in terms of the  $\text{CaBe}_2\text{Ge}_2$ -type. It should be mentioned, however, that six reflections violated the space group extinction rules: (010), (210), (210), (230), (230) and (340). In comparison to the highest intensity observed (12000 counts), the (210), (210), (230), (230) reflection intensities are below 2 counts and can be disregarded, whereas the (010) intensity (below 7 counts) may stem from a ‘Renninger enhancement’ effect.

Interestingly, the site occupation of the transition metal and tetrel atoms are exchanged, i.e. the tetrel atoms occupy sites  $2c$  ( $1/4, 1/4, \sim 0.1$ ) and  $2b$ , whilst the transition metal atoms occupy sites  $2c$  ( $1/4, 1/4, \sim 0.35$ ) and  $2a$ . This site exchange configuration gives rise to the intensity of the primitive reflections, therefore the  $\text{CaBe}_2\text{Ge}_2$ -type phases can be identified easily in the quaternary system by X-ray powder diffraction.

Although the small differences in the X-ray scattering power of Ni and Zn make it difficult to unambiguously differentiate between these atom types, it was possible to define the site occupation of Zn by analyzing site ADPs. As the ADPs of the two Si sites did not show any anomalies, it was certain that Zn occupied one or both of the Ni sites. Among all remaining combinations of Zn site occupations, the lowest  $R_F$  was found when Zn substituted Ni in the  $2a$  site. Despite it was possible to refine the Ni/Zn occupancy in this site, the resulting value (0.48(3)Ni+0.52(3)Zn) deviates far from the value obtained by EPMA: 0.22Ni+0.78Zn. Therefore, in the final refinement the Ni/Zn occupancy was fixed according to EPMA, resulting in the structure formula  $\text{Ce}(\text{Ni}_{1-x}\text{Zn}_x)_2\text{Si}_2$ ,  $x=0.39$  (i.e.  $\text{Ce}_{20}\text{Ni}_{24.4}\text{Zn}_{15.6}\text{Si}_{40}$ ). The final refinement converged to  $R_F = 0.0134$  and residual electron densities less than  $\pm 1.48$  electrons/ $\text{\AA}^3$  for three metal and two Si positions with a Wyckoff sequence  $abc^3$ . Crystal data for  $\text{Ce}(\text{Ni}_{1-x}\text{Zn}_x)_2\text{Si}_2$ ,  $x=0.39$ , with the  $\text{CaBe}_2\text{Ge}_2$ -type along with the ADPs are summarized in Table 2; interatomic distances are presented in Table 3; coordination polyhedra for all atom sites and a three-dimensional view on the crystal structure are presented in Figure 5.

The comparison of the structures of  $\text{CeNi}_{2+x}\text{Si}_{2-x}$  and  $\text{Ce}(\text{Ni,Zn})_2\text{Si}_2$  in Figure 5 clearly reveals an atom site exchange in the tetrahedra-layers sandwiching the Ce-atoms: Ni- and Si layers exchanged. However, it is interesting to see, that the random substitution Ni/Si and Ni/Zn always occurs at the same site ( $2a$  site).

Several examples of such site exchange variants of the  $\text{CaBe}_2\text{Ge}_2$ -structure type can be found in the literature, particularly for ternary stannides and antimonides, e.g.  $\text{Ce}\{\text{Ni,Cu,Pd,Ir,Pt}\}_2\text{Sn}_2$  [12]. For ternary silicides, only the high temperature modification

$\text{LaIr}_2\text{Si}_2$  [38] is known to exhibit such a site exchange arrangement. A similar situation is also encountered in quaternary  $\text{Ce}(\text{Cu}_{1-x}\text{Ag}_x)_2\text{Sb}_2$  [41].

In contrast to primitive  $\text{Ce}(\text{Ni}_{1-x}\text{Zn}_x)_2\text{Si}_2$ , where the occupation of Zn/Si sites is inverted, body centered  $\text{Ce}(\text{Ni}_{1-x}\text{Zn}_x)_2\text{Si}_2$  as well as off-stoichiometric  $\text{CeZn}_{2+x}\text{Si}_{2-x}$  ( $x \sim 0.5$ ) do not exhibit such a site exchange. Rietveld refinement performed on single-phase body centered  $\text{Ce}(\text{Ni}_{1-x}\text{Zn}_x)_2\text{Si}_2$  ( $x=0.18$ ) shows that Zn substitutes for Ni in the 4d site, while the 4e site remains fully occupied by Si. In case of ternary  $\text{CeZn}_{2+x}\text{Si}_{2-x}$  ( $x=0.5$ ) due to excess Zn in the structure, Zn and Si share the 4e site with ratio of 3:7 whereas the 4d site is fully occupied by Zn [14].

In analogy to the section  $\text{Ce}(\text{Ni}_{1-x}\text{Zn}_x)_2\text{Si}_2$ , phase relations have also been explored for the isopleth  $\text{La}(\text{Ni}_{1-x}\text{Zn}_x)_2\text{Si}_2$  (see Figure 3). Combined EPM and X-ray powder intensity data analyses revealed a solid solution with the  $\text{ThCr}_2\text{Si}_2$ -type for  $0 \leq x \leq 0.18$ , followed by a change to a primitive tetragonal symmetry typical for the  $\text{CaBe}_2\text{Ge}_2$ -type for  $0.2 \leq x \leq 0.56$ . The solid solution terminates at  $x=0.56$  as for higher Zn-concentrations multiphase X-ray spectra were observed. Rietveld refinement data for  $\text{La}(\text{Ni}_{0.53}\text{Zn}_{0.47})_2\text{Si}_2$  are summarized in Table 2 and Figure 6.

### 3.3. Physical properties of $\text{La}(\text{Ni}_{1-x}\text{Zn}_x)_2\text{Si}_2$ and $\text{Ce}(\text{Ni}_{1-x}\text{Zn}_x)_2\text{Si}_2$

Two samples,  $\{\text{La,Ce}\}(\text{Ni,Zn})_2\text{Si}_2$  were selected from the solid solution to check for physical properties of this series.

$\text{La}(\text{Ni}_{1-x}\text{Zn}_x)_2\text{Si}_2$ ,  $x = 0.44$  was studied down to 400 mK; no phase transition, indicating e.g., superconductivity was observed. The temperature dependent heat capacity,  $C_p$ , of  $\text{La}(\text{Ni,Zn})_2\text{Si}_2$  is shown in Fig. 7(a) and plotted as  $C_p/T$  vs.  $T$ . Unexpectedly,  $C_p/T(T)$  exhibits a minimum around 2.5 K below which the electronic contribution tends towards 20 mJ/molK<sup>2</sup> for  $T \sim 0$ , a value larger than what is likely for simple intermetallic compounds. The overall shape, however, reminds of spin fluctuation systems like  $\text{YCo}_2$  or  $\text{UAl}_2$  [42]. In order to proof such a preposition, the standard spin fluctuation ansatz,  $C_p(T) = \gamma T + \beta T^3 + \delta T^3 \ln(T/T^*)$  is employed to the experimental data, revealing excellent agreement for  $\gamma = 13$  mJ/molK<sup>2</sup> and  $T^* = 8.7$  K (solid line, inset Fig. 7(a)). This agreement would suggest spin fluctuations in the nearly localized regime being present in  $\text{La}(\text{Ni,Zn})_2\text{Si}_2$ . The fit parameter  $\beta = 0.00013$  J/molK<sup>4</sup> allows to estimate a Debye temperature of about 460 K, referring to a rather stiff lattice of this system.

The temperature dependent resistivity,  $\rho$ , of  $\text{La}(\text{Ni,Zn})_2\text{Si}_2$  was studied within the temperature range 4.2-300 K. At elevated temperatures ( $T > 100$  K)  $\rho(T)$  behaves metallic-



like. The almost linear slope of  $\rho(T)$  refers predominantly to electron-phonon interaction. A shallow minimum is observed at about 25 K and below this temperature the resistivity increases with decreasing temperature (see Fig. 7(b)). A model, employing variable hopping conductivity (VRH, for more details see Ref. [43]) was used to account for the low temperature resistivity of  $\text{La}(\text{Ni},\text{Zn})_2\text{Si}_2$ . The temperature dependent hopping conductivity was initially derived by Mott [44] as

$$1/\rho = \sigma(T) = \sigma_0(T) \exp(-A/T^{1/4}), \quad (1)$$

where  $\sigma_0$  is a material constant and  $A$  corresponds to a characteristic temperature. A proper graphical representation to prove such a mechanism follows from a  $-\ln(1/\rho)$  vs.  $T^{1/4}$  plot. As can be seen from this representation (inset, Fig. 7(b)), the experimental data at low temperatures are satisfactorily described in terms of the VRH model. The characteristic temperature is found to be 78 K. The origin of variable range hopping might be found from disorder present in the system. As evidenced by the x-ray study discussed above, the 2a site of the tetragonal  $\text{CaBe}_2\text{Ge}_2$  crystal structure is occupied by both Ni and Zn. The absence of super-cell peaks in the diffraction pattern of this system hints to a statistical distribution of both elements on this site. As a consequence, disorder is created and localization might result.

Figures 7 and 8 reveal experimental results regarding magnetic  $\text{Ce}(\text{Ni}_{1-x}\text{Zn}_x)_2\text{Si}_2$ ,  $x = 0.39$ . Ce in its atomistic form possesses one electron in the 4f shell, constituting the  $4f^1$  electronic configuration (EC) and thus carries a total angular momentum  $j = 5/2$ . This gives rise to a non-vanishing magnetic moment. A simple proof whether or not this EC is preserved in the solid state of  $\text{Ce}(\text{Ni},\text{Zn})_2\text{Si}_2$  can be obtained from measurements of the temperature dependent magnetization. The inverse magnetic susceptibility for a 3 T run is shown in Fig. 8 (a). Phase transitions above 2.5 K are not obtained from this measurement. A quantitative description of the magnetic susceptibility can be made by applying the modified Curie Weiss law, revealing a temperature independent Pauli susceptibility ( $\chi_0 = 3.9 \cdot 10^{-4}$  emu/mol), the effective magnetic moment, which is related to the Curie constant ( $\chi_{\text{eff}} = 2.20 \mu_B/\text{Ce}$ ) and a paramagnetic Curie temperature ( $\theta_p = -32$  K) from a least squares fit of this model to the experimental data (solid line, Fig 8 (a)). A negative paramagnetic Curie temperature, in general, refers to antiferromagnetic interactions between conduction electrons and the almost localized Ce 4f electrons. Crystalline electric field (CEF) effects, lifting the  $2j+1=6$  fold degenerate ground state, as well as the Kondo effect, modify, however, the absolute value of  $\theta_p$ . The effective magnetic moment observed from the Curie

Weiss law is below that ( $2.54 \mu_B$ ) expected for the magnetic  $Ce^{3+}$  state (EC:  $4f^1$ ). The slight curvature observed in the  $1/\chi$  vs.  $T$  data-set might result from CEF effects which are simply modeled here by adjusting  $\chi_0$ .

Fig. 8 (b) exhibits the temperature dependent electrical resistivity,  $\rho$ , of  $Ce(Ni,Zn)_2Si_2$  in comparison to that of  $La(Ni,Zn)_2Si_2$ . In distinct contrast to  $\rho(T)$  of  $La(Ni,Zn)_2Si_2$  the electrical resistivity of  $Ce(Ni,Zn)_2Si_2$  evidences a negative value of  $d\rho/dT$  in the entire temperature range. Additionally, much larger  $\rho(T)$  values are observed as a consequence of additional magnetic scattering processes. If  $\rho(T)$  of  $La(Ni,Zn)_2Si_2$  is assumed to primarily derive from electron-phonon interaction, besides a constant residual resistivity, the magnetic scattering processes of electrons on the  $4f$  moments of Ce can be isolated by simply subtracting the resistivity curve of  $La(Ni,Zn)_2Si_2$  from that of  $Ce(Ni,Zn)_2Si_2$ . Results are shown in Fig. 8(b) on a semi-logarithmic temperature scale. Obviously, two temperature ranges can be identified, where  $\rho_{mag}(T)$  behaves in a negative-logarithmic manner (see the solid lines in Fig. 8(b) as a guide for the eyes). Such a behaviour is a hallmark of Kondo-type interactions, as present in a huge amount of cerium based compounds. Following the preposition of Cornut and Coqblin [45] the logarithmic resistivity ranges at low and high temperatures can be understood as derived from the Kondo effect in the CEF ground state and in an excited CEF state, respectively. If these levels are well separated in energy, a pronounced maximum in  $\rho_{mag}(T)$  would be expected as well. Overall, the present resistivity study strongly indicates a Kondo effect existing in  $Ce(Ni,Zn)_2Si_2$ .

In Fig. 9 the heat capacity data of  $Ce(Ni,Zn)_2Si_2$ , measured down to 400 mK, are displayed as  $C_p$  vs.  $T$ . For comparison,  $C_p(T)$  of  $La(Ni,Zn)_2Si_2$  is added, too. Below 2 K, the specific heat of  $Ce(Ni,Zn)_2Si_2$  shows a distinct anomaly, indicating, presumably, a magnetic phase transition into a long range ordered state. The height of the anomaly, however, is rather small and well below  $12.5 \text{ J/molK}$  expected for magnetic ordering in a doublet as CEF ground state. The latter is a consequence of the tetragonal structure and  $j = 5/2$ . Reduction of this anomaly with respect to unperturbed ordering is expected e.g., from the Kondo effect, present in many Ce based compounds. In order to calculate the magnetic entropy, released at the ordering temperature, the specific heat data of  $LaNiZnSi_2$  are assumed to represent the phonon contribution to this quantity, i.e.,  $C_{mag} = C(Ce(Ni,Zn)_2Si_2) - C(La(Ni,Zn)_2Si_2)$ . Results of this procedure are shown in Fig.9 (a) as well. Integrating  $C_{mag}/T$  from zero to the upper limit of the present measurements reveals the temperature

dependent magnetic entropy,  $S$ , shown as solid line in Fig. 9 (a). At  $T = T_{\text{mag}} \sim 1.8$  K, the entropy reaches just 25 % of  $R\ln 2$ ; this strong reduction can be used to conclude for the presence of a Kondo effect. At 3.9 K, the entropy reaches  $0.45R\ln 2$ . According to Desgranges and Schotte [46], this temperature corresponds to the Kondo temperature, i.e.,  $T_K = 3.9$  K. As it is obvious from Fig. 9 (a) that  $S(T)$  continuously increases above the phase transition, reaching a value of  $R\ln 2$  around 20 K. This distinct temperature dependence refers to the first excited CEF doublet of this compound, not well separated from the ground state level. The response of the system to an application of magnetic fields is shown in Fig. 9(b), where the heat capacity data are plotted as  $C_p/T$  vs.  $T$ . The anomaly found at low temperature confirms the magnetic phase transition as discussed above. Contrary to general expectations that the phase transition temperature becomes suppressed if externally applied magnetic fields are increasing, even fields of 8 T do not substantially shift the position of the anomalies in  $C_p/T(T)$  of  $\text{Ce}(\text{Ni,Zn})_2\text{Si}_2$ . The maxima of the anomalies, however, are diminished upon increasing fields, and entropy is moved to higher temperature regions. The fact that the phase transition temperature keeps almost unchanged indicates that magnetic interactions are not of primary importance; rather thermodynamics is the relevant driving force as large densities of low energy excitations are collected below the low temperature anomaly in  $\text{Ce}(\text{Ni,Zn})_2\text{Si}_2$ .

#### 4. Conclusions

Solid solutions exist starting from  $\text{CeNi}_2\text{Si}_2$  by the addition of Zn, which substitutes Ni. The homogeneity range has been studied up till  $\{\text{La,Ce}\}(\text{Ni}_{1-x}\text{Zn}_x)_2\text{Si}_2$ ,  $0 \leq x \leq 0.55$ . Single crystal X-ray diffraction data define the  $\text{CaB}_2\text{Ge}_2$ -type for the crystals of the compounds  $\text{Ce}(\text{Ni}_{0.61}\text{Zn}_{0.39})_2\text{Si}_2$  ( $P4/nmm$ ;  $a=0.41022(1)$  nm,  $c=0.98146(4)$  nm) and  $\text{CeNi}_{2+x}\text{Si}_{2-x}$ ,  $x=0.26$  ( $P4/nmm$ ;  $a=0.40150(2)$  nm,  $c=0.95210(2)$  nm). While the quaternary  $\text{CaB}_2\text{Ge}_2$ -type phase is stable at  $800^\circ\text{C}$ , a reinvestigation of the Ce-Ni-Si system near the stoichiometric composition 1:2:2 revealed that the  $\text{CaB}_2\text{Ge}_2$ -type phase exists only at high temperature ( $\geq 1000^\circ\text{C}$ ) in the Ni-rich side. Bravais lattice changes from body centered to primitive have been observed at  $800^\circ\text{C}$  starting from  $\text{RE}(\text{Ni}_{1-x}\text{Zn}_x)_2\text{Si}_2$  ( $0 \leq x \leq 0.18$ )  $I4/mmm$  to  $\text{RE}(\text{Ni}_{1-x}\text{Zn}_x)_2\text{Si}_2$ ,  $0.18 < x \leq 0.55$ - $P4/nmm$ , however on further Zn substitution the stability of the 1:2:2 phase is reduced ( $< 695^\circ\text{C}$ ) and it exists only with excess amount of Zn as  $\text{CeZn}_2(\text{Si}_{1-x}\text{Zn}_x)_2$  with  $\text{ThCr}_2\text{Si}_2$  type.

The effective paramagnetic moment of Ce of  $\text{Ce}(\text{Ni}_{0.61}\text{Zn}_{0.39})_2\text{Si}_2$  suggests that the ground state of Ce ion in this compound is close to trivalent. Additionally a long range magnetic

order below 2 K and a Kondo effect are observed in  $\text{Ce}(\text{Ni}_{0.61}\text{Zn}_{0.39})_2\text{Si}_2$ .  $\text{La}(\text{Ni}_{0.56}\text{Zn}_{0.44})_2\text{Si}_2$  exhibits spin fluctuations behavior and a hopping type conductivity below 25 K.

## 5. Acknowledgements

FF is thankful for the support from the Austrian Federal Ministry of Science and Research (BMWF) under the scholarship scheme: Technology Grant Southeast Asia (Ph.D) in the frame of the ASEA UNINET. ZM acknowledged the support from the Higher Education Commission of Pakistan (HEC) under the scholarship scheme “PhD in Natural & Basic Sciences from Austria”. We thank Dr. S. Puchegger for his expert assistance in EPMA measurements and Dr. N. Ponweiser and P. Wibner for their contributions to Ce-Ni-Si at the early stage of this work.

## 6. References

- [1] K.R. Andress, E. Alberti, Röntgenographische Untersuchung der Legierungsreihe aluminium-barium, *Z. Metallkde.* 27 (1935).
- [2] Z. Ban, M. Sikirica, The crystal structure of ternary silicides  $\text{ThM}_2\text{Si}_2$  ( $\text{M} = \text{Cr}, \text{Mn}, \text{Fe}, \text{Co}, \text{Ni}$  and  $\text{Cu}$ ), *Acta Crystallogr.* 18 (1965) 594–599.
- [3] O.S. Zarechnyuk, P.I. Kripyakevich, E.I. Gladyshevskii, Ternary intermetallic compounds with  $\text{BaAl}_4$ -type superstructure., *Kristallografiya.* 9 (1965) 706–708.
- [4] B. Eisenmann, N. May, W. Müller, H. Schäfer, Eine neue strukturelle Variante des  $\text{BaAl}_4$ -Typs: Der  $\text{CaBe}_2\text{Ge}_2$ -Typ, *Z. Für Naturforschung B.* 27 (1972) 1155–1157.
- [5] W. Dörrscheidt, H. Schäfer, Die Struktur des  $\text{BaPtSn}_3$ ,  $\text{BaNiSn}_3$  und  $\text{SrNiSn}_3$  und ihre Verwandtschaft zum  $\text{ThCr}_2\text{Si}_2$ -strukturtyp, *J. Less Common Met.* 58 (1978) 209–216.
- [6] E. Parthé, B. Chabot, H.F. Braun, N. Engel, Ternary  $\text{BaAl}_4$  -type derivative structures, *Acta Crystallogr. B.* 39 (1983) 588–595.
- [7] O.I. Bodak, E.I. Gladyshevskii, Cerium-nickel-silicon system in the 0-33.3 atomic % cerium range., *Izv. Akad. Nauk SSSR Neorganicheskie Mater.* 5 (1969) 2060–5.
- [8] O.I. Bodak, M.G. Mis’kiv, A.T. Tyvanchuk, O.I. Kharchenko, E.I. Gladyshevskii, Cerium-nickel-silicon system containing 33.3-100 atomic % cerium., *Izv. Akad. Nauk SSSR Neorganicheskie Mater.* 9 (1973) 864–6.

- [9] B. Chabot, E. Parthé,  $\text{Ce}_2\text{Co}_3\text{Si}_5$  and  $\text{R}_2\text{Ni}_3\text{Si}_5$  ( $\text{R} \equiv \text{Ce, Dy, Y}$ ) with the orthorhombic  $\text{U}_2\text{Co}_3\text{Si}_5$ -type structure and the structural relationship with the tetragonal  $\text{Sc}_2\text{Fe}_3\text{Si}_5$ -type structure, *J. Less Common Met.* 97 (1984) 285–290.
- [10] E.R. Hovestreydt, Crystal data for  $\text{Ce}_{14}\text{Ni}_6\text{Si}_{11}$  isotypic with  $\text{Pr}_{14}\text{Ni}_6\text{Si}_{11}$ , *J. Less Common Met.* 102 (1984) L27–L29.
- [11] F. Merlo, M.L. Fornasini, M. Pani, On the existence and the crystal structure of novel  $\text{R}_3\text{TSi}_3$  intermetallic phases ( $\text{R}$  = rare earth;  $\text{T}$  = Fe, Co, Ni), *J. Alloy Compd.* 387 (2005) 165–171.
- [12] P. Villars, K. Cenzual, Pearson's Crystal Data—Crystal Structure Database for Inorganic Compounds, release 2014/15, ASM International, Materials Park, OH, USA, 2014.
- [13] Z. Malik, A. Grytsiv, P. Rogl, G. Giester, Phase equilibria and crystal structures in the system Ce–Zn–Si, *Intermetallics*. 36 (2013) 118–126.
- [14] F. Failamani, A. Grytsiv, R. Podloucky, H. Michor, E. Bauer, P. Brož, et al., The system Ce–Zn–Si for <33.3 at.% Ce: phase relations, crystal structures and physical properties, *RSC Adv.* 5 (2015) 36480–36497.
- [15] F. Steglich, J. Aarts, C.D. Bredl, W. Lieke, D. Meschede, W. Franz, et al., Superconductivity in the Presence of Strong Pauli Paramagnetism:  $\text{CeCu}_2\text{Si}_2$ , *Phys. Rev. Lett.* 43 (1979) 1892–1896.
- [16] M. Rotter, M. Tegel, D. Johrendt, I. Schellenberg, W. Hermes, R. Pöttgen, Spin-density-wave anomaly at 140 K in the ternary iron arsenide  $\text{BaFe}_2\text{As}_2$ , *Phys. Rev. B.* 78 (2008) 020503.
- [17] M. Rotter, M. Tegel, D. Johrendt, Superconductivity at 38 K in the Iron Arsenide  $(\text{Ba}_{1-x}\text{K}_x)\text{Fe}_2\text{As}_2$ , *Phys. Rev. Lett.* 101 (2008) 107006.
- [18] A.S. Sefat, R. Jin, M.A. McGuire, B.C. Sales, D.J. Singh, D. Mandrus, Superconductivity at 22 K in Co-Doped  $\text{BaFe}_2\text{As}_2$  Crystals, *Phys. Rev. Lett.* 101 (2008) 117004.
- [19] E. Bauer, R.T. Khan, H. Michor, E. Royanian, A. Grytsiv, N. Melnychenko-Koblyuk, et al.,  $\text{BaPtSi}_3$ : A noncentrosymmetric BCS-like superconductor, *Phys. Rev. B.* 80 (2009) 064504.
- [20] F. Kneidinger, E. Bauer, I. Zeiringer, P. Rogl, C. Blaas-Schenner, D. Reith, et al., Superconductivity in non-centrosymmetric materials, *Phys. C Supercond. Its Appl.* 514 (2015) 388–398.

- [21] G. Knebel, M. Brando, J. Hemberger, M. Nicklas, W. Trinkl, A. Loidl, Ground state properties of  $\text{Ce}(\text{Pd}_{1-x}\text{Ni}_x)_2\text{Ge}_2$  and  $\text{CeNi}_2(\text{Ge}_{1-y}\text{Si}_y)_2$ , *Phys. B Condens. Matter.* 259–261 (1999) 399–400.
- [22] E.V. Sampathkumaran, R. Vijayaraghavan, Evidence for 4f-ligand dehybridization in the evolution of heavy-fermion behavior in the series  $\text{CeCu}_{2-x}\text{Ni}_x\text{Si}_2$ , *Phys. Rev. Lett.* 56 (1986) 2861–2864.
- [23] M. Koterlyn, I. Shcherba, R. Yasnitskii, G. Koterlyn, Peculiarities of the intermediate valence state of Ce in  $\text{CeM}_2\text{Si}_2$  ( $\text{M} = \text{Fe}, \text{Co}, \text{Ni}$ ) compounds, *J. Alloy Compd.* 442 (2007) 176–179.
- [24] T. Toliński, K. Synoradzki, M. Koterlyn, G. Koterlyn, R. Yasnitskii, Competing energy scales in the compounds  $\text{Ce}(\text{Ni}_{1-x}\text{Cu}_x)_2\text{Si}_2$ , *J. Alloy Compd.* 580 (2013) 512–516.
- [25] R.K. Singhal, N.L. Saini, K.B. Garg, J. Kanski, L. Ilver, P.O. Nilsson, et al., Study of some Ce intermetallics by core-level photoemission, *J. Phys. Condens. Matter.* 5 (1993) 4013.
- [26] M. Bertin Tchoula Tchokonté, P. de Villiers du Plessis, A. Michael Strydom, T. Brian Doyle, S. Ghosh, D. Kaczorowski, Antiferromagnetic Kondo lattice to intermediate valence transition in  $\text{Ce}(\text{Au}_{1-x}\text{Ni}_x)_2\text{Si}_2$  ( $0 \leq x \leq 1$ ), *J. Phys. Chem. Solids.* 77 (2015) 56–61.
- [27] E.M. Levin, O.I. Bodak, E.I. Gladyshevskii, V.G. Sinyushko, Composition Effects on Crystal and Electronic Structure of  $\text{CeM}_{2-x}\text{Si}_{2+x}$  ( $\text{M} = \text{Fe}, \text{Co}, \text{Ni}, \text{Cu}$ ) Alloys, *Phys. Status Solidi A.* 134 (1992) 107–117.
- [28] J. Rodriguez-Carvajal, FULLPROF, a program for Rietveld refinement and pattern matching analysis, Abstract of the satellite meeting on powder diffraction of the XV congress, p. 127, Int. Union of Crystallography, Talence, France, 1990.
- [29] Nonius Kappa CCD Program Package COLLECT, DENZO, SCALEPACK, SORTAV, Nonius Delft, The Netherlands, 1998.
- [30] G.M. Sheldrick, A short history of SHELX, *Acta Crystallogr. A.* 64 (2007) 112–122.
- [31] L.J. Farrugia, WinGX suite for small-molecule single-crystal crystallography, *J. Appl. Crystallogr.* 32 (1999) 837–838.
- [32] H. Zhou, Q. Yao, S. Yuan, J. Liu, H. Deng, Phase relationships in the La–Ni–Si system at 673 K, *J. Alloy Compd.* 366 (2004) 161–164.

- [33] O.I. Bodak, E.I. Gladyshevskii, P.I. Kripyakevich, Crystal structures of the  $\text{CeNi}_2\text{Si}_2$  compound and isostructural compounds in related systems., *Izv. Akad. Nauk SSSR Neorganicheskie Mater.* 2 (1966) 2151–5.
- [34] A.V. Morozkin, A.V. Knotko, V.O. Yapaskurt, F. Yuan, Y. Mozharivskyj, R. Nirmala, New orthorhombic derivative of  $\text{CaCu}_5$ -type structure:  $\text{RNi}_4\text{Si}$  compounds ( $\text{R}=\text{Y, La, Ce, Sm, Gd-Ho}$ ), crystal structure and some magnetic properties, *J. Solid State Chem.* 208 (2013) 9–13.
- [35] Z.P. Malik, On the quaternary systems  $\text{Ce-Ni-Zn}\{\text{B, Si}\}$ , Ph.D. Thesis, University of Vienna, 2012.
- [36] L.M. Gelato, E. Parthé, STRUCTURE TIDY – a computer program to standardize crystal structure data, *J. Appl. Crystallogr.* 20 (1987) 139–143.
- [37] A.V. Morozkin, Y.D. Seropegin, A.V. Griбанov, I.A. Sviridov, J.M. Kurenbaeva, A.L. Kurenbaev, Analysis of the melting temperatures of  $\text{RTX}_2$  ( $\text{CeNiSi}_2$  structure) and  $\text{RT}_2\text{X}_2$  ( $\text{CeGa}_2\text{Al}_2$  structure) compounds [ $\text{R}=\text{La, Ce, Sm, Er, Tm}$ ;  $\text{T}=\text{Fe, Co, Ni}$ ;  $\text{X}=\text{Si, Ge}$ ], *J. Alloy Compd.* 264 (1998) 190–196.
- [38] H.F. Braun, N. Engel, E. Parthé, Polymorphism and superconductivity of  $\text{LaIr}_2\text{Si}_2$ , *Phys. Rev. B.* 28 (1983) 1389–1395.
- [39] I. Zeiringer, A. Grytsiv, E. Bauer, G. Giester, P. Rogl, Phase Relations and Crystal Structures in the Ternary Systems  $\text{Sr}-\{\text{Ag, Au}\}-\{\text{Si, Ge}\}$ , *Z. Anorg. Allg. Chem.* 641 (2015) 1404–1421.
- [40] B. Belan, O. Bodak, R. Gladyshevskii, I. Soroka, B. Kuzhel, O. Protsyk, et al., Interaction of the components in the systems  $\text{Ce-Ag-Si}$  at 500 °C and  $\text{Eu-Ag-Si}$  at 400 °C, *J. Alloy Compd.* 396 (2005) 212–216.
- [41] A. Guzik, E. Talik, Electronic structure of the  $\text{Ce}(\text{Ag}_x\text{Cu}_{1-x})_2\text{Sb}_2$  compounds, *J. Alloy Compd.* 346 (2002) 10–16.
- [42] K. Ikeda, S.K. Dhar, M. Yoshizawa, K.A. Gschneidner Jr., Quenching of spin fluctuations by high magnetic fields, *J. Magn. Magn. Mater.* 100 (1991) 292–321.
- [43] B.Y. Kotur, A.M. Palasyuk, E. Bauer, H. Michor, G. Hilscher, Uncommon conductivity of  $\text{R-Mn-Al}$  ( $\text{R} = \text{Gd, Tb}$ ) ternary compounds, *J. Phys. Condens. Matter.* 13 (2001) 9421.
- [44] N.F. Mott, Conduction in non-Crystalline systems, *Philos. Mag.* 22 (1970) 7–29.
- [45] B. Cornut, B. Coqblin, Influence of the Crystalline Field on the Kondo Effect of Alloys and Compounds with Cerium Impurities, *Phys. Rev. B.* 5 (1972) 4541–4561.

- [46] H.-U. Desgranges, K.D. Schotte, Specific heat of the Kondo model, *Phys. Lett. A.* 91 (1982) 240–242.



**Table 1.** X-ray single crystal data for CeNi<sub>2+x</sub>Si<sub>2-x</sub>, x=0.33 and x-ray powder diffraction data for CeNi<sub>2</sub>Si<sub>2</sub> and LaNi<sub>2</sub>Si<sub>2</sub> (samples annealed at 800°C) (modified from ref. [35]).

Compound	CeNi <sub>2+x</sub> Si <sub>2-x</sub> , x=0.33	CeNi <sub>2</sub> Si <sub>2</sub>	LaNi <sub>2</sub> Si <sub>2</sub>
EMPA composition [at. %]	Ce <sub>20.1</sub> Ni <sub>46.5</sub> Si <sub>33.4</sub>	Ce <sub>20.4</sub> Ni <sub>38</sub> Si <sub>41.6</sub>	La <sub>20.3</sub> Ni <sub>37.9</sub> Si <sub>41.8</sub>
Refinement composition [at. %]	Ce <sub>20</sub> Ni <sub>46.5</sub> Si <sub>33.5</sub>	Ce <sub>20.6</sub> Ni <sub>39.4</sub> Si <sub>40</sub>	La <sub>20.6</sub> Ni <sub>39.2</sub> Si <sub>40.7</sub>
Space group	<i>P4/nmm</i> , No. 129, origin choice 2	<i>I4/mmm</i> , No. 139	<i>I4/mmm</i> , No. 139
Structure type	CaBe <sub>2</sub> Ge <sub>2</sub>	ThCr <sub>2</sub> Si <sub>2</sub>	ThCr <sub>2</sub> Si <sub>2</sub>
Data collection	Nonius KappaCCD	Guinier Image Plate	Guinier Image Plate
Radiation	MoK <sub>α</sub>	CuK <sub>α1</sub>	CuK <sub>α1</sub>
$\theta$ range	2.14 < $\theta$ < 36.16	10 < 2 $\theta$ < 100	10 < 2 $\theta$ < 100
Crystal size [ $\mu$ m]	40x50x50	-	-
<i>a</i> [nm]	0.40150(2)	0.4037(1)	0.411237(2)
<i>c</i> [nm]	0.95210(2)	0.9571(1)	0.971184(8)
Reflections in refinement	226 F <sub>o</sub> > 4 $\sigma$ (F <sub>o</sub> ) of 262	38	39
Z, volume [nm <sup>3</sup> ]	2, 0.153.5(1)	2, 0.156(1)	2, 0.164(1)
Number of variables	15	22	22
R <sub>F</sub> = $\Sigma F_o - F_c /\Sigma F_o$	0.0163	R <sub>F</sub> = 0.024	R <sub>F</sub> = 0.028
R <sub>Int</sub>	0.0107	R <sub>I</sub> = 0.024	R <sub>I</sub> = 0.028
GOF	1.195	$\chi^2$ = 1.72	$\chi^2$ = 3.09
Extinction (Zachariasen)	0.044(2)	-	-
RE; Occ.; B <sub>iso</sub> . U <sub>11</sub> <sup>b</sup> =U <sub>22</sub> ;U <sub>33</sub> ;U <sub>23</sub> =U <sub>13</sub> ;U <sub>12</sub> = 0	Ce in 2 <i>c</i> (1/4, 1/4, <i>z</i> ); <i>z</i> =0.75072(4); 1.00(1) 0.0057(1); 0.0068(2)	Ce in 2 <i>a</i> (0, 0, 0) 1.00(1); 0.14(2)	La in 2 <i>a</i> (0, 0, 0) 1.00(1); 0.95(2)
Ni; Occ.; B <sub>iso</sub> . U <sub>11</sub> <sup>b</sup> =U <sub>22</sub> ;U <sub>33</sub> ;U <sub>23</sub> =U <sub>13</sub> ;U <sub>12</sub> = 0	Ni1 in 2 <i>c</i> (1/4, 1/4, <i>z</i> ); <i>z</i> =0.1264(1); 1.00(1) 0.0134(3); 0.0120(4)	Ni in 4 <i>d</i> (0, 1/2, 1/4) 1.00(2); 0.60(5)	Ni in 4 <i>d</i> (0, 1/2, 1/4) 0.95(2); 0.19(3)
Ni; Occ. U <sub>11</sub> <sup>b</sup> =U <sub>22</sub> ;U <sub>33</sub> ;U <sub>23</sub> =U <sub>13</sub> =U <sub>12</sub> =0	Ni2 in 2 <i>b</i> (3/4, 1/4, 1/2); 1.00(1) 0.0085(2); 0.0074(3)		
Si; Occ.; B <sub>iso</sub> . U <sub>11</sub> <sup>b</sup> =U <sub>22</sub> ;U <sub>33</sub> ; U <sub>23</sub> =U <sub>13</sub> ;U <sub>12</sub> = 0	Si1 in 2 <i>c</i> (1/4, 1/4, <i>z</i> ); <i>z</i> =0.3717(2); 1.00(1) 0.0056(4); 0.0077(7)	Si in 4 <i>e</i> (0, 0, <i>z</i> ); <i>z</i> =0.3804(3); 1.00(1); 0.26(7)	Si in 4 <i>e</i> (0, 0, <i>z</i> ); <i>z</i> =0.3684(2); 1.00(1); 0.49(5)
M; Occ. U <sub>11</sub> <sup>b</sup> =U <sub>22</sub> ;U <sub>33</sub> ;U <sub>23</sub> =U <sub>13</sub> =U <sub>12</sub> =0	M in 2 <i>a</i> (3/4, 1/4, 0); 0.33(-) Ni3+0.67(-) Si2 <sup>c</sup> 0.0163(4); 0.0102(6)		
Residual electron density; max; min in [electrons/nm <sup>3</sup> ] x 1000	1.18; -1.53	-	-

<sup>a</sup>crystal structure data are standardized using the program Structure Tidy[36].

<sup>b</sup>anisotropic atomic displacement parameters U<sub>ij</sub> in [10<sup>-2</sup> nm<sup>2</sup>].

<sup>c</sup>Fixed after EPMA

**Table 2.** X-ray single crystal data for Ce(Ni<sub>1-x</sub>Zn<sub>x</sub>)<sub>2</sub>Si<sub>2</sub>, x=0.39 and Rietveld XPD data for La(Ni<sub>1-x</sub>Zn<sub>x</sub>)<sub>2</sub>Si<sub>2</sub>; x=0.44 (space group *P4/nmm*; No. 129, origin at center)<sup>a</sup>. (modified from ref. [35]).

Compound	Ce(Ni <sub>1-x</sub> Zn <sub>x</sub> ) <sub>2</sub> Si <sub>2</sub> , x=0.39	La(Ni <sub>1-x</sub> Zn <sub>x</sub> ) <sub>2</sub> Si <sub>2</sub> , x=0.44
EMPA composition [at. %]	Ce <sub>19.4</sub> Ni <sub>25.3</sub> Zn <sub>16.1</sub> Si <sub>39.2</sub>	La <sub>19.9</sub> Ni <sub>22.3</sub> Zn <sub>17.2</sub> Si <sub>40.7</sub>
Refinement composition [at. %]	Ce <sub>20</sub> Ni <sub>24.4</sub> Zn <sub>15.6</sub> Si <sub>40</sub>	La <sub>20</sub> Ni <sub>22.6</sub> Zn <sub>17.4</sub> Si <sub>40</sub>
Structure type	CaBe <sub>2</sub> Ge <sub>2</sub>	CaBe <sub>2</sub> Ge <sub>2</sub>
Data collection	Nonius KappaCCD	Guinier-Huber IP
Radiation	MoK <sub>α</sub>	CuK <sub>α1</sub>
$\theta$ range	2.08 < $\theta$ < 36.05	8 < 2 $\theta$ < 100
Crystal size [ $\mu$ m]	40x50x50	-
<i>a</i> [nm]	0.41022(1)	0.41680(6) <sup>c</sup>
<i>c</i> [nm]	0.98146(4)	0.99213(7) <sup>c</sup>
Reflections in refinement	266 F <sub>o</sub> > 4 $\sigma$ (F <sub>o</sub> ) of 272	72
Mosaicity	0.65	-
Z, density [gm/cm <sup>3</sup> ]	2, 6.44	2, 6.022
Number of variables	15	26
R <sub>F</sub> = $\Sigma F_o - F_c /\Sigma F_o$	0.0134	R <sub>F</sub> =0.043
R <sub>Int</sub>	0.0135	R <sub>I</sub> =0.025
GOF	1.153	$\chi^2$ =2.78
Extinction (Zachariasen)	0.024(1)	R <sub>w</sub> =2.75
RE in 2 <i>c</i> (1/4, 1/4, <i>z</i> ); Occ. B <sub>iso</sub> U <sub>11</sub> <sup>b</sup> =U <sub>22</sub> ; U <sub>33</sub> ; U <sub>23</sub> =U <sub>13</sub> ; U <sub>12</sub> =0	<i>z</i> =0.73977(3); 1.00(1) 0.0050(1); 0.0058(1)	<i>z</i> =0.73833(7); 1.00(1); B <sub>iso</sub> =0.28(1)
M in 2 <i>a</i> (3/4, 1/4, 0); Occ. U <sub>11</sub> <sup>b</sup> =U <sub>22</sub> ; U <sub>33</sub> ; U <sub>23</sub> =U <sub>13</sub> =U <sub>12</sub> =0	0.78(-)Zn1+0.22(-)Ni <sup>d</sup> 0.0099(2); 0.0070(2)	0.87(1) Zn1+0.13 Ni1 B <sub>iso</sub> =0.26(3)
Ni2 in 2 <i>c</i> (1/4, 1/4, <i>z</i> ); Occ. U <sub>11</sub> <sup>b</sup> =U <sub>22</sub> ; U <sub>33</sub> ; U <sub>23</sub> =U <sub>13</sub> ; U <sub>12</sub> =0	<i>z</i> =0.38514(6); 1.00(1) 0.0063(2); 0.0071(3)	<i>z</i> =0.3883(1); 1.00(1); B <sub>iso</sub> =0.36(4)
Si1 in 2 <i>b</i> (3/4, 1/4, 1/2); Occ. U <sub>11</sub> <sup>b</sup> =U <sub>22</sub> ; U <sub>33</sub> ; U <sub>23</sub> =U <sub>13</sub> =U <sub>12</sub> =0	1.00(1) 0.0061(3); 0.0060(5)	1.00(1); B <sub>iso</sub> =0.54(6)
Si2 in 2 <i>c</i> (1/4, 1/4, <i>z</i> ); Occ. U <sub>11</sub> <sup>b</sup> =U <sub>22</sub> ; U <sub>33</sub> ; U <sub>23</sub> =U <sub>13</sub> ; U <sub>12</sub> =0	<i>z</i> =0.1474(2); 1.00(1) 0.0106(4); 0.0096(6)	<i>z</i> =0.1537(3); 1.00(1); B <sub>iso</sub> =0.68(7)
Residual electron density; max; min in [electrons/nm <sup>3</sup> ] x 1000	1.48; -0.97	

<sup>a</sup>crystal structure data are standardized using the program Structure Tidy [36].

<sup>b</sup>anisotropic atomic displacement parameters U<sub>ij</sub> in [10<sup>-2</sup> nm<sup>2</sup>].

<sup>c</sup>Ge standard

<sup>d</sup>Fixed after EPMA

**Table 3.** Interatomic distances for Ce(Ni<sub>1-x</sub>Zn<sub>x</sub>)<sub>2</sub>Si<sub>2</sub>, x=0.39 (*P4/nmm*; No. 129).

Atom 1	Atom 2	d <sub>1,2</sub> [nm]
Ce1	Si2 (4x)	0.31047
	Si1 (4x)	0.31217
	Ni2 (4x)	0.31491
	M (4x)	0.32757
M	Si2 (4x)	0.25102
	M (4x)	0.29007
	Ce1 (4x)	0.32757
Ni2	Si2 (1x)	0.23329
	Si1 (4x)	0.23405
	Ce1 (4x)	0.31491
Si1	Ni2 (4x)	0.23405
	Si1 (4x)	0.29007
	Ce1 (4x)	0.31217
Si2	Ni2 (1x)	0.23329
	M (4x)	0.25102
	Ce1 (4x)	0.31047

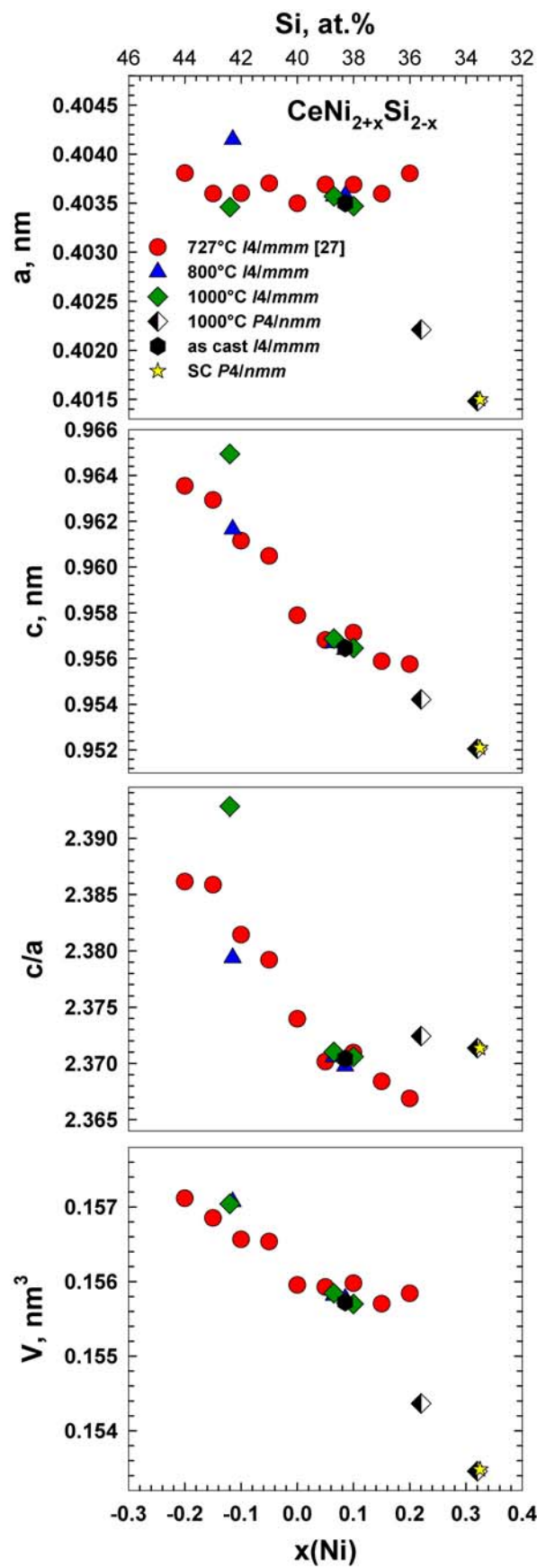


**Figure 1.** Compositional dependence of lattice parameters of  $\text{CeNi}_{2+x}\text{Si}_{2-x}$ .

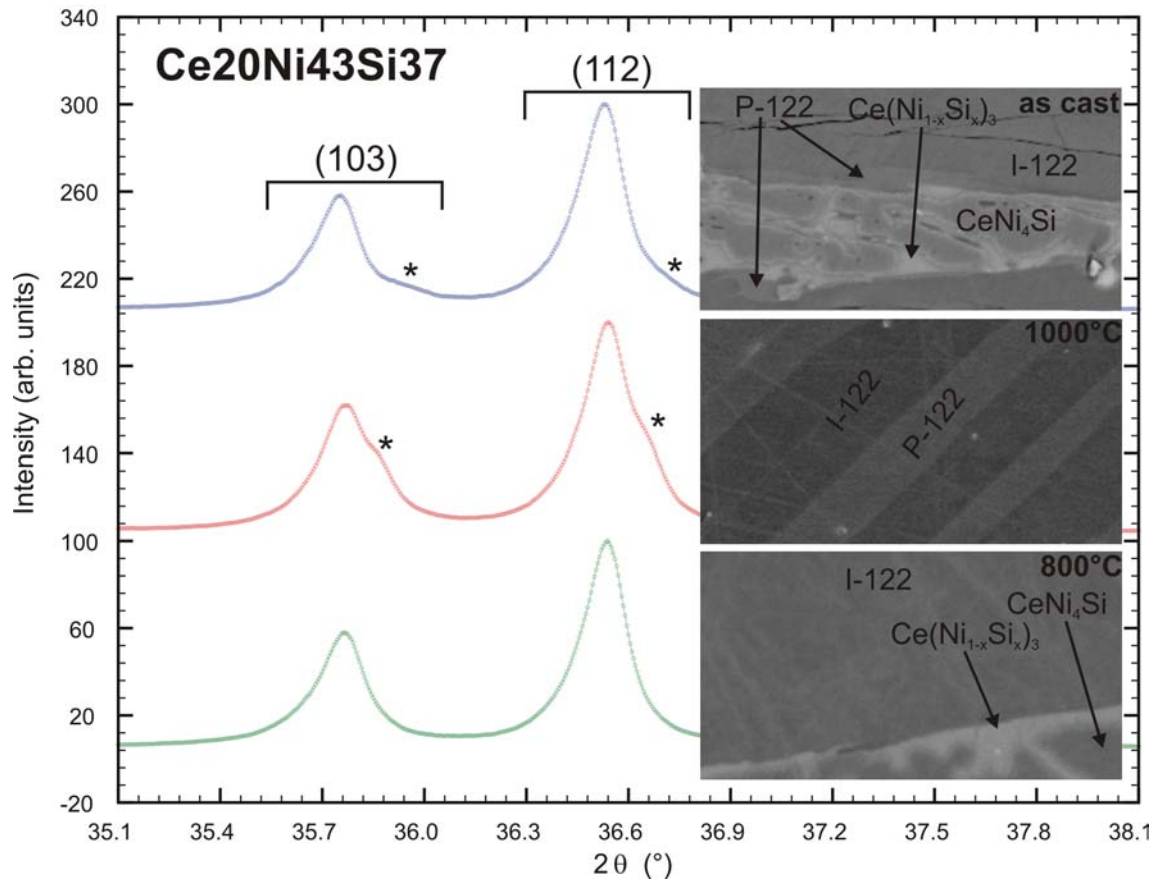


**Figure 2.** The strongest BaAl<sub>4</sub>-type reflections and the micrograph of Ce<sub>20</sub>Ni<sub>43</sub>Si<sub>37</sub> alloys in as cast, annealed at 1000°C and 800°C. The asterisks represent the CaBe<sub>2</sub>Ge<sub>2</sub>-type reflections (see section 3.1.1 for detailed explanation).

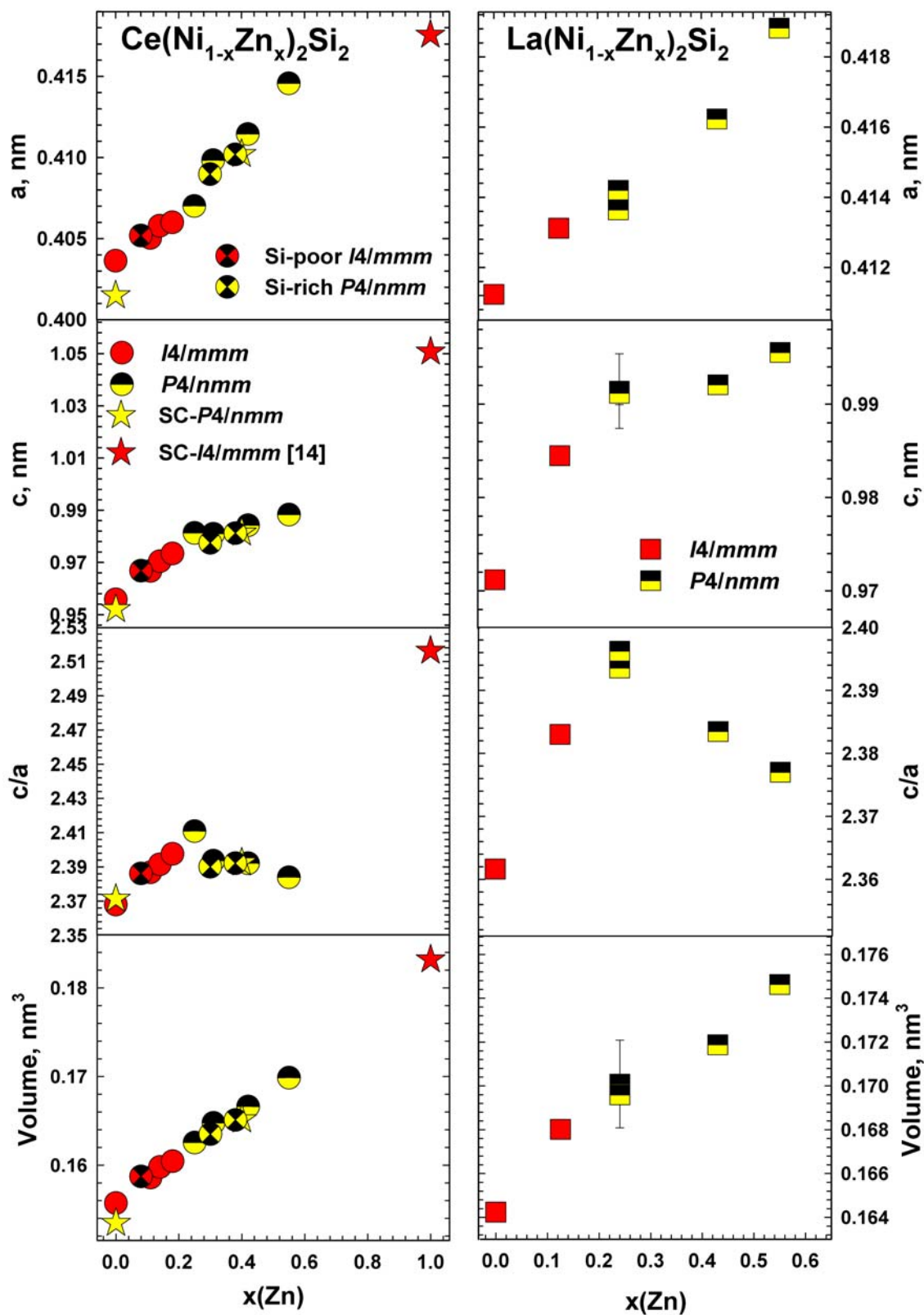


**Figure 3.** Unit cell parameters vs. Zn-content in the phases {La,Ce}[Ni<sub>1-x</sub>Zn<sub>x</sub>]<sub>2</sub>Si<sub>2</sub> (annealed at 800°C) revealing a transition from body centered to primitive symmetry as a consequence of Ni/Zn substitution (compositions from EPMA) (modified from ref. [35]).

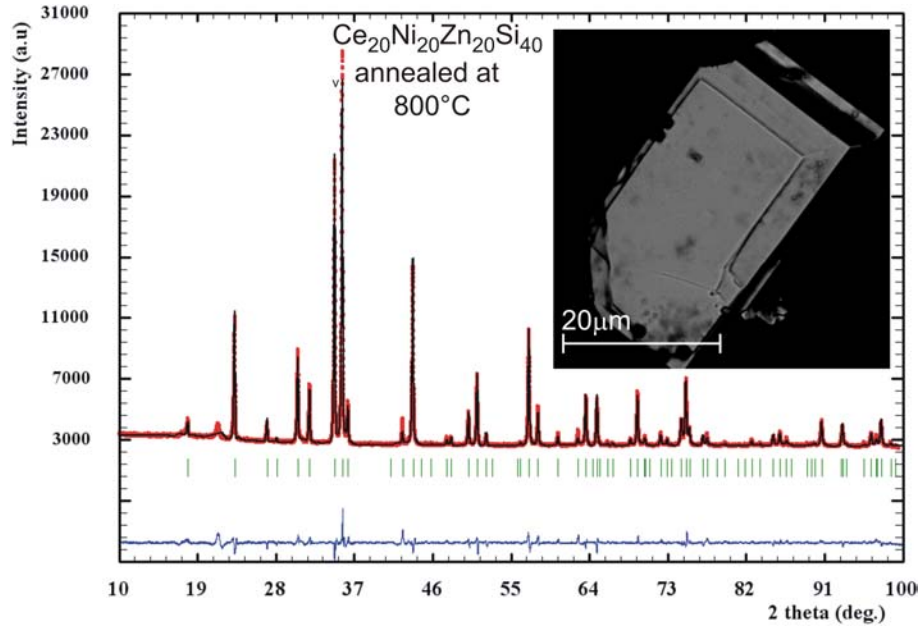


**Figure 4.** Rietveld refinement of the alloy with composition  $\text{Ce}_{20}\text{Ni}_{20}\text{Zn}_{20}\text{Si}_{40}$  at.% showing  $\text{Ce}(\text{Ni}_{1-x}\text{Zn}_x)_2\text{Si}_2$  with  $\text{CaBe}_2\text{Ge}_2$ -type (space group  $P4/nmm$ ) and the micrograph of the single crystal obtained from Zn flux (sample  $\text{Ce}_2\text{Ni}_4\text{Si}_8\text{Zn}_{86}$  at. %).

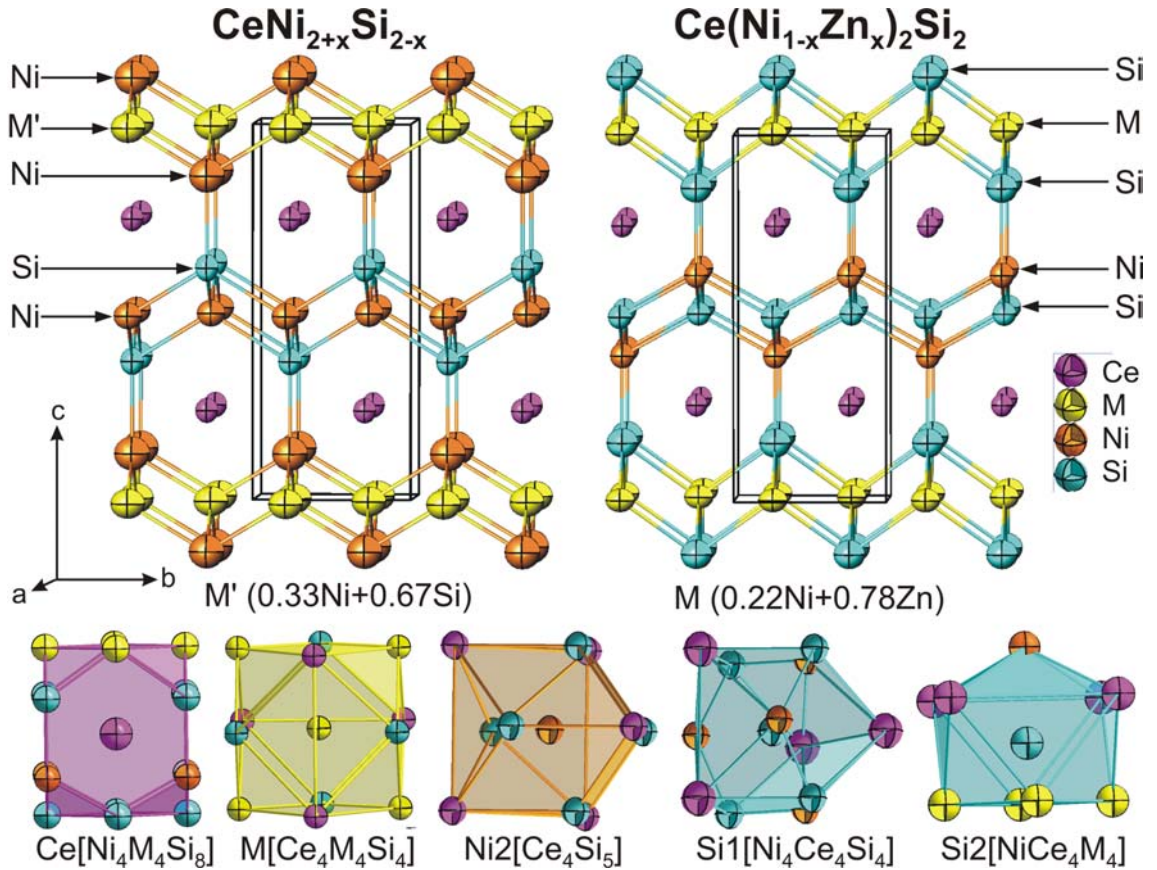


**Figure 5.** Site exchange arrangement in the  $\text{CaBe}_2\text{Ge}_2$ -type quaternary  $\text{Ce}(\text{Ni}_{1-x}\text{Zn}_x)_2\text{Si}_2$  (right) and normal  $\text{CaBe}_2\text{Ge}_2$ -type arrangement of ternary  $\text{CeNi}_{2+x}\text{Si}_{2-x}$  (left). Coordination polyhedra are presented for the  $\text{CaBe}_2\text{Ge}_2$ -type quaternary  $\text{Ce}(\text{Ni}_{1-x}\text{Zn}_x)_2\text{Si}_2$ . (modified from ref. [35])



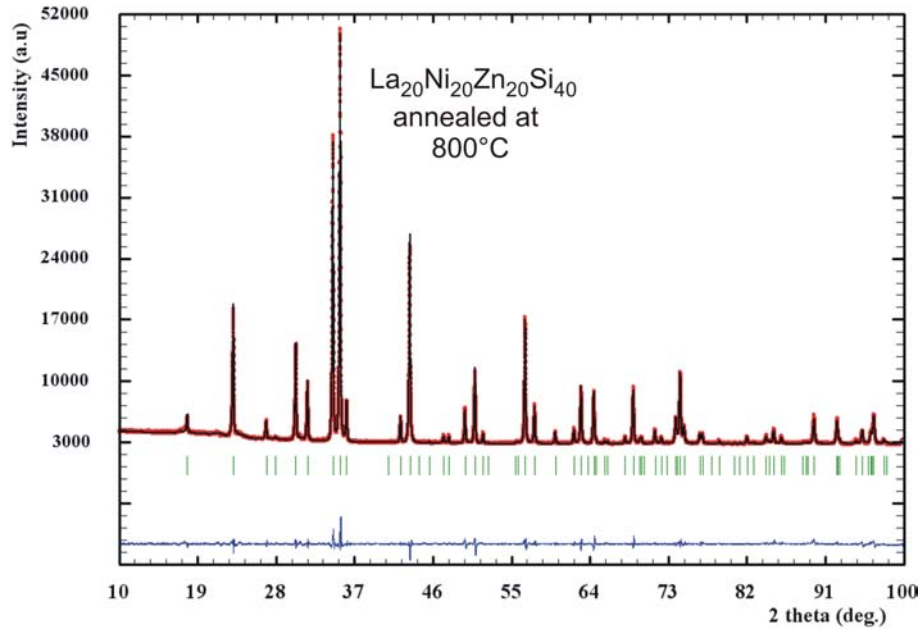


**Figure 6.** Rietveld refinement of single phase  $\text{La}(\text{Ni}_{1-x}\text{Zn}_x)_2\text{Si}_2$ ;  $x=0.44$  ( $\text{CaBe}_2\text{Ge}_2$ -type, space group  $P4/nmm$ ) from the alloy with composition  $\text{La}_{20}\text{Ni}_{20}\text{Zn}_{20}\text{Si}_{40}$  at.%, annealed at  $800^\circ\text{C}$ .

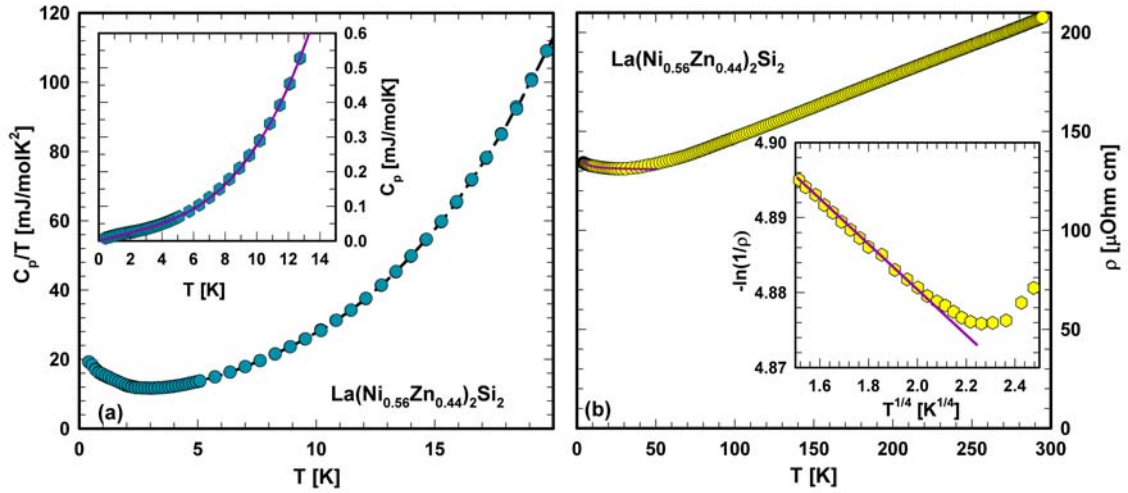


**Figure 7.** (a) Temperature dependent specific heat  $C_p$  of  $\text{La}(\text{Ni}_{0.56}\text{Zn}_{0.44})_2\text{Si}_2$  plotted as  $C_p/T$  vs.  $T$ . The inset shows the data as  $C_p$  vs  $T$ . The solid line is a least squares fit according to the spin fluctuation model (see text). (b) Temperature dependent electrical resistivity  $\rho$  of  $\text{La}(\text{Ni}_{0.56}\text{Zn}_{0.44})_2\text{Si}_2$ . The inset shows the data as  $-\ln(1/\rho)$  vs.  $T^{1/4}$  to reveal evidence of variable range hopping conductivity. The solid line is a guide for the eyes.



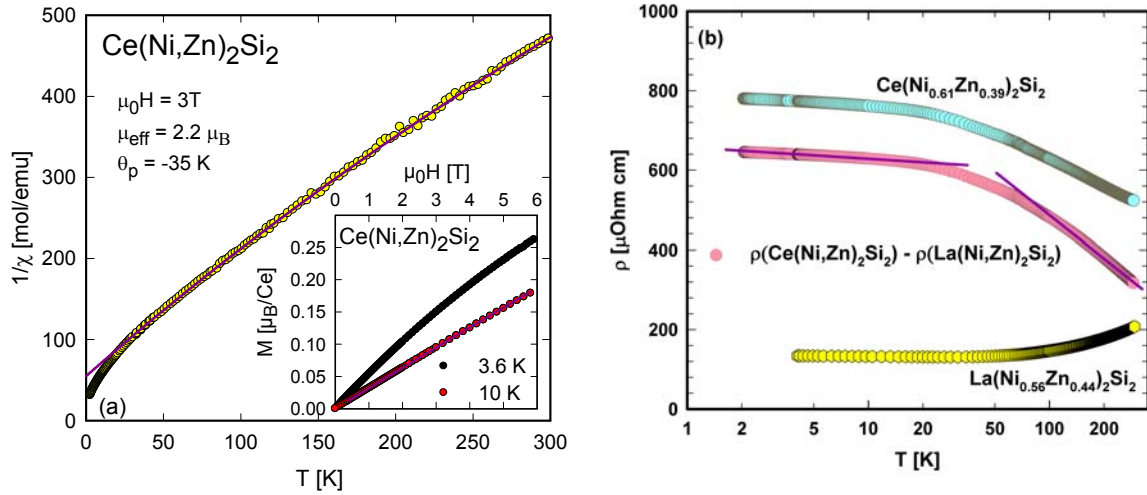


**Figure 8.** (a) Temperature dependent magnetic susceptibility  $\chi$  of  $\text{Ce}(\text{Ni}_{0.61}\text{Zn}_{0.39})_2\text{Si}_2$  plotted as  $1/\chi$  vs.  $T$ . The solid line is the result of a least squares fit of the modified Curie Weiss law to the experimental data above 50 K. (b) Temperature dependent electrical resistivity  $\rho$  of  $\text{Ce}(\text{Ni}_{0.61}\text{Zn}_{0.39})_2\text{Si}_2$  and  $\text{La}(\text{Ni}_{0.56}\text{Zn}_{0.44})_2\text{Si}_2$ . The magnetic contribution to the electrical resistivity,  $\rho_{\text{mag}}$ , of  $\text{Ce}(\text{Ni}_{0.61}\text{Zn}_{0.39})_2\text{Si}_2$  is shown as well. The solid lines are guides for the eyes.

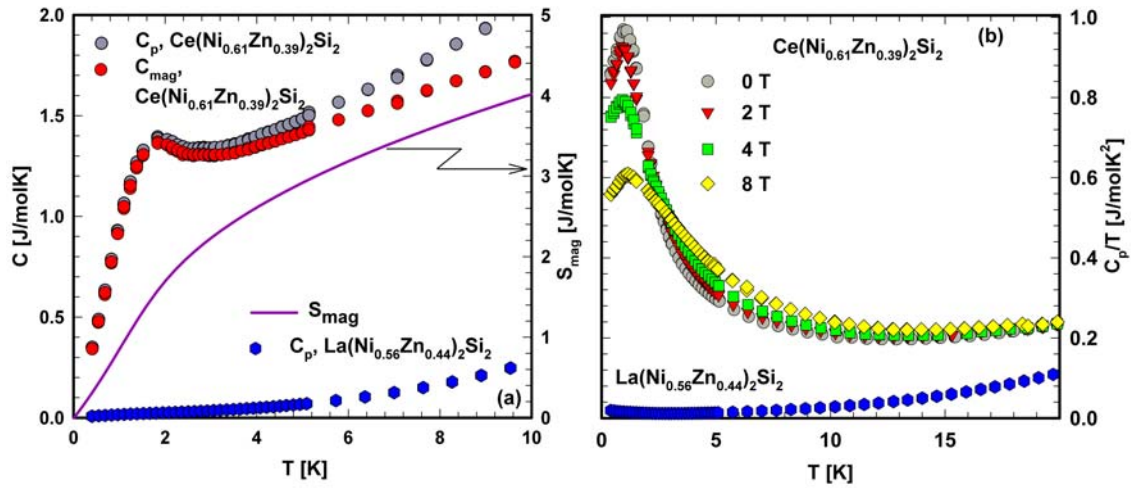


**Figure 9.** (a) Temperature dependent specific heat  $C_p$  of  $\text{Ce}(\text{Ni}_{0.61}\text{Zn}_{0.39})_2\text{Si}_2$  and  $\text{La}(\text{Ni}_{0.56}\text{Zn}_{0.44})_2\text{Si}_2$ .  $C_{\text{mag}}(T)$  is derived by subtracting both data-sets. The temperature dependent magnetic entropy  $S_{\text{mag}}$  (solid line, referring to the right axis) originates from the integration of  $C_{\text{mag}}/T(T)$ . (b) Field and temperature dependent heat capacity data of  $\text{Ce}(\text{Ni}_{0.61}\text{Zn}_{0.39})_2\text{Si}_2$  plotted as  $C_p/T$  vs.  $T$  for various externally applied magnetic fields. Data of  $\text{La}(\text{Ni}_{0.56}\text{Zn}_{0.44})_2\text{Si}_2$  are added for purpose of comparison.

## Summary

The present PhD thesis deals with various aspects of thermoelectric (TE) materials and device development: (i) improvement of TE performance of  $\text{CoSb}_3$ -based materials by nanostructuring, (ii) interaction between group V metals and various skutterudites to define suitable diffusion barriers for the hot electrodes of the TE devices, and (iii) search for new materials by means of phase diagram investigation in ternary and quaternary RE-TM-Si systems (RE=La,Ce, TM=Ni,Zn).

Nano-structuring is known as an efficient way to improve thermoelectric (TE) properties. Formation of in-situ nano precipitates via a disproportionation reaction was investigated in order to induce nano precipitation of metals, silicides, and antimonides in n-type  $\text{Ep}_y\text{Co}_4\text{Sb}_{12}$  (Ep = La, Ce, Pr, Sm) skutterudites. Significant reduction of lattice thermal conductivity was found in case of unfilled  $\text{CoSb}_3$  with addition of W or  $\text{TaSb}_2$ . The optimisation of composition and preparation techniques performed during the current investigation resulted in maximum  $ZT_{723\text{K}}=1.3(1)$  for multifilled  $(\text{Ce,Sm,Pr})_{0.13}\text{Co}_4\text{Sb}_{12}$  and  $ZT_{823\text{K}}=1.2(1)$  for single filled  $\text{Ce}_{0.1}\text{Co}_4\text{Sb}_{12}/\text{CoSi}$ , being among the highest ZT-values for n-type skutterudites filled with trivalent rare-earths.

A preliminary study on the possibility to introduce borides as a secondary phase of a Skutterudite/boride composite was also performed. In this case the crystal structure of novel high temperature ternary FeB-type phases  $\text{Ta}_{1-x}\{\text{Hf,Zr,Ti}\}_x\text{B}$  were investigated by means of X-ray diffraction (single crystal and powder) in combination with EPMA. Interestingly these novel high temperature FeB-type phases can be formed by small addition (less than  $\sim 10$  at. %) of group IV metals to TaB, which crystallizes in the CrB-type. These materials are currently being investigated as additive to skutterudites in order to check their influence on the TE properties.

Diffusion couple experiment between various metals (particularly group V metals) and skutterudites gave hints on the formation of various phases in the diffusion zones. In order to define suitable diffusion barriers for the hot electrode of TE devices, the knowledge of binary  $\{\text{V,Nb,Ta}\}\text{-Sb}$  phase diagrams as well as the physical properties of phases formed in the diffusion zones are important requirements.

The phase diagrams V-Sb and Ta-Sb were constructed for the first time. In the V-Sb system five stable binary phases:  $\text{V}_{3+x}\text{Sb}_{1-x}$  ( $\text{Cr}_3\text{Si}$ -type),  $\ell\text{T-V}_3\text{Sb}_2$  ( $\text{Fe}_3\text{Sn}_2$ -type),  $\text{hT-V}_{2-x}\text{Sb}$  ( $\text{Ni}_2\text{In}$ -type),  $\text{V}_{7.46}\text{Sb}_9$  (own type), and  $\text{V}_{1-x}\text{Sb}_2$  ( $\text{CuAl}_2$ -type) were observed, while in the Ta-Sb system three binary phases exist:  $\text{Ta}_{3+x}\text{Sb}_{1-x}$  ( $\text{Cr}_3\text{Si}$ -type),  $\text{Ta}_5\text{Sb}_4$  ( $\text{Ti}_5\text{Te}_4$ -type),

and TaSb<sub>2</sub> (OsGe<sub>2</sub>-type). Phase relations in the V-Sb system are characterized by various types of transitions, while the Ta-Sb phase diagram closely resembles the Nb-Sb system. The existence of interstitial carbon in the V<sub>5</sub>Sb<sub>4</sub> phase was confirmed by X-ray single crystal data of V<sub>5</sub>Sb<sub>4</sub>C<sub>1-x</sub>, the first representative of a filled Ti<sub>5</sub>Te<sub>4</sub>-type structure. A re-investigation of the Nb-Sb system proved validity of the Nb-Sb system as earlier presented by Melnyk et al. All group-V metal di-antimonides exhibit metallic conductivity over a wide temperature range. They have low resistivity and high thermal conductivity. Various measurement methods were employed to extract the Debye temperature of these compounds. The thermal expansion coefficient increases from TaSb<sub>2</sub> to V<sub>1-x</sub>Sb<sub>2</sub>, in which the CTE of NbSb<sub>2</sub> is in the range of the average value for Sb-based skutterudites. Good CTE compatibility and similar shear modulus between {Nb,Ta}Sb<sub>2</sub> and Sb-based skutterudites together with their high thermal stability as well as good thermal and electrical conductivity promote the potential use of Ta and Nb as diffusion barrier and/or hot electrode contact material for Sb-based skutterudite in TE applications.

Novel compounds, Ba<sub>5</sub>{V,Nb}<sub>12</sub>Sb<sub>19+x</sub>, were found in diffusion couple experiments between Ba-filled skutterudite Ba<sub>0.3</sub>Co<sub>4</sub>Sb<sub>12</sub> and group V transition metals (V,Nb,Ta). These compounds (Ba<sub>5</sub>V<sub>12</sub>Sb<sub>19.41</sub>, *a* = 1.21230(1) nm, *R*<sub>F2</sub> = 0.0189 and Ba<sub>5</sub>Nb<sub>12</sub>Sb<sub>19.14</sub>, *a* = 1.24979(2) nm, *R*<sub>F2</sub> = 0.0219, both crystallize in space group *P* $\bar{4}$ 3*m*) are the first representatives of the Ba<sub>5</sub>Ti<sub>12</sub>Sb<sub>19+x</sub>-type. In contrast to the aristotype, the structure of Ba<sub>5</sub>V<sub>12</sub>Sb<sub>19.41</sub> shows additional site occupation and atom disorder. Temperature dependent ADPs and specific heat of Ba<sub>5</sub>{V,Nb}<sub>12</sub>Sb<sub>19+x</sub> confirmed the rattling behaviour of Ba and Sb<sub>7</sub> (in case of Ba<sub>5</sub>V<sub>12</sub>Sb<sub>19+x</sub>) atoms within the framework built by {V,Nb} and Sb atoms. The rattling behaviour in these compounds is reflected in various physical properties such as electrical resistivity, specific heat, and low thermal conductivity. Ba<sub>5</sub>Nb<sub>12</sub>Sb<sub>19+x</sub> possesses an extremely low lattice thermal conductivity, close to the minimum thermal conductivity of ~0.43 Wm<sup>-1</sup>K<sup>-1</sup>. A resistivity upturn at low temperatures occurs in both compounds, as well as a change from p- to n-type conductivity in Ba<sub>5</sub>Nb<sub>12</sub>Sb<sub>19+x</sub> above 300 K, suggesting the existence of a narrow gap in close proximity of the Fermi level. Vicker's hardness of (3.8±0.1) GPa (vanadium compound) and (3.5±0.2) GPa (niobium compound) are comparable to Sb-based filled skutterudites. However, the indentation Young's moduli for these compounds *E*<sub>I</sub>(Ba<sub>4.9</sub>V<sub>12</sub>Sb<sub>19.0</sub>) = (85±2) GPa and *E*<sub>I</sub>(Ba<sub>4.9</sub>Nb<sub>12</sub>Sb<sub>19.4</sub>) = (79±5) GPa are significantly smaller than those of skutterudites, which range from about 130 to 145 GPa. Moreover the CTE of these compounds are significantly higher than those of the p-type skutterudites. Incompatibility of Ba<sub>5</sub>{V,Nb}<sub>12</sub>Sb<sub>19+x</sub> with Ba-filled Sb-based

skutterudites in respect to a high coefficient of thermal expansion and dissimilar shear moduli together with the low thermal and electrical conductivity highly recommends to avoid formation of these phases in a hot contact zone between V, Nb-based electrodes and the skutterudite material.

As a continuation of the previous study on the Ce-Zn-Si system at 800°C by Malik et al., phase relations in the same system at  $\leq 33.3$  at.% Ce were investigated at a lower temperature of 600°C, particularly concerning two novel ternary compounds (labeled as  $\tau_5$  and  $\tau_6$ ). Five ternary compounds ( $\tau_1$ ,  $\tau_2$ ,  $\tau_5$  to  $\tau_7$ ) exist at the investigated region at 600°C. Several four-phase reactions in the Zn rich corner were detected by DTA, including the peritectic decomposition temperatures of  $\tau_5$  and  $\tau_6$  at  $865 \pm 5^\circ\text{C}$  and  $695 \pm 5^\circ\text{C}$ , respectively. A Schultz–Scheil diagram was constructed from DTA measurements and partial isothermal sections determined at various temperatures. The crystal structures of  $\tau_5$  (CeNiSi<sub>2</sub>-type, *Cmcm*,  $a = 0.42079(1)$ ,  $b = 1.76522(3)$ ,  $c = 0.41619(1)$  nm), and  $\tau_6$  (ThCr<sub>2</sub>Si<sub>2</sub>-type, *I4/mmm*,  $a = 0.41757(1)$ ,  $c = 1.05073(2)$  nm) were solved from X-ray single crystal diffraction data. An interesting case was met in the stabilization by extremely small amounts of Ge (less than  $\sim 2$  at.%) of the ternary phases  $\{\text{La,Ce}\}_7\text{Zn}_{21}(\text{Zn}_{1-x}\text{Ge}_x)_2$ , both isotypic with the structure of  $\text{Ce}_7\text{Zn}_{21}(\text{Zn}_{1-x}\text{Si}_x)_2$ . DFT calculations elucidated the extent and nature of the stabilizing effect of Ge in  $\text{Ce}_7\text{Zn}_{23-x}\text{Ge}_x$  discussing the electronic structure in terms of the density of states (DOS) and determining enthalpies of formation for  $\text{Ce}_7\text{Zn}_{23-x}\text{Ge}_x$ , as well as for several neighbouring binary Ce–Zn phases. Physical property measurements document that neither  $\tau_5$  nor  $\tau_6$  are near a metal to insulator transition and thus exhibit rather metallic than semiconducting (thermoelectric) behaviour. Magnetic measurements as well as specific heat and electrical resistivity data reveal interesting ferromagnetic Kondo lattice behavior for  $\tau_5$  with a Curie temperature  $T_C = 4.4$  K, whereas  $\tau_6$  displays Curie–Weiss type paramagnetic behavior down to 3 K. The effective paramagnetic moments of Ce obtained from Curie–Weiss suggest that the ground state of Ce-ions in these compounds is trivalent or close to 3+.

An interesting case was found in the quaternary  $\{\text{La,Ce}\}-(\text{Ni,Zn})\text{-Si}$  system at 800°C. Despite the BaAl<sub>4</sub>-type phases do not exist in the end member ternary systems  $\{\text{La,Ce}\}\text{-Zn-Si}$  at 800°C, solid solution  $\{\text{La,Ce}\}(\text{Ni}_{1-x}\text{Zn}_x)_2\text{Si}_2$  exist with Ni/Zn substitution starting from  $\{\text{La,Ce}\}\text{Ni}_2\text{Si}_2$  (ThCr<sub>2</sub>Si<sub>2</sub>-type) up to  $0 \leq x \leq 0.18$ . For higher Zn-contents  $0.22 \leq x \leq 0.55$  the solutions adopt the CaBe<sub>2</sub>Ge<sub>2</sub>-type. The investigations are backed by XRSC data for  $\text{Ce}(\text{Ni}_{0.61}\text{Zn}_{0.39})_2\text{Si}_2$  (*P4/nmm*;  $a=0.41022(1)$  nm,  $c=0.98146(4)$  nm;  $R_F=0.012$ ), and XRPD for  $\text{La}(\text{Ni}_{1-x}\text{Zn}_x)_2\text{Si}_2$  ( $x=0.44$ ; *P4/nmm*;  $a=0.41680(6)$  nm,  $c=0.99364(4)$  nm;  $R_F=0.043$ ).

Interestingly the primitive tetragonal phase with  $\text{CaBe}_2\text{Ge}_2$ -type has also been observed in the Ce-Ni-Si system,  $\text{CeNi}_{2+x}\text{Si}_{2-x}$ ,  $x=0.33$  (single crystal data,  $P4/nmm$ ;  $a=0.40150(2)$  nm,  $c=0.95210(2)$  nm;  $R_F=0.016$ ). While the quaternary  $\text{CaB}_2\text{Ge}_2$ -type phase is stable at  $800^\circ\text{C}$ , the ternary  $\text{CaB}_2\text{Ge}_2$ -type phase exists only at high temperature ( $\geq 1000^\circ\text{C}$ ) in the Ni-rich side. Physical properties measurements on quaternary  $\text{Ce}(\text{Ni}_{0.61}\text{Zn}_{0.39})_2\text{Si}_2$  with  $\text{CaBe}_2\text{Ge}_2$ -type revealed a long range magnetic order below 2 K and a Kondo effect. In contrast to the intermediate valence behaviour in ternary  $\text{CeNi}_2\text{Si}_2$  with  $\text{ThCr}_2\text{Si}_2$ -type, the ground state of Ce in  $\text{Ce}(\text{Ni}_{0.61}\text{Zn}_{0.39})_2\text{Si}_2$  with  $\text{CaBe}_2\text{Ge}_2$ -type is close to trivalent as indicated by the effective magnetic moment derived from a fit to the modified Curie-Weiss law ( $\chi_{\text{eff}}= 2.20 \mu_B/\text{Ce}$ ). Spin fluctuations behaviour and variable range hopping conductivity are observed in  $\text{La}(\text{Ni}_{0.56}\text{Zn}_{0.44})_2\text{Si}_2$ .

## Acknowledgements

*In the name of Allah, Most Gracious, Most Merciful. Praise be to Allah, The Lord of the worlds, and blessing to the Holy Prophet Muhammad.*

I would like to express my sincere gratitude to my advisors, Prof. Peter Franz Rogl and Prof. Wolfgang Kautek for the continuous support of my Ph.D study, for their patience, motivation, and immense knowledge.

I am grateful to Dr. Andriy Grytsiv who introduced me to various experimental techniques, for his motivation, guidance, and valuable discussion. I am thankful to Dr. Gerda Rogl not only for her support in my research and study, but also for her special care for me during my stay in Vienna.

I would like to thank Prof. Ernst Bauer (Institute of Solid State Physics, TU Wien) and his research group for their help in physical properties measurement and analysis. I am grateful to Prof. Gerald Giester (Institute of Mineralogy and Crystallography, Univ. of Vienna) for the X-ray single crystal diffractions. I am thankful to Dr. Pavel Broz (Masaryk Univ., Czech Republic) for the DTA measurements. I am also thankful to Prof. Adriana Saccone (Univ. of Genova, Italy) for providing me the opportunity to work in her research group and for her support during my stay in Genova.

I would like to thank Dr. Stephan Puchegger for the SEM-EDX measurement time and for the elastic moduli measurements. I would like to thank also Prof. Carlos Nunes (Univ. of Sao Paulo, Brazil) and his research group for providing the boride samples.

I thank all my colleagues at the Institute of Physical Chemistry and Institute of Materials Chemistry and Research, Univ. of Vienna for their cooperation and support, and for the nice working environment.

I would like to thank all Indonesian community in Vienna for their friendship during my stay in Vienna. Special thanks to my mother, my sisters and my brother, and all my family for their support all the way through my study.

In this opportunity I would like to acknowledge the support from the Austrian Federal Ministry of Science and Research (BMWF) under the scholarship scheme: Technology Grant Southeast Asia (Ph.D) in the frame of the ASEA UNINET. This work was supported in part by the Christian Doppler Laboratory for Thermoelectricity. The scientific collaboration with Masaryk University was supported by the Scientific and Technological Cooperation (WTZ) between Austria and Czech Republic (Project CZ12/2013).

## Curriculum Vitae

Name : Fainan Failamani

Date of birth, place : 18<sup>th</sup> January 1988, Purwokerto, Central Java, Indonesia

Nationality : Indonesian

### Education

1993-1999 : SD Al Irsyad Al Islamiyyah 1 Purwokerto, Indonesia (elementary school)

1999-2002 : SMP N 1 Purwokerto, Indonesia (junior high school)

2002-2005 : SMA N 1 Purwokerto, Indonesia (senior high school)

2005-2009 : Bachelor study (S.Si., cum laude), Dept. of Chemistry, Institut Teknologi Bandung, Title of thesis: "Photoluminescence properties of nanocrystalline  $\text{Sr}_2\text{SnO}_4:\text{Ti}^{4+}$  synthesized by sonochemical method"

2009-2010 : Master study (M.Si., cum laude), Dept. of Chemistry, Institut Teknologi Bandung, Title of thesis: "Ferroelectric properties of  $\text{Pb}_{1-x}\text{Sr}_x\text{TiO}_3$ ".

2012-2015 : Doctoral study, Institute of Physical Chemistry, University of Vienna, Austria. Title of thesis: "Nanoscale thermoelectric materials"

### Work and research

2007-2010 : Basic and inorganic chemistry laboratory assistant, Dept. of Chemistry, Insitut Teknologi Bandung

2008-2009 : Bachelor thesis, Dept. of Chemistry, Insitut Teknologi Bandung. Supervisor: Dr. Bambang Prijamboedi

2-7/2010 : Exchange research stay (master thesis) at University of Groningen (RuG), The Netherlands. Supervisor: Dr. Bambang Prijamboedi and Prof. Dr. Beatriz Noheda

2011-2012 : Research assistant at Dept. of Chemistry, Insitut Teknologi Bandung. Supervisor: Dr. Bambang Prijamboedi

7-12/2011 : Part time high school teacher (chemistry) at SMA N MH Thamrin, Jakarta

2012-2015 : Doctoral thesis, Institute of Physical Chemistry, University of Vienna, Austria. Supervisor: Prof. Dr. W. Kautek and Prof. Dr. P. Rogl

2013-2015 : Research visit at Masaryk University, Brno, Czech Republic, working with Dr. Pavel Broz

6/2014 : Research stay at University of Genova, Italy. Supervisor: Prof. Adriana Saccone

## List of Publications

1. The system Ce-Zn-Si for <33.3 at.% Ce: phase relations, crystal structures and physical properties  
F. Failamani, A. Grytsiv, R. Podlucky, H. Michor, E. Bauer, P. Broz, G. Giester, P. Rogl. RSC Advances (2015), 5(46), 36480-36497.
2. Electronic structure and optical properties of  $\text{Sr}_2\text{SnO}_4$  studied with FP-LAPW method in density functional theory.  
 B. Prijamboedi, S. Umar, F. Failamani. AIP Conference Proceeding (2015), 1656, 030001.
3. Constitution of the systems  $\{\text{V}, \text{Nb}, \text{Ta}\}\text{-Sb}$  and physical properties of di-antimonides  $\{\text{V}, \text{Nb}, \text{Ta}\}\text{Sb}_2$   
F. Failamani, P. Broz, D. Maccio, S. Puchegger, H. Müller, L. Salamakha, H. Michor, A. Grytsiv, A. Saccone, E. Bauer, G. Giester, P. Rogl. Intermetallics (2015), 65, 94-110.
4.  $\text{Ba}_5\{\text{V}, \text{Nb}\}_{12}\text{Sb}_{19+x}$ , novel variants of the  $\text{Ba}_5\text{Ti}_{12}\text{Sb}_{19+x}$  - type: crystal structure and physical properties  
F. Failamani, A. Grytsiv, G. Giester, G. Polt, P. Heinrich, H. Michor, E. Bauer, M. Zehetbauer, P. Rogl. Physical Chemistry Chemical Physics (2015). (accepted).
5. High temperature FeB-type phases in the systems Ta- $\{\text{Ti}, \text{Zr}, \text{Hf}\}$ -B  
F. Failamani, K. Göschl, G. Reisinger, C.A. Nunes, G.C. Coelho, A. J. da Silva Machado, L. E. Correa, J. C. P. dos Santos, G. Giester, P. Rogl. (submitted to Journal of Phase Equilibria and Diffusion)
6. Nanostructuring of  $\text{CoSb}_3$ -based skutterudites via chemical disproportionation  
 F. Failamani, A. Grytsiv, P. Rogl, E. Bauer. (to be submitted)
7.  $\text{BaAl}_4$  derivative phases in the sections  $\{\text{La}, \text{Ce}\}\text{Ni}_2\text{Si}_2\text{-}\{\text{La}, \text{Ce}\}\text{Zn}_2\text{Si}_2$ : phase relations, crystal structures and physical properties  
F. Failamani, Z. Malik, F. Kneidinger, A. Grytsiv, H. Michor, L. Salamakha, E. Bauer, P. Rogl and G. Giester. (to be submitted)
8. Photoluminescence properties of Ti-doped  $\text{Sr}_2\text{SnO}_4$  prepared by sonochemical method and its electronic structure  
 B. Prijamboedi, F. Failamani, S. Umar. (to be submitted)



## List of Conference Contributions

1. Electronic structure and optical properties of  $\text{Sr}_2\text{SnO}_4$  studied with FP-LAPW method in density functional theory (oral presentation)  
B. Prijamboedi, S. Umar, F. Failamani.  
5<sup>th</sup> Asian Physics Symposium (APS), 10-12 July 2012, Bandung, West Java, Indonesia.
2. The system Ce-Zn-Si at <33.3 at.% Ce (oral presentation)  
F. Failamani, A. Grytsiv, Z. Malik, P. Broz, G. Giester, P. Rogl.  
19<sup>th</sup> International Conference on Solid Compounds of Transition Elements (SCTE), 21-26 June 2014, Genova, Italy.
3. The system Ce-Zn-Si at <33.3 at.% Ce: phase equilibria, crystal structures, and physical properties (oral presentation)  
F. Failamani, A. Grytsiv, Z. Malik, P. Broz, G. Giester, P. Rogl, H. Michor, E. Bauer.  
16<sup>th</sup> Annual Conference YUCOMAT, 1-5 September 2014, Herceg Novi, Montenegro.
4. Constitution of {Ta,Nb,V}-Sb systems (poster presentation)  
F. Failamani, A. Grytsiv, P. Broz, D. Maccio, H. Müller, S. Puchegger, P. Rogl, A. Saccone, E. Bauer.  
14<sup>th</sup> Discussion Meeting on Thermodynamics of Alloys (TOFA), 7-11 September 2014, Brno, Czech Republic.
5. Ferromagnetic Kondo lattice behaviour of  $\text{CeZn}(\text{Zn}_{0.29}\text{Si}_{0.71})_2$  (oral presentation)  
H. Michor, F. Failamani, A. Grytsiv, G. Giester, E. Bauer, P. Rogl.  
20<sup>th</sup> International Conference on Magnetism (ICM), 5-10 July 2015, Barcelona, Spain.